A CUMULUS ENSEMBLE MODEL WITH SIMPLE MESOSCALE STRUCTURE

by

GEORGE JOHN HUFFMAN

B.S., The Ohio State University, 1976

SUBMITTED TO THE DEPARTMENT OF METEOROLOGY AND
PHYSICAL OCEANOGRAPHY IN PARTIAL FULFILLMENT
OF THE REQUIREMENTS FOR THE DEGREE OF

DOCTOR OF PHILOSOPHY

at the

© MASSACHUSETTS INSTITUTE OF TECHNOLOGY

January, 1982

Signature of Author _____
Department of Meteorology and
Physical Oceanography, 8 January 1982

Certified by _____
Frederick Sanders
Thesis Supervisor

Accepted by _____
Peter H. Stone
Chairman, Departmental Committee on Graduate Students

Undgren
WITHDRAWN
MASSACHUSETTS INSTITUTE OF TECHNOLOGY
FROM
JUL 9 1982
LIBRARIES
LIBRARIES

A CUMULUS ENSEMBLE MODEL WITH SIMPLE MESOSCALE STRUCTURE

by

GEORGE JOHN HUFFMAN

Submitted to the Department of Meteorology and Physical Oceanography on 8 January 1982 in partial fulfillment of the requirements for the degree of Doctor of Philosophy

Abstract

In this study we consider the transport and release of heat and moisture by a cumulus cloud ensemble, including an examination of the role which mesoscale organization plays in the ensemble's activities. A numerical model is constructed and the results of the model are compared with observations.

Observations reveal that many properties of cumulus ensembles are lognormally distributed over the ensemble. Mesoscale structure is frequently observed, often as clumps of cumuli with or without other organization. The largest, longest-lasting clouds producing the most rain tend to be found in mesoscale clumps. Residual budget calculations from large scale observation show warming and drying at nearly all levels, although the details depend on geographic location.

A new cumulus ensemble model is developed. First, a time-dependent, axisymmetric, anelastic cumulus cloud model is formulated after Asai and Kasahara (1967) and Yau (1980), but with a careful analysis of lateral entrainment. This analysis shows no horizontal scale dependence due to entrainment; scale dependence arises instead from the pressure perturbation associated with the cumulus cloud. Other tests show that the Kessler (1969) microphysical parameterization yields the largest errors at cloud top and below cloud base.

This individual cumulus cloud model is generalized to a time-dependent cumulus ensemble model with tophat variable profiles in each model region. The numbers of clouds in different size classes are free parameters, determined by requiring that the model simulate the domain-averaged subcloud moisture budget. The mesoscale feature is assumed to contain all cumulus clouds.

Starting at 00Z on Day 245 of GATE, the cumulus ensemble model predicts minimal cloud activity until the sounding becomes more unstable than the initial sounding. The amount of destabilization required depends only weakly on the cloud size distribution chosen. Members of the ensemble tend to be either shallow/weak or deep/vigorous: There are relatively few middle-sized clouds. The mesoscale version produces more vigorous convection. Mesoscale contributions are shown to be important in the budgets of heat, moisture, and mass. A mesoscale anvil forms only after the outer environment saturates.

Thesis Supervisor: Dr. Frederick Sanders

Title: Professor of Meteorology

Acknowledgements and Dedication

I wish to thank Dr. David Randall and Professor Frederick Sanders for serving as my advisors during the course of this thesis. Early work on this thesis was carried out under Dr. Randall, who continued to maintain an active interest after moving to the NASA GLAS. The thesis was completed under Professor Sanders. Their diverse insights into the problem at hand and meteorology in general had a significant effect on my studies at MIT. I also wish to thank the members of the MIT Convection Club for helpful suggestions, particularly Frank Colby and Brad Colman, who read early drafts of the thesis.

Several sources of assistance made this project possible. Funding was provided by NSF grants 79-10844 ATM and 80-19301 ATM. The NASA Goddard Laboratory for Atmospheric Sciences provided the computer time required to develop and run the thesis model and to prepare the thesis. Diana L. Spiegel, site manager of the Department of Meteorology and Physical Oceanography's computer facility, provided unstinting assistance in dealing with the computer. Prof. Man-Kong Yau of McGill University provided an early version of the one-cloud model. The GATE data for model initialization and budget comparison were processed by a group at the University of Washington under Prof. Richard Reed. The thesis was printed at NASA GSFC assistance of James Abeles. Figures were expertly prepared by Isabelle Kole (line drawings) and Frank Colby (photographs).

A special acknowledgement is due Randy Dole, with whom I shared an office during this thesis. He was a ready source of encouragement and consultation throughout our striving towards our respective graduations. I am also grateful to the congregation of Old West Church for encouragement and a sense of perspective. Finally, I wish to dedicate this thesis to my parents, for their concern and understanding over the years.

GH

Table of Contents

Page

Title 1

Abstract 2

Acknowledgements and Dedication 3

Table of Contents 4

Figure Legends 6

Table Legends 12

Chapter 1: Introduction 13

Chapter 2: Observations 16

2.1 Introduction 16
2.2 Cumulus ensembles 16
2.3 Mesoscale structure 24
2.4 Residual calculations 28
2.5 Summary 32

Chapter 3: Cumulus Ensemble Models 33

3.1 Introduction 33
3.2 Models with explicit horizontal structure 34
3.3 Models with parameterized horizontal structure 43
3.4 Cloud-environment interactions 50
3.5 Summary 51

Chapter 4: The Model: One Cloud 53

4.1 General design 53
4.2 Preliminary remarks 55
4.3 Entrainment and the conservation laws 56
4.4 Application to a two-cylinder model 63
4.5 The complete cloud model 66
4.6 Cloud model behavior and sensitivity 70
4.7 Summary 96

Chapter 5: The Model: Ensemble 98

5.1 Introduction 98
5.2 Many clouds in a common environment 98
5.3 Including mesoscale organization 101
5.4 Additional details 105
5.5 Summary 111

Page

Chapter 6: Model Results 112

6.1 Introduction 112
6.2 Observations of Day 245 115
6.3 A case without mesoscale structure 118
6.4 A case with mesoscale structure 144
6.5 Test of varying mesoscale region cloud coverage 180
6.6 Test of varying cloud distribution 187
6.7 Test of increasing the allowed range of cloud radii 197
6.8 Test of starting 3 hr earlier 202
6.9 Summary 209

Chapter 7: Summary and Concluding Remarks 211

Appendix A: Symbols 217

Appendix B: A Stochastic Model of Cumulus Clumping 220

B.1 Introduction 220
B.2 Model formulation 221
B.3 Results 223
B.4 The stabilization profile 230
B.5 Discussion and conclusions 232

Appendix C: A Two-Cylinder Cloud Model 234
C.1 Introduction 234
C.2 Model equations 234
C.3 Microphysical parameterizations 236
C.4 Perturbation pressure treatment 237
C.5 Computational considerations 243

Appendix D: GATE Data Analysis 245

D.1 Introduction 245
D.2 Soundings and budgets 245
D.3 Radiative transfer 246
D.4 Precipitation 249

Appendix E: Budget Derivation 250

References 255

Biographical Note 263

Figure Legends

Figure — Page

2.1 Variation with altitude of 50 percentile (o) and 10 percentile (Δ) up- and downdraft cores, with respect to core diameter, mean vertical velocity of cores, maximum 1 s vertical velocity within core, and core mass flux. (LeMone and Zipser, 1980, Fig. 5) 19

2.2 Mean vertical velocity in up- and downdraft cores as a function of height. GATE data for 50 percentile (o) and 10 percentile (Δ) cores from LeMone and Zipser (1980), Fig. 5; Thunderstorm Project data adopted from Byers and Braham (1949), Tables 7 and 10; for the 4.5 km level only, hurricane data from Gray (1965), Fig. 13 (●,▲). (Zipser and LeMone, 1980, Fig. 1) 19

2.3 Mean "cloud"-average updraft and maximum up- and downdraft speeds as a function of height from GATE (dashed) and eastern Australia (solid). GATE values approximated from LeMone and Zipser (1980), Figs. 4b-c for cores; Australia values from Warner (1970). 21

2.4 Cumulative frequency distribution of (a) maximum area, (b) lifetime, (c) total rainfall, in log-probability coordinates for the cells of composite echoes (groups) and for single-cell echoes (individual) in GATE. (López, 1978, Figs. 6, 7, 8) 26

2.5 (a) Duration, (b) average rainfall, (c) total rain as a function of average area for the cells of composite echoes (groups) and for single-cell echoes (individual) in GATE. (López, 1978, Figs. 9, 10, 11) 27

2.6 Vertical profiles of the apparent sensible heat source (Q_1) and apparent latent heat sink (Q_2) for the B-scale area in GATE (E. ATL) and the Marshall Islands (W. PACIFIC). (after Thompson et al., 1979, Fig. 8) 31

3.1 Temperature (T) and dewpoint (T_d) soundings taken from the ship Researcher at 00Z 12 August 1974. Dotted line is a moist adiabat. (after Soong and Tao, 1980, Fig. 5) 37

3.2 Computed ω at 3 h intervals within the ITCZ rainband during 00-24Z 12 August 1974. (Soong and Tao, 1980, Fig. 3) 38

3.3 Domain-averaged cloud heating and moistening effects (subscripted c) for each 6 h during 00-24Z 12 August 1974 simulated by Soong and Tao (1980, "ST"), with the corresponding observed Q_1-Q_R and $-(c_p/L)Q_2$. (ST, Fig. 19) 38

3.4 A hypothetical ω profile and the changes of θ and q_v at every

Figure Page

2 h interval using the ω profile as simulated by Soong and Tao (1980, "ST"). (ST, Fig. 20) 40

3.5 Schematic time history of a cluster of convective cells simulated by Jones (1980, "J"). Areas denote upward motion greater than 2.5 m/s at 500 mb. Numbers above and below the gridpoint are, respectively, maximum updraft speed in the column (m/s) and level of occurrence (mb). Vortex center is located 25 km east and 85 km south of lower right corner gridpoint. (J, Fig. 7) 42

3.6 "Peak" and "dip" stabilization profiles tested by Randall and Huffman (1980, "RH"). The two curves have the same area-averaged values (over the disk). The constant stabilization case is shown for reference only. (RH, Fig. 1) 44

3.7 Environmental mass flux ($\tilde{M}$), mean mass flux ($\overline{M}$), and net convective-mesoscale mass flux (M_c+M_{md}), for category 4 of the Reed et al. (1977) wave for Johnson's (1980, "J") spectral diagnostic models with convective updrafts alone, convective up- and downdrafts, and convective up- and downdrafts plus mesoscale downdrafts. (J, Fig. 18) 47

4.1 Schematic diagram depicting the "pie-slice" of cloud over which integration is performed to obtain (4.2). 59

4.2 Initial temperature (T) and dewpoint (T_d) soundings used in Chapter 4. 72

4.3 Detailed time-height plots of area-averaged inner cylinder variables for Version P: $\overline{W}_a$, vertical velocity (m/s, values < -1 m/s shaded); $\delta\overline{\theta}_a$, deviation from initial potential temperature profile (°C); $\overline{q_{ca}}$, cloud water mixing ratio (g/kg); $\overline{q_{ra}}$, rain water mixing ratio (g/kg). Heavy dashed line at 35 min is the 20% cutoff point (see Section 4.6). . . 73

4.4 Microphysical parameterization comparison. Version P, (a) moistening, and (b) heating; Version K, (c) moistening, and (d) heating. The net change (——) is the sum of net vertical transports, both cloud-scale (-+-) and turbulent (-X-), condensational heating/drying (- -), and evaporative cooling/moistening, both cloud (-o-) and rain (-•-) evaporation. (e) Inner cylinder up- and downdraft mass fluxes for P (-+-) and K (——). 79

4.5 Cloud lifespan criterion test. As in Fig. 4.4, except for Versions; (a) P.C, (b) P.C, (c) K.C, (d) K.C, (e) P.C (-+-), K.C (——). 85

4.6 Horizontal rain advection test. As in Fig 4.4, except for Versions; (a) P.R, (b) P.R, (c) K.R, (d) K.R, (e) P.R (-+-),

Figure Page

K.R (——). 88

4.7 Vertical resolution test. As in Fig. 4.4, except for Versions; (a) K.G, (b) K.G; and (c) as in Fig. 4.4e, except K.G (——). 92

4.8 Large-scale lifting test. As in Fig. 4.4, except for Versions; (a) K.W, (b) K.W, and (c) as in Fig. 4.4e, except K.W (——). Large-scale moistening, heating, and mass flux are shown as dotted lines. 94

5.1 Schematic representation of a cumulus cloud ensemble. (a) Clouds in a homogeneous large-scale environment (bounded by E). (b) A system containing clouds, a mesoscale feature (bounded by M), and an outer environment (bounded by E). A cross section (C-C') is shown in Fig. 5.2. 100

5.2 Schematic vertical cross section through Fig. 5.1b, showing some atmospheric levels and the maximum sizes clouds attain over their lifecycles. Level 4 is depicted as carrying a mesoscale anvil (not shown in Fig. 5.1b). E and M are the boundaries in Fig. 5.1b. 103

6.1 (a) 700 mb and (b) surface maps, including streamlines at 12Z Day 245 over the GATE region. 116

6.2 Infrared satellite picture (4x4 km) at (a) 00Z Day 245 and (b) 00Z Day 246 over the GATE region. 116

6.3 Estimates of precipitation on Day 245; (-·-) radar-derived over the "Master Array", a circle circumscribing the B Array (Hudlow and Patterson, 1978); (——) heat budget-derived over the A/B Array (after Frank, 1979). 117

6.4 (a) Large scale vertical mass flux averaged over 3 hr intervals, (b) temperature and water vapor changes from initial state at 3 hr intervals due to all prescribed forcings, and (c) observed temperature and moisture changes from initial state at the end of each period. All data from Thompson et al. (1979). 119

6.5 Temperature (T) and dewpoint (T_d) soundings averaged over the GATE B Array at 00Z Day 245. 123

6.6 Cumulative frequency distribution for Cases in Chapter 6; (-●-) LN1, (-X-) LN2, (-+-) LN3, (-o-) AIC. 124

6.7 Maximum upward vertical velocity in the cloud column, and surface rainfall rate at 2 min intervals over (a) 0-3 hr, (b) 3-6 hr, (c) 6-9 hr; Case LN1.NOM. (o) 0.50 km, (+) 0.78 km, (···) 1.23 km, (-·-) 1.92 km, (——) 3.00 km radius

Figure Page

clouds. 125

6.8 Heat and moisture budgets over (a) 0-3 hr, (b) 3-6 hr, (c) 6-9 hr; Case LN1.NOM. Observed and simulated budgets are solid and dashed lines, respectively. 129

6.9 Domain-averaged temperature and moisture changes from initial state at 3 hr intervals; Case LN1.NOM. 133

6.10 Individual subensemble and region contributions to (a) heat, and (b) moisture budgets; Case LN1.NOM. 137

6.11 Vertical mass fluxes in cloud updrafts (M_u), cloud downdrafts (M_d), clouds (M_c), and the environment ($\tilde{M}$) over (a) 0-3 hr, (b) 3-6 hr, (c) 6-9 hr; Case LN1.NOM. 140

6.12 Time-height plot of vertical velocity in the mesoscale region over 6-9 hr; Case LN1.M20. 146

6.13 As in 6.8 for Case LN1.M20. 148

6.14 As in 6.9 for Case LN1.M20. 151

6.15 As in 6.9 for Case LN1.M20, except for (a) outer environment-averaged, and (b) mesoscale region-averaged. 153

6.16 As in 6.11 for Case LN1.M20, with vertical mass flux in the mesoscale region (M_m). 155

6.17 Schematic diagram illustrating LeMone and Zipser (1980) flight paths. ECS is Effective Cross Section of a cloud (measured perpendicular to a flight path). Path A shows a flight sampling a large cloud, missing a smaller cloud. Path B shows a flight with an in-cloud path length > 0.5 km. Path C shows a flight with in-cloud path length < 0.5 km (even though cloud diameter > 0.5 km). 159

6.18 Up- and downdraft average vertical velocity 50 percentile (o) and 10 percentile (Δ) speeds as a function of height. Solid symbols are LeMone and Zipser's (1980) GATE aircraft samples of "cores". All other data are for Case LN1.M20 over 6-9 hr, processed as in Section 6.4. Lines are level-by-level values, isolated symbols are layer averages, plotted at event-weighted heights. 161

6.19 Subensemble and region contributions to vertical mass flux; Case LN1.M20. 164

6.20 Accelerations in the mesoscale region vertical velocity equation, averaged over 6-9 hr for Case LN1.M20, (a) with and (b) without vertical perturbation pressure gradient in the

Figure Page

mesoscale region. 165

6.21 Vertical mass flux in the mesoscale region, averaged over 6-9 hr for Case LN1.M20, with and without vertical perturbation pressure gradient in the mesoscale region. 169

6.22 As in Fig. 6.10 for Case LN1.M20. 171

6.23 Subensemble and region contributions to the heat and moisture budgets over 6-9 hr for Case LN1.M20 for various processes; (a) net condensation, (b) vertical eddy heat flux convergence, (c) vertical eddy vapor flux convergence, (d) vertical turbulent heat flux convergence, (e) vertical turbulent vapor flux convergence (see Appendix E for formulae). 173

6.24 As in Fig. 6.8 for Case LN1.M10. 181

6.25 As in Fig. 6.8 for Case LN1.M30. 184

6.26 As in Fig. 6.9 for Case LN2.M20. 188

6.27 As in Fig. 6.8 for Case AIC.M20. 192

6.28 As in Fig. 6.10 for Case AIC.M20. 195

6.29 As in Fig. 6.8 for Case LN3.M20. 198

6.30 As in Fig. 6.9 for Case LN3.M20, after 9 hr for outer environment-averaged (-+-) and mesoscale region-averaged (——). . . . 201

6.31 As in Fig. 6.10 for Case LN3.M20. 203

6.32 As in Fig. 6.8 for Case LN1.M20 starting at 21Z Day 244, except (a) (-3)-0 hr, (b) 0-3 hr, (c) 3-6 hr, (d) 6-9 hr. . . 205

B.1 The predicted I field over steps 110-124: (a) peak, (b) dip. The contour interval is 8, with the zero line omitted; particularly intense regions are stippled. (RH, Fig. 2) 225

B.2 The predicted J field: (a) peak, step 125; (b) dip, step 125. The contour interval is 15, with negative values shaded. (RH, Figs. 3b, 3f) 225

B.3 Lagged spatial autocorrelations of J, percent: (a) peak, step 125; (b) dip, step 125. Negative areas are shaded. (RH, Figs. 4b, 4d) 226

B.4 Time autocorrelation of J, lagged from step 125: lower curve is peak, upper curve is dip. (RH, Fig. 5) 228

B.5 Time evolution of J: solid line is the spatial average for

Figure Page

both peak and dip, dotted lines are maximum and minimum values for peak, dashed lines are maximum and minimum values for dip. (RH, Fig. 6) 229

B.6 Schematic diagram illustrating a cloud's modification of its environment through induced subsidence, detrainment, and radiative cooling. (RH, Fig. 7) 231

C.1 Schematic representation of Model P microphysical interactions: cloud water condensation (CC), cloud water evaporation (EC), rain water evaporation (ER), autoconversion of cloud droplets into rain drops (AU), accretion of cloud droplets by rain drops (AC), rain drop collection by larger rain drops (CO), spontaneous (BS) and induced (BI) rain drop breakup, and "spectral" shifting of mass from one rain drop class to another (SH). Model K parameterizes all interactions within the dashed box. 238

D.1 Example of interpolating Cox and Griffith (1978) radiation data (shaded) to 500 m layers (dashed). Results of the last interpolation in p-space are shown as a heavy solid line. The particular case is 2 September 1974, long-wave, B Array. . 248

Table Legends

Table		Page
3.1	Domain size, grid spacing, and lateral boundary conditions for models reviewed in Section 3.2. The gridcell (abbreviated g.c.) is an arbitrary unit, roughly scaled to 1 cloud radius.	35
4.1	Versions, processes included (denoted by X), and results for scale dependence studies. All processes not listed are as in Version K. Version K.NoF.NoP presents identical values for all the three radii.	75
4.2	Versions and associated assumptions for sensitivity tests. . .	82
5.1	Model sensitivity as a function of radius to initiating perturbation parameters; (a) ultimate cloud height (km), together with the value of H_o for H_o = a+0.5 (km); (b) peak maximum vertical velocity (m/s).	108
6.1	Cumulus ensemble model configurations for Cases discussed in Chapter 6. See Fig. 6.6 for cloud distributions.	113
6.2	Cloud populations (per 1°x1° lat.) and rainfall (3 hr accumulation) for the Cases in Chapter 6 (a) over 0-3, 3-6, and 6-9 hr, and (b) over (-3)-0 hr. Radar-derived rainfall is Hudlow and Patterson's (1979) estimate for the B Array. . . .	134
C.1	Size categories for liquid water.	239
C.2	Variable values for evaluating anelastic pressure.	242

1. Introduction

Cumulus clouds appear in many sizes and in many different patterns of organization; cloud "streets", squall lines, and scattered cumulus humilis to name a few. Residual budget calculations show that this seemingly endless variety of clouds has important net effects on the large scale environment (e.g., Yanai et al., 1973). The first goal of this thesis is to examine the contributions by cumulus clouds (collectively forming an "ensemble") of various sizes to the heat, moisture, and mass budgets of the large scale environment (although we have not yet given a definition of "size").

In recent years it has become increasingly clear that cumulus clouds routinely exhibit organization on space and time scales falling between those of individual clouds and those of synoptic systems.[1] The presence of such "mesoscale" organization is easy to see in strong cases, such as squall lines, but López (1978) demonstrated that mesoscale organization was also present for seemingly random rain showers during the Global Atmospheric Research Project (GARP) Atlantic Tropical Experiment (GATE). Even with these observations, however, we do not know whether such organization is a passive rearrangement of the clouds which would have occurred anyway, or whether the nature of the clouds depends on the organization. The second goal of this thesis is to examine the large scale effects of mesoscale organization within the cumulus ensemble.

We pursue these two goals with the aid of a new numerical model of a

---

1 Loosely, scales of order 30 km and 3 hr. See Fujita (1981) for a summary of the various definitions of "mesoscale" and Emanuel (1979) for a specific dynamical scaling. The exact size of mesoscale events is not crucial to this study.

cumulus ensemble. As discussed in Chapter 3, a number of researchers have addressed similar goals using models which have been either relatively complete and costly, or highly parameterized and economical. The results of the more parameterized models are hard to compare with observations. The third goal of this thesis is to create an economical model in which many of the questionable assumptions of the highly parameterized models are relaxed, and which generates results which can be compared directly with observational results. The model design is presented in Chapter 4.

We begin the study by undertaking a review of the current literature on cumulus ensembles. Reviews exist on related topics, such as cumulus clouds (Ludlam, 1980) and cumulus parameterizations (Arakawa, 1974), but no summary has been published for the cumulus ensemble. The first part of our review, contained in Chapter 2, concerns observations. Photographic and radar data provide the basis for specifying the numbers of clouds in different size categories as a function of time, as well as an estimate of some microphysical parameters (rainwater mass, hydrometeor phase). Aircraft flights provide detailed data on the atmosphere at a few points in time and space. Successive sets of upper air soundings provide a means for estimating the net heating and drying due to the cumulus cloud ensemble. These techniques are limited by observational accuracy and data coverage, but when available they provide a solid basis of facts.

The second part of our review concerns numerical models. Models allow a researcher the freedom to isolate and follow specific mechanisms and variables with results available over the entire domain, but they suffer limitations from simplifying physical assumptions, numerical

approximations, and initialization errors. Chapter 3 provides a review of cumulus ensemble models, with emphasis on the effects of mesoscale organization.

Following these reviews, we proceed to develop the cumulus ensemble model. The method adopted in the present study combines observational and modelling approaches; the observed cumulus budgets discussed in Chapter 2 represent the integrated effect of all clouds, so that it is possible, in principle, to find the subensemble populations if an ensemble model is formulated with subensemble populations as free parameters. This approach is similar to the "spectral diagnostic budget study" discussed in Section 3.3 (see Ogura and Cho, 1973). In Chapter 4 we develop a simple model of an isolated cloud based on the Asai and Kasahara (1967) "two-cylinder" cloud model. Tests are performed to examine various approximations, including the microphysical parameterization. Scale dependence is examined. Chapter 5 describes the generalization from the one-cloud model to the cumulus ensemble model, including a simple model of mesoscale structure. This model incorporates the numbers of clouds of different radii and the area of the mesoscale structure as adjustable parameters.

Chapter 6 presents the results obtained by applying this cumulus ensemble model in several configurations to a particular case from Phase III of GATE (2 September 1974, Julian Day 245). The role of mesoscale structure and cloud population are examined by considering heat, moisture, and mass budgets, including contributions to those budgets by individual subensembles and regions.

Finally, a general discussion is presented in Chapter 7.

2. Observations

2.1 Introduction

We start our study by reviewing some observations of cumulus cloud ensembles. As stated in Chapter 1, observations constitute our basic source of information about the atmosphere, yet the space and time scales of cumulus ensembles typically limit the information which we may collect. In particular, it is not possible to observe the heating and drying by clouds of various sizes or to observe the effect of mesoscale organization on those processes. Instead, we will point out various data which provide guidance on the design and behavior of the model to be developed in later chapters.

In the next section we consider various properties of the ensemble, such as cloud size distribution and mass fluxes, which the model should simulate. Then we review observations dealing with mesoscale structure in ensembles to investigate the typical form of such structures. Finally, we consider the residual heat and moisture budgets calculated from large-scale observations. Except for observational error, these residuals tell us the total rates of heating and drying by the whole ensemble.

2.2 Cumulus ensembles

A variety of observational techniques has been applied to study the cumulus cloud ensemble. The most direct is to fly one or more instrumented aircraft through the region of interest at various levels, giving successive "snapshots" of the conditions along the flight path. Although these individual passes sample very small fractions of the cloud field, it is typically assumed that making a large number of

passes gives a representative sample of the directly measured quantities, such as vertical velocity. The method has potential for yielding heat and moisture fluxes, but the aircraft data are generally too sparse to permit such calculations, since these fluxes depend on area-average correlations.

The Thunderstorm Project, which was described by Byers and Braham (1949), studied thunderstorms in Florida (1946) and Ohio (1947). It represented a large, integrated effort at understanding cumulus convection and yielded many results which still stand. The basic observational system included a surface network, PPI and RHI radar, rawinsondes, and aircraft flying at 5 levels. Observations were concentrated on cumulonimbi, both isolated and in lines. Gray (1965) reported on a second aircraft data set, recorded during hurricane penetration flights in 1957-1958 at flight level (4.6 km). Warner (1970) reported observations of "active" and "mature" members of a field of shallow (average depth less than 2 km) cumuli on the east coast of Australia in 1964, 1966, and 1967. The results include peak vertical velocities and r.m.s. values averaged over the flight paths inside the visible cloud. Finally, GATE provided satellite, radar, rawinsonde, aircraft, and other observations in the eastern tropical Atlantic in 1974. During GATE, the aircraft were equipped with inertial navigational systems, allowing greater accuracy in computing vertical velocity than was previously possible. LeMone and Zipser (1980) and Zipser and LeMone (1980) (LZ, ZL respectively) studied flight data from six convectively active days at various levels from the surface to 8 km. They defined updrafts and downdrafts strictly on vertical velocity structure without reference to other variables: An updraft or downdraft "core"

was defined as having magnitude of at least 1 m/s for a flight track length of at least 0.5 km.

LZ and ZL's analyses are the most extensive available. As such, several of their results will be used to provide a measure of the successes and shortcomings of our model. The most important aspects of their analyses are as follows:

1. Diameter, average vertical velocity, maximum vertical velocity, and mass flux are approximately[1] lognormally distributed[2] within each altitude group (refer to Fig. 2.1 for illustrations of this and succeeding points).
2. Downdraft cores are narrower than updraft cores. The size distributions are nearly constant with height. Downdraft cores are about two-thirds as frequent as updraft cores. In the mid-troposphere up- and downdraft cores cover some 4.7% and 2.8% of the flight track lengths.
3. The magnitude of downdraft core vertical velocities and mass fluxes are smaller than the comparable numbers for updraft cores, except

---

1 Apparently judged by visually comparing the data to a straight line on lognormal paper, e.g., graph paper having the argument of the cumulative normal distribution as one axis and the logarithm of the variable as the other axis (cf. Fig. 2.4).

2 The basic "lognormal" distribution is defined as the logarithm of the variate displaying a normal distribution. Compared to an exponential distribution, the lognormal has "too few" occurances in the midrange of values. Compared to a normal distribution, the lognormal peaks at smaller values. Since the prototypical generating function of the normal distribution is the addition of random numbers, and since the sum of the logarithms of several numbers equals the logarithm of the product of those numbers, it can be shown that the prototypical generating function of the lognormal distribution is the multiplication of random numbers (Aitchison and Brown, 1963). Nonetheless, one must be very careful in identifying this generating function with particular physical mechanisms.

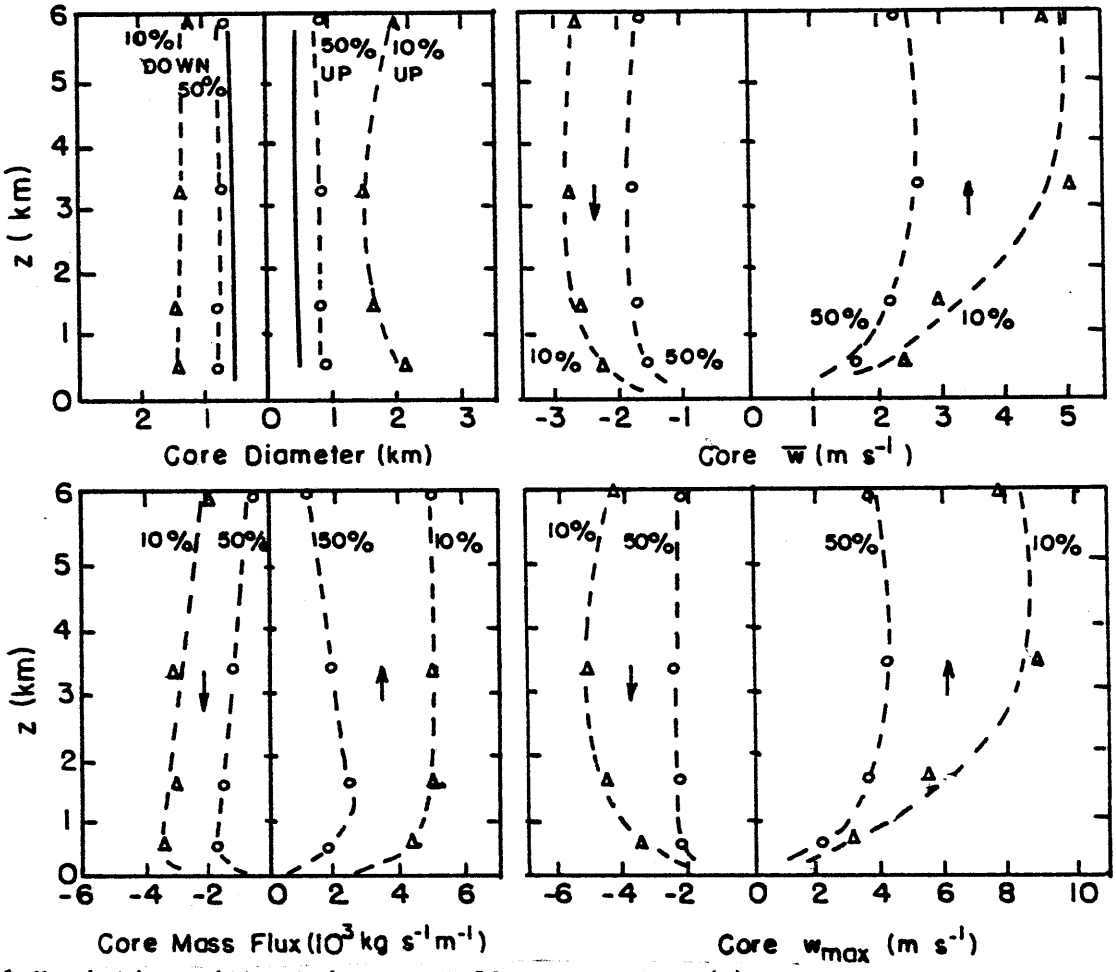


Fig. 2.1 Variation with altitude of 50 percentile (o) and 10 percentile (Δ) up- and downdraft cores, with respect to core diameter, mean vertical velocity of cores, maximum 1 s vertical velocity within core, and core mass flux. (LeMone and Zipser, 1980, Fig. 5)

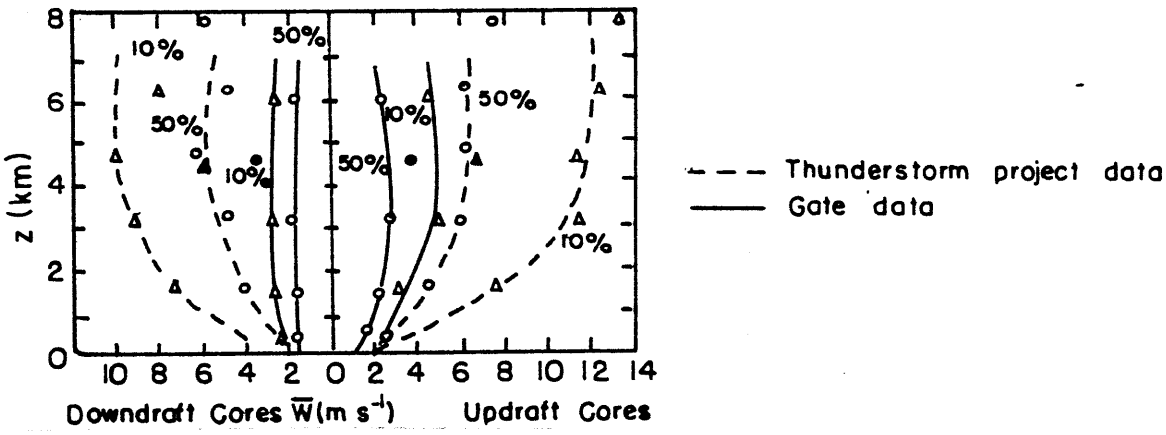


Fig. 2.2 Mean vertical velocity in up- and downdraft cores as a function of height. GATE data for 50 percentile (o) and 10 percentile (Δ) cores from LeMone and Zipser (1980), Fig. 5; Thunderstorm Project data adopted from Byers and Braham (1949), Tables 7 and 10; for the 4.5 km level only, hurricane data from Gray (1965), Fig. 13 (●,▲). (Zipser and LeMone, 1980, Fig. 1)

near cloud base, where they are similar.

4. In the mid-troposphere, only the upper decile[3] of GATE updraft cores exceed a 2 km diameter and reach a 5 m/s mean vertical velocity. No core in the data sample has a mean vertical velocity as great as 8 m/s.

ZL reanalyzed the Thunderstorm Project and hurricane penetration studies for comparison with their own work, presenting a convenient summary:

1. Diameter and vertical velocity are approximately lognormally distributed in the three data sets.
2. Measurement techniques differed, but ZL state that "the true diameter population in all three data sets is very nearly identical."
3. The general shapes of the vertical velocity profiles in GATE and the Thunderstorm Project are similar (Fig. 2.2), however, the magnitudes differ by a factor of 3. Additionally, the hurricane statistics (shown as shaded symbols in Fig. 2.2) are much closer to the GATE magnitudes than to those in the Thunderstorm Project. This result is consistent with the greater conditional instability displayed in the upper-air soundings collected in the Thunderstorm Project.
4. The Thunderstorm Project downdraft statistics fluctuate more with height than the GATE statistics.

Warner's study of shallow cumuli is not reported in the same format as the other studies, but it is possible to make a few comparisons if we estimate the means of various quantites from Fig. 4 of LZ. Fig. 2.3

---

3 "Percentiles" tell what fraction of the samples have a value smaller than the stated value. Here, only 10% of cores exceed 2 km and 5 m/s.

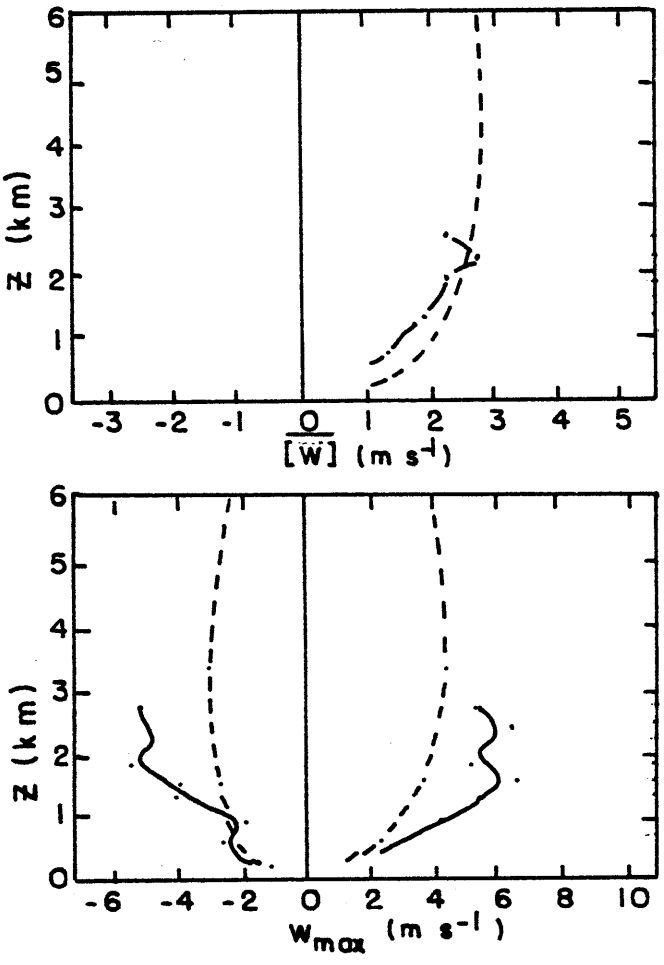


Fig. 2.3 Mean "cloud"-average updraft and maximum up- and downdraft speeds as a function of height from GATE (dashed) and eastern Australia (solid). GATE values approximated from LeMone and Zipser (1980), Figs. 4b-c for cores; Australia values from Warner (1970).

presents Warner's ensemble-average r.m.s. vertical velocity and peak up- and downdraft velocity profiles, together with estimates of the ensemble-mean average vertical velocity and peak up- and downdraft velocity profiles for LZ's cores. Note that the estimated means for LZ are very close to their medians shown in Fig. 2.1. The major differences between the two data sets are that

1. Warner uses r.m.s. while LZ use linear averages,
2. Warner defines the averaging area by the visible cloud while LZ specify vertical velocity threshholds, and
3. Warner considers active and mature clouds while LZ include all phases of growth.

We see that, even though shallow, the cumuli in Warner's sample still manage to generate updrafts which are about as powerful as those in GATE. In fact, the maximum velocities that Warner recorded appear to be significantly larger than the maxima seen in GATE. The peak velocities seen in the Thunderstorm Project (not plotted) are larger than in either of the others. We conclude that the depth of the convection in different synoptic situations need not be closely related to the vigor of the drafts within the clouds.

It is important to remember (as pointed out in the studies described) that NONE of these statistics describe individual drafts, but rather present random samples of drafts at the various levels, which need not have continuity with the samples included at other levels.

In contrast to penetration flights, the incoherent radar provides an instantaneous picture of the atmosphere over many km^3 for one parameter, radar reflectivity, allowing researchers to estimate the size of many clouds at once. López (1977) provides a summary of many of the recent

studies in the literature. All studies examined, from many different areas of the world, yield ensemble populations which are not significantly different from a lognormal distribution with respect to height, area, and duration (as measured by the chi-squared statistical test at the 5% level).

Houze and Cheng (1977) tagged each echo recorded by the Oceanographer at 1200 GMT each day of GATE, and traced their life histories. Although Houze and Cheng chose to work with constant-reflectivity threshholds, they also found lognormality in echo area, echo duration, and maximum echo height. Since the data set covers all three phases of GATE, Houze and Cheng are able to show that the quantitative details change with time, but that the basic behavior described above does not change.

Another radar technique uses Doppler shifts in the reflected signal to infer velocities. The direct Doppler measurement of vertical velocities requires that the antenna axis be vertically oriented, resulting in successive 1-dimensional velocity profiles (Battan and Theis, 1970). Alternatively, 3-dimensional scans from 2 or more Doppler radars may be combined with assumptions about mass conservation to derive the 3 velocity components (Heymsfield, 1978, among others). The chief limitation of these methods is that reliable results are only available in regions filled with sufficiently reflective material. No large inventory of Doppler statistics on cloud ensembles has yet been reported. Nonetheless, on a cloud-by-cloud basis the large gradients in vertical velocity within the cumulus cloud are easy to see in Doppler data (e.g., Fig. 2 in Battan and Theis, 1970).

A final method for observing cumulus ensembles is photography from

high-altitude aircraft or satellites. Such efforts typically yield data on the visible cloud dimensions and geometry in the ensemble over many tens of km² at the same time, although it is easy for one cloud to hide another. Plank (1965) gives a complete account of manually reducing photographic data from aircraft, as well as general descriptions of various cases of ensemble evolution over Florida in August-September 1957. He found it possible to identify and tabulate cumuli with diameters as small as 50 feet, a size which would certainly escape radar detection. Based on that study, Plank (1969) compiled detailed statistics for 19 observations in 4 cases. He fitted exponential curves to the number density distributions (as functions of diameter) and considered them to be sufficiently accurate. However, López (1978) reanalyzed the distribution for 0905 EST (on 10 August 1957) and showed that it was lognormal at the 95% confidence level in a chi-squared test. Inspection of the distributions for the other observation times reveals that Plank systematically found "too many" of the smallest and largest clouds for an exponential distribution, which would be anticipated if the distribution was actually lognormal.

2.3 Mesoscale structure

Various strong forms of mesoscale structure, such as squall lines, have long been known, but recent observations show that less spectacular forms are quite common. In examining the life histories of representative echoes recorded by the Oceanographer on 9-14 August and 1-6 September 1974 (in GATE, Phases II and III, respectively) López (1978) found the same lognormal relations as in previous studies, but he made an important additional discovery. When an echo contained several maxima

in reflectivity, referred to as "cells", he would designate that echo as "composite" and record the statistics of each cell separately.[4] Following Randall and Huffman (1980) we define a "clump" as a group of cumulus clouds whose members are much more closely spaced than the average spacing over the population, and which maintains its identity over many cloud lifetimes. This is somewhat similar, but not identical, to Cho's (1978) concept of the independent cloud group. By this definition the López composite echo is also a clump. López found that cells which were members of composite echoes generally attain larger size, last longer, and produce more rain than cells which are isolated (Fig. 2.4). Even when average cell area is taken into account, duration, average rainfall rate, and total rain production are all larger for members of composite echoes (Fig. 2.5). It is not surprising that during the period López studied the largest 10% of the GATE echoes (which he showed to be composite echoes) produced 90% of the rainfall.

Along the same lines, the Houze and Cheng (1977) study noted above showed the tendency for large echoes to contain multiple maxima in reflectivity over their whole data set.

Among the many researchers who have examined the convection associated with mid-latitude cyclones, several have noted long-lived mesoscale areas of heavy precipitation, for example, Browning and Harrold (1969), Kreitzburg and Brown (1970), Austin and Houze (1972), and Hill and Browning (1979). Besides radar, these studies considered other data sources such as raingage and rawinsonde networks. Browning and Harrold

---

4 Independently, Crane (1979) has successfully automated this cell-tracking process, a significant improvement over the manual procedure in López (1978) and the threshhold-dependent procedures of others.

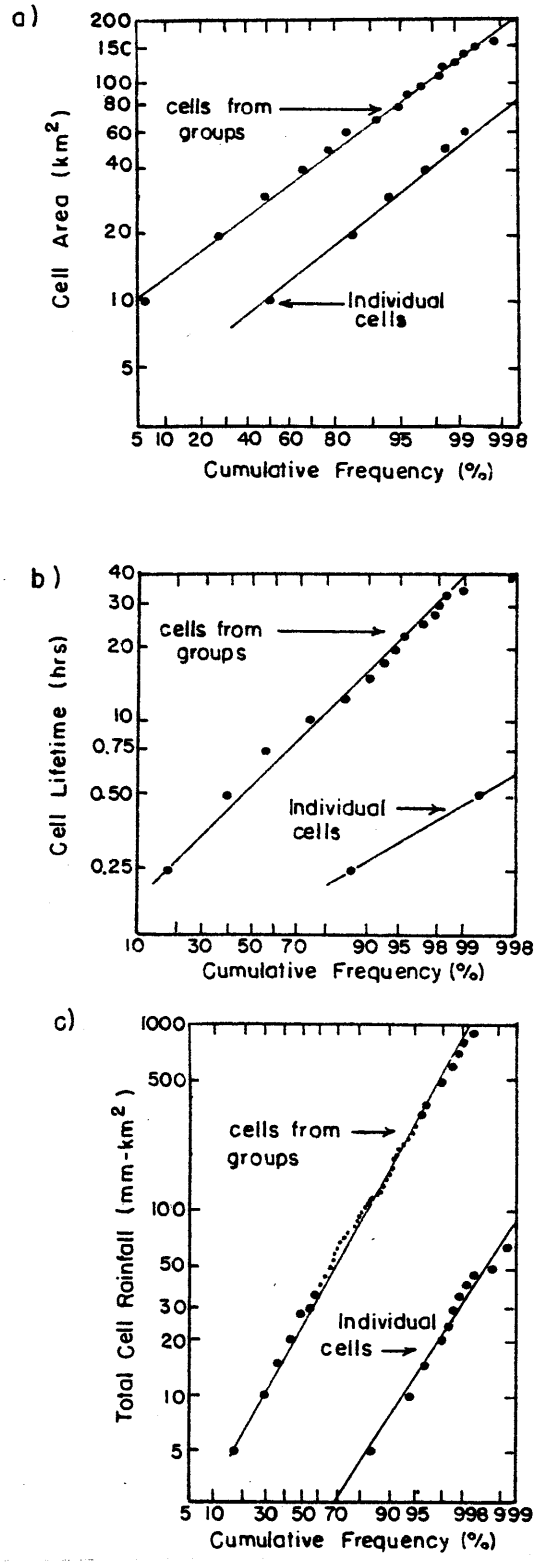


Fig. 2.4 Cumulative frequency distribution of (a) maximum area, (b) lifetime, (c) total rainfall, in log-probability coordinates for the cells of composite echoes (groups) and for single-cell echoes (individual) in GATE. (Lopez, 1978, Figs. 6, 7, 8)

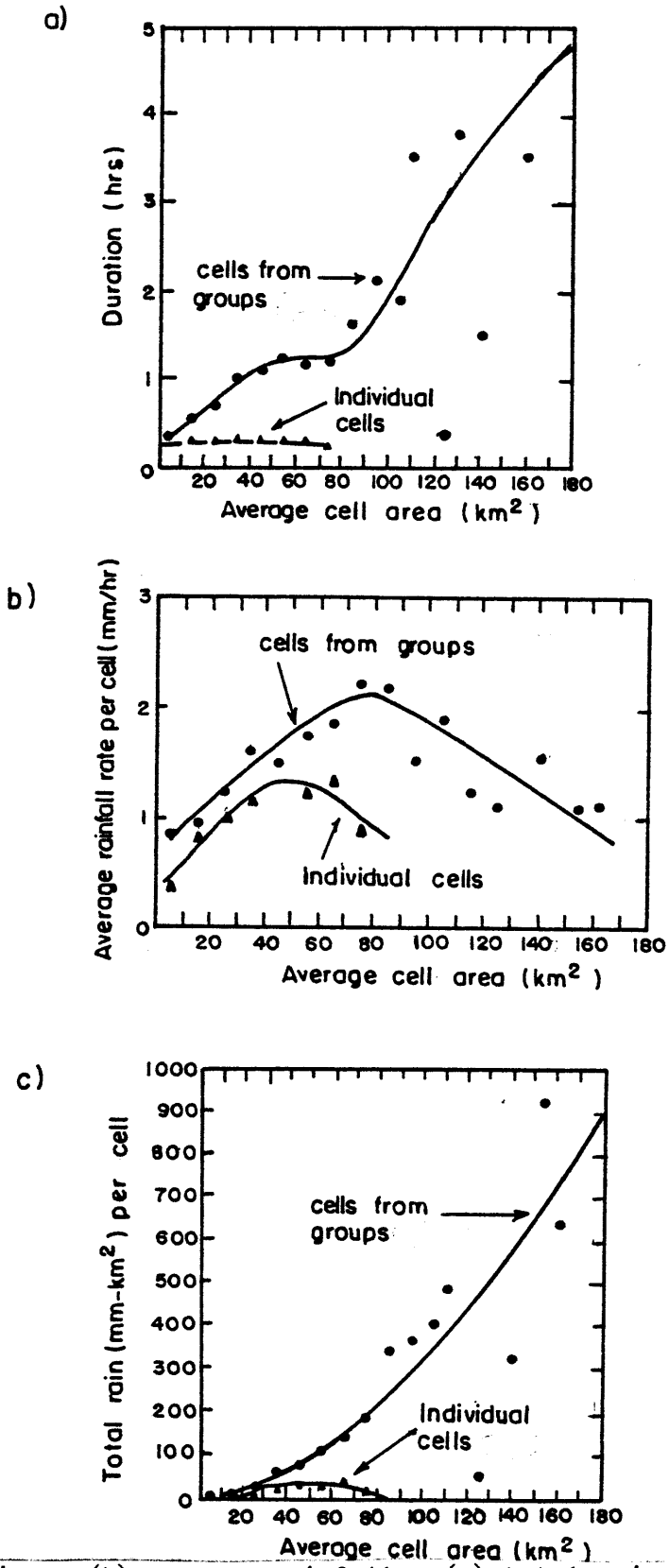


Fig. 2.5 (a) Duration, (b) average rainfall, (c) total rain as a function of average area for the cells of composite echoes (groups) and for single-cell echoes (individual) in GATE. (Lopez, 1978, Figs. 9, 10, 11)

describe a "rain area", and Austin and Houze describe a "small mesoscale area" (SMSA), both of which fit our description of clumps (persistent groups of convective cells). Austin and Houze catalogued the time-average cross-sectional area for 25 SMSA's (their Fig. 8), and these data nearly follow a straight line when plotted on lognormal graph paper. This result is similar to the finding for the López (1978) composite echoes. Although the rain areas and SMSA's were typically embedded in larger precipitation areas, the occurance and persistance of such mesoscale features were not strongly dependent on the overall organization.

Returning to Plank (1969), we find a discussion of the existance of groups of cumuli which were either connected at the base or very closely spaced compared to the average spacing, i.e., the existance of clumps. He found clumps to have sizes up to 2-3 times the size of the largest single cloud and he commented that the largest individual clouds tended to be associated with clumps. Finally, Plank found that the size distributions and the group structures were not affected by the degree of large-scale "patternform" organization (streets or bands).

2.4 Residual calculations

The final form of observation to be discussed is based on calculating the net heat and moisture effects of the cumulus ensemble. Following Yanai et al. (1973), we rewrite the conservation equations for sensible and latent heat in Reynolds-average form, partitioning variables into horizontal-average and -deviation components and then averaging the equations horizontally. Terms are grouped according to whether or not they are (in principle) directly calculable from a widely-spaced collection of rawinsonde observations, yielding the apparent source of sensi-

ble heat and the apparent sink of latent heat:

$$Q_1 = \frac{\partial \bar{s}}{\partial t} + \overline{\nabla \cdot s\vec{V}} + \frac{\partial}{\partial p}(\bar{s}\ \overline{\omega})$$

$$= L(c-e) - \frac{\partial}{\partial p}(\overline{s'\omega'}) + Q_R \qquad (2.1)$$

$$Q_2 = -L\left[\frac{\partial \bar{q}_v}{\partial t} + \overline{\nabla \cdot q_v\vec{V}} + \frac{\partial}{\partial p}(\bar{q}\ \overline{\omega}) \right]$$

$$= L(c-e) + L\frac{\partial}{\partial p}(\overline{q_v'\omega'}) \qquad (2.2)$$

where the variables have their conventional meaning (see Appendix A for a complete listing). The more specialized symbols include

- $\overline{(\ )}$ large-scale horizontal average
- $(\ )'$ $(\ ) - \overline{(\ )}$
- s dry static energy (strictly conserved only for dry adiabatic processes and $dp/dt = \vec{V}\cdot\nabla p$); $s = C_pT + gz$
- c horizontally averaged rate of condensation per unit mass of air
- e horizontally averaged rate of water drop evaporation per unit mass of air
- Q_R horizontally averaged radiational heating (local effects are neglected because of the complexity in their calculation).

Note that radiation and phase change are placed with the residual terms because they are not calculated from the rawinsonde data. Also, horizontal turbulent flux divergences are neglected. Except for errors in approximating the large-scale terms, Q_1 and Q_2 represent the net effects

of the cumulus ensemble, including the mesoscale features.

These budget terms describe the basic cloud effects on the atmosphere, so many investigators have calculated Q_1 and Q_2. Thompson et al. (1979) present average values of each from the Marshall Islands (W. Pacific) and GATE (E. Atlantic), reproduced in Figure 2.6. We know that eddies driven by moist convection should have upward vertical motion deviations correlated with warm, moist deviations (and, conversely, downward-cool-dry correlations) over the depth of the cloud, but not above or below it. That is, the vertical eddy flux divergence of both heat and moisture is generally positive just above cloud base and negative around cloud top. Comparing the cloud ensemble expressions in (2.1) and (2.2), we see that, except for a small radiative term, Q_1 and Q_2 only differ by the sign of the vertical eddy flux divergence terms. Additionally, we know that saturation mixing ratio decreases quasi-exponentially with height. Thus, we should expect Q_2 to peak at a lower altitude than Q_1, as it does in Fig. 2.6. Comparing the two regions, we see that the GATE data display maxima which are larger and which occur at lower altitudes than in the Marshall Island data. If we recall that horizontal gradients and changes with time are small over the tropical oceans for s and q_v (Betts, 1974), then we would expect the large scale expressions in (2.1) and (2.2) to depend on the vertical flux divergence terms. As Thompson et al. point out, the vertical profiles of temperature and moisture are similar in the two regions, so it is the respective average vertical velocities which account for most of the differences between the profiles for the two regions. Nonetheless, the general action of the cloud ensemble is the same in both regions, adding heat and removing moisture.

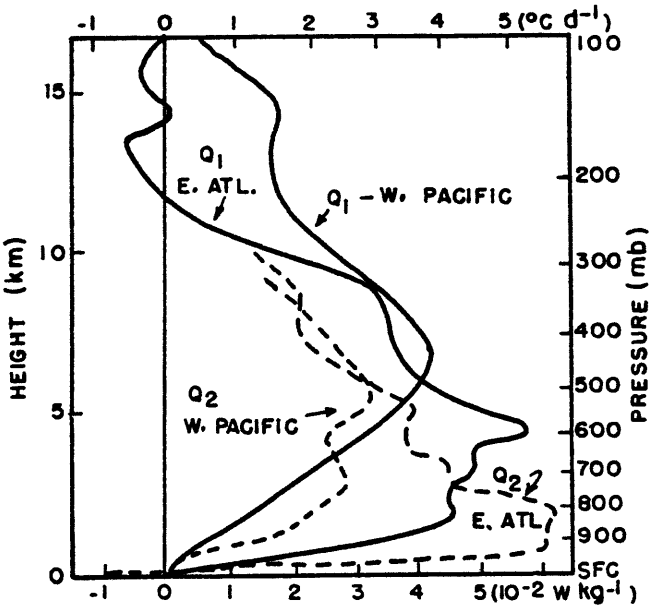


Fig. 2.6 Vertical profiles of the apparent sensible heat source (Q_1) and apparent latent heat sink (Q_2) for the B-scale area in GATE (E. ATL) and the Marshall Islands (W. PACIFIC). (after Thompson et al., 1979, Fig. 8)

In the next chapter we will see how it is possible to estimate individual cloud contributions to these net budgets by applying a cloud model in the "spectral diagnostic budget study".

2.5 Summary

Observations provide a basic description of cumulus ensembles upon which we will build in succeeding chapters:

1. Many properties of cells seem to be lognormally distributed, including diameter, duration, total rainfall, average vertical velocity, and maximum vertical velocity.
2. Up- and downdraft "core" diameter distributions are nearly constant with height in GATE. (This statement implies nothing about the size of individual cores as a function of height.)
3. Up- and downdraft mass fluxes are comparable at cloud base, with updraft mass fluxes dominating above cloud base.
4. Mesoscale structure is frequently observed, often as clumps of cumuli appearing with or without other kinds of organization.
5. The largest, longest-lived clouds producing the most rain tend to be found within cumulus clumps. Normalization by cloud cross-sectional area does not change these results.
6. The net effect of the ensemble is to warm and dry the bulk of the troposphere for areas which are of synoptic scale or larger. Profiles from the western Pacific and eastern Atlantic show warming and drying at nearly all levels, although details depend on the region.
7. Over the tropical oceans the convective motions are much weaker than those in midlatitudes, yet large amounts of heat and moisture are transported.

3. Cumulus Ensemble Models

3.1 Introduction

A second approach to understanding cumulus ensembles and the role of mesoscale structure is afforded by numerical models. The advantage, of course, is that a model may be formulated so as to yield quantities which are not easily observed, such as heat and moisture budget terms. At the same time it is very important that at least some of the key model output variables be observable, so that the results can be verified against observations. Limitations of the modelling approach arise from physical approximations, numerical approximations, and inexact input data. The review in this chapter has two objectives; first, to assess previous approaches to modelling ensembles, as a preliminary to describing the model used in this study, and second, to summarize results obtained by other studies of the roles of the cumulus ensemble and mesoscale structure in causing the large-scale heat and moisture effects we see.

A straightforward approach to modelling the cumulus cloud ensemble is to approximate the exact equations on a high resolution, three-dimensional grid and integrate forward in time. The fact that this method is too expensive, in general, has prompted a variety of approximations to the ideal model. The fundamental issue in describing these approximations is the treatment of horizontal structure. When a model possesses explicit horizontal structure, the equations must completely describe the spatial and temporal distribution of clouds (on the scale of the grid spacing). Thus, we say that models with explicit horizontal structure are "intrinsically closed".

There are many other cases in which resource limitations block the use of explicit horizontal structure in representing the cumulus ensemble, for example in global circulation models. Under these conditions it is still possible to formulate a complete set of model equations by "extrinsic closure", substituting a "closure assumption" (Arakawa and Schubert, 1974) for the detailed structure which depended on the horizontal grid. That is, the horizontal structure is "parameterized" by relating the cloud distribution to the variables which are known.

In the next two Sections we consider models with and without explicit horizontal structure, respectively. Then a short discussion of cloud-environment interactions is presented.

3.2 Models with explicit horizontal structure

The more complete and expensive of the two approaches is to explicitly simulate the horizontal structure of the cloud field. The ideal stated above, of a high-resolution three-dimensional model, is just now becoming practical. The closest approaches include the high resolution model of the trade wind boundary layer which admits tiny, non-precipitating clouds, reported by Sommeria (1976) and Sommeria and LeMone (1978), and the description in Klemp et al. (1980) of two interacting cumulonimbi. Table 3.1 summarizes some of the details of the papers reviewed in this Section.

Up to now, most cumulus ensemble models have employed slab-symmetric geometry, an economical approximation which partially preserves the horizontal structure. Hill (1974) used a model having a slab-symmetric, shallow domain to show instantaneous maps of cloud, rain, and velocity at various times, demonstrating the evolution of the ensemble. He found

Table 3.1 Domain size, grid spacing, and lateral boundary conditions for models reviewed in Section 3.2. The grid-cell (abbreviated g.c.) is an arbitrary unit, roughly scaled to 1 cloud radius.

Model	Domain (km) hor.	vert.	Grid (m) hor.	vert.	Lateral BC
Sommeria (1976), S. + LeMone (1978)	2, 2	2.	50	50	periodic
Klemp et al. (1980)	94, 70	17.5	2000	700	open
Hill (1974)	16	5.	250	250	periodic
Hill (1977)	32	9.	250	250	periodic
Soong + Ogura (1980)	6.4	3.2	100	100	periodic
Soong + Tao (1980)	64	15.6	1000	300	periodic
Gordon (1978)	150, 12	15.	400#	250*	open#
Yamasaki (1977)	1350	20.	400*	600*	closed
Jones (1980)	300@	1000mb&	10000@	35mb*	nested@
Randall + Huffman (1980)	50g.c.	None	1g.c.	None	periodic

* Minimum grid spacing.
\# Minimum grid spacing and B.C. in 150 km direction. In 12 km direction they are 3 km and reflective, respectively.
@ Innermost grid only; middle, outer grids are 3 times nested size; outer B.C. is open.
& Sigma coordinates.

that new cloud initiation depends on the current configuration of clouds, and small circulations "too close" to the large clouds are suppressed or ingested by them. Hill (1977) extended the domain and initialized the model from data. The time behavior of maximum cloud top heights is shown to agree with observations until (as in his previous paper) the deep clouds fill the depth of the domain and are stopped at the model top.

Soong and Ogura (1980) constructed a slab-symmetric, anelastic model to study a suppressed trade wind boundary layer. They specified the initial sounding, radiative heating, and horizontal average vertical velocity from a particular case in BOMEX (the Barbados Oceanographic and Meteorological EXperiment), then followed the evolution of the system in time, finding fair agreement with the observed evolution. The model ensemble acted to maintain the tradewind inversion, warming and moistening the atmosphere, except for evaporative cooling at the base of the inversion and vertical eddy flux drying at the top of the inversion. Soong and Tao (1980) enlarged the mesh length to study a case of deep convection in GATE. Because the domain is relatively small and slab-symmetric, they oriented the domain perpendicular to the main band in which the convection occurred and considered the entire region to be representative of the mesoscale system.

Since the present study also deals with a cumulus ensemble and GATE data, it is of interest to carefully consider Soong and Tao's results. Given the initial sounding shown in Fig. 3.1 and the kinematically calculated vertical velocities shown in Fig. 3.2, they proceeded to calculate heat and moisture effects simulated by the model for comparison with the observed budgets of Q_1 and Q_2 (Fig. 3.3). The simulated budg-

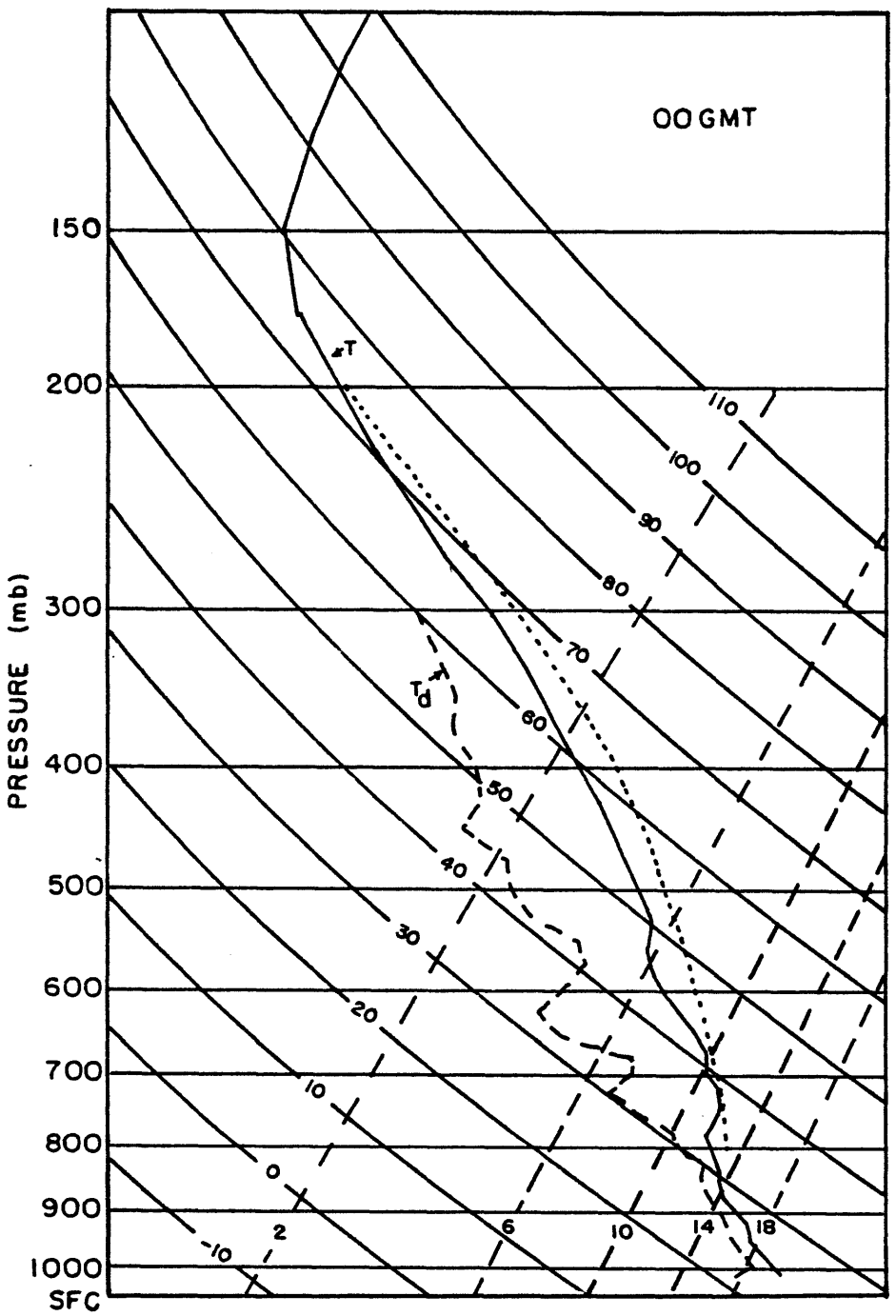


Fig. 3.1 Temperature (T) and dewpoint (T_d) soundings taken from the ship Researcher at 00Z 12 August 1974. Dotted line is a moist adiabat. (after Soong and Tao, 1980, Fig. 5)

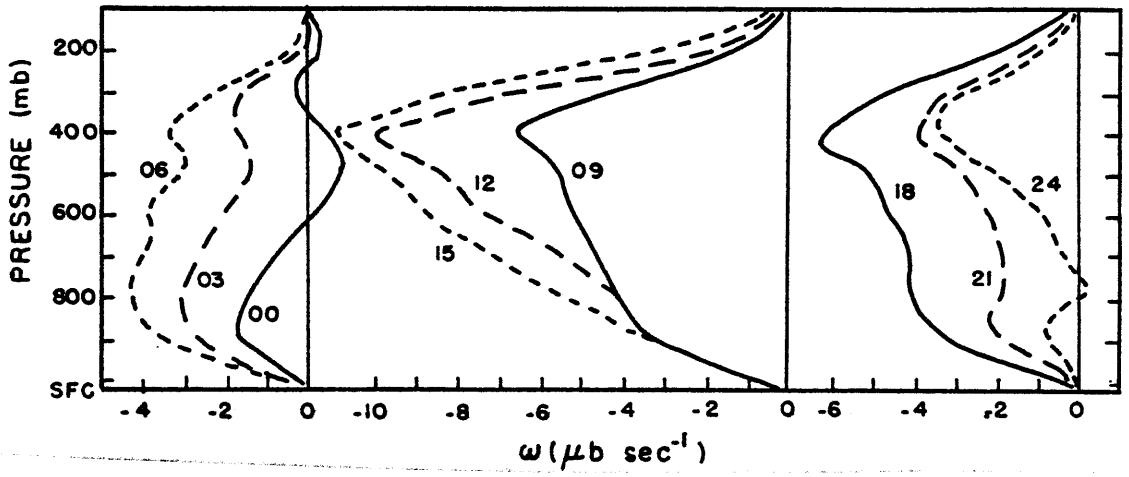


Fig. 3.2 Computed ω at 3 h intervals within the ITCZ rainband during 00-24Z 12 August 1974. (Soong and Tao, 1980, Fig. 3)

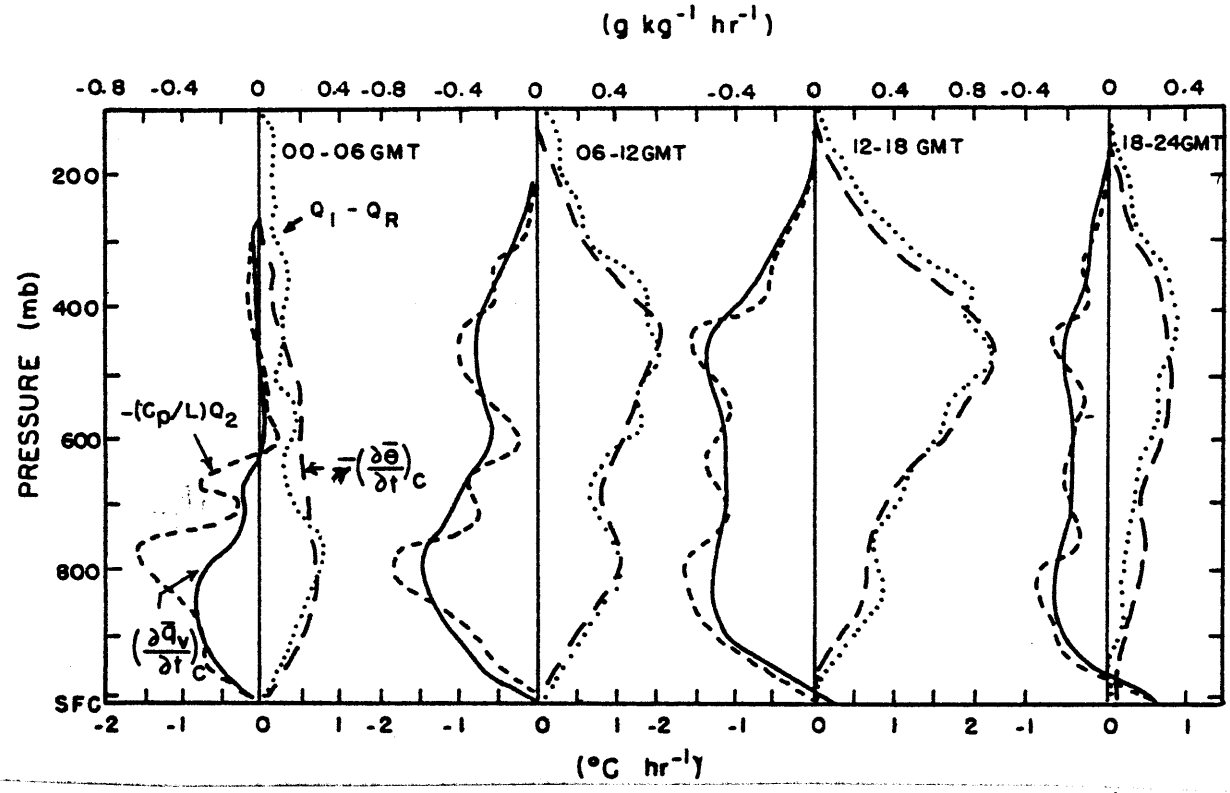


Fig. 3.3 Domain-averaged cloud heating and moistening effects (subscripted c) for each 6 h during 00-24Z 12 August 1974 simulated by Soong and Tao (1980, "ST"), with the corresponding observed Q_1-Q_R and $-(c_p/L)Q_2$. (ST, Fig. 19)

ets are good, for the most part, reproducing the large increase in cloud-induced heating and drying which accompanies the shift to a large upward mass flux in the 12-18 GMT period and the subsequent decay in activity. The worst agreement arises in the first 6 hours, when the model underpredicts the removal of water vapor by some 0.4 g/(kg hr) at 780 mb, a difference of 50%. At the end of the 6 hours the model is some 2.0-2.5 g/kg moister at 780 mb than the corresponding observations. Subsequent model budgets are in close agreement with observations, so this excess appears to be maintained over the whole integration. As will be discussed more fully in Chapter 7, we believe that this moistening, which appears to be an error according to the large-scale budget analysis, is an integral part of the initiation of a mesoscale environment suitable for deep convection. As added evidence, we note a second experiment in which Soong and Tao specified a hypothetical area-average vertical velocity profile, then plotted the horizontal average departures of θ and q_v from the initial sounding (Fig. 3.4). Once again, there is a rapid moistening, achieving a deviation of more than 2 g/kg by 6 hr at 760 mb. Noting the cooling at the same level, we see that the model rapidly destabilizes the environment in the first 2 hr, but then changes more slowly at the lower levels as the deep clouds appear.

In a few cases it is possible to simplify the domain (while retaining explicit horizontal structure) by considering systems with known symmetry. Gordon (1978) modelled an Oklahoma cold front with a stretched grid in the horizontal and vertical, giving the minimum grid spacing around the leading edge of the cold air, near the ground. The computer storage required was sufficiently small that the model could be made "quasi-three dimensional" by carrying 3 gridpoints in the along-front

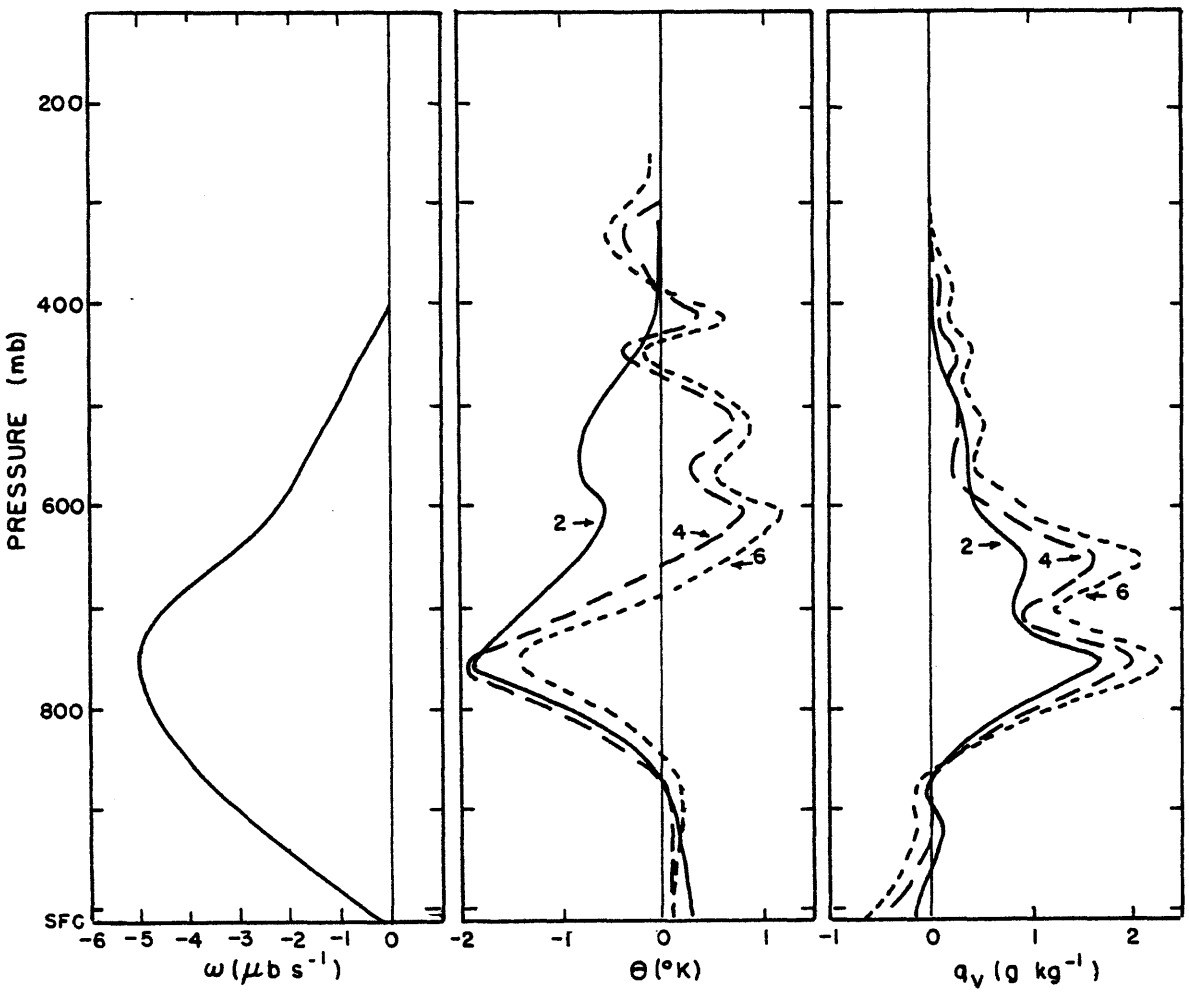


Fig. 3.4 A hypothetical ω profile and the changes of θ and q_v at every 2 h interval using the ω profile as simulated by Soong and Tao (1980, "ST"). (ST, Fig. 20)

direction and assuming periodicity. The model successfully demonstrated many of the observed characteristics, including the recurring generation of new convective cells. Yamasaki (1977) discussed a two dimensional, axisymmetric hurricane model with coordinates stretching away from the central axis and the lower boundary. The small domain prevents direct comparison to real storms, but it is of interest to see the traveling cells in the time-radius rainfall patterns.

The most drastic simplification of horizontal structure is to increase the grid spacing to the point that each cloud in the ensemble which exists occupies one gridcell. One such "gridcell-cloud model" is the three-dimensional, doubly-nested grid, 12 layer, hydrostatic hurricane model described in Jones (1980). Rainout occurs instantly upon supersaturation (without evaporation). Jones cites observations that 10 km diameter cells are possible in hurricanes, and he notes that the subgrid mixing parameterizations probably make up for this overly large scale. Although preliminary, the results are encouraging. In particular, he finds clusters of adjacent cells which sustain vigorous convection and propagate cyclonically (Fig. 3.5). It is not completely clear how much of a role the finer grid plays, but the resulting simulation of a growing hurricane appears more realistic than is the case for models with parameterized convection. For example, the interaction of clusters and downdrafts in adjacent gridcells is new, providing a realistic "broken" eyewall in the initial stages.

Randall and Huffman (1980) developed a highly simplified gridcell-cloud model to examine the possible role of the spatial distribution of cloud-induced stabilization in forming mesoscale "clumps" of convection. Cloud "strength" is assumed proportional to local "instability", and

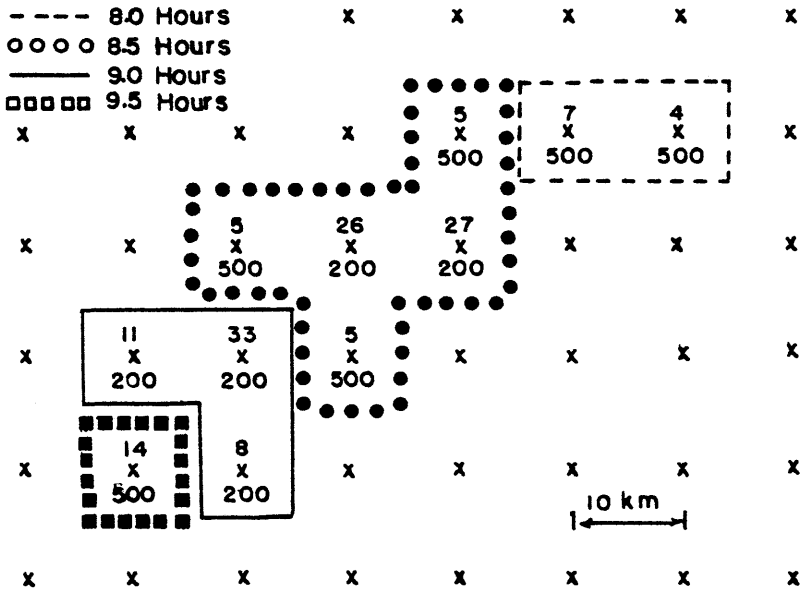


Fig. 3.5 Schematic time history of a cluster of convective cells simulated by Jones (1980, "J"). Areas denote upward motion greater than 2.5 m/s at 500 mb. Numbers above and below the gridpoint are, respectively, maximum updraft speed in the column (m/s) and level of occurrence (m_b). Vortex center is located 25 km east and 85 km south of lower right corner gridpoint. (J, Fig. 7)

each cloud's net stabilization of the environment is a prescribed function of distance from the cloud, with an amplitude proportional to cloud "intensity". Domain boundaries are periodic and clouds are assumed to last for one timestep. At each step clouds are randomly initiated in regions which are unstable and a spatially constant amount of "large-scale destabilization" is added. When runs for two different stabilization profiles (Fig. 3.6) were compared, Randall and Huffman showed that it is possible to dramatically change the structure of the cloud field in space and time; the dip profile (which they argue is more realistic than the peak profile) displays persistent clumps of convective cells, whereas the peak profile shows no such behavior. In both cases the net cloud stabilization rate balances the large scale destabilization rate, but the amplitude of individual clouds in the dip case is not well-predicted by the domain-average value of instability. Rather, it is necessary to include information about the mesoscale structure. Appendix B contains a more complete summary.

3.3 Models with parameterized horizontal structure

As was stated in Section 3.1, there are many cases in which the explicit treatment of horizontal structure is not feasible, forcing the use of a closure assumption to complete the system of model equations. It is not obvious how to capture the essence of the horizontal structure in a simple assumption; Ooyama (1971) left the rate of cloud formation (which he called the "dispatcher function") as an unknown in his theoretical parameterization study. Synoptic- and global-scale prognostic models include cumulus convection by parameterizations which directly relate cloud feedback on the environment to some internally calculated

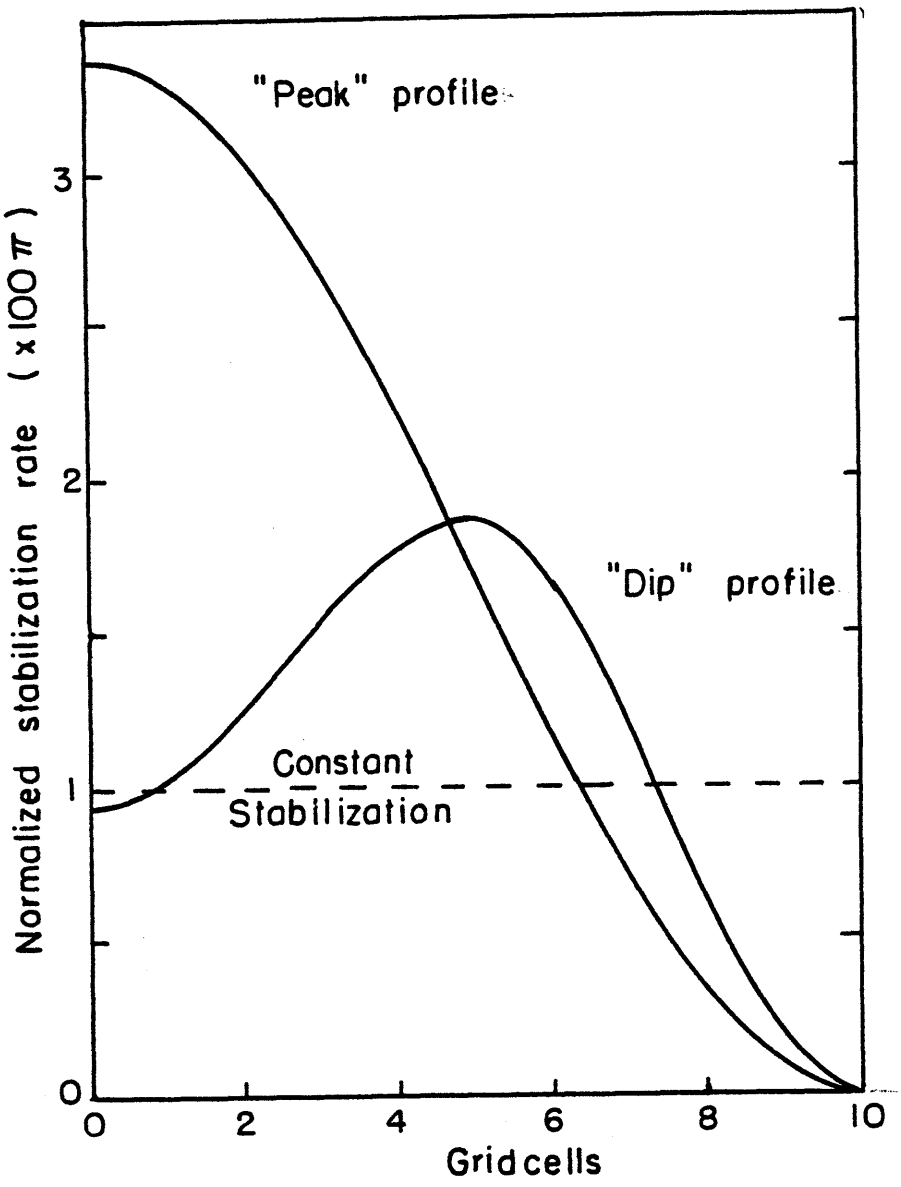


Fig. 3.6 "Peak" and "dip" stabilization profiles tested by Randall and Huffman (1980, "RH"). The two curves have the same area-averaged values (over the disk). The constant stabilization case is shown for reference only. (RH, Fig. 1)

measure of the rate of destabilization of the environment with respect to convection (Smagorinsky, 1956; Kuo, 1965; Arakawa and Schubert, 1974; Fritsch and Chappell, 1980). All aspects of the ensemble are highly parameterized.

Recently, Lord (1982) tested the Arakawa-Schubert paramterization by applying it to GATE observations. Treating the GATE region as one gridcell of a model, and adopting the quasi-equilibrium closure assumption, he generated cumulus ensemble heating and drying rates (including precipitation) and cumulus mass fluxes from the observed large scale fluxes of mass, heat, moisture, and radiation. His use of observed large scale fluxes prevents uncertainty due to model deficiencies other than those associated with the cumulus ensemble model. The predicted cumulus heating and drying rates ($Q_1 - Q_R$ and Q_2, described in Chapter 2) tend to match observations, although the heating is somewhat underpredicted at most levels, and the drying shifted to lower levels. Lord does not display M_c, net cloud vertical mass flux, but he does show $M_b(p)$, cloud base mass flux for various cloud depths. Recalling that Arakawa-Schubert clouds are assumed to have mass fluxes which grow exponentially with height, it is apparent that Lord's $M_b(p)$'s imply M_c's which are small at cloud base and peak at some intermediate level.

In the last 10 years researchers have also employed a second type of closure assumption; observations may be used to specify the total cloud activity in a model, which may then be used to "diagnose" other attributes of the cumulus ensemble. The predominant application of this approach is the "spectral diagnostic budget study", which considers a spectrum of cloud sizes and employs the heat and moisture budgets (Q_1 and Q_2) described in Chapter 2 to specify the total feedback of the

ensemble on the environment. The simplest studies, such as Ogura and Cho (1973) and Nitta (1975), directly adopted the Arakawa and Schubert (1974) cloud spectrum model: One-dimensional plume clouds are assumed to be growing in a horizontally homogeneous environment. Fractional entrainment rate (inflow as a fraction of the upward mass flux) is a constant, detrainment occurs in an infinitesmal layer at cloud top, downdrafts are ignored, and microphysics are highly parameterized. For a given environment, cloud size is strictly a function of fractional entrainment rate. These assumptions greatly simplify the computations, but their generality is uncertain. The major result for such models is the derivation of mass fluxes for the various subensembles (size classes). This is good to the extent that the model results can take the place of observations, but it is unfortunate that the model-predicted mass fluxes cannot be verified against current observations.

Johnson's (1980) "no downdraft" curve on Fig. 3.7 shows M_c in Category 4 of the Reed et al. (1977) composite wave for GATE. It typifies the results from these models: The curve peaks near cloud base with a second maximum (perhaps) at upper levels. Although the Johnson (1980) "no downdraft" configuration and Lord's (1982) model are based on similar cloud models, Lord does not offer an explanation of the differences at low levels between Johnson's typical M_c and his own. Evidently, an increased low-level mass mass flux would improve the agreement between Lord's results and observations. This is consistent with the fact that Lord does not include the forcing due to turbulent fluxes of sensible heat and moisture in the subcloud layer. These fluxes are presumably important for driving shallow clouds.

Diagnostic models have been further developed to include parameter-

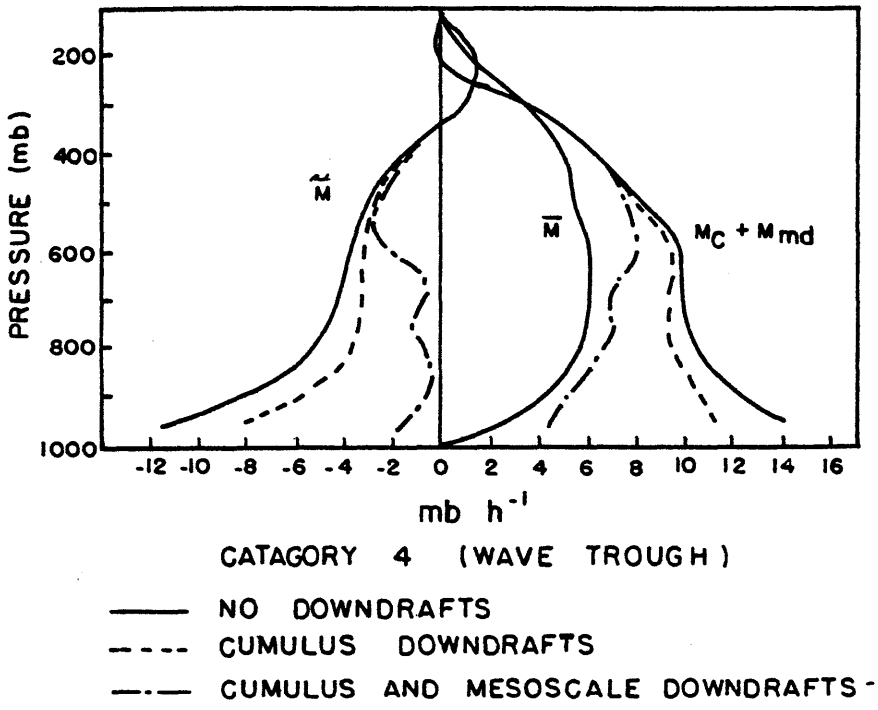


Fig. 3.7 Environmental mass flux ($\tilde{M}$), mean mass flux ($\bar{M}$), and net convective-mesoscale mass flux (M_c+M_{md}), for category 4 of the Reed et al. (1977) wave for Johnson's (1980, "J") spectral diagnostic models with convective updrafts alone, convective up- and downdrafts, and convective up- and downdrafts plus mesoscale downdrafts. (J, Fig. 18)

ized (one-dimensional) cloud scale downdrafts (Johnson, 1976; Nitta, 1977; McBride, 1981) and mesoscale downdrafts and storage (Johnson, 1980). Johnson represents the average temperature and moisture profiles in the mesoscale downdraft with a composite of observations. Then, by assuming that the mesoscale features are all similar and that they vary only on large-scale time scales, he computes the bulk mesoscale downdraft mass flux. In this scheme the mesoscale downdraft mass flux turns out to be nearly constant with height below the assumed top of the downdraft (600 mb). Fig. 3.7 compares results for the different model configurations in wave Category 4. We see that the diagnosed deep cumulus activity is unchanged from the earlier models, but that shallow cloud activity is quantitatively sensitive to the assumptions about convective scale downdrafts and qualitatively sensitive to the assumptions about mesoscale downdrafts. This sensitivity brings into question the drastic simplifications in Johnson's downdraft formulation. Johnson could not generate completely quantitative results because he required poorly-observed parameters such as the ratio of mesoscale and convective cloud areas. One inference that these results suggest is that Lord's (1982) model could simulate observations more accurately if he included downdrafts.

An interesting modification in the spectral diagnostic budget approach was introduced by Soong and Ogura (1976), who represented the effects of each subensemble as the time average heat and moisture transports in an isolated cloud of that size as modelled by a two-dimensional, axisymmetric cloud model. Unfortunately, they could not closely reproduce the observed Q_1 and Q_2 with any combination of model clouds.

An alternative to the budget approach is the diagnostic radar study,

which specifies the cloud population by quantitative meteorological radar observations. Austin and Houze (1973), López (1973), Houze (1973), and Houze and Leary (1976) used model clouds very similar to those in the early spectral diagnostic budget studies, except that (in some cases) the fractional entrainment rate is not a constant and detrainment occurs over a finite layer at cloud top. The papers by Houze et al. (1980), Cheng and Houze (1980), Leary and Houze (1980), and Houze and Cheng (1981) reported various aspects of a diagnostic radar study which parallels that of Johnson (1980), except that it deals with radar observations, utilizes a different entrainment model, and incorporates a different parameterization of the mesoscale anvil. They assume that the mesoscale downdraft has a constant mass flux profile and introduce a parabolic mesoscale updraft mass flux profile. Both profiles are highly simplified algebraic forms based on observations and models of precipitating anvils. As with Johnson's work, the results were preliminary, but again we see that fluxes due to the mesoscale anvil are important. By allowing mesoscale updrafts, Leary and Houze find modifications to the mass flux of even the deepest clouds. Finally, Houze et al. (1980) show that the budget and radar approaches yield similar cloud ensemble budgets for the cases they chose.

For completeness, we note the work of Fraedrich (1976) in which he used empirical relations among cloud top height, vertical velocity, entrainment rate, and population distributions to infer mass fluxes in cumulus ensembles. The example he presented depended on several arbitrarily chosen constants.

3.4 Cloud-environment interactions

Another basis for comparison of cumulus ensemble models is their representation of the basic cloud-environment interactions:

1. Various environmental processes, such as horizontal and vertical advection, radiative heating, and surface fluxes, tend to change the environment's stability with respect to cumulus convection. Observations generally show that these processes vary on time and space scales much larger than those associated with single clouds (Arakawa and Schubert, 1974; Fritsch and Chappell, 1980), so we shall refer to the processes collectively as "large-scale forcing".
2. Various small-scale processes, such as dry convection in the Planetary Boundary Layer, continually create small anomalies in the environment. Depending on the environmental temperature, moisture, and wind fields, a few of these anomalies start to grow by moist convection, resulting in "cloud initiation".
3. Once a cumulus cloud is initiated, its subsequent development critically depends on the properties of its environment. Cloud properties such as buoyancy are measured against the environmental state, and cloud properties are modified by the entrainment of air carrying environmental properties. In this sense the environment exerts a "static control" over the development of each cloud during its lifespan (Schubert, 1974).
4. The net transports and sources/sinks generated by the clouds modify the environment. A direct effect of this "cloud feedback" is to statically stabilize the environment, reducing cumulus convection, although interactions in the environment may result in an increased instability to further cumulus convection (as in Conditional Insta-

bility of the Second Kind, Charney and Eliassen, 1964).

It is easy to see how fundamental the representation of horizontal structure is; every item in the preceeding list depends on the horizontal relationships between clouds and the environment and among clouds. Closure assumptions are particularly difficult to formulate because these four cloud-environment interactions do not always occur in the same way. In some cases cloud initiation is easily accomplished, so that cloud feedback is observed to very nearly balance large-scale forcing. Lord (1982) shows examples of "quasi-equilibrium" in moist tropical settings. On the other hand, Fritsch et al. (1976) show examples from mid-latitudes in which the forcing is "stored" because cloud initiation is suppressed by low-level inversions. When cloud initiation finally occurs, the resulting clouds differ from those predicted by assuming quasi-equilibrium over the whole time.

In the context of these various interactions we see that a prognostic closure assumption must include a theoretical expression for each point, while a diagnostic closure assumption needs a theoretical expression for only 3 points. The cloud feedback or cloud initiation is specified by observations (the budget and radar methods, respectively).

Finally, within an extrinsically closed system there are still many levels of approximation possible for the static control.

3.5 Summary

With present-day computers, it is difficult to simulate both clouds and their environment in numerical models. The slower, more complete approach retains explicit horizontal structure, in which case the system of model equations is intrinsically closed (on the scale of the clouds).

The faster, more simplified approach parameterizes horizontal structure via extrinsic closure. In the latter approach the closure assumption may relate cloud activity either to other model variables or to observations, yielding prognostic or diagnostic models, respectively.

Soong and Tao (1980) showed the importance of mesoscale lifting for conditioning the environment for cloud growth. Randall and Huffman (1980) suggest that one generation of clouds might modify the environment for the next generation, in such a way as to form inhomogeneities in the stability field. The diagnostic approach demonstrates the importance of mesoscale transports during strong convective events.

4. The Model: One Cloud

4.1 General design

We now proceed to carry out one goal of this thesis, namely developing an economical cumulus ensemble model in which there are fewer assumptions than in previous simple models. It will be designed to help us address the other two goals; examining the heat, moisture, and mass budget contributions of clouds of various sizes, and examining the role of mesoscale organization in modifying those contributions. Recalling the preceeding review of cumulus cloud ensemble observations and models, we may summarize the model design as follows:

1. The basic framework to be adopted will follow that used in the spectral diagnostic budget study. The arguments of Chapter 3 lead one to expect that the spectral diagnostic method represents a relatively simple means of modelling the actions of a cumulus cloud ensemble. That is, we eliminate explicit horizontal structure by writing the model with the subensemble populations (numbers of clouds of different sizes) as free parameters and then requiring that the model cloud feedback must reproduce the observationally derived apparent sources of heat and moisture. This allows us to examine the ensemble's response to large-scale forcing by varying the number of clouds in each subensemble.
2. The spectral diagnostic framework treats clouds as distinct entities. Computationally, the cumulus ensemble model will look like a collection of individual model clouds. By contrast, the prognostic models apply the same equations to each point on a grid covering the entire domain, creating and sustaining clouds as frequently in time and

space as the instabilities demand.

3. The model should be formulated in terms of numbers of clouds. The spectral diagnostic models discussed in Chapter 3 expressed subensemble populations in terms of mass flux, leading to confusion over the results. In Appendix E we will show that considering numbers of individual clouds requires information about the horizontal scale of each cloud.
4. The model must be economical, since it will be run many times as the free parameters are varied. Soong and Ogura (1976) were severely limited by considering an overly-expensive ensemble model. Also, the "complete" prognostic models reviewed in Chapter 3 are very expensive and unsuited for frequent use.
5. The model should be time-dependent. Most spectral diagnostic budget studies have sacrificed explicit time-dependence for the sake of economy by incorporating a one-dimensional plume cloud model representing the mature phase of the cloud lifecycle. This simplification ignores storage and lifecycle effects, which Cho (1977) has shown to be important. More importantly, by retaining explicit time-dependence we are able to relax many of the assumptions which previous simple models were forced to include concerning mass flux, entrainment/detrainment, and microphysics.
6. The model will include mesoscale structure. The observational review of Chapter 2 clearly shows the ubiquity of mesoscale organization, so that its recognition seems essential. The complexity of the mesoscale structure included should be commensurate with the complexity of the cloud model used.

The execution of this design is a two-step process. First, a cumulus

cloud model is constructed which follows the design goals applicable to a single cloud: definite horizontal scale, economy, and time-dependence (points 3-5). Second, the design is completed by incorporating the cloud model into an ensemble model. The remainder of this chapter concerns the cloud model, while Chapter 5 deals with the formulation of the ensemble model. We will maintain the distinction between the cloud model and the ensemble model throughout this study. The two are closely coupled, but logically distinct. We will take advantage of this fact by carefully developing and testing the cloud model, then moving on to the ensemble model.

4.2 Preliminary remarks

The simplest cumulus cloud model which meets the criteria of time-dependence and definite horizontal scaling is a "two-cylinder" model such as that studied by Asai and Kasahara (1967), hereafter referred to as AK, and subsequently improved by Yau (1980). However, we are not free to take up the Yau model intact because the AK formulation of entrainment is incorrect, as we will show. Many researchers, starting with Stommel (1947), have considered the effects of cloud dilution by the lateral entrainment of environmental air. Byers and Braham (1949) and Houghton and Cramer (1951) discussed two entrainment mechanisms. The first is "dynamic entrainment", described as an organized flow of environmental air into the cloud; the second is "turbulent entrainment", described as a turbulent mixing of environmental air into the cloud. Although Houghton and Cramer and others (e.g., AK) realized that these two entrainment mechanisms are not independent, the nature of their interdependence has not been fully explored. In particular, AK simply

wrote an independent expression for each mechanism on intuitive grounds.

We will present a careful discussion in order to resolve the question of "turbulent" versus "dynamic" entrainment (to appear in Randall and Huffman, 1982). To do so, we will derive the general equations which explicitly show how entrainment tends to modify the properties of the air inside and at the edge of a cumulus cloud. The method is similar to that employed in deriving entrainment at the edge of a mixed layer (see Ball, 1960, among others). In Section 4.4 these equations are specialized to the two-cylinder geometry employed by AK. We then describe the rest of the model equations (Section 4.5) and present some sensitivity tests (Section 4.6). One unexpected result in the two-cylinder geometry is that entrainment does not introduce scale dependence.

4.3 Entrainment and the conservation laws

We begin by considering the ways in which entrainment and turbulent exchange in and near a cumulus cloud tend to modify the distribution of a scalar variable ψ which satisfies a conservation equation of the form

$$\frac{\partial}{\partial t}(\rho\psi) + \nabla\cdot(\rho\,\vec{V}\psi + \vec{F}_\psi) = S_\psi \,. \qquad (4.1)$$

Here ρ is density, ∇ is the three-dimensional operator, $\vec{F}_\psi$ is the vector turbulent flux of ψ, and S_ψ represents any sources or sinks.

A fundamental question is whether the subcloud-scale turbulence which accounts for $\vec{F}_\psi$ is sufficiently scale-separated from the cloud-scale motions that it can be accurately parameterized in terms of the bulk structure of the cloud. A definitive answer can probably best be

obtained from high-resolution three-dimensional modeling studies. As in many previous studies, we simply assume that such parameterization is possible.

We adopt a cylindrical coordinate system, in which the boundary of the cloud is given by $r = R(\varphi,z,t)$, where r, φ, and z are the radial, azimuthal, and vertical coordinates, respectively. First consider the effects of entrainment on a "pie-slice" of cloud, as schematically illustrated in Fig. 4.1. Multiplying (4.1) by r, and integrating the result with respect to r, from r=0 to r=R-ϵ (just inside the boundary), we find that

$$\frac{\partial}{\partial t}\left(\overline{\rho\psi}^{R-\epsilon}\cdot\frac{R^2}{2}\right)+\frac{\partial}{\partial\varphi}\left\{\left[\overline{\rho\dot{\varphi}\psi}^{R-\epsilon}+\overline{\frac{1}{r}(F_\psi)_\varphi}^{R-\epsilon}\right]\frac{R^2}{2}\right\}$$
$$+\frac{\partial}{\partial z}\left\{\left[\overline{\rho w\psi}^{R-\epsilon}+\overline{(F_\psi)_z}^{R-\epsilon}\right]\frac{R^2}{2}\right\} \qquad (4.2)$$
$$+R\left[-\psi E+(F_\psi)_n\right]_{R-\epsilon}=\overline{S_\psi}^{R-\epsilon}\frac{R^2}{2}$$

where

$$E\equiv\left[\rho\left(\frac{\partial R}{\partial t}+\dot{\varphi}\frac{\partial R}{\partial\varphi}+w\frac{\partial R}{\partial z}-\dot{r}\right)\right]_{R-\epsilon} \qquad (4.3)$$

is the entrainment mass flux;

$$(F_\psi)_{n,R-\epsilon}=\left[(F_\psi)_r-(F_\psi)_\varphi\frac{1}{R}\frac{\partial R}{\partial\varphi}-(F_\psi)_z\frac{\partial R}{\partial z}\right]_{R-\epsilon} \qquad (4.4)$$

is the part of $\vec{F}_\psi$ which, as shown below, is directly related to the entrainment rate; and we define an averaging operator

$$\overline{(\quad)}^{R-\epsilon} \equiv \frac{2}{R^2}\int_0^{R-\epsilon} (\quad) r\,dr . \tag{4.5}$$

Further integration of (4.2) with respect to φ, from $\varphi=0$ to $\varphi=2\pi$, would give the integral of (4.1) over the cross sectional area of the cloud. Putting $\psi=1$ in (4.1), we obtain

$$\frac{\partial}{\partial t}\left(\overline{\rho}^{R-\epsilon}\cdot\frac{R^2}{2}\right)+\frac{\partial}{\partial\varphi}\left(\overline{\rho\dot{\varphi}}^{R-\epsilon}\cdot\frac{R^2}{2}\right)+\frac{\partial}{\partial z}\left(\overline{\rho w}^{R-\epsilon}\cdot\frac{R^2}{2}\right)-RE=0 , \tag{4.6}$$

which expresses the conservation of cloud mass.

The entrainment mass flux $E(\varphi,z,t)$ is the rate at which air enters the cloud. For a cylindrical cloud of time-independent radius, (i.e., R is constant in φ, z, and t), E is equal to the radial mass flux $(-\rho\dot{r})_{R-\epsilon}$; more generally, several of the terms on the right-hand side of (4.3) contribute to E. For E>0, the cloud is entraining. For E=0, the cloud boundary moves as a material surface. For E<0, the cloud is detraining. The actual value of E must be parameterized in terms of the properties of the cloud.

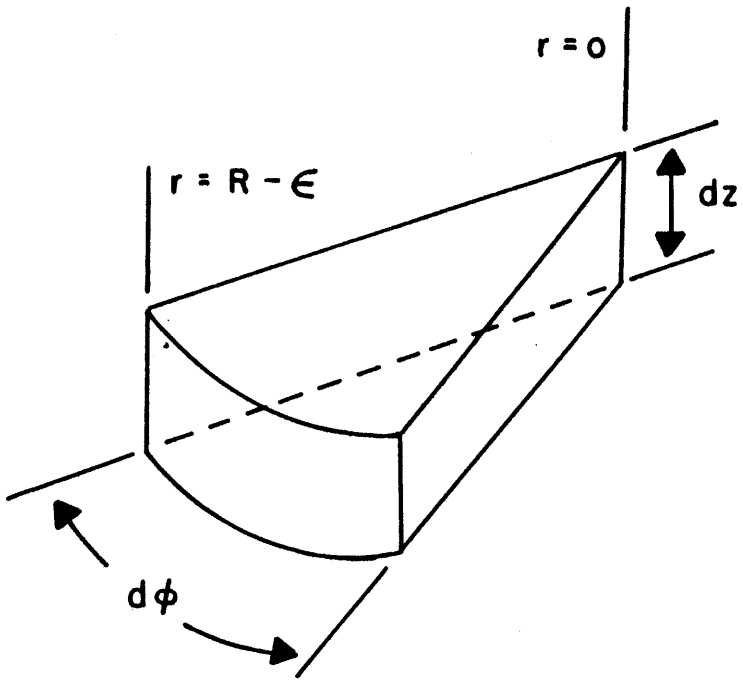


Fig. 4.1 Schematic diagram depicting the "pie-slice" of cloud over which integration is performed to obtain (4.2).

Mixed layer entrainment theories have been developed to explain the advance and retreat of turbulent layers. In attempts to apply these theories to cumulus clouds, it is important to keep in mind that the boundary of a cumulus cloud need not necessarily coincide with the boundary of the turbulence associated with the cloud. To say that an air parcel is at one moment outside the visible cloud and at the next moment inside the visible cloud is not necessarily to say that the parcel is entrained. Entrainment is by its nature a turbulent process; it is the active growth of turbulence by annexation of quiet air. It can occur in the absence of clouds, as it often does at the top of the planetary boundary layer. Detrainment, on the other hand, is the passive retreat of turbulence; air which has been turbulent becomes quiet as dissipation destroys turbulence energy. Just as it is possible for entrainment to occur entirely within clear air, it is also possible for detrainment to occur entirely within cloudy air, i.e., for the final quenching of turbulence energy to precede the evaporation of all liquid water. During a cloud's period of growth, the cloud and turbulence boundaries are observed to nearly coincide, even in the anvil outflow region. As long as the anvil air remains turbulent, it cannot be considered to have been detrained. But as a cloud decays, the turbulence in its interior can be dissipated long before the cloud disappears.

In this paper, we speak, for convenience, of the "cloud boundary". But more precisely we refer to the boundary of the mass of turbulent air associated with the cloud.

Now considering this boundary region, multiply (4.1) by r, integrate the result with respect to r, from $r=R-\epsilon$ to $r=R+\epsilon$, and take the limit as $\epsilon \to 0$. In accordance with the preceeding discussion, assume that the

turbulence is confined to the cloud ($r<R$), so that $\vec{F}_\psi$ vanishes at $r=R+\epsilon$. The result is

$$
\begin{aligned}
&-\Delta(\rho\psi)\frac{\partial R}{\partial t}+\Delta(\rho\,\dot{r}\,\psi)\\
&-\Delta(\rho\,\dot{\varphi}\,\psi)\frac{\partial R}{\partial \varphi}-\Delta(\rho w\psi)\frac{\partial R}{\partial z} \qquad (4.7)\\
&-(F_\psi)_{n,R-\epsilon}=\int_{R-\epsilon}^{R+\epsilon} S_\psi\,dr\ ,
\end{aligned}
$$

where

$$\Delta(\quad)=(\quad)_{R+\epsilon}-(\quad)_{R-\epsilon} \qquad (4.8)$$

denotes the outward radial increase of a quantity across the annulus $R-\epsilon<r<R+\epsilon$. Observations (e.g., Warner, 1977) show that temperature, total mixing ratio, vertical velocity, and turbulence intensity can all undergo very sharp "jumps" at cumulus cloud boundaries, so that it seems necessary to allow $\Delta\psi=0$. Where entrainment is occurring, the active advance of the turbulent cloudy region into the quiet clear region creates and maintains such jumps. But where detrainment is occurring, the passive retreat of turbulence leaves behind any jumps created by earlier entrainment; the boundary of the retreating turbulence is not sharply defined, and is not marked by jumps.

The single term on the right-hand side of (4.7) represents a possible

concentrated source or sink of Ψ within the annulus. For example, if Ψ is temperature, this term can represent intense radiative and/or evaporative cooling concentrated at the cloud edge. On the other hand, if Ψ is a highly conservative variable such as the total water susbstance mixing ratio, then the term vanishes.

Putting $\Psi=1$ in (4.7) gives

$$\Delta\rho \frac{\partial R}{\partial t} + \Delta(\rho \dot{r}) - \Delta(\rho \dot{\varphi}) \frac{\partial R}{\partial \varphi} - \Delta(\rho w) \frac{\partial R}{\partial z} = 0 \ , \qquad (4.9)$$

which expresses the conservation of mass for the annulus. We can use (4.3) and (4.9) to rewrite (4.7) as

$$-E \Delta \psi - (F_\psi)_{n,\, R-\epsilon} = \int_{R-\epsilon}^{R+\epsilon} S_\psi \, dr \ . \qquad (4.10)$$

Although the components of the vector $\vec{F}_\psi$ must be such that $(F_\psi)_{n,R-\epsilon}$ satisfies (4.10), the vector itself is not completely determined by (4.10).

Suppose that E, $\Delta\psi$, and $\int_{R-\epsilon}^{R+\epsilon} S_\psi dr$ are known. Then (4.10) fixes the value of $(F_\psi)_{n,R-\epsilon}$; we are not free to parameterize it independently. This means that turbulent transport near the cloud edge is closely coupled to the entrainment rate. When a jump in Ψ exists at the boundary of a cloud, a given rate of organized mass flow across the jump must be balanced by a combination of turbulent flux convergence and any concentrated source or sink of Ψ at the jump. Further discussion is given in

the next Section.

4.4 Application to a two-cylinder model

Now we apply the general form of the conservation equations to a two-cylinder cumulus cloud model such as AK considered. The model domain consists of a vertical cylinder and a concentric annulus, the boundaries of which are fixed in time and space at constant radii. Each level in the vertical has two values for every variable, a horizontal average over the inner region and a horizontal average over the outer region.[1] Thus, the model may be referred to as "axisymmetric and 1 1/2 -dimensional". The model is time-dependent and anelastic. Since AK allowed turbulent fluxes at r=a, we let "a" correspond to "R-ϵ" in our notation. Then (4.2), (4.3), (4.6), and (4.10) become

$$\rho_0 \frac{\partial}{\partial t}\overline{\psi}^a + \frac{\partial}{\partial z}\left[\overline{\rho_0 w \psi}^a + \overline{(F_\psi)_z}^a\right] + \frac{2}{a}\left[-\psi E + (F_\psi)_r\right]_a = \overline{S_\psi}^a \qquad (4.11)$$

$$E = (-\rho_0 \dot{r})_a \,, \qquad (4.12)$$

$$\frac{\partial}{\partial z}(\rho_0 \overline{w}^a) - \frac{2E}{a} = 0 \qquad (4.13)$$

---

1 Radial velocity, u, is carried on the two region boundaries, with algebraic profiles elsewhere which are specified by mass continuity:

$$u \sim \begin{cases} r & , \ 0<r<a \\ \dfrac{b^2 - r^2}{r} & , \ a<r<b \end{cases}$$

where r is radius, a and b denote inner and outer cylinder radii.

$$-E\,\Delta\psi - (F_\psi)_{r,a} = \int_a^{a+2\epsilon} S_\psi\, dr \tag{4.14}$$

respectively. Here and throughout this section $\overline{(\,)}^a$ denotes an areal average over $0<r<a$. According to (4.12), the entrainment mass flux is just equal to the inward radial mass flux at the cloud edge. This is a direct result of the assumption R=constant; <u>therefore, this assumption is the lateral entrainment closure assumption of the AK model</u>. If w is predicted, (4.13) allows E (and so $(\rho\dot{r})_a$) to be diagnostically computed. Then, according to (4.), $(F_\psi)_{r,a}$ is detemined for given $\Delta\psi$ and S_ψ.

Suppose that E>0, i.e. that there is inflow. As argued in Section 4.3, We expect a discontinuity in ψ at the cloud edge. In the AK notation,

$$\Delta\psi = \psi_b - \psi_a\,, \tag{4.15}$$

so that (4.14) becomes

$$(F_\psi)_{r,a} = -E\,(\psi_b - \psi_a) - \int_a^{a+2\epsilon} S_\psi\, dr\,. \tag{4.16}$$

This to be compared with AK's assumption that

$$(F_\psi)_{r,a} = -\frac{\rho_0 K}{a}(\psi_b - \psi_a), \tag{4.17}$$

where K is a mixing coefficient.

Now suppose that $E<0$, i.e. that there is outflow across the cloud boundary. As argued in Section 4.3, there is no discontinuity of ψ in this case, so that

$$(F_\psi)_{r,a} = 0. \tag{4.18}$$

AK allowed $(F_\psi)_{r,a} = 0$ even for $E<0$.

It is convenient to summarize (4.16) and (4.18) as

$$(F_\psi)_{r,a} = \begin{cases} -E(\psi_b - \psi_a) - \displaystyle\int_a^{a+2\epsilon} S_\psi \, dr & , \ E>0 \\ 0 & , \ E\leq 0. \end{cases} \tag{4.19}$$

Use of (4.19) to eliminate $(F_\psi)_{r,a}$ in (4.11) gives

$$\rho_0 \frac{\partial}{\partial t}(\overline{\psi})^a + \frac{\partial}{\partial z}\left[\rho_0 \overline{w\psi}^a + \overline{(F_\psi)_z}^a\right] - \frac{2E}{a}\psi_x = \overline{S_\psi}^{a+2\epsilon}, \tag{4.20}$$

where, for convenience, we define

$$\psi_x \equiv \begin{cases} \psi_b & , \ E > 0 \\ \psi_a & , \ E \leq 0 \ . \end{cases} \tag{4.21}$$

By use of (4.13), we can eliminate E in (4.20), giving

$$\rho_o \frac{\partial}{\partial t}(\overline{\psi})^a + \frac{\partial}{\partial z}\left[\rho_o \overline{w\psi}^a + (\overline{F_\psi})_z^a\right] - \psi_x \frac{\partial}{\partial z}(\rho_o \overline{w}^a) = \overline{S_\psi}^{a+2\epsilon}. \qquad (4.22)$$

It is worth noting that (4.20-4.22) are equivalent to equations used by AK, except that the mixing length terms do not appear. Of course, we could have arrived at (4.20) and (4.22) more directly by integrating the conservation law for from r=0 to r=a+2ϵ. Such a derivation would not have required consideration of $(F_\psi)_{r,a}$.

An interesting property of (4.22) is that the radius a does not appear explicitly. Some a-dependence may be hidden in S_ψ or $(F_\psi)_z$ (whose forms we have not specified), but if this is not the case then the solution obtained from (4.22) is independent of a.

4.5 The complete cloud model

We are now in a position to complete the system of model equations. Since the correct entrainment formulation (Eq. 4.20-4.22) is identical to AK's form except for the omission of the mixing length terms, we take the version of the AK model developed by Yau (1980) as our starting point. The model is initialized by setting the basic state in both regions to some large-scale sounding of temperature and moisture, then imposing a vertical velocity and humidity perturbation in the lower portion of the inner cylinder. On each succeeding time step, the anelastic system of equations is solved using modified upstream differencing

and a staggered grid in the vertical. First, the inner region vertical velocity is predicted. This new velocity, continuity, and the fixed geometry of the model are combined to diagnose the radial velocity and the vertical velocity in the outer region. The temperature and moisture variables are then predicted. Liquid water processes are parameterized either according to Kessler (1969) (K microphysics) or to Yau and Austin (1979) (P microphysics). The former is quick, simply assuming an exponential raindrop size distribution, while the latter takes 2.5 times as long, providing a relatively complete treatment of warm rain over 10 raindrop size classes. Finally, the perturbation pressure field induced by the cloud is diagnosed as in Yau (1980). In the radial direction, the pressure deviation from the domain-averaged hydrostatic conditions is expanded in a Fourier-Bessel series and is solved semi-analytically, then the vertical structure is solved by finite differencing. Appendix C contains a more complete summary of the basic model.

We next change several features of the Yau cloud model and add several new features in order to increase its realism.

First, we allow a prescribed large-scale vertical velocity profile. This allows the possibility that there is a net rising or sinking in the immediate environment of the cloud, creating vertical heat and moisture transports, as well as the possibility that heat and moisture are being imported or exported across the outer boundary. Cloud motions are still compensated in the environment of the cloud, but over time the parcels will not follow the same trajectories as before, since we are prescribing the addition or removal of mass at the r=b boundary at various levels. If we assume that $\overline{w}$, the area-average vertical velocity, is known as a function of height and time, the major computational changes

are that the diagnostic equation for $\bar{w}_b$, the outer-cylinder vertical velocity, becomes

$$\bar{w}_b = \frac{1}{(1-\sigma^2)} (\bar{w} - \sigma \bar{w}_a) \tag{4.23}$$

where $\sigma = a/b$

a,b are the radii of the inner,outer cylinders

and $\hat{u}_b$, the horizontal velocity on the outer boundary (r=b) is nonzero at some levels:

$$\hat{u}_b = - \frac{b}{2} \frac{1}{\rho_o} \frac{\partial}{\partial z} (\rho_o \bar{w}) \ . \tag{4.24}$$

Here ρ_o is the density (a function of height alone).

If this imposed circulation is in hydrostatic balance, and if the pressure perturbations are small enough to be additive, then the diagnostic equation for the cloud-scale pressure perturbation is unchanged, except for some additional terms in the forcing function (Appendix C). Physically, it is reasonable to assume that allowing open lateral boundaries does not change the requirement that the cloud perturbation pressure gradient disappears at the "edge" of the pressure domain. Thus, the homogeneous lateral boundary condition

$$\frac{\partial}{\partial r} \pi' = 0 \text{ at } r=0, \ r=b \tag{4.25}$$

still applies, and the Fourier-Bessel expansion of the cloud perturbation pressure which Yau (1980) described is still valid.

The second modification is the inclusion of vertical turbulent fluxes. Previous tests of the Yau model indicated that it simulates

clouds which are shallower than those observed to occur in the sounding (Stailey, 1978). Preliminary tests for this study showed that the cloud tended to break into separate layers, indicating a deficiency in vertically transporting moisture. Following Lilly (1962) and Cotton (1975), we adopt a simple vertical diffusion parameterization in which the magnitude of the diffusion coefficient depends on the local Richardson number. We assume that turbulent fluxes occur only inside the cloud, so the coefficient is identically zero outside the cloud.

$$K_m = \begin{cases} \dfrac{(k_2 \Delta_z)^2}{\sqrt{2}} |Def| \left[1 - (K_h/K_m)\, Ri\right]^{1/2} & : Ri < K_h/K_m \text{ and both adjacent layers cloudy} \\ 0 & : Ri >= K_h/K_m \text{ or one adjacent layer clear} \end{cases} \tag{4.26}$$

where $Ri = \dfrac{g}{\theta^*} \dfrac{\partial \theta^*}{\partial z} / (Def)^2$ the gradient Richardson number for a moist process (only considered inside the cloud)

$Def = \left|\dfrac{\partial w}{\partial z}\right|$ an approximation of the deformation tensor

$\Delta_z = (A\, \delta z)^{1/3}$, an averaging length scale

θ^* is the saturation equivalent potential temperature

A is cloud cross-sectional area

δz is vertical grid spacing

K_h/K_m is chosen as 1 (so that the heat diffusion coefficient, K_h, equals the momentum coefficient)

k_2 is chosen as 0.16 after Cotton (1975) .

The third modification is the introduction of a prescribed large scale radiative heating profile. For all regions, at each time step, and at each level in the vertical, a temperature change may be prescribed, on the basis of observed (i.e., diagnosed) or assumed area-average heating (cooling) by the flux divergence of long- and short-wave radiation. The fourth modification is the introduction of prescribed surface fluxes of sensible and latent heat. At each time step prescribed temperature and water vapor changes in the lowest 500 m (the nominal depth of the Planetary Boundary Layer) are imposed in each region to account for diagnosed or assumed area-average surface fluxes. Finally, we neglect the detrainment of rainwater into the environment. This choice was made on the basis of preliminary tests, which indicated unrealistically large amounts of rain evaporating in the environment (see next Section).

4.6 Cloud model behavior and sensitivity

We now turn to an examination of the behavior and sensitivity exhibited by this one-cloud model. The major points which we discuss in this Section are: the scale dependence of the cloud, and the sensitivity of the results to various assumptions in the model. Except as noted, the tests are carried out with the new entrainment formulation, pressure perturbations, vertical turbulent fluxes, no lateral transport of rain, and K microphysics (referred to as Version K). The same configuration but with P microphysics is designated as Version P. The timestep is 20 s, the vertical grid interval is 250 m, the radius is 1 km, and the ratio of inner to outer cylinder radius is $a/b = 0.32$. In all cases the initial temperature and moisture soundings are those shown

in Fig. 4.2, an idealization of the July mean profiles at Buffalo, NY, with increased moisture. The cloud is initiated by specifying a vertical velocity perturbation in the inner cylinder as

$$\overline{w_a} = \begin{cases} W_o \sin(\pi z/H_o) & z<2 \text{ km} \\ 0 & z>2 \text{ km} \end{cases} \qquad (4.27)$$

where W_o = 1 m/s, and H_o = 2 km,

and specifying saturation in the region of the inner cylinder between nominal cloud base (875 m) and H_o (2 km). In addition, these conditions imply compensating subsidence in the environment and a non-hydrostatic pressure field. In order to conform to the conventions adopted and explained in the next chapter, the cloud lifecycle is defined as finished when the instantaneous rainfall rate and the peak vertical velocity have each declined to less than 20 percent of their maximum values over the cloud lifetime. All remaining rain is assumed to fall out and any leftover cloud is evaporated into the environment before the final statistics are computed. This assumption is examined below in Versions K.C and P.C.

To gain familiarity with the model, consider the Version P configuration described above. The time-height cross-sections in Fig. 4.3 provide a detailed record of four parameters on the inner cylinder, vertical velocity, potential temperature deviation from the initial state, cloud water mixing ratio, and rain water mixing ratio. At the beginning of the lifecycle the release of latent heat warms the air near the velocity maximum, acting to accelerate the air upwards. The cloud water created from supersaturated air starts autoconverting into rainwater when $\overline{q_{ca}} > 1$ g/kg. By 15 min enough rainwater has accumulated that

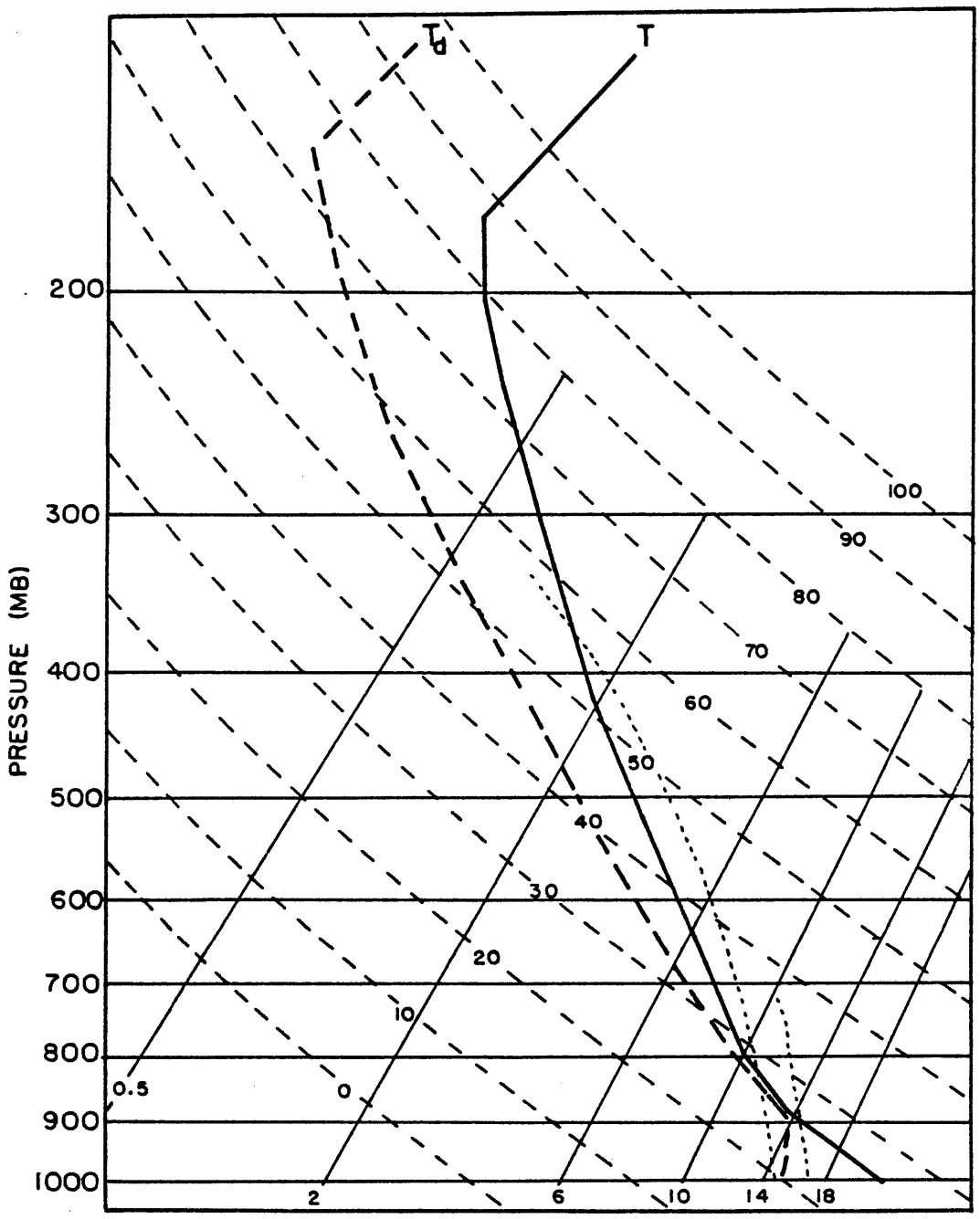


Fig. 4.2 Initial temperature (T) and dewpoint (T_d) soundings used in Chapter 4.

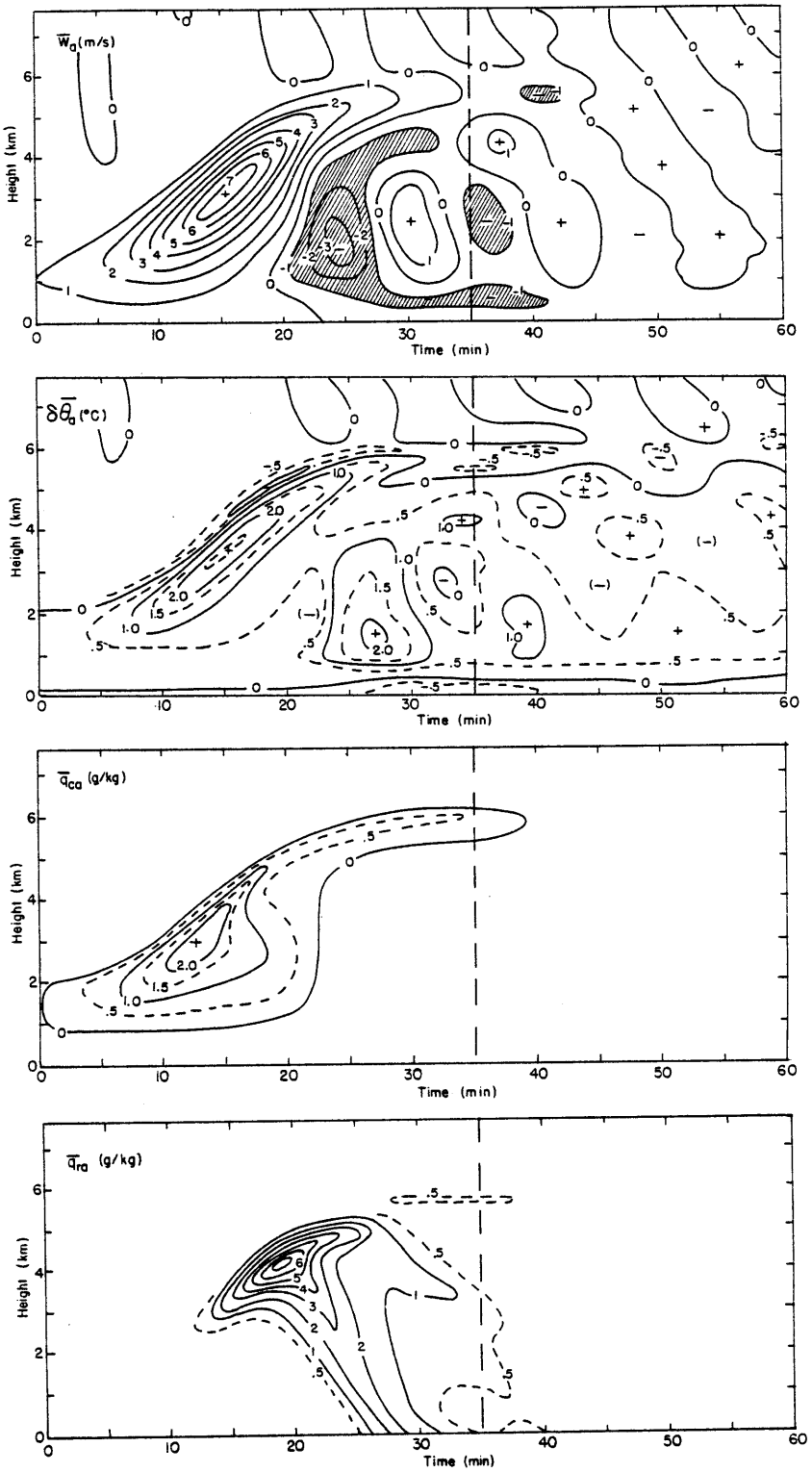


Fig. 4.3 Detailed time-height plots of area-averaged inner cylinder variables for Version P: $\overline{W}_a$, vertical velocity (m/s, values < -1 m/s shaded); $\delta\overline{\theta}_a$, deviation from initial potential temperature profile (°C); $\overline{q_{ca}}$, cloud water mixing ratio (g/kg); $\overline{q_{ra}}$, rain water mixing ratio (g/kg). Heavy dashed line at 35 min is the 20% cutoff point (see Section 4.6).

the conversion of cloud to rain by accretion rapidly depletes the cloud water. The increased drag of liquid overcomes the buoyancy force, causing the peak vertical velocity to decrease. Simultaneously, the rate of condensation, and so latent heating, decreases. By 20 min the rain has a net downward motion below 4 km. This "rain gush" drives a downdraft, adiabatic warming, and subsaturation (evidenced by the evaporation of cloud in the downdraft). Thereafter, the cloud and rain gradually disappear, as vertically propagating gravity waves fill the vertical velocity and temperature fields, decaying with time. For similar examples, see AK or Yau (1980), among others. The phase relationships among the various parameters tend to be similar for a wide range of parameters, so subsequent tests will utilize more compact summaries of the model behavior.

The first issue which we study is scale dependence. Recall that Eq. 4.20-4.22 unexpectedly showed that horizontal scale information does not appear in the entrainment term, but that the vertical turbulent flux parameterization (Eq. 4.26) and the perturbation pressure (Appendix C) do carry scaling information. Using K microphysics throughout to save computer time, 5 different model configurations were run for 3 radii, 0.5, 1.0, and 2.0 km. All parameters were fixed as in Version K, except for a 10 s timestep in the no-pressure perturbation cases, required by the large vertical velocity gradients at cloud top in those cases. Table 4.1 summarizes maximum cloud top height, total rainfall, maximum peak vertical velocity (and time of occurence), and the time that the 20 percent threshhold is crossed, signaling the cloud's end.

Comparing Versions K.M and K (with and without the old mixing length entrainment) we see that the extra entrainment of K.M always weakens the

Table 4.1 Versions, processes included (denoted by X), and results for scale dependence studies. All processes not listed are as in Version K. Version K.NoF.NoP presents identical values for the three radii.

Version		K.M	K	K.NoF	K.NoP	K.NoF.NoP
Mixing length entrainment		X				
Pert. press.		X	X	X		
Vert. turb. fluxes		X	X		X	
Timestep (s)		20	20	20	10	10
Maximum cloud top height (km)	0.5	4.50	5.50	5.25	6.25	6.25
	1.0	5.50	6.00	5.50	6.25	"
	2.0	6.50	6.75	6.00	6.25	"
Total rain (cm)	0.5	.134	.323	.333	.477	.486
	1.0	.322	.464	.394	.454	"
	2.0	.673	.812	.590	.450	"
Max. peak vertical velocity (m/s) at (min)	0.5	4.30(14)	7.29(14)	7.14(14)	7.24(16)	7.43(15)
	1.0	5.71(17)	8.16(17)	7.63(16)	6.99(16)	" "
	2.0	6.51(21)	8.37(21)	7.24(20)	6.95(16)	" "
Lifespan (min)	0.5	31	34	33	38	39
	1.0	33	35	34	37	"
	2.0	37	38	36	37	"

cloud. However, Version K.M is closer to Version K at 2.0 km than at 0.5 km due to the inverse cloud radius proportionality specified by the mixing length term. Such scale dependence might be useful in another context, but it is redundant in the current model.

Version K.NoF.NoP displays no scale dependence, as anticipated. In addition, the time-height cross-sections (not shown) differ from Version P (Fig. 4.3) in having very strong gradients at cloudtop. That is, the line tracing peak values in various quantities run just below cloudtop, rather than in the center of the cloud.

The first possibility for recovering scale dependence is the addition of perturbation pressure (Version K.NoF). This Version shows scale dependence such as real clouds exhibit; clouds of larger radius heat and dry the atmosphere more. We know that the wider clouds are more nearly hydrostatic (Yau, 1979), i.e., the pressure perturbation more completely cancels the other vertical accelerations. As a result, the height of the vertical velocity peak does not rise as rapidly, allowing more time for moist low-level air to enter the cloud and to provide additional latent heat release. The approach to hydrostatic conditions also explains the behavior of peak vertical velocity in Version K.NoF. For radii smaller than about 1.1 km (determined by additional tests) an increase in radius introduces enough additional water vapor that condensational heating eventually overcomes the stronger pressure forces and drives a larger peak in vertical velocity. For radii larger than about 1.1 km the pressure perturbation dominates and peak vertical velocity declines as radius increases (although total mass flux continues to increase).

The second possibility for recovering scale dependence is the addi-

tion of vertical turbulent fluxes of heat, moisture, and momentum (Version K.NoP). We do see a slight scale dependence, but not in the sense we might expect: Version K.NoP clouds with larger radii develop less vigorously! Physically, a larger radius permits larger "sub-gridscale" eddies, which we expect to be more efficient at mixing. The vertical turbulent flux parameterization (Eq. 4.26) includes this effect by a dependence on A, the cloud cross-sectional area. Our tentative explanation of scale dependence by turbulent mixing is based on the opposing effects of water vapor diffusion and momentum diffusion. The dominant term is water vapor diffusion, which acts to provide additional moisture to the saturated parcels near cloud top at the expense of the cloud base. This shift apparently moves the instantaneous latent heating upwards, hastening the rise of the vertical velocity peak, and so the entrainment of dry midlevel air. Meanwhile, momentum diffusion strengthens the cloud, apparently by keeping the vertical velocity peak at a lower elevation in the cloud and so encouraging the entrainment of moist low-level air.

When both perturbation pressure and vertical turbulent fluxes are included (Version K), we see a greater scale dependence than Version K.NoF exhibits. Additional tests suggest that the smoothing due to the perturbation pressure causes the momentum diffusion term to dominate the water vapor term, yielding increased scale dependence. A more detailed examination of scale dependence is left for future research.

A related calculation is the examination of lateral entrainment/detrainment into up- and downdrafts, as well as cloud top entrainment. Here we simply summarize the time-averaged results reported by Randall and Huffman (1982) for Version K.NoF: Fractional lateral entrainment

into updrafts is nearly a constant above cloud base, as is frequently assumed in plume-cloud models, but the fractional entrainment changes very slowly with cloud radius. The fractional detrainment rate from updrafts is a steadily increasing function of height. The exact form of the model predicts zero cloud top entrainment, but numerical diffusion provides a positive value which is close to the vertically averaged net entrainment mass flux.

The second topic to be discussed in this Section is the model's sensitivity to various assumptions. All tests are carried out as in Version K, except as noted in Table 4.2. Results are shown as layer-by-layer domain average changes in water vapor mixing ratio and potential temperature, and the inner cylinder mass fluxes, all summed over the life of the cloud (cf. Fig. 4.4). The vapor and temperature diagrams follow identical plotting conventions; the solid line shows the net change over the life of the cloud, the long dashed lines show net vertical transports (both cloud-scale, with +'s, and turbulent, with x's), the short dashed lines show condensational heating/drying, and the lines with o's show evaporative effects (o's for cloud evaporation, •'s for rain evaporation). Updraft and downdraft mass fluxes in the inner cylinder are summed separately.

Broadly speaking, the cloud dries the lower half of the layer in which it grows and moistens the upper half, although the net effect is drying, since there is rainfall. The net change is primarily a balance among condensation, cloud evaporation, and cloud-scale vapor transport. The temperature change shows warming, except near the cloud top and in the subcloud layer. The net change is primarily the difference between condensation and cloud evaporation, with cloud-scale transport entering

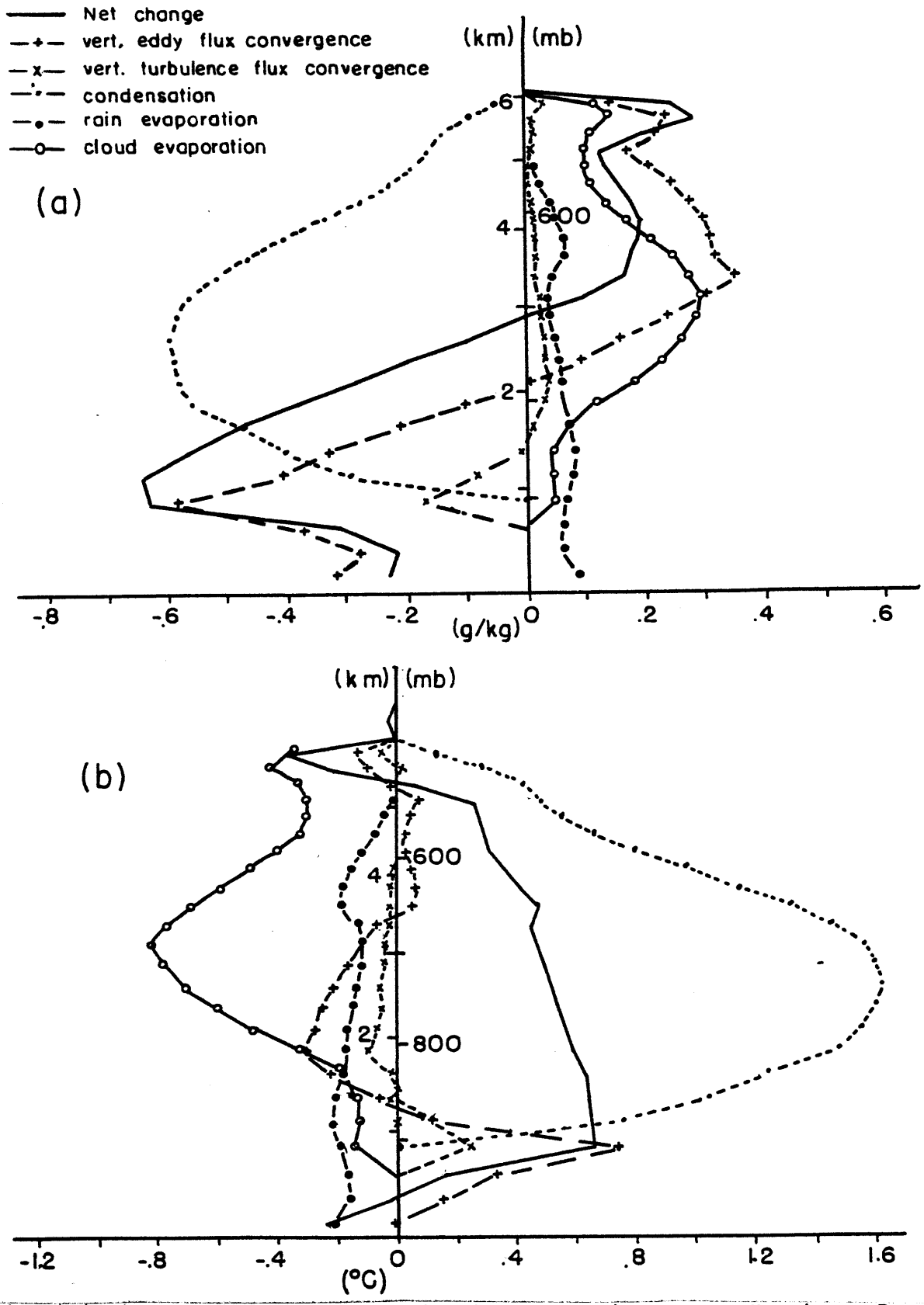


Fig. 4.4 Microphysical parameterization comparison. Version P, (a) moistening, and (b) heating; Version K, (c) moistening, and (d) heating. The net change (——) is the sum of net vertical

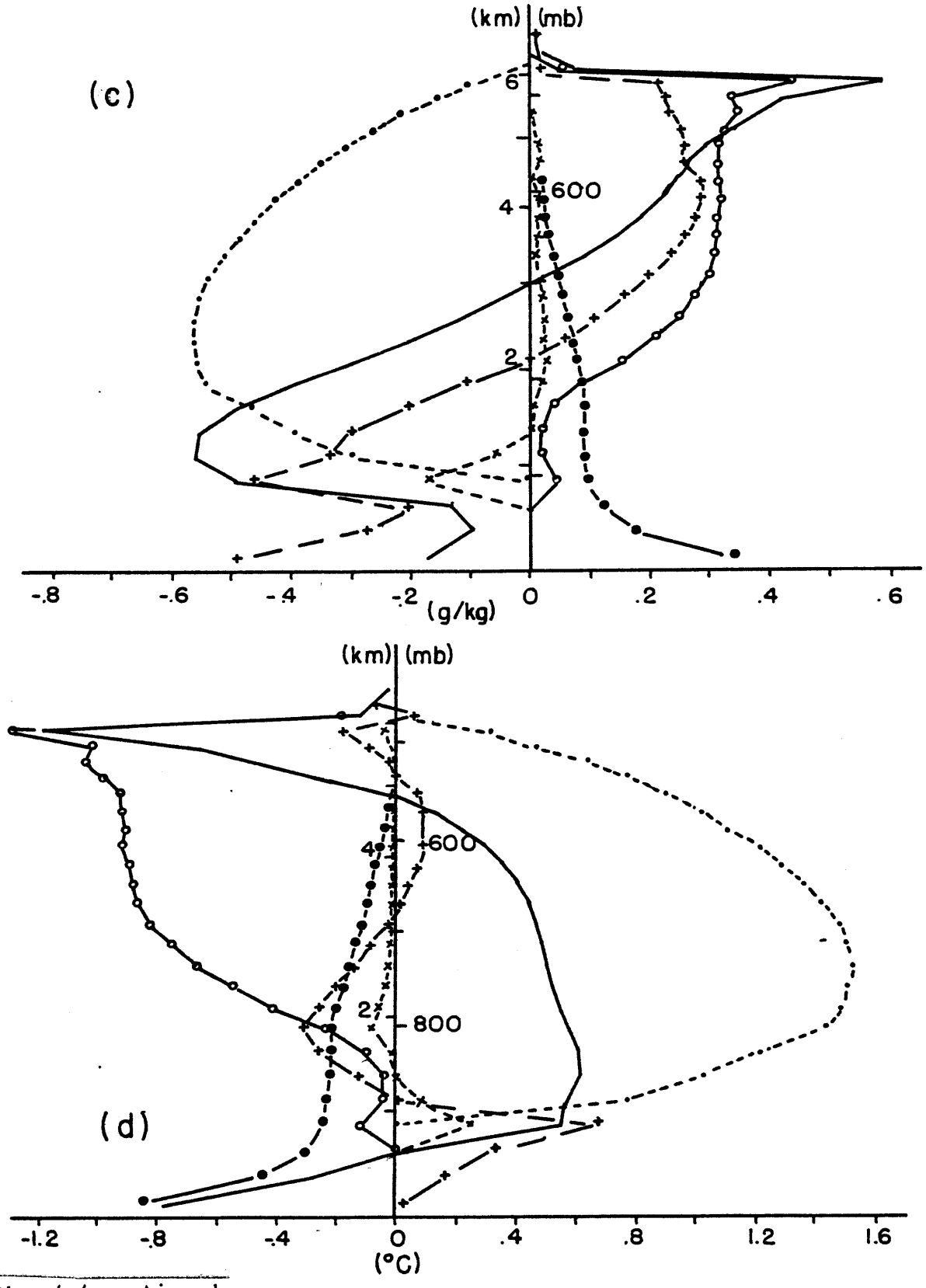


Fig. 4.4 continued.

transports, both cloud-scale (-+-) and turbulent (-X-), condensational heating/drying (- -), and evaporative cooling/moisten-

(e)

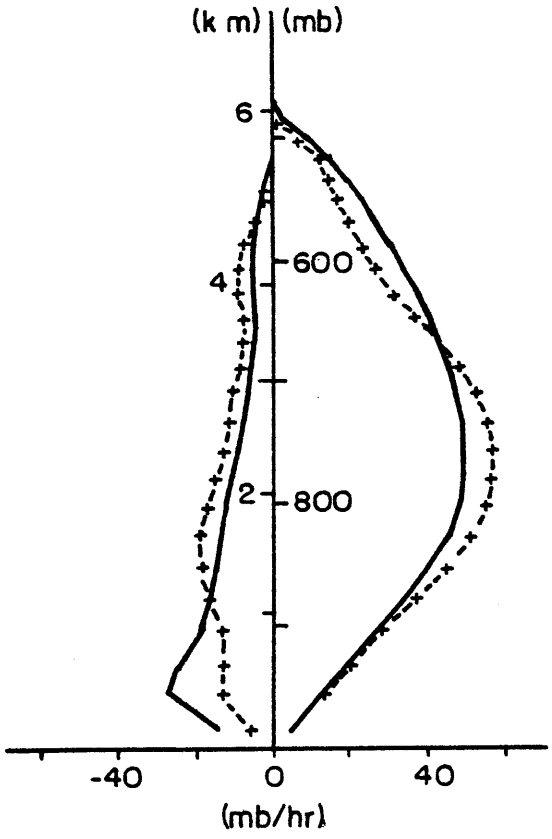


Fig. 4.4 continued.

ing, both cloud (-o-) and rain (-•-) evaporation. (e) Inner cylinder up- and downdraft mass fluxes for P (-+-) and K (——).

Table 4.2. Versions and associated assumptions for sensitivity tests.

Version	P	K	P.C	K.C	P.R	K.R	K.G	K.W
Microphysics	P	K	P	K	P	K	K	K
Grid size (m)	250	250	250	250	250	250	500	250
$\overline{w}$	n	n	n	n	n	n	n	y
Rain transfer	n	n	n	n	y	y	n	n
Cloud cutoff	20%	20%	1hr	1hr	20%	20%	20%	20%

near and below cloud base. In both budgets, rain evaporation and vertical turbulent fluxes are small, except near and below cloud base. The area-averaged changes shown here are similar to those which Soong and Ogura (1976) derive from their two-dimensional, axisymmetric, one-cloud model.

The first test compares Versions P and K to examine the effects of changing the microphysical parameterization (Fig. 4.4). The heat budget, moisture budget, and mass fluxes for the two parameterizations are substantially the same, as Yau (1980) observed. For this reason, it was legitimate to run the scale dependence study above with the simpler K microphysics. However, there are differences. First, the evaporation of cloud near the maximum cloud top height is about 2.5 times as large in Version K as in P, resulting in much more moistening and cooling in the upper cloud for Version K. This difference stems from a more efficient accretion of cloud water by rain in the case of many small raindrops for the (more realistic) P microphysics. The difference in accretion efficiency helps to explain the difference in total rainfall. A second difference is that the rainwater evaporation in Version K peaks sharply near the surface, while it varies slowly with height in Version P. Physically, and in Version P, the small drops rapidly evaporate, leaving the the larger drops to fall out without substantial evaporation. On the other hand, the assumed size distribution in K forces a continuing evaporation of presumed small drops. Murray and Koenig (1972) provide more detail on the role of evaporation in the subcloud downdraft. The third difference is related to the second. The extra cooling below cloud base in Version K drives a larger downward mass flux, drying out the lowest layers by transport of the subsaturated

downdraft air. Inspecting Fig. 4.4c, the additional vertical flux of dry air overwhelms the extra moistening from the rain evaporation. We conclude that Version P is superior to Version K, particularly in cases involving quantitative estimates. The penalty is a larger computer program which requires about 2.5 times as much computer time as Version K.

We next test the effect of the 20% criterion by considering a cloud lifespan of 1 hr (Versions K.C and P.C, shown in Fig. 4.5). Again, the profiles for the two microphysics are substantially the same, with K displaying about 2.5 times the cloud evaporation near cloud top as P, and K rain evaporation peaking near the ground versus the more even profile for P. Now, however, both P and K show a large drying at low levels by vertical moisture fluxes, and a corresponding peak in downward mass flux. Based on the LeMone and Zipser (1980) observations and Soong and Tao (1980) model results reviewed above, we expect upward and downward mass fluxes near cloud base to nearly balance. On the other hand, the lifecycle-averaged mass flux which Murray and Koenig (1975) calculated for their axisymmetric, one-cloud model shows large downward values below cloud base directly under the cloud. On the whole, we regard the 20% threshhold as an acceptable simplification.

The third test is to allow the transfer of rain between the inner and outer cylinders (Versions K.R and P.R, shown in Fig. 4.6). The various profiles are similar to the corresponding no-transfer profiles, particularly Version K. For the P microphysics, mid-level evaporative cooling by detrained rain drives additional upward mass flux in the inner cylinder, resulting in the detrainment of more cloud and vapor near the cloud top. The fact that the resulting upper-cloud profiles for Version P.R

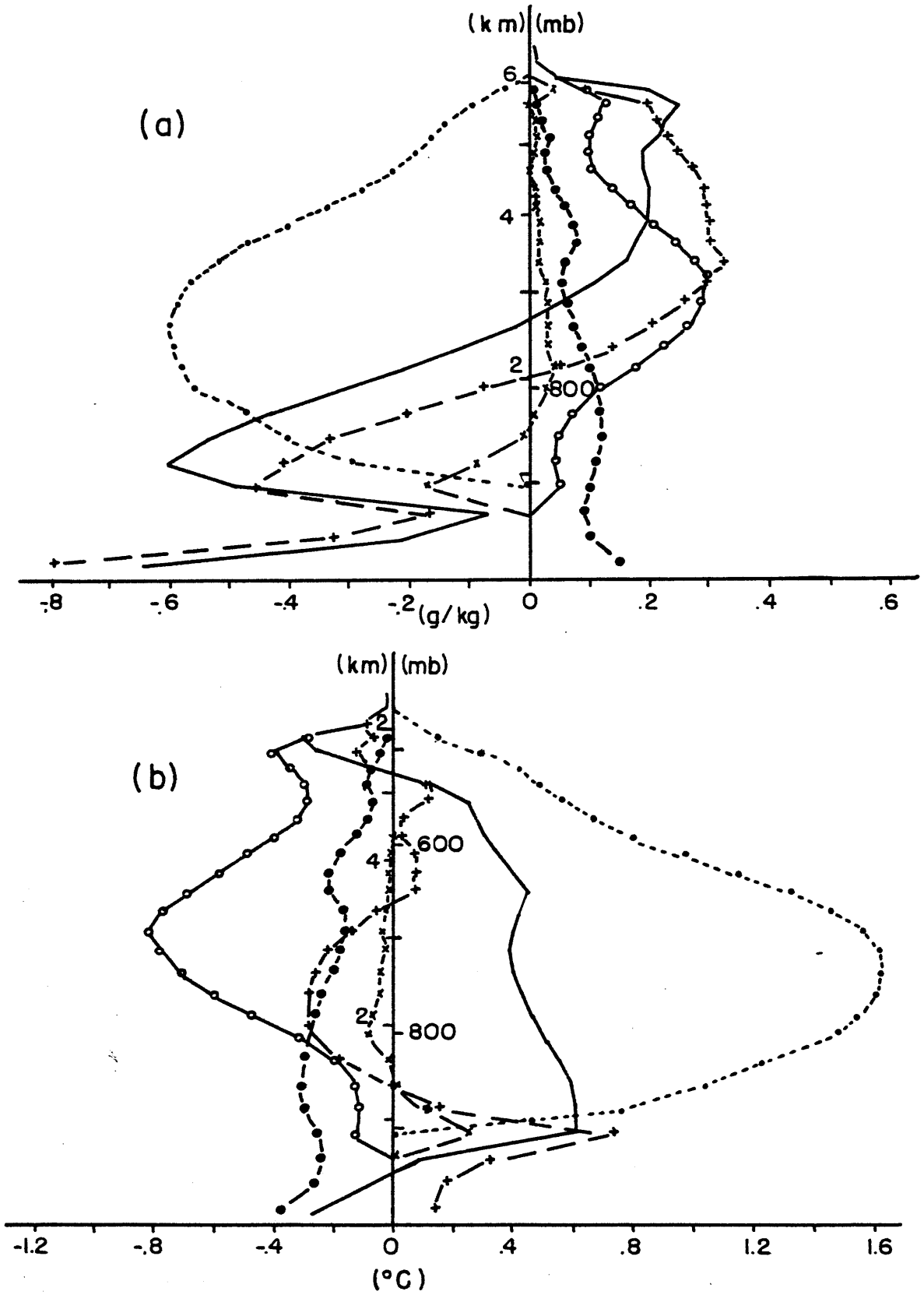


Fig. 4.5 Cloud lifespan criterion test. As in Fig. 4.4, except for Versions; (a) P.C, (b) P.C, (c) K.C, (d) K.C, (e) P.C (-+-), K.C (——).

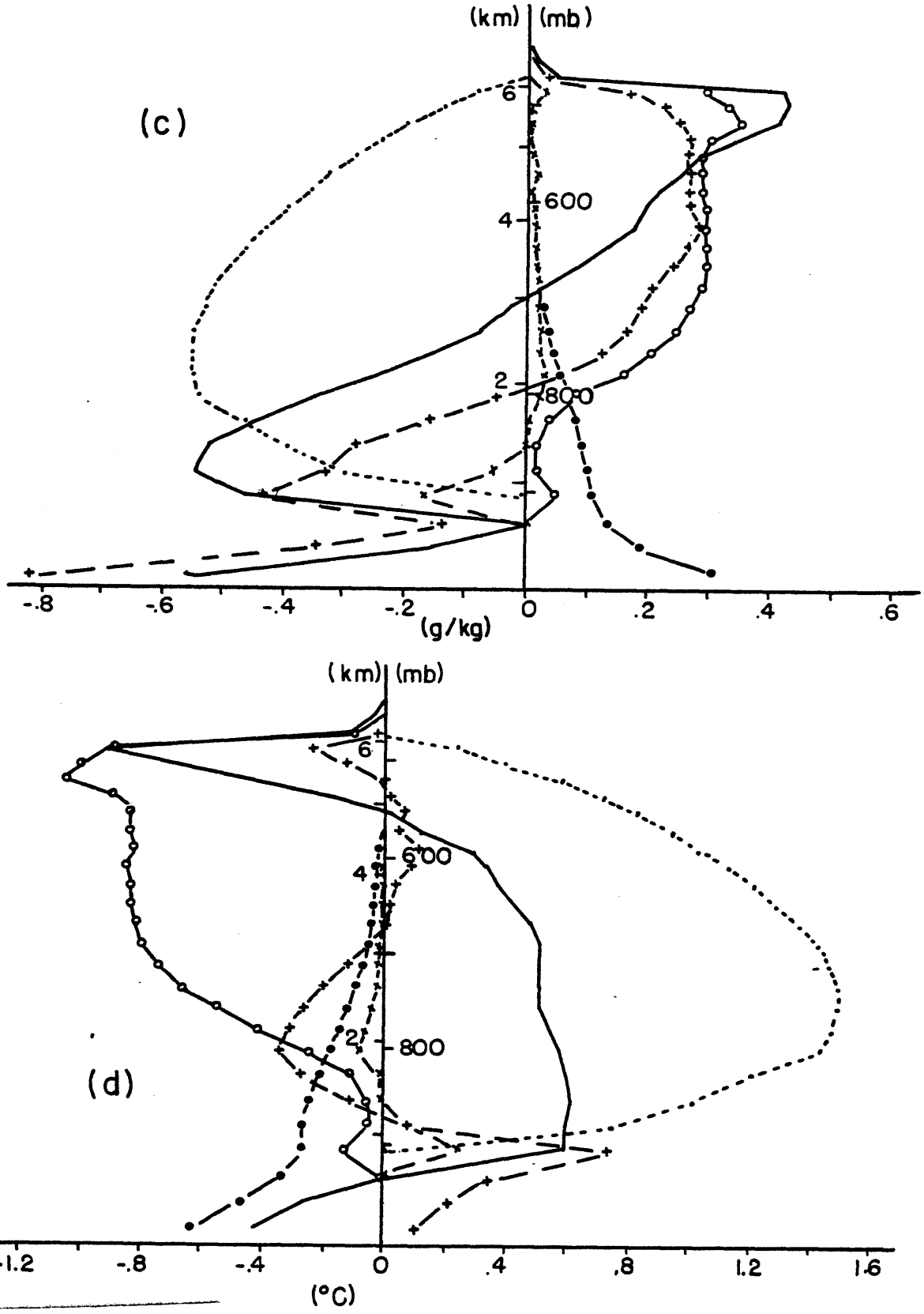


Fig. 4.5 continued.

(e)

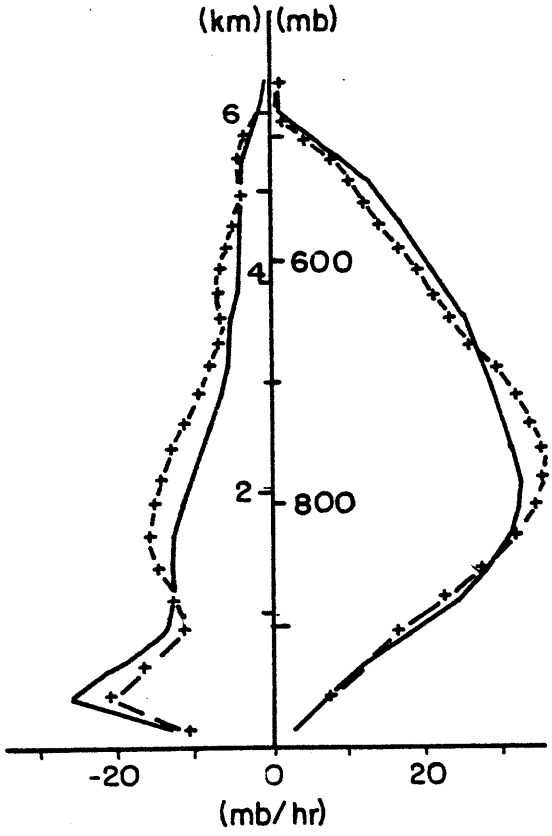


Fig. 4.5 continued.

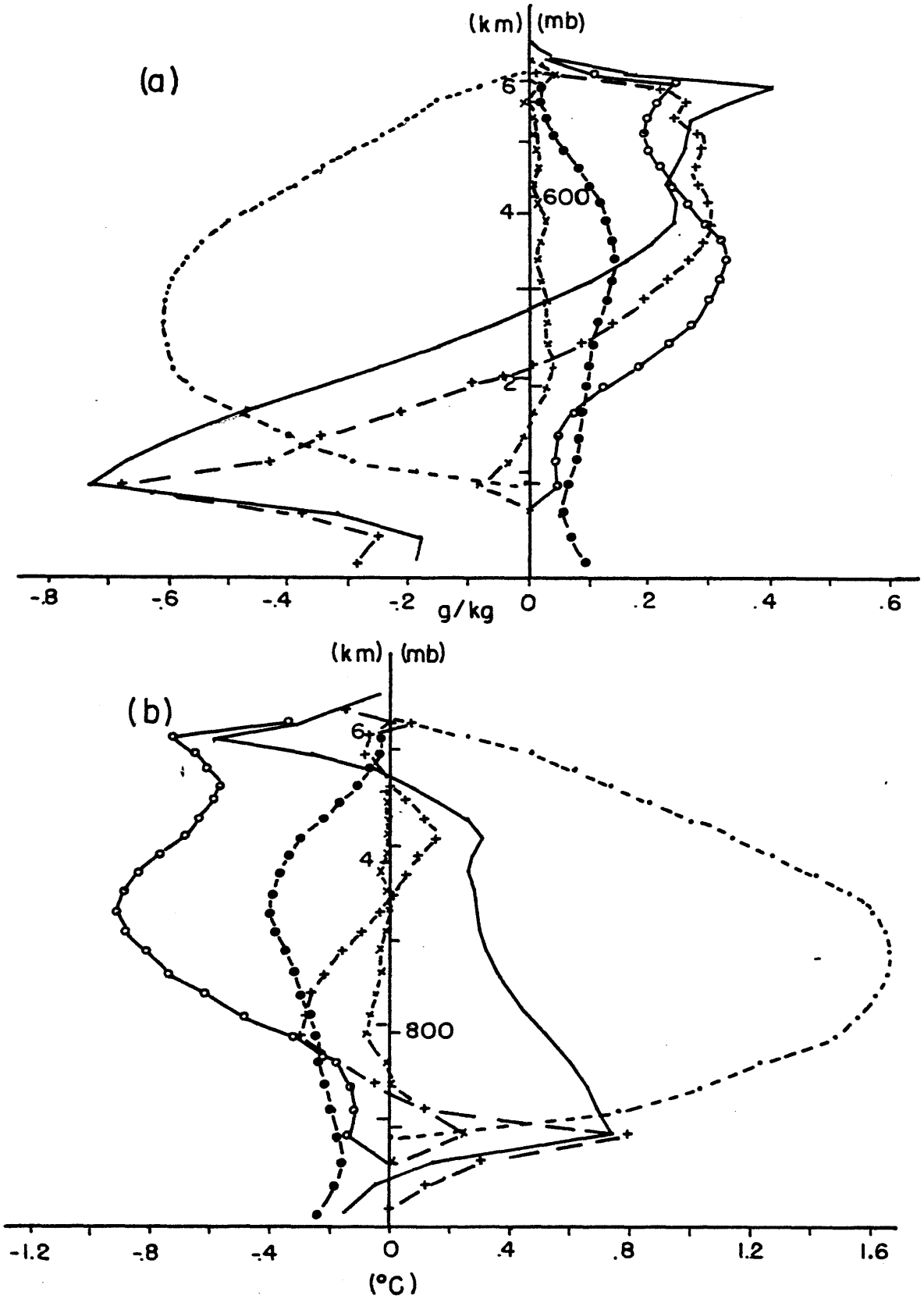


Fig. 4.6 Horizontal rain advection test. As in Fig 4.4, except for Versions; (a) P.R, (b) P.R, (c) K.R, (d) K.R, (e) P.R (-+-), K.R (——).

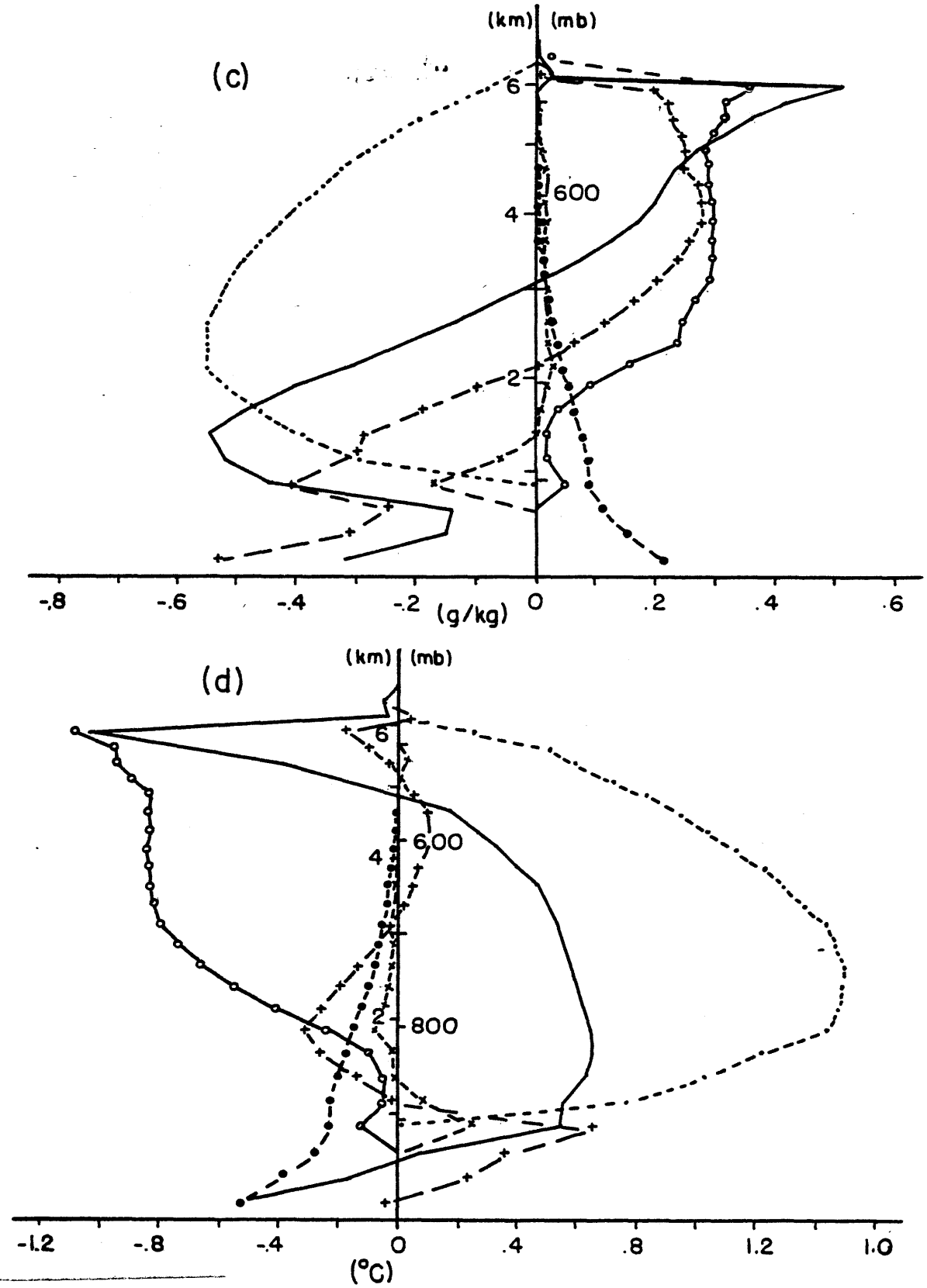


Fig. 4.6 continued.

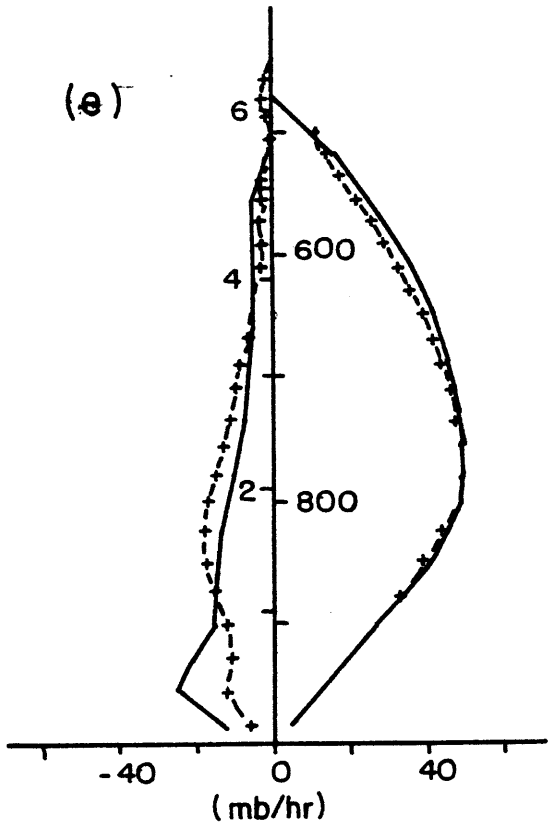


Fig. 4.6 continued.

are closer to those of K.R than the corresponding K - P comparison is interpreted as a shift away from the more realistic Version P.

The fourth test is to change the resolution to 500 m (Version K.G, Fig. 4.7), a configuration which takes half the storage and execution time of Version K. Making the comparison with Version K (Fig. 4.4c-e), we see general qualitative agreement, but there are major differences in the profiles near cloud base, particularly in vertical water vapor fluxes, and the vertical development of the cloud is different. Since we expect the higher resolution version to be more accurate, we are forced to conclude that Version K.G is useful only for preliminary tests.

Finally, we consider Version K.W, Version K with an imposed large-scale lifting (Fig. 4.8). The imposed vertical velocity has an exponentially damped sinusoidal amplitude, peaking at 5 cm/s at 850 mb (plotted as mass flux in Fig. 4.8c). Making the comparison to Version K (Fig. 4.4c-e), we see two responses. In the upper part of the cloud we see additional condensation, opposing and even overcoming the cooling and moistening due to the lifting. In the lower part the condensational heating is nearly the same in the two Versions, so the large-scale effects directly contribute to the net temperature and moisture changes. Since these alterations in low-level temperature and moisture bring the cloud base closer to its initial state, we might expect a subsequent cloud in Version K.W to be stronger than a subsequent cloud in Version K.

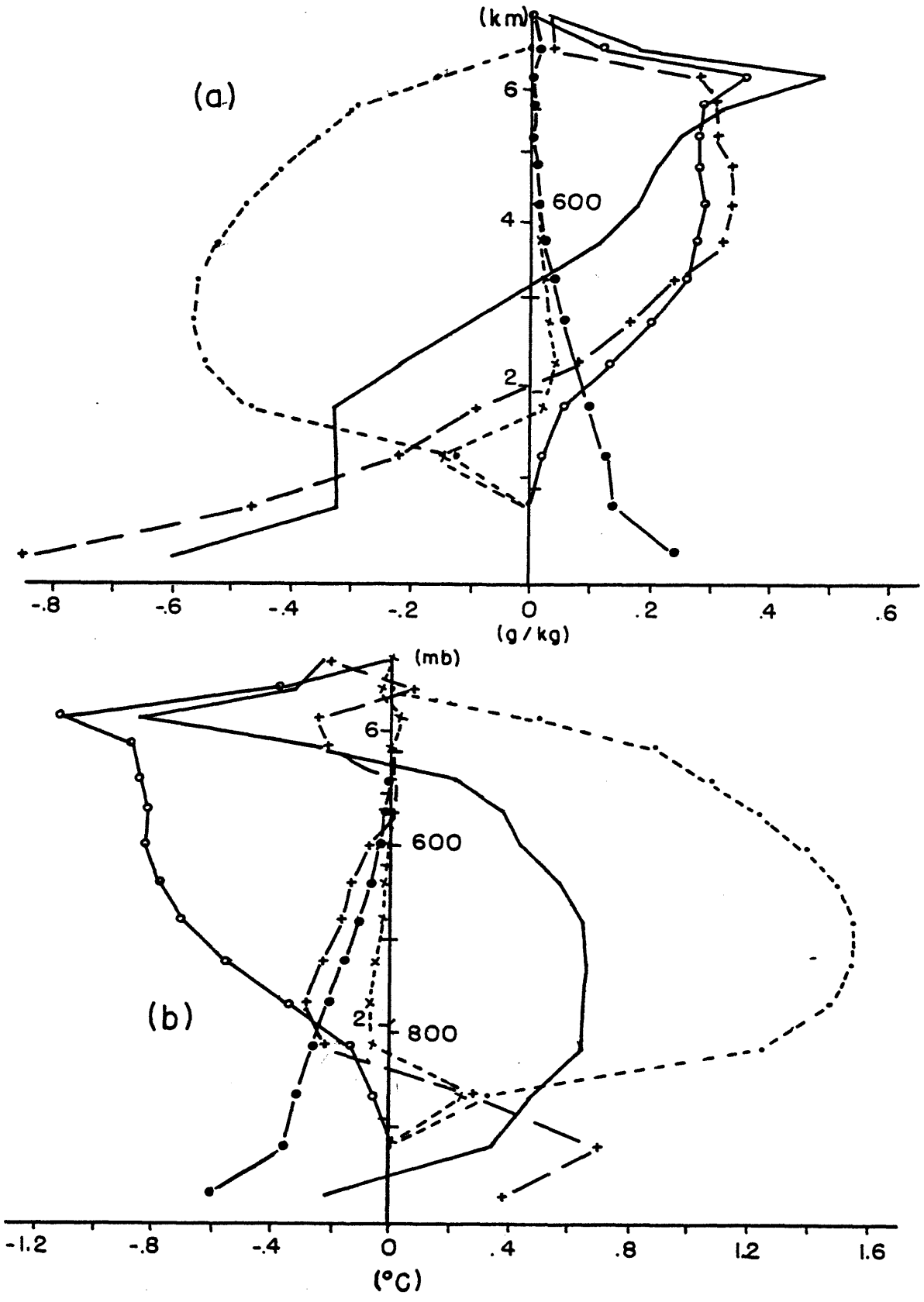


Fig. 4.7 Vertical resolution test. As in Fig. 4.4, except for Versions; (a) K.G, (b) K,G; and (c) as in Fig. 4.4e, except K.G (——).

(c)

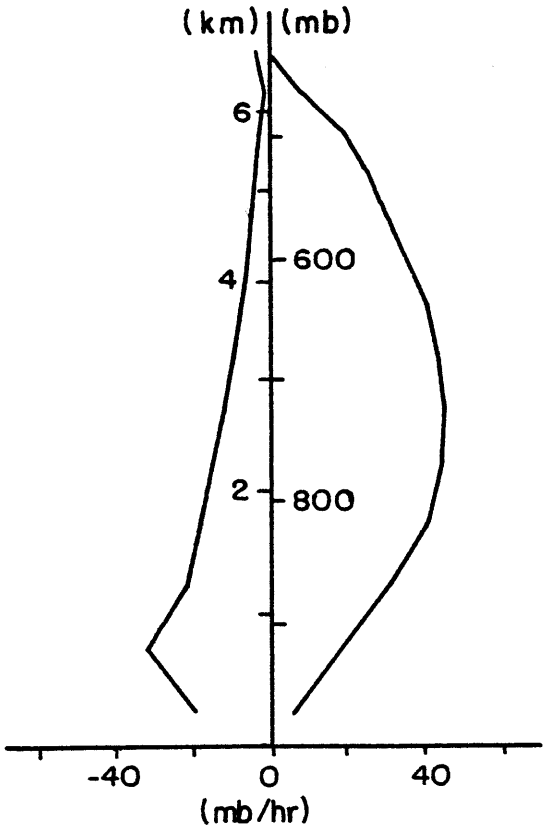


Fig. 4.7 continued.

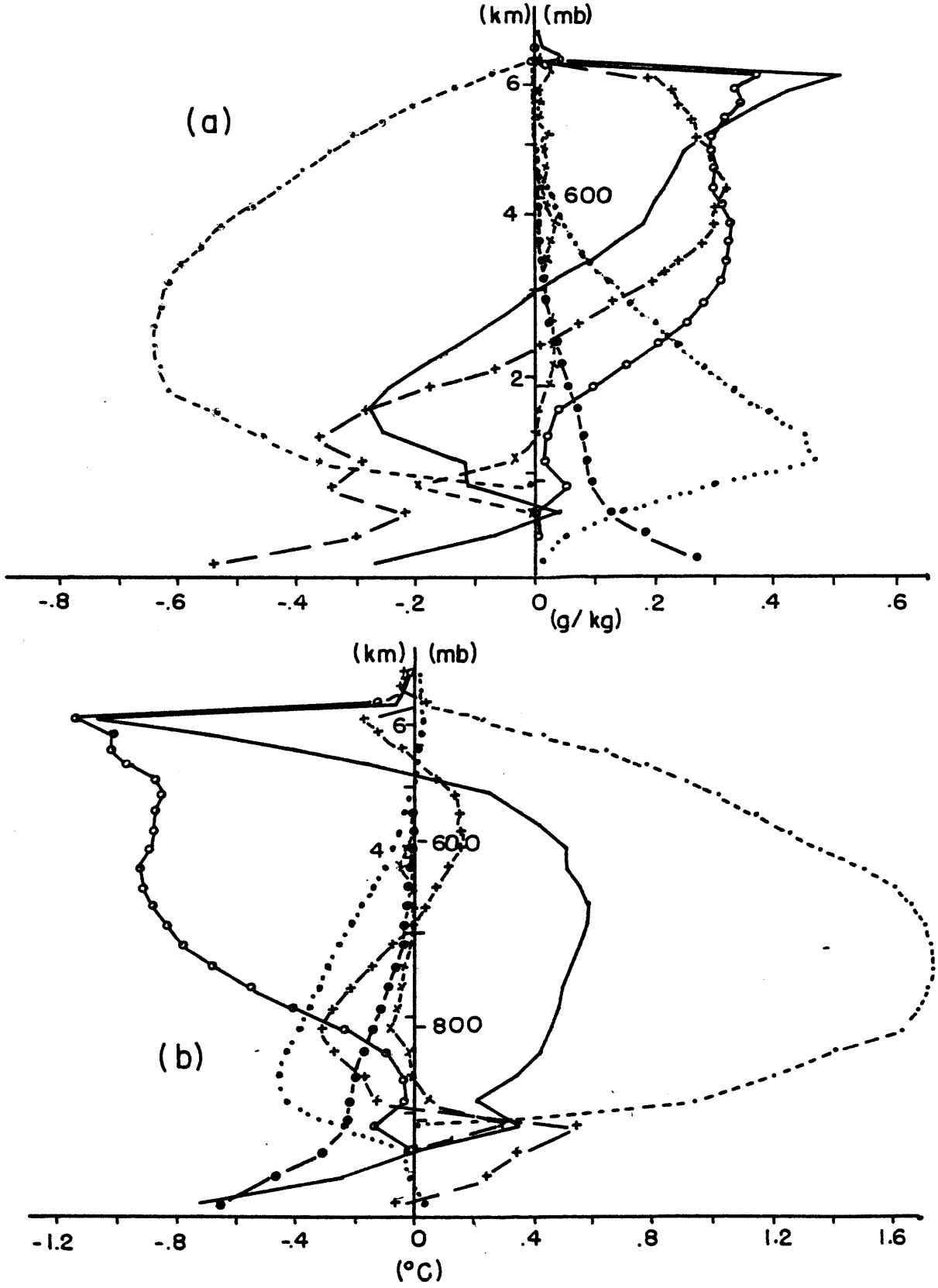


Fig. 4.8 Large-scale lifting test. As in Fig. 4.4, except for Versions; (a) K.W, (b) K.W, and (c) as in Fig. 4.4e, except K.W (——). Large-scale moistening, heating, and mass flux are

(c)

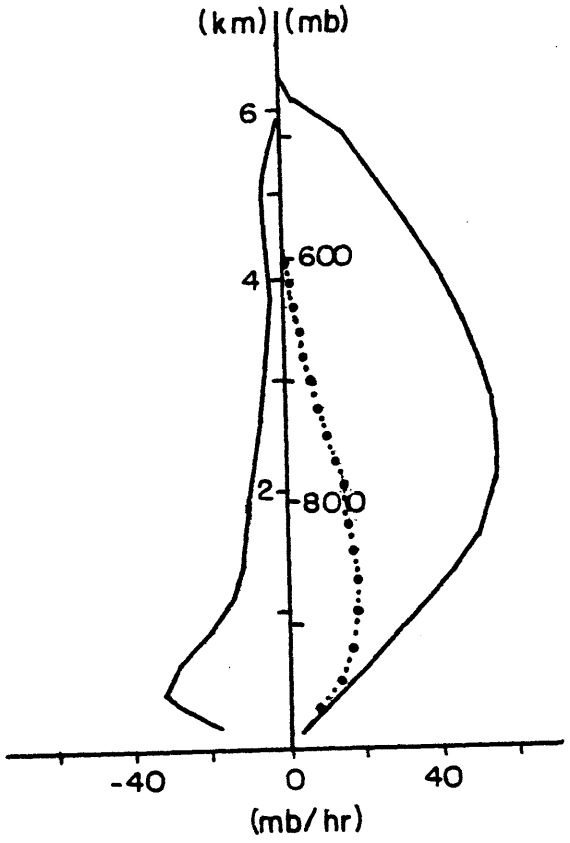


Fig. 4.8 continued.

shown as dotted lines.

4.7 Summary

This chapter presented the first half of the development of a new cumulus cloud ensemble model. We choose to follow a spectral diagnostic budget approach, in which the properties of a spectrum of possible cloud sizes are diagnosed by requiring that that the model reproduce observed heat and moisture budgets. After considering specific design criteria, we proceeded to develop a suitable one-cloud model. First, assuming that a cloud is a turbulent region within a quiescent environment and that the turbulent motions are scale-separated from cloud-scale motions, we showed that the mass flux across the cloud boundary is closely coupled to turbulence and source-sink terms on the boundary (Eq. 4.10). By applying 4.10 to the two-cylinder geometry, we arrived at Eq. 4.20-4.22. These equations are equivalent to the equations in Asai and Kasahara (1967), except that their mixing length entrainment terms are absent. We noted that the correct formulation has no horizontal scale information. The system of equations was completed, including a choice of Kessler (1969) or Yau and Austin (1979) microphysical parameterizations, non-hydrostatic pressure perturbations, vertical turbulent fluxes, large-scale vertical velocity, prescribed large-scale surface fluxes of heat and moisture, and prescribed large-scale radiative heating. The horizontal transport of rain was neglected.

We then examined the model's behavior. Horizontal scale dependence is reintroduced primarily by the perturbation pressure. Adding vertical turbulent fluxes increases the dependence shown by including perturbation pressure alone, but vertical turbulent fluxes by themselves create a slightly negative correlation between cloud radius and cloud intensity. The choice of microphysical parameterization was shown to be

unimportant for the qualitative model behavior, but large quantitative differences occur at the bottom and top of the cloud. We also examined the effect of varying the vertical grid spacing, changing the endpoint of the cloud lifetime, and allowing the horizontal transport of rain water out of the inner cylinder. In the last two cases the behavior of Version P (configured at the beginning of Section 4.6) was found to be slightly preferable. In the first two cases Version P was strongly preferable. This conclusion must be balanced against the greater cost of Version P compared to Version K or K.G, 2.5 and 5 times as much, respectively. Finally, we considered the effect of imposing a large-scale lifting. In the case chosen, it caused increased cloud activity at high levels, canceling or overwhelming the lifting effects, while at low levels the lifting effects dominate the net temperature and vapor changes.

5. The Model: Ensemble

5.1 Introduction

In this chapter we carry out the second step in formulating our new model of an ensemble of cumulus clouds. Having detailed a particular cloud model in the previous chapter, we now extend those concepts to form the ensemble model. To recapitulate the design goals of Section 4.1;

1. The model follows the spectral diagnostic budget approach;
2. each cloud is modelled as a distinct entity;
3. the numbers of clouds of various sizes are free parameters;
4. the model is economical;
5. the model is time-dependent;
6. the model includes mesoscale structure.

The next Section will describe the basic multi-cloud model, while the third Section concerns the inclusion of mesoscale structure. The fourth Section presents various choices and tests which are needed to complete the model.

5.2 Many clouds in a common environment

How are we to economically harness several model clouds to run in a common environment? The simple cloud model we described previously provides the answer. The Asai and Kasahara (1967, hereafter AK) approach of using area-average "tophat" values reduces the number of gridpoints at each level to two, one each for the cloud and the environment. Such averaging removes all of the information about the horizontal structure in the model except that specifically retained by the choice of geometry, namely the shapes and areas of the regions. In the

case of the one-cloud model, it is physically reasonable (as well as computationally simple) for the cloud to be round and for the environment to uniformly surround it. To form the ensemble, we stretch the outer boundary of the "outer cylinder" and place additional "inner cylinders" (of various sizes) inside this new, larger domain. Then we again apply area-averaging, reducing each variable to one value at each level for each cloud and one value at each level for the environment. By averaging away the details of the environment, we are assuming that it is not necessary to carry such detail explicitly (statistical homogeneity). Nevertheless, this assumption implies a geometry: The various clouds should be randomly scattered across the environment in order to yield net cloud effects which are similar in all parts of the domain (on the average), a sort of "plum pudding" model (Fig. 5.1a). It continues to be reasonable (and computationally simple) to specify round clouds. This picture of various clouds (many "inner cylinders") scattered across a uniform environment (one "outer cylinder") is similar to the Arakawa and Schubert (1974) concept of a cumulus ensemble, although the specific model approximations such as time-dependence are quite different.

Most details carry over from the cloud model already described. The microphysics and vertical turbulent fluxes are parameterized as described in Chapter 4. Radiative heating, boundary fluxes, and large-scale vertical velocity are prescribed. The vertical velocity in the environment is diagnosed from continuity, although it now compensates the motion of many clouds instead of just one. Horizontal velocity is calculated explicitly from continuity on cloud and environment boundaries.

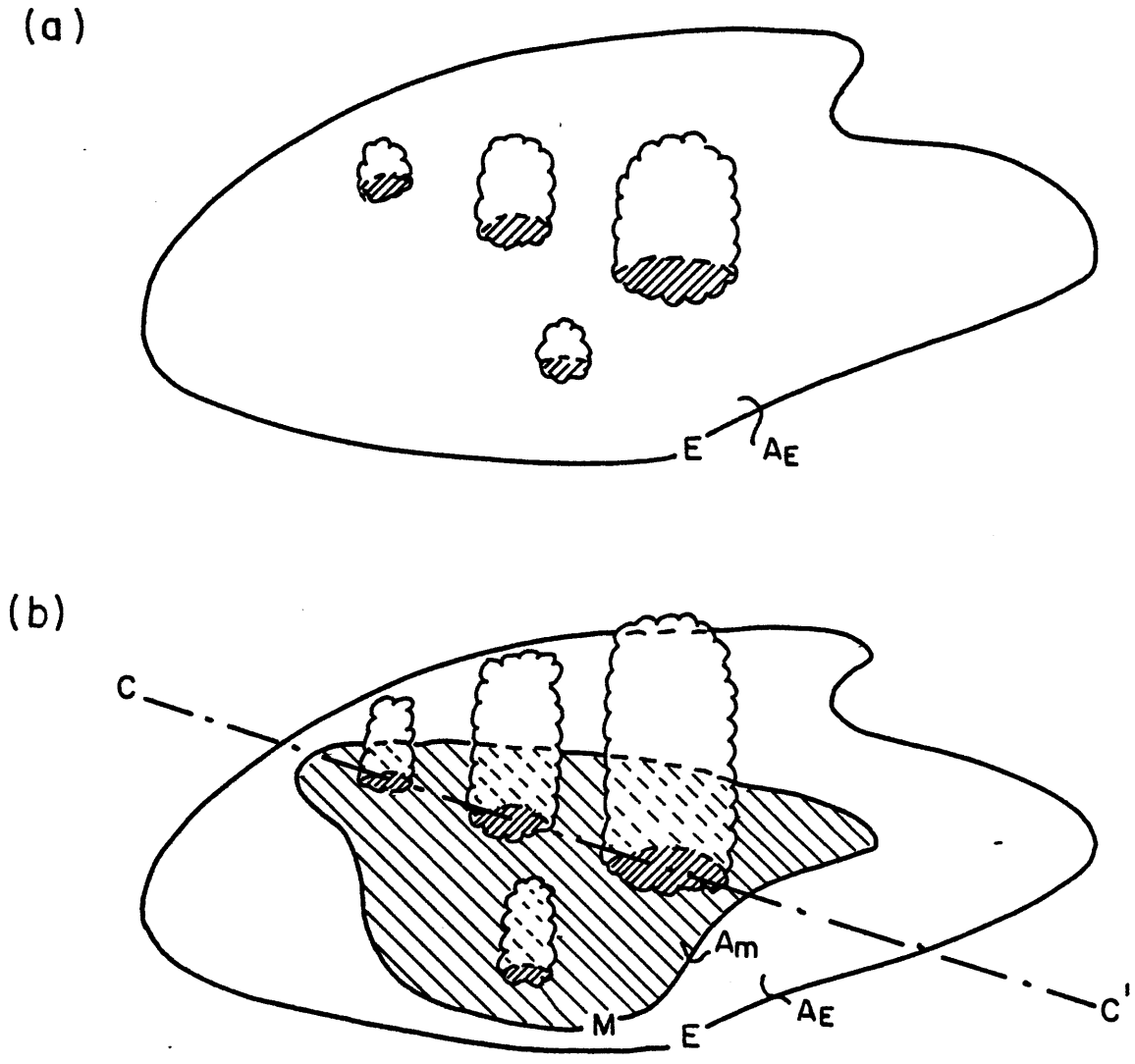


Fig. 5.1 Schematic representation of a cumulus cloud ensemble. (a) Clouds in a homogeneous large-scale environment (bounded by E). (b) A system containing clouds, a mesoscale feature (bounded by M), and an outer environment (bounded by E). A cross section (C-C') is shown in Fig. 5.2.

The pressure perturbation is potentially more problematic because the model geometry enters the calculation. However, the assumptions already made are nearly sufficient to allow us to retain the Fourier-Bessel representation of perturbation pressure introduced in Chapter 4. First, the horizontal averaging eliminates direct cloud-cloud interactions, so that each cloud's pressure perturbation can be (in fact, must be) treated separately. Second, the assumption that the clouds are round gives the proper geometry for the Bessel representation. Third, the top-hat profiles of the various variables provide the same algebraic profiles as before. Two additional assumptions complete the transition:

1. Each cloud's perturbation pressure is assumed to extend into the near environment axisymmetrically, ending at some radius from the cloud center proportional to cloud radius. This is the same assumption adopted in the one-cloud model, except that now the pressure domain does not necessarily coincide with the region which compensates cloud mass fluxes.
2. The horizontal wind entering the pressure perturbation calculation is based solely on cloud-induced mass divergence. This approximation is consistent with the assumption of axisymmetric clouds, which precludes wind shear. We are free to make this choice because area-averaging removes the necessity of calculating horizontal wind, except as mass fluxes at region boundaries.

5.3 Including mesoscale organization

The review presented in Chapter 2 clearly shows that mesoscale organization is common and seems important. It is a straightforward task to

incorporate mesoscale structure into the model under the technique of area-averaging the equations in the various regions. The environment (the old "outer cylinder") is partitioned into mesoscale and "outer environment" regions, with each having horizontal-average (tophat) values for variables (see Fig. 5.1b). Following the observations in Lopez (1978) concerning the occurrence of cumulus cells inside mesoscale features, we assume that the mesoscale features, when present, encompass all convective clouds. We continue to diagnose vertical velocity in the outer environment, so the vertical velocity of the mesoscale region is predicted, based on accelerations due to buoyancy, drag, momentum advection, pressure forcing (in the "outer region" of each perturbation pressure domain), and residual diffusion (to control small-scale noise). The free parameter for the mesoscale feature is its area. Fig. 5.2 shows a schematic vertical cross-section of the ensemble model.

Even this simple representation of mesoscale structure allows for several important effects:

1. The feature may provide "mutual protection" (Randall and Huffman, 1980): Cumulus clouds may create, in their near environments, relatively favorable conditions for the development of succeeding clouds. The clouds can do this by moistening the near environment (even while drying the distant environment), and by steepening the near environmental lapse rate (even while stabilizing the distant environmental lapse rate). The relatively moist, unstable near environment then serves to "protect" succeeding clouds by sheltering them from the relatively dry, stable air of the distant environment. Hill (1974) found that moist anomalies were left behind by the decay of his numerically simulated clouds. This is actually an old idea, first

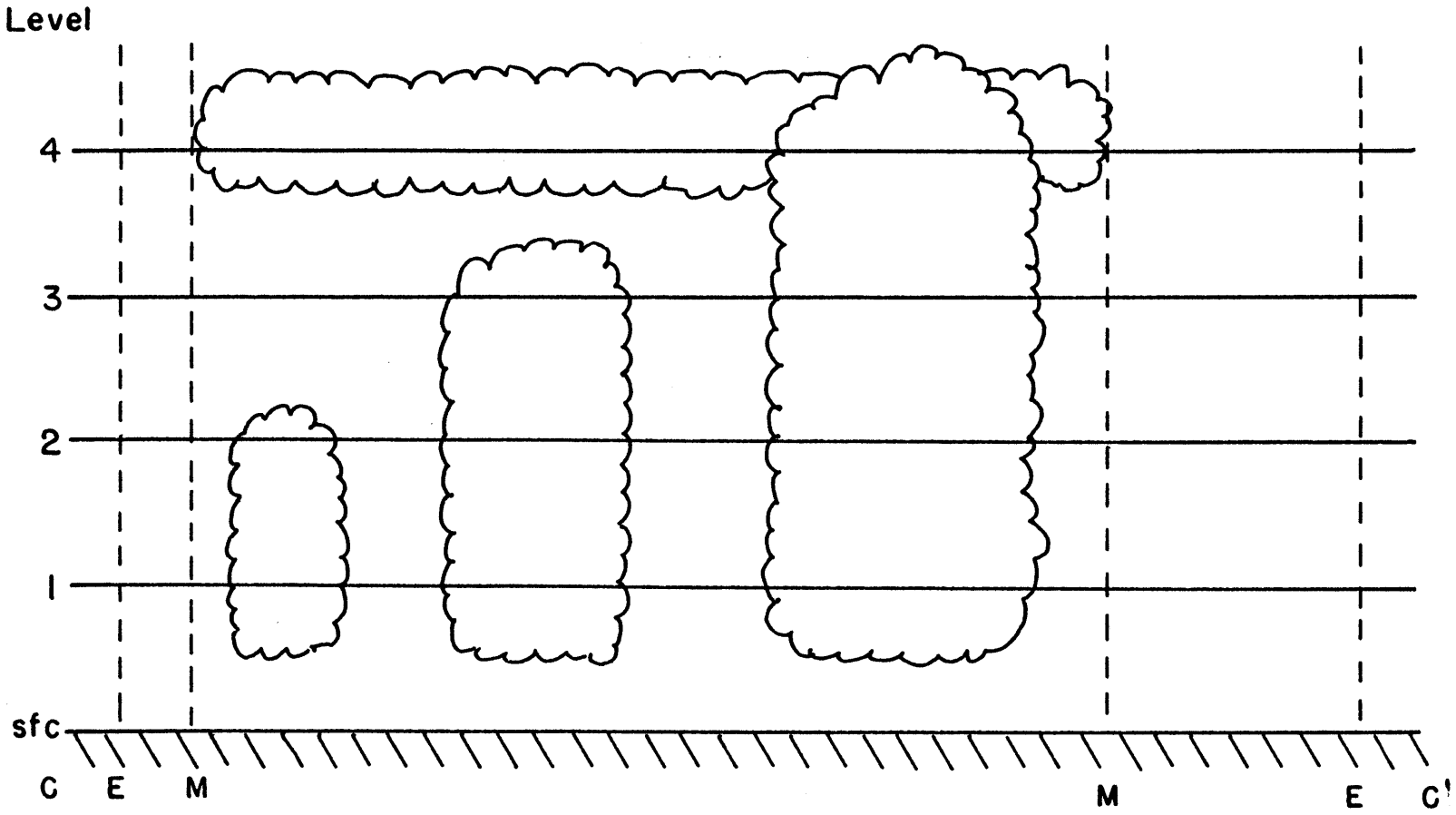


Fig. 5.2 Schematic vertical cross section through Fig. 5.1b, showing some atmospheric levels and the maximum sizes clouds attain over their lifecycles. Level 4 is depicted as carrying a mesoscale anvil (not shown in Fig. 5.1b). E and M are the boundaries in Fig. 5.1b.

advanced by Scorer and Ludlam (1953), and resurrected by Lopez (1978).

2. At various levels the mesoscale feature as a whole may become saturated, forming an anvil, as discussed by Houze (1977). In GATE such anvils were important contributors to the moisture budget, providing some 40% of the total rainfall (Cheng and Houze, 1979). Additionally, anvils may significantly contribute to water storage. On the basis of ship-board all-sky cameras and satellite data, Johnson (1980) estimated that storage in "inactive" cloud may amount to 20% of Q_2 when cloud coverage is changing rapidly. Frank (1979) calculated the storage necessary to reconcile the time behavior of precipitation estimates based on heat and moisture budgets with those based on radar measurements. Depending on assumptions, the average storage is 0.22-0.56 g/cm^2.
3. There may be mesoscale updrafts and downdrafts, as discussed by Zipser (1977) and Houze (1977). The Johnson (1980), Houze et al. (1980), and Houze and Cheng (1981) model results indicate that mesoscale transports are important for modifying the heat and moisture budgets which the cumulus ensemble must satisfy (taking a diagnostic viewpoint). Of course, in the current model mesoscale motions may significantly change the environment of the clouds, changing the static control.

Various other mechanisms for creating mesoscale structure are excluded by our simplifications. The horizontal equation of motion is not integrated, excluding non-convective instability (eg., inertial instability, Emanuel, 1979). Surface forcing is assumed uniform, excluding direct forcing by local "hot spots" (Malkus, 1957), orography,

or other surface features. The geometric configuration of clouds is ignored, excluding squall lines and squall line/mesoscale anvil systems (Zipser, 1969, 1977, among others). A final limitation is that the simple geometry prevents us from saying whether the area of the mesoscale region is in several separate pieces.

5.4 Additional details

In order to complete the ensemble model we must deal with two general questions. The first is, how do we represent the cloud population numerically? Obviously, we need a measure for cloud "size", yet rainfall rate and ultimate cloud height are not parameters which we control directly. In our model the only externally specified geometric parameters for each cloud are the cloud radius and the ratio of cloud radius to outer pressure domain radius. The ratio is not a well-observed quantity, but a reasonable choice is to make it a constant (bigger clouds affect a larger area). Thus, we specify cloud size by cloud radius.

The range of radii is problematic. In the distribution of radar echo cross sectional area which Lopez (1978) showed for cells from groups, the 50 percentile equivalent radius occurred at 3.1 km and the 10 percentile equivalent radius occurred at 4.6 km (Fig. 2.4a). In contrast, the updraft core diameters which LeMone and Zipser (1980, hereafter LZ) observed showed the 50 percentile pathlength to be 0.9 km, with the 10 percentile pathlength varying between 1.6-2.0 km (Fig. 2.1). If we correct the LZ figures for random sampling of circular drafts,[1]

---

1 Equivalent radius = pathlength * $2/\pi$.

the 50 and 10 percentile equivalent radii are 0.6 and 1.0-1.3 km respectively. The discrepancy between these two sources is partly resolved by referring to Stailey (1978), who applied the Yau (1980) model to several cases in GATE. In order to set the model geometry, he computed the average inner cylinder (cloud) radius and outer cylinder (environment) radius for various criteria on the radar reflectivity observed in several lines and clusters of convective cells. Stailey's values for cloud radii fall in the range of radii shown by LZ, while his values for environmental radius correspond to the range of radii shown by Lopez. On this basis, we consider the range of radii displayed by LZ to be more representative of our cloud sizes. In particular, radii between 0.5 km and 3.0 km are permitted.

At a given instant we observe clouds of all sizes at all points in their lifecycles, so further approximation is clearly necessary. We choose to represent the size distribution by a small number of subensembles having fixed radii. Five subensembles are used in the present study. Furthermore, for the sake of economy we make the assumption that explicitly timestepping one member of the subensemble and multiplying all transports by the population of that subensemble will represent the lifecycle and feedback of that subensemble with sufficient accuracy. Although this approximation implies that all members of the subensemble are at the same stage of their development at a given instant, we expect the lifecycle average properties to be relatively unaffected.

The second question is, in what parts of the cloud lifecycle must we intervene? We know that some perturbation in velocity, moisture, and/or temperature must be given at the beginning to initiate the cloud. Murray (1971) presented theoretical and observational evidence for per-

turbing the moisture field, but not the temperature field. His comments are reinforced by Nicholls and LeMone (1980), who showed that the fluxes of mass and moisture into the bases of nascent trade cumuli are positive, while no temperature flux is apparent. We will specify a perturbation in moisture and velocity, but not temperature, as in Chapter 4; we pick a perturbation top, H_o, and a maximum perturbation vertical velocity, W_o, then specify a sine profile of perturbation vertical velocity according to Eq. 4.27, and specify saturation between nominal cloud base (500 m) and H_o. When H_o falls within a layer, the layer is moistened according to the fraction that lies within the perturbation. Additionally, the moisture added to the perturbation to bring it to saturation is removed from the lowest 500 m (the nominal PBL) of the region in which the cloud is growing. This process conserves total water in the system and models the growth of the nascent cloud out of boundary layer air.

When we use this procedure to initiate model clouds in typical GATE temperature and moisture soundings, we find that the subsequent simulation is sensitive to H_o, but insensitive to W_o (see Table 5.1). In constructing Table 5.1 the no-mesoscale version (NOM) of the ensemble model was integrated for 1 hr with cloud distribution LN1 (see Chapter 6 for details), 3% cloud coverage, and cloud/pressure domain ratio 0.32. In the first three tests W_o is held constant, while H_o is varied (for all radii). We see a strong sensitivity to H_o, with cloud radius altering ultimate cloud height only for the deep perturbation. Peak maximum vertical velocity is dominated by the approach to hydrostatic conditions as radius increases. Aside from our hope that the character of the perturbation is unimportant, there is no physical basis for

Table 5.1 Model sensitivity as a function of radius to initiating perturbation parameters; (a) ultimate cloud height (km), together with the value of H_o for H_o = a+0.5 (km) (last line); (b) peak maximum vertical velocity (m/s).

(a)

W_o (m/s)	H_o (km)	Radius (km) 0.50	0.78	1.22	1.92	3.00
1.0	1.25	1.50	1.50	1.50	1.50	1.50
1.0	1.72	2.00	2.00	2.00	2.25	2.25
1.0	3.50	4.75	5.00	5.00	5.50	5.75
2.0	a+0.5	1.25	1.50	2.25	3.25	5.75
1.0	a+0.5	1.25	1.50	2.00	3.25	5.75
0.5	a+0.5	1.25	1.50	2.00	3.25	5.75
0.2	a+0.5	1.25	1.50	2.00	3.25	5.75
0.1	a+0.5	1.25	1.50	2.00	3.25	5.75
value of a+0.5		1.00	1.28	1.78	2.42	3.50

(b)

W_o (m/s)	H_o (km)	Radius (km) 0.50	0.78	1.22	1.92	3.00
1.0	1.25	1.8	1.5	1.3	1.2	1.2
1.0	1.72	2.7	2.4	2.0	1.6	1.4
1.0	3.50	6.4	6.0	5.5	4.8	4.0
2.0	a+0.5	2.0	2.1	2.4	3.0	4.5
1.0	a+0.5	1.2	1.5	2.1	2.6	4.6
0.5	a+0.5	1.1	1.5	1.9	2.5	4.6
0.2	a+0.5	1.1	1.4	1.8	2.4	4.7
0.1	a+0.5	1.1	1.4	1.8	2.4	4.7

expecting wide clouds to grow from perturbations of the same depth as narrow clouds. Rather, recalling the Scorer and Ludlam (1953) bubble model of convection, we expect an approximate geometric relation between perturbation depth and width. Accordingly, we set the depth of the saturated region equal to the cloud radius, so that the total perturbation depth is

$$H_o = a + 0.5 \text{ km} \qquad (5.1)$$

(displayed in Table 5.1b). This formulation allows us to continue measuring cloud size by the radius, even though these tests indicate that the perturbation depth is important for some soundings. Three-dimensional models also appear to require large initiating perturbations to simulate deep GATE convection (Simpson and Van Helvoirt, 1980; Simpson et al., 1982).

Keeping this distribution of H_o fixed, we consider a range of W_o. The clouds are relatively insensitive to variations in W_o, except when it is larger than the peak maximum vertical velocity which the particular cloud achieves for smaller values of W_o. Because the larger perturbation decreases the integration time for a lifecycle by cuttng down the startup period when the instability is growing in place, we choose $W_o = 1$ m/s.

We must also intervene at the end of a cloud's lifecycle to simulate the fact that a subsequent cloud of the same size grows in a new place. That is, at some point the current cloud must be considered sufficiently "dead" that we may parameterize its subsequent decay, and initiate a new cloud of the same size on the current environmental conditions. In this study we parameterize cloud decay by precipitating out the rainwa-

ter and diffusing all other properties into the environment.

The criteria for reinitializing a cloud are based on an inspection of Fig. 4.3 and similar diagrams, which show a typical lifecycle; the maximum vertical velicity peaks, then the rainfall rate peaks, then the cloud decays away. By comparing the instantaneous rainfall rate, R, and maximum upward vertical velocity, W_{max}, with the respective peak values achieved over the life of the current cloud, it is possible to objectively define the decay stage of the cloud. In this study we choose a 20% basic threshhold for each parameter:

$$R < 20\% \ (R)_{peak} \tag{5.2a}$$

and

$$W_{max} < 20\% \ (W_{max})_{peak} \ e^{\frac{t-t_{peak}}{1118 sec}} \tag{5.2b}$$

The slowly amplifying exponential for W_{max} yields a criterion of 100% $(W_{max})_{peak}$ at 1800 sec after the occurrance of $(W_{max})_{peak}$ at t_{peak}, eventually choking off those clouds which are so weak that gravity wave noise exceeds a fixed 20% threshhold. The particular one-cloud case displayed in Fig. 4.3 is representative; the cutoff comes at the heavy vertical dash-dot vertical line (time=35 min), which falls in the decay phase of the cloud. The further tests in Chapter 4 with Versions P.C and P.K demonstrated that only small quantitative differences arise from adopting the 20% cutoff and parameterizing the decay rather than allowing the model cloud to decay explicitly (cf. Figs. 4.5 and 4.6).

5.5 Summary

We applied the area-averaging approach of the AK model to derive a simple, yet time-dependent system of equations for describing many clouds in a common emvirnoment. We then extended this approach to include a mesoscale feature (or features) which encloses all clouds. Even this simple representation allows "mutual protection", the formation of a mesoscale anvil, and mesoscale transports.

Next, we considered the numerical representation of the cloud population, which we assumed to consist of 5 discrete classes distinguished by fixed radii between 0.5 and 3.0 km. The members within each class are represented by one model cloud. To complete the model, we considered the points at which we are required to intervene in the cloud lifecycle. The initiating perturbation is a combination of moisture and velocity. The value of the maximum velocity perturbation is not critical, up to the value chosen (1 m/s), but the depth of the perturbation (actually, the depth of the saturated layer) is important. We related the perturbation depth to cloud radius, using the physical argument that the larger clouds probably grow from larger "bubbles" of perturbation than small clouds do. At the opposite end of the lifecycle, each cloud is terminated by a "20% threshhold" criterion on vertical velocity and rainfall rate, which tests revealed to satisfactorily simulate a long decay period.

6. Model Results

6.1 Introduction

We now examine the behavior of the cumulus ensemble, as simulated by the model developed over the last two Chapters, for a particular day of GATE, 2 September 1974 (Julian Day 245). The next Section briefly outlines the synoptic situation of this day, which featured the development of a major convective complex in an easterly wave trough. Tests for various model configurations are presented in the succeeding Sections. These tests, summarized in Table 6.1, examine cases with no mesoscale region, various mesoscale region sizes, and various cloud distributions. Results are presented in several different forms, including mass fluxes, changes of temperature and moisture with time, and heat and moisture budgets. As shown in Appendix E, the budgets for this study are written as

$$A\,Q_\psi = P_{\psi e} + P_{\psi m} + \sum_i P_{\psi i} \qquad (6.1)$$

where $Q_\psi = \begin{cases} Q_1 - Q_R, & = \psi = \begin{cases} \text{sensible heat} \\ \text{latent heat} \end{cases} \\ -Q_2 \end{cases}$,

$$P_{\psi e} = A_e S_{\psi e} + A \frac{1}{\rho_0} \frac{\partial}{\partial z}\left[\rho_0 \overline{w}\,(\bar{\psi} - \psi_e)\right] - A_e \frac{\partial}{\partial z} F_{\psi z e}$$

$$P_{\psi m} = A_m \left\{ S_{\psi m} + \frac{1}{\rho_0} \frac{\partial}{\partial z}\left[\rho_0 w_m (\psi_e - \psi_m)\right] - \frac{\partial}{\partial z} F_{\psi z m} \right\}$$

$$P_{\psi i} = N_{mi} A_i \left\{ S_{\psi mi} + \frac{1}{\rho_0} \frac{\partial}{\partial z}\left[\rho_0 w_{mi} (\psi_e - \psi_i)\right] - \frac{\partial}{\partial z} F_{\psi z mi} \right\} .$$

In a few cases we also consider the individual terms in the P's in order to examine the contributions from various processes.

In all cases, the computations were performed as follows: A particular cloud population distribution (say, LN1) was chosen, together with the fractional cloud coverage over the mesoscale region (say, M20).

Table 6.1 Cumulus ensemble model configurations for Cases discussed in Chapter 6. See Fig. 6.6 for cloud distributions.

Case	Cloud Distribution	Fractional Cloudiness in Mesoscale (%)	Initialization Time
LN1.NOM	LN1	10 *	00Z Day 245
LN1.M20	LN1	20	00Z Day 245
LN1.M10	LN1	10	00Z Day 245
LN1.M30	LN1	30	00Z Day 245
LN2.M20	LN2	20	00Z Day 245
AIC.M20	AIC	20	00Z Day 245
LN3.M20	LNC	20	00Z Day 245
LN1.M20 from (-3 hr)	LN1	20	21Z Day 244

* No mesoscale region; cloud-to-pressure domain ratio given.

This fraction also served as the ratio of cloud-to-pressure domain area. An initial guess for the total number of clouds was parceled out over the population distribution. All regions were initialized from a specific observation time (say, 00Z Day 245), and the model was integrated forward for 3 hr, with the appropriate radiative fluxes and boundary fluxes of heat and moisture prescribed from data. The model heat and moisture budgets differed from the observed budgets, in general, so the numbers of clouds were revised. Various problems, particularly the lack of very deep clouds, seemed to preclude a classical subensemble-by-subensemble revision, so a simpler alternative was adopted. We demanded that the observed domain-averaged budget of moisture in the nominal PBL (the lowest 500 m) be satisfied, since that is the region into which the surface flux of moisture is placed and from which the clouds draw their vapor. This is an integral constraint, so we retained the cloud distribution and the fractional cloud coverage over the mesoscale region as before, while revising the total number of clouds. That is, the populations of the subensembles changed, but not the distributions; the mesoscale area changed, but it was still a constant multiple of the total cloud area. Given these new parameters, the model was once again initialized at the starting time and integrated for 3 hr. The result was considered "final" when the model budget differed from the observed budget (over the domain-averaged PBL) by less than 5% (over the 3 hr simulation). Succeeding time periods were treated identically, except that the initial state of the current period was given by the concluding state of the previous period, including all variables in each region (cloud water content, temperature, etc.). When the results from several periods are considered together, we have a

long time integration in which the number of clouds jumps discontinuously every 3 hr.

6.2 Observations of Day 245

In this Section, we describe the observed synoptic situation over the GATE Array on Day 245 (2 September 1974), together with basic derived quantities. The major event during this day was the passage of an easterly wave. On 12Z Day 245 the surface and 700 mb maps (Figs. 6.1a-b) show the wave trough (Category 4 of the Reed et al., 1977, composite) just entering the GATE Array. The 700 mb map shows the trough on which the Categories are keyed. The surface flow is dominated by confluence, with significant cross-equatorial flow from the south. The wave's progression is clearly visible in the infrared satellite pictures for 00Z Day 245 and 00Z Day 246 (Figs. 6.2a-b). The large, cold cloud mass associated with deep convection in the wave trough moves from the African coast (to the east of the GATE Array) to 24°W (just west of the Array) over the day.

Radar summaries (Arkell and Hudlow, 1977) display an increasing number of thin lines advancing from the northeast during the day, until a broad band forms around 18Z and moves east, leaving the Array nearly as empty of echoes at 00Z Day 246 as it was at 00Z Day 245. The radar-derived precipitation time series (Fig. 6.3) shows an increase to 17Z, then a precipitous decrease. Also displayed in Fig. 6.3 is Frank's (1979) diagnosis of net condensation based on his own analysis of the heat budget over the A/B Array. Note the characteristic early peak in budget-derived condensation (8 hr before the radar-derived peak on this day). This phase shift is attributed to storage (Section 5.3).

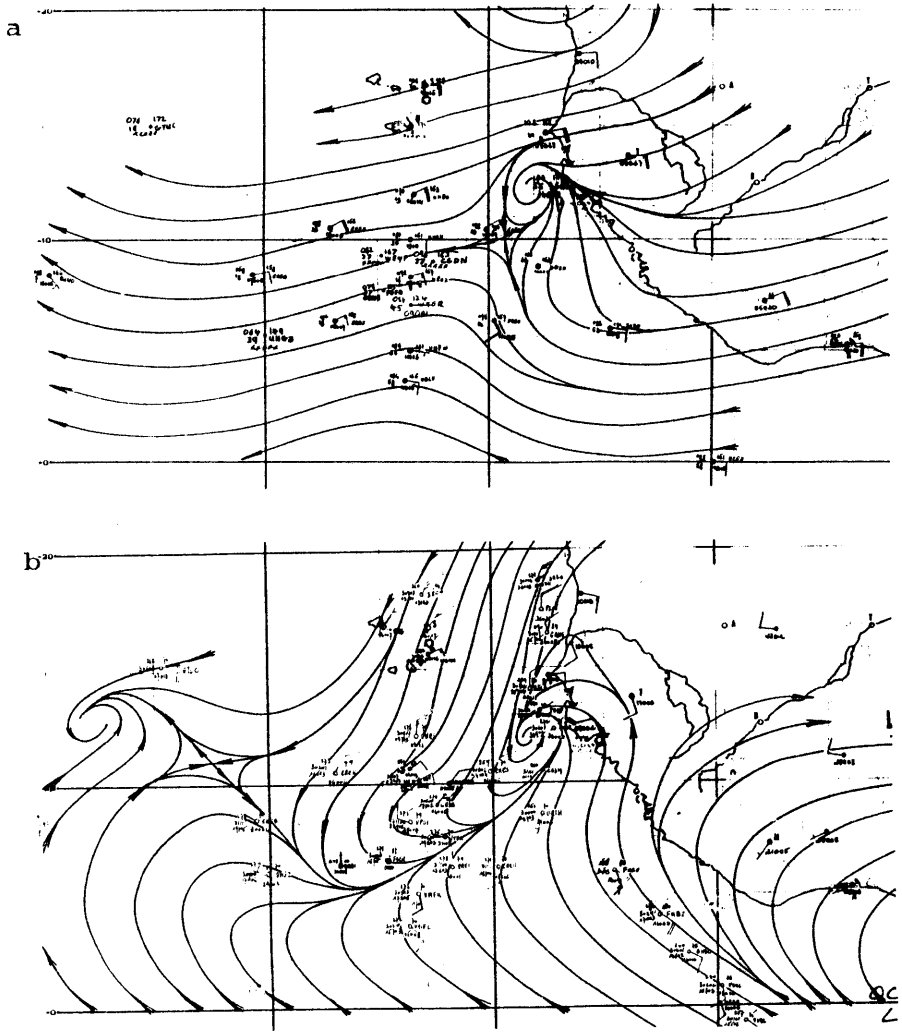


Fig. 6.1 (a) 700 mb and (b) surface maps, including streamlines at 12Z Day 245 over the GATE region.

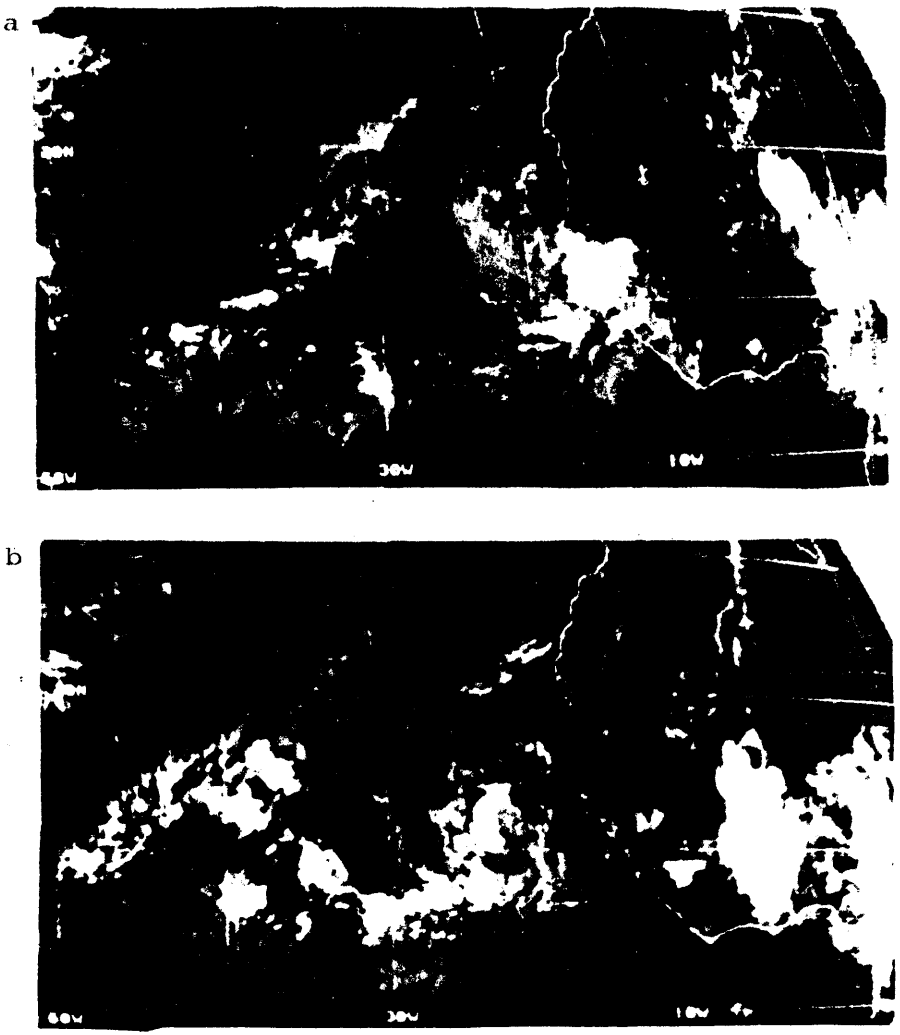


Fig. 6.2 Infrared satellite picture (4x4 km) at (a) 00Z Day 245 and (b) 00Z Day 246 over the GATE region.

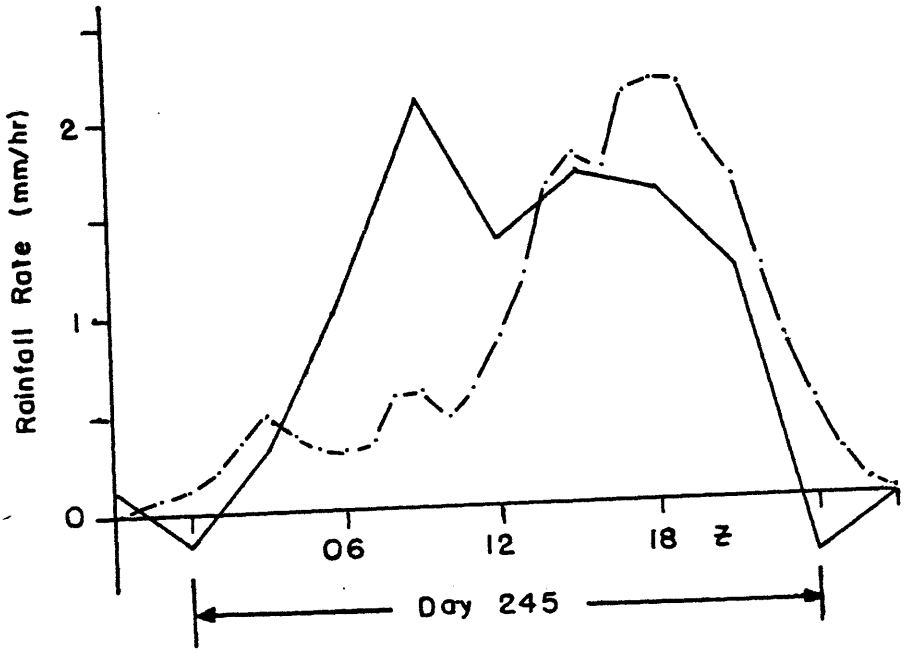


Fig. 6.3 Estimates of precipitation on Day 245; (- · -) radar-derived over the "Master Array", a circle circumscribing the B Array (Hudlow and Patterson, 1978); (——) heat budget-derived over the A/B Array (after Frank, 1979).

Two convective lines in the vicinity of the ship Quadra were investigated by aircraft flights over the period 12-14Z. Warner (1979) reported that the lines exhibited a series of convective towers of variable height, generally peaking above 7 km, as well as a stratus deck at 5 km and some anvil at 11 km. His inventory of visible cloud tops includes a few which rose above the 13 km level. Dr. Frank Marks (personal communication) confirmed that similar events were seen on radar from the ship Gillis during Day 245. Beyond the qualitative observation that over half of the tops noted by Warner (1979) fall below 8 km, no systematic echo top census is available.

A more general measure of the convective activity is given by the heat and moisture budgets. The diagnosed 3 hr average mass fluxes are shown in Fig. 6.4a. Note the increase in amplitude with time. The temperature and moisture changes driven by this lifting, as well as horizontal advection and surface fluxes, are shown at the end of each 3 hr period in Fig. 6.4b. There is general cooling and moistening with time, with extreme moistening in the nominal PBL. Of course, the environment doesn't change this radically - the changes are small (Fig. 6.4c). The cooling and moistening is opposed by the cumulus ensemble, resulting in the apparent source of heat and sink of moisture (which are displayed as solid lines in Fig. 6.8).

6.3 A case without mesoscale structure

The first model configuration we consider is Case LN1.NOM, in which all mesoscale structure is suppressed. Besides providing the basis for mesoscale - no mesoscale comparison, Case LN1.NOM provides the conceptually simplest introduction into the model behavior. The simulation is

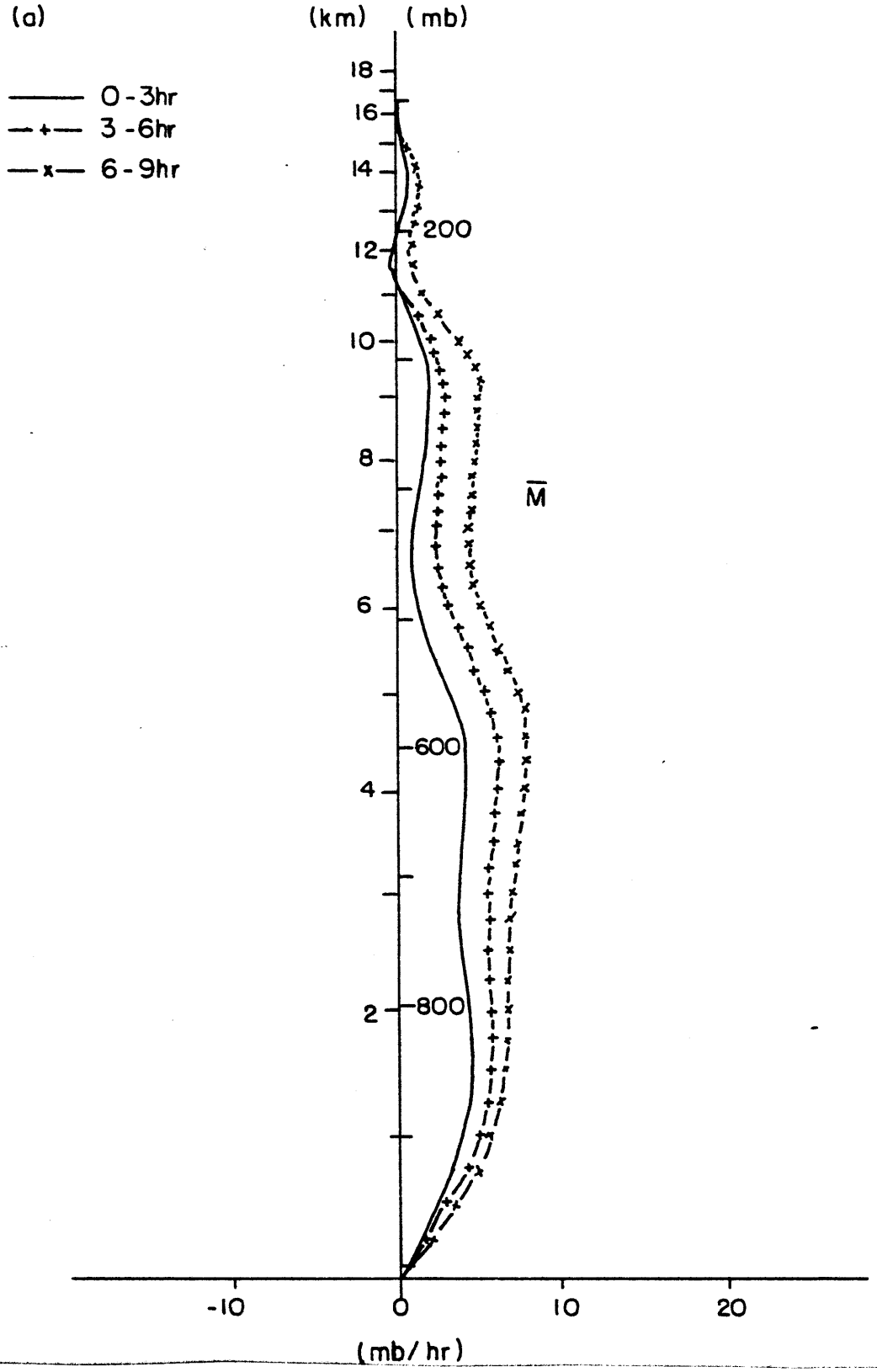


Fig. 6.4 (a) Large scale vertical mass flux averaged over 3 hr intervals, (b) temperature and water vapor changes from initial state at 3 hr intervals due to all prescribed forcings, and (c) observed temperature and moisture changes from initial state at

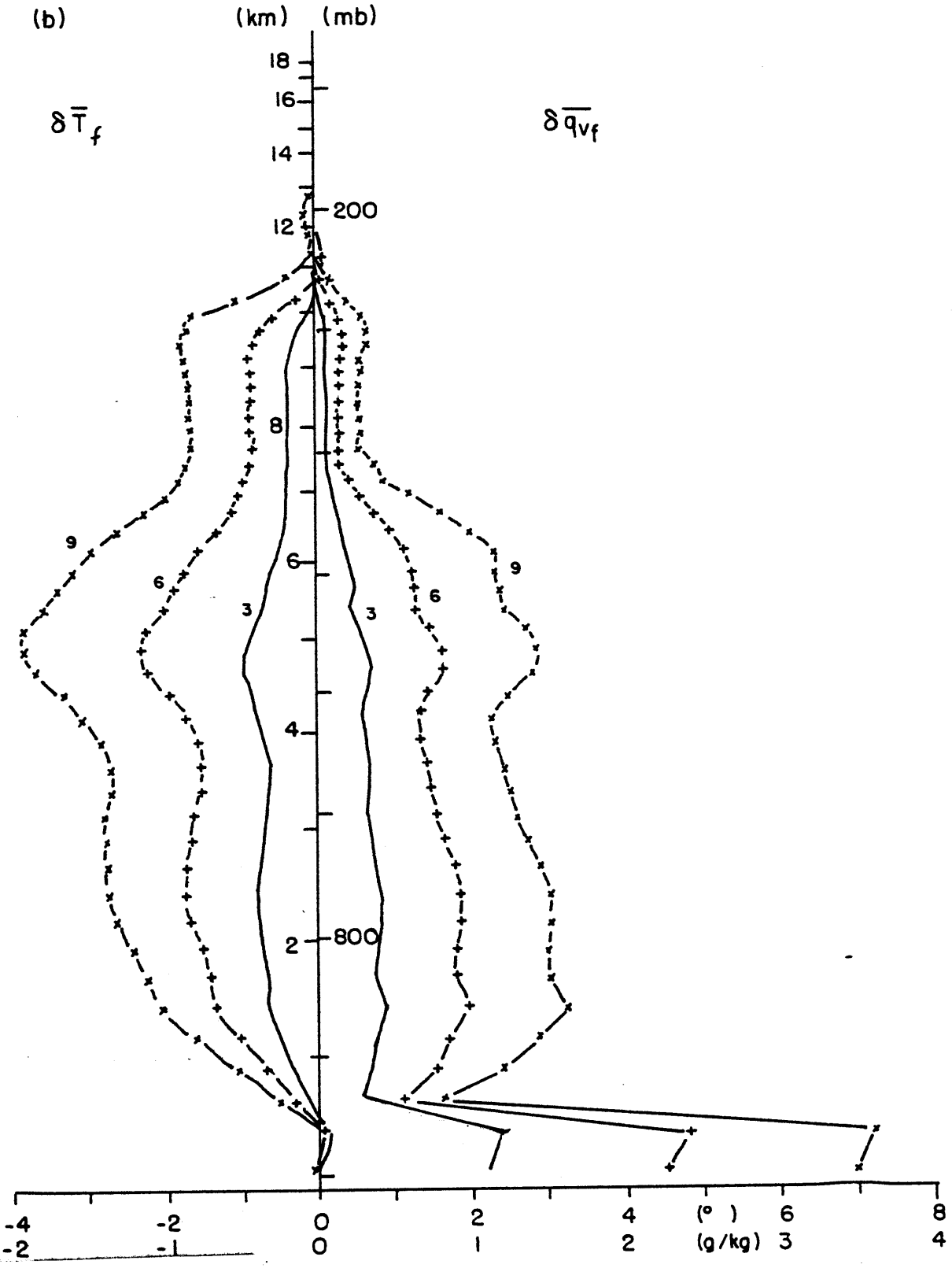


Fig. 6.4 continued.
the end of each period. All data from Thompson et al. (1979).

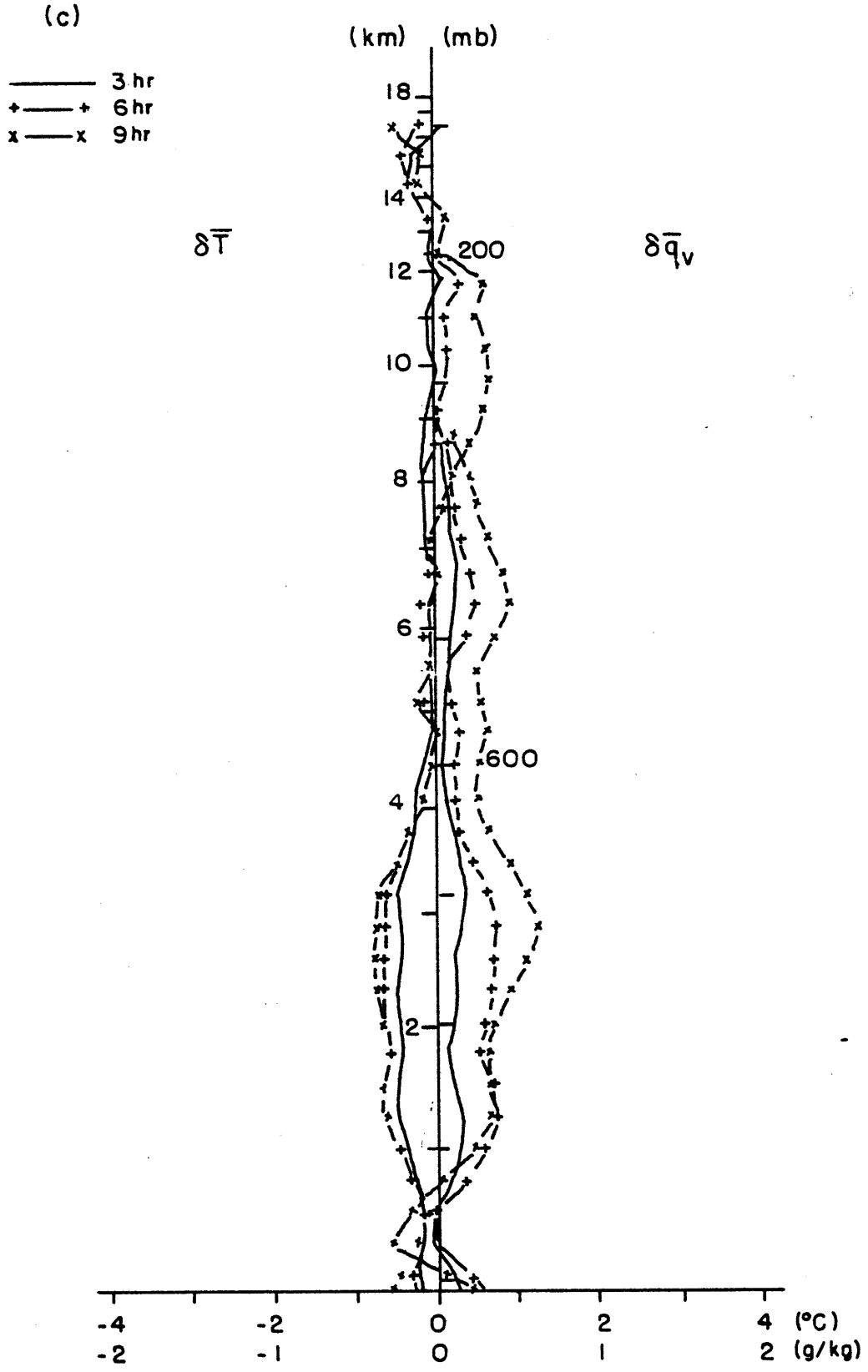


Fig. 6.4 continued.

initialized from the large scale average temperature and moisture soundings for 00Z Day 245, displayed in Fig. 6.5.

The cloud distribution in Case LN1.NOM is chosen to approximately correspond to the LeMone and Zipser (1980) updraft core statistics. In particular, we assume a lognormal distribution, specifying that 50% of the clouds have radius 0.50 km, and specifying that 99.9% (essentially all) of the clouds have radius 3.00 km or less. We choose a geometric progression in the radii of the five subensembles between 0.50 and 3.00 km in order to spread the number of clouds among the subensembles more evenly, resulting in the LN1 distribution listed in Table 6.1 and graphed in Fig. 6.6. There is no mesoscale region to which pressure domain size can be related, so the ratio of cloud to pressure domain area is set at 0.10, a value which maximizes heat transport in the one-cloud model (Asai and Kasahara, 1967). The alternative of filling the whole environment with pressure domains yields ridiculously small cloud-to-pressure domain ratios when the model is just starting up.

The detailed time-dependent behavior of individual cloud lifecycles is much like that displayed in Fig. 4.4, except that a new cloud is started immediately at the cutoff point (the heavy vertical lines at 35 min in Fig. 4.4), and the maxima in height, vertical velocity, etc. vary with cloud size. A summary of the time-dependent behavior is shown in Fig. 6.7, which displays rainfall rate and maximum vertical velocity for each subensemble. The first few cloud lifecycles are weak for all subensembles, as one might expect from the tests carried out in Chapter 5 (see Table 5.1). Then, as the imposed large scale lifting destabilizes the environment, the large clouds become more vigorous. Notice that the successive cloud lifecycles for a particular subensemble

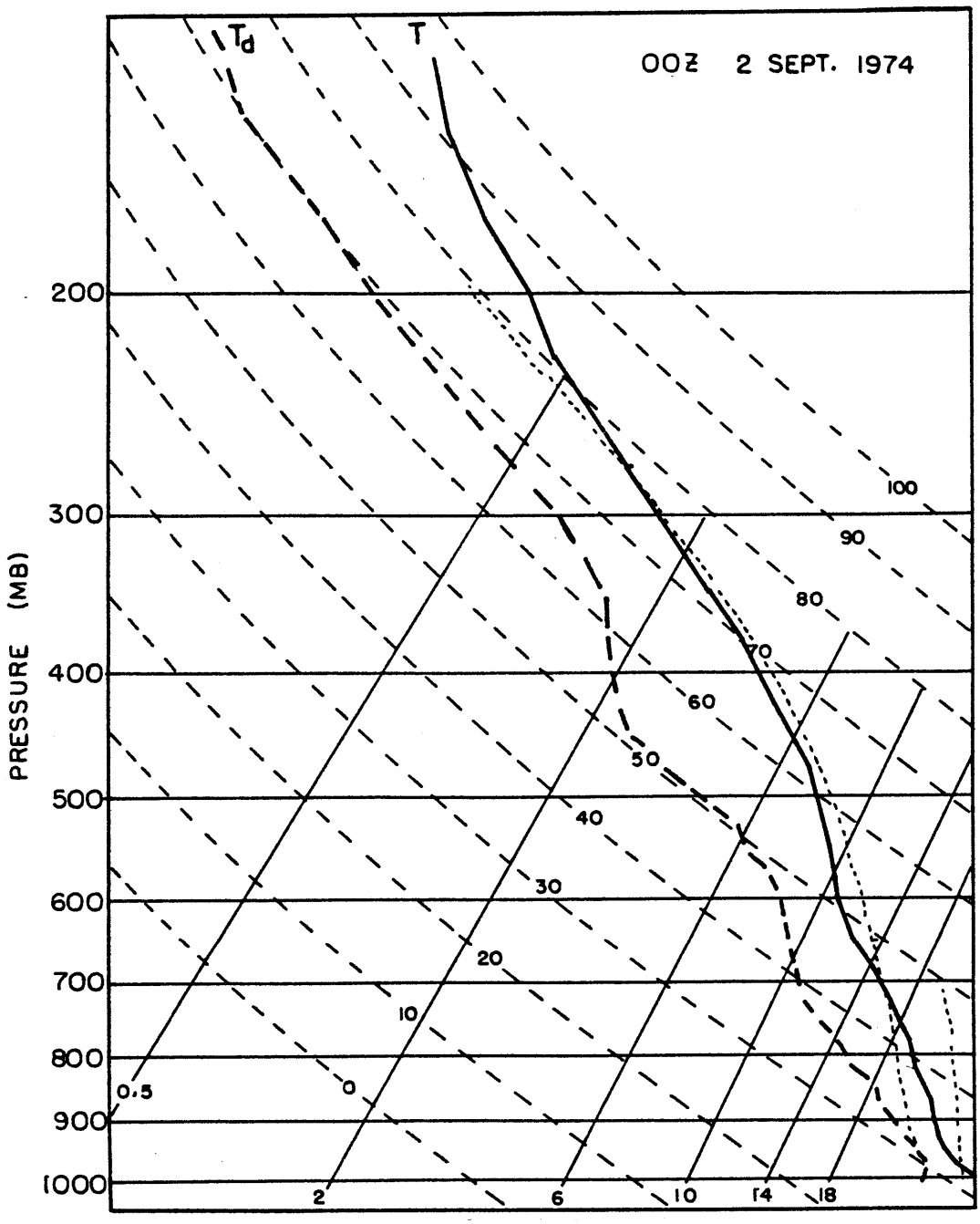


Fig. 6.5 Temperature (T) and dewpoint (T_d) soundings averaged over the GATE B Array at 00Z Day 245.

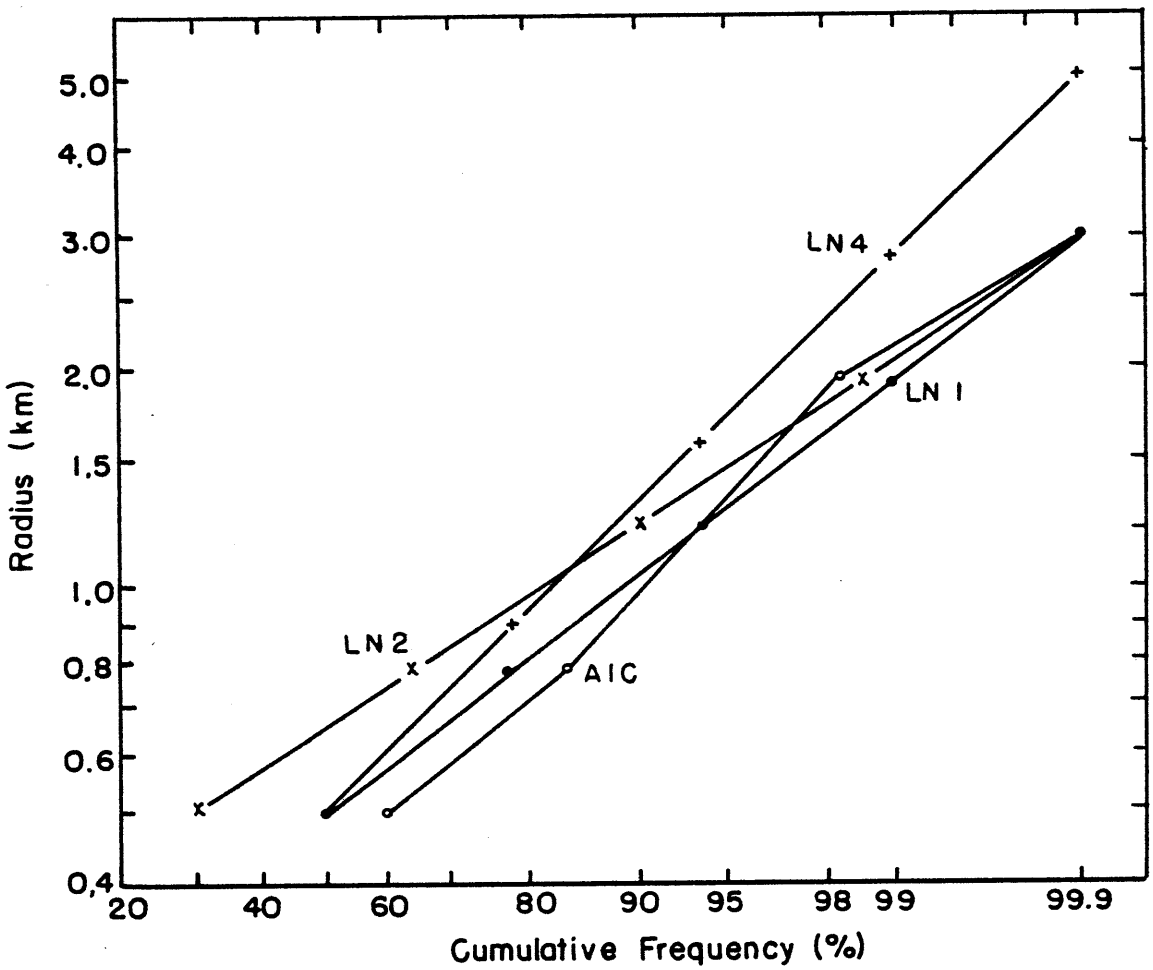


Fig. 6.5 Cumulative frequency distribution for Cases in Chapter 6; (-•-) LN1, (-X-) LN2, (-+-) LN3, (-o-) AIC.

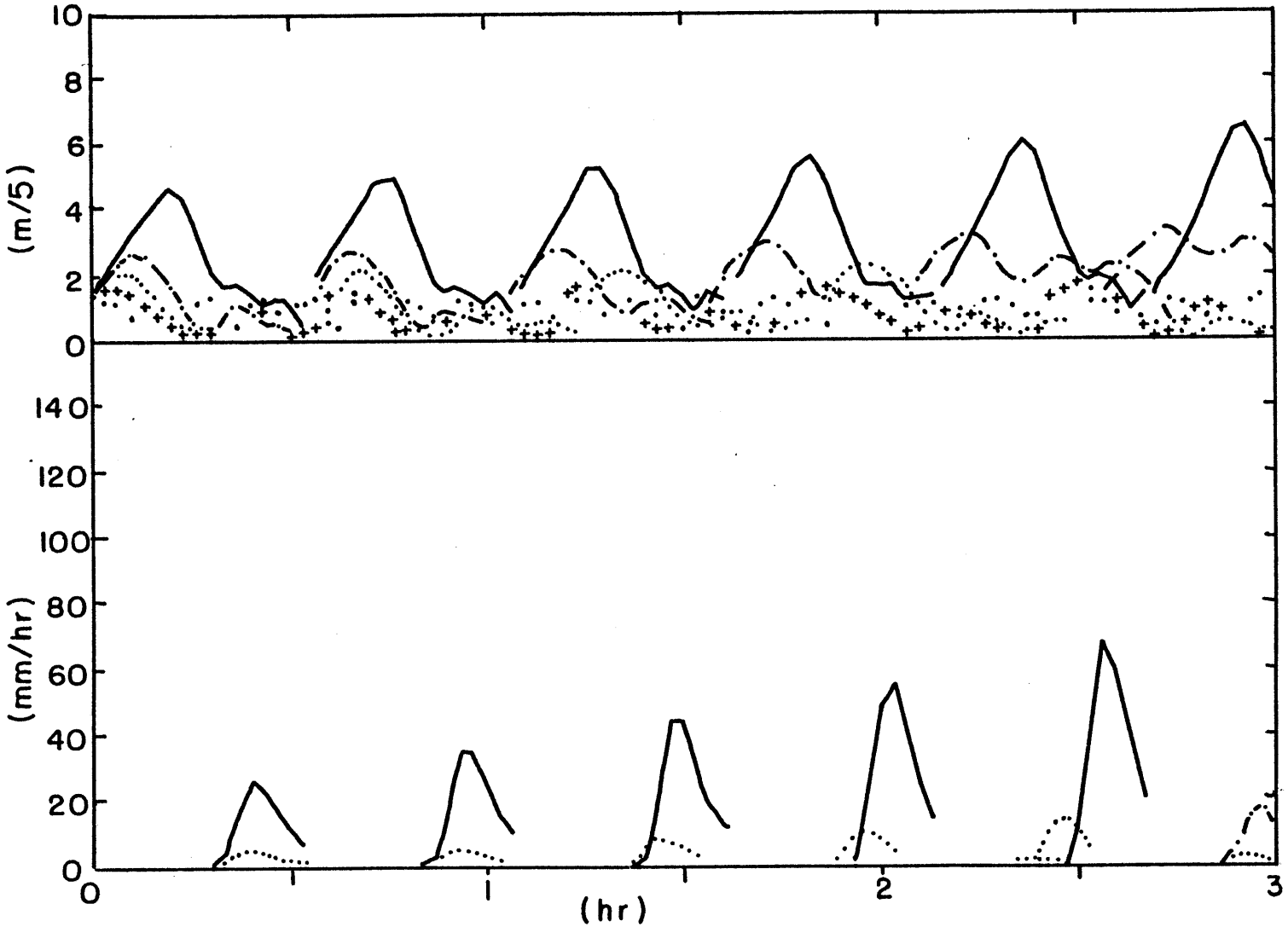


Fig. 6.7 Maximum upward vertical velocity in the cloud column, and surface rainfall rate at 2 min intervals over (a) 0-3 hr, (b) 3-6 hr, (c) 6-9 hr; Case LN1.NOM. (•) 0.50 km, (+) 0.78 km, (···) 1.23 km, (-·-) 1.92 km, (——)

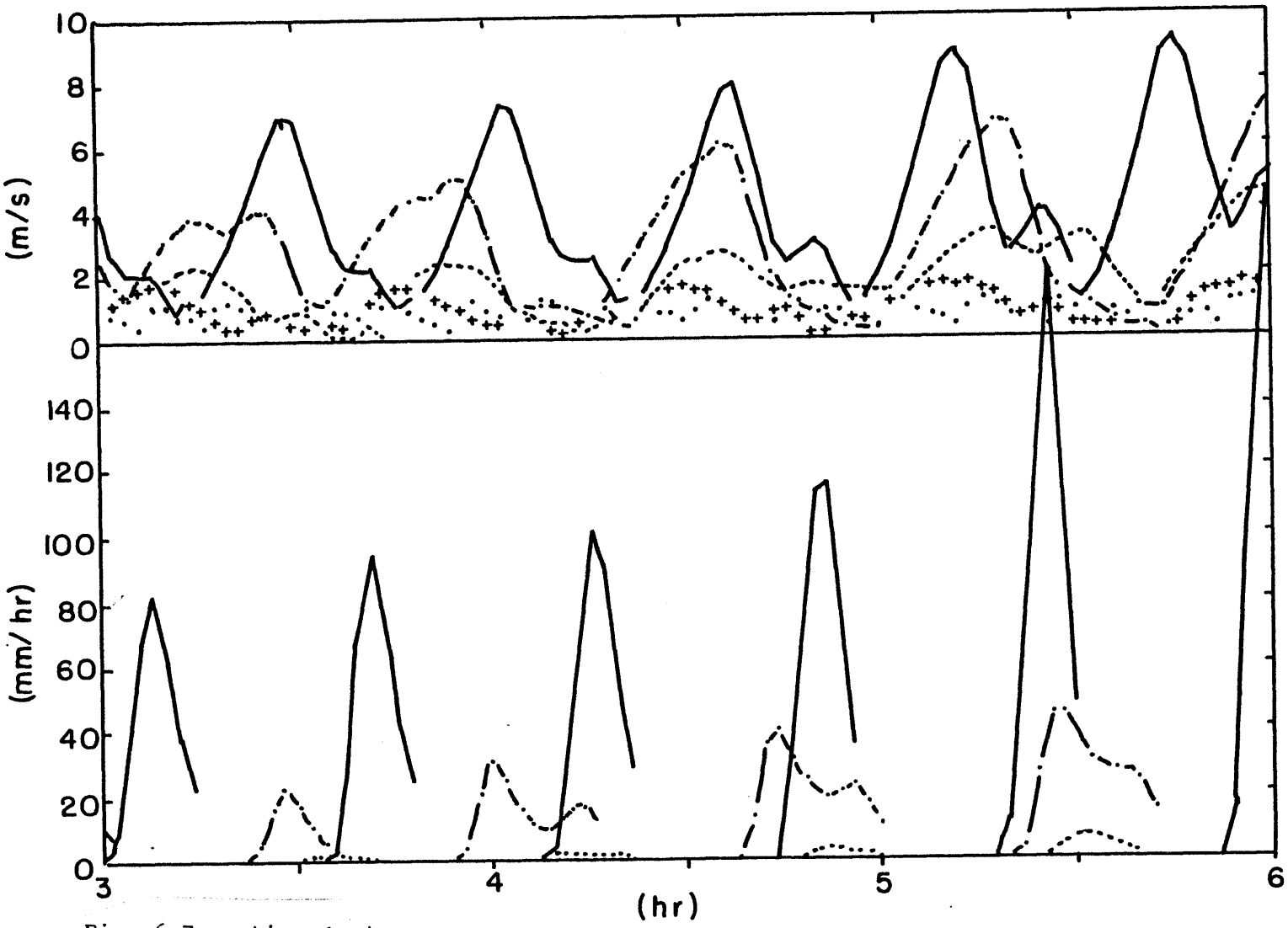


Fig. 6.7 continued.
3.00 km radius clouds.

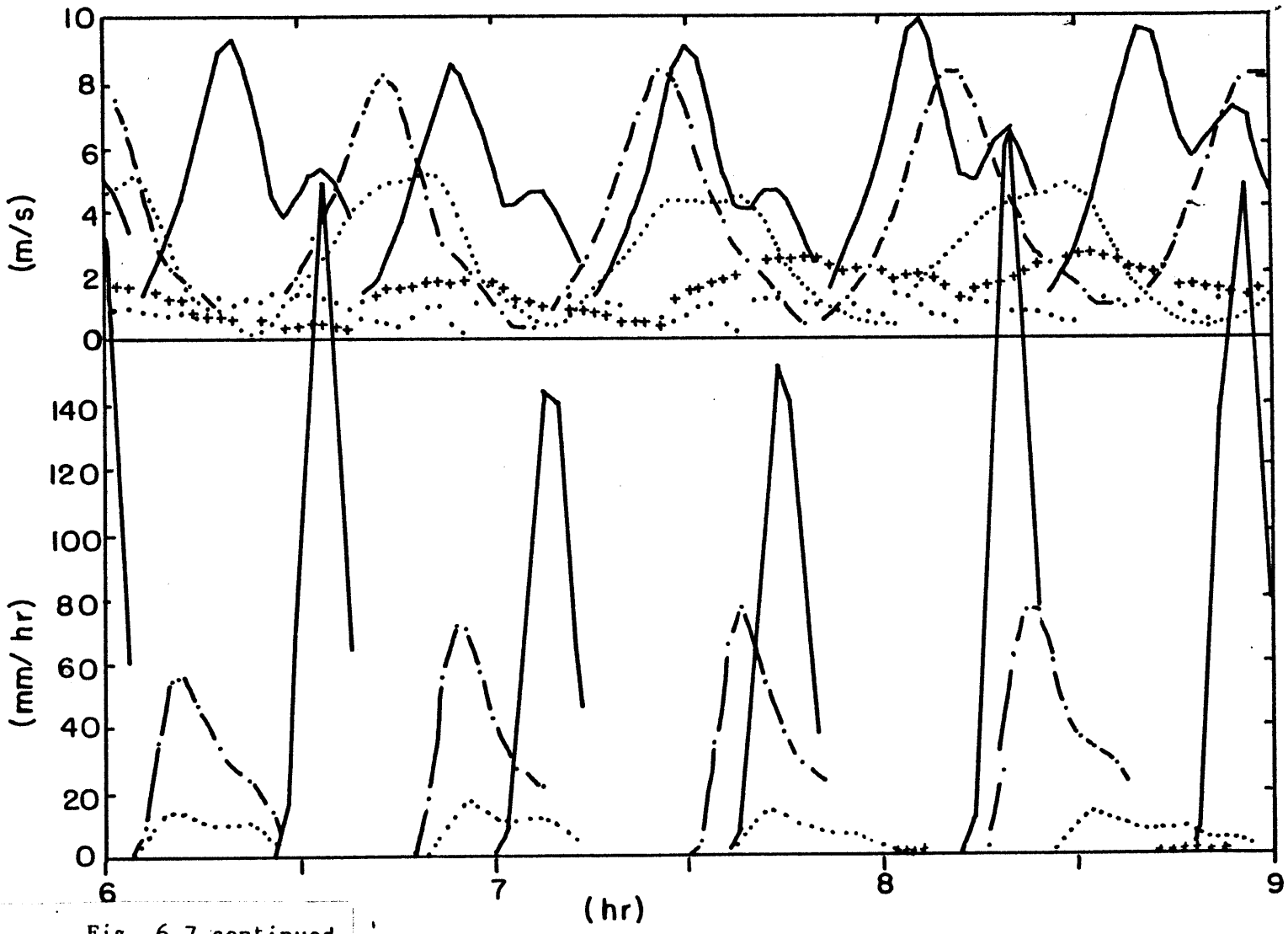


Fig. 6.7 continued.

are quite similar during the 6-9 hr period. Although the total lifespans of the bigger clouds are longer, the growing and mature phases, as defined by the 20% threshhold criterion for reinitializing clouds, tend to be similar in length. Nevertheless, there are no conspicuous phase relationships among the various subensembles over time. This assures us that assuming all members of a subensemble to be at the same point in their lifecycles is not causing systematic cloud-cloud interference.

The heating and drying due to the cumulus ensemble is shown in Fig. 6.8 over each 3 hr period. The solid lines are the budgets calculated from observations, while the dashed lines are the simulated budgets (Q_1-Q_R, $-Q_2$ and $Q_{1c}-Q_R$, $-Q_{2c}$, respectively). Recall that these budgets are simply scaled changes between lines on Fig. 6.4b, minus surface fluxes and the observed time changes (Fig. 6.4c). As the large scale lifting increases, the heating and drying that the ensemble must accomplish also increase. In the first 3 hr (Fig. 6.8a) the weak, shallow convection in the ensemble is ineffective in reproducing the budgets. In fact, there is general moistening in the 2-6 km layer, rather than drying. The 3-6 hr period (Fig. 6.8b) shows a much more organized response to the forcing. Q_{1c} is rather similar to Q_1 up to 4 km, while both Q_{1c} and Q_{2c} show qualitative agreement with observation up to 6 km. Once again, the amount of drying is less than diagnosed. The 6-9 hr period (Fig. 6.8c) shows quantitative agreement below 6.5 km, except near cloud base in moisture.

How does this successively better agreement come about? During the 0-3 hr period none of the subensembles produced clouds which were sufficiently deep to cause warming and drying at, say, 6 km. Thus, no combination of clouds would accurately simulate the budgets. However, by

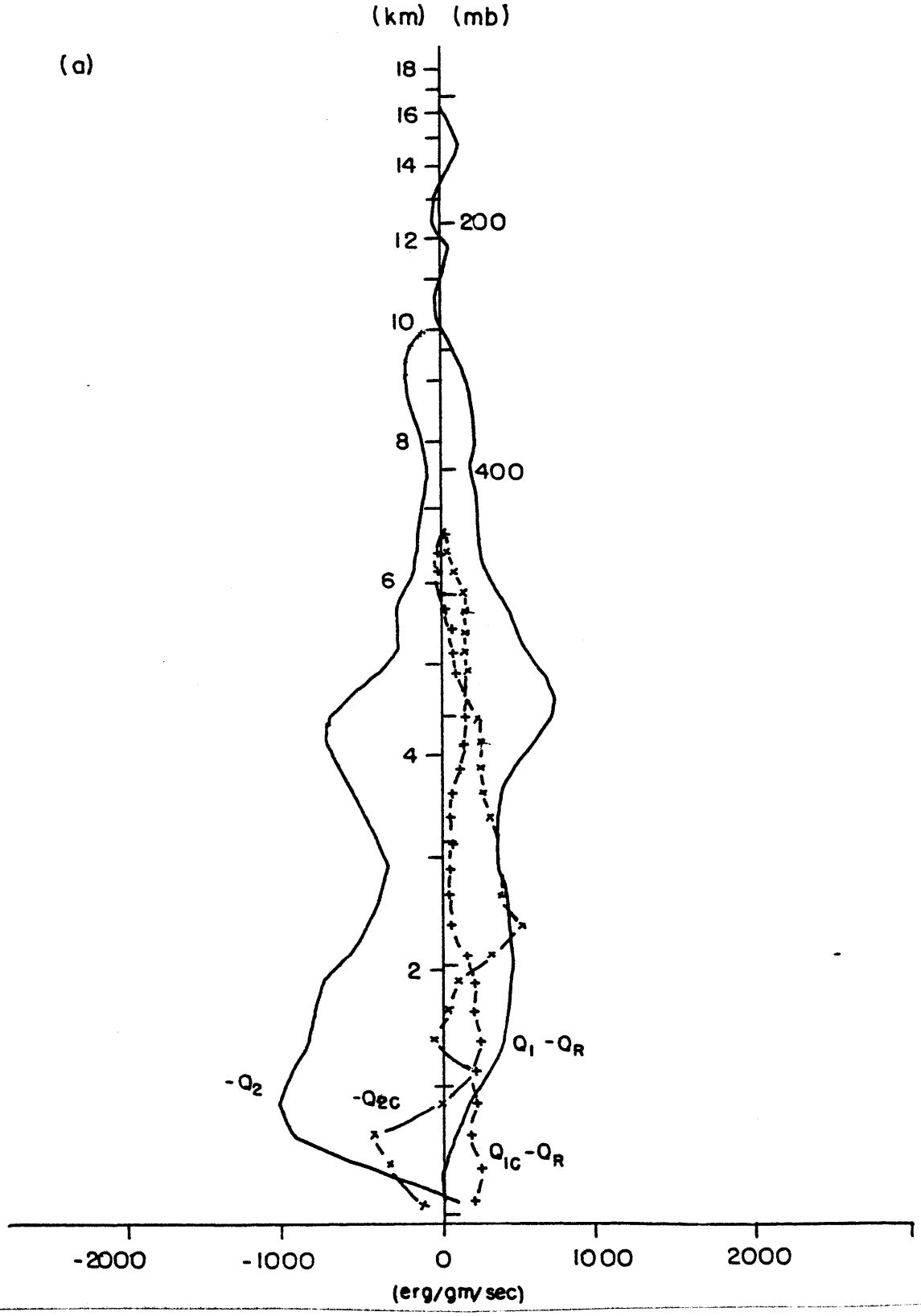


Fig. 6.8 Heat and moisture budgets over (a) 0-3 hr, (b) 3-6 hr, (c) 6-9 hr; Case LN1.NOM. Observed and simulated budgets are

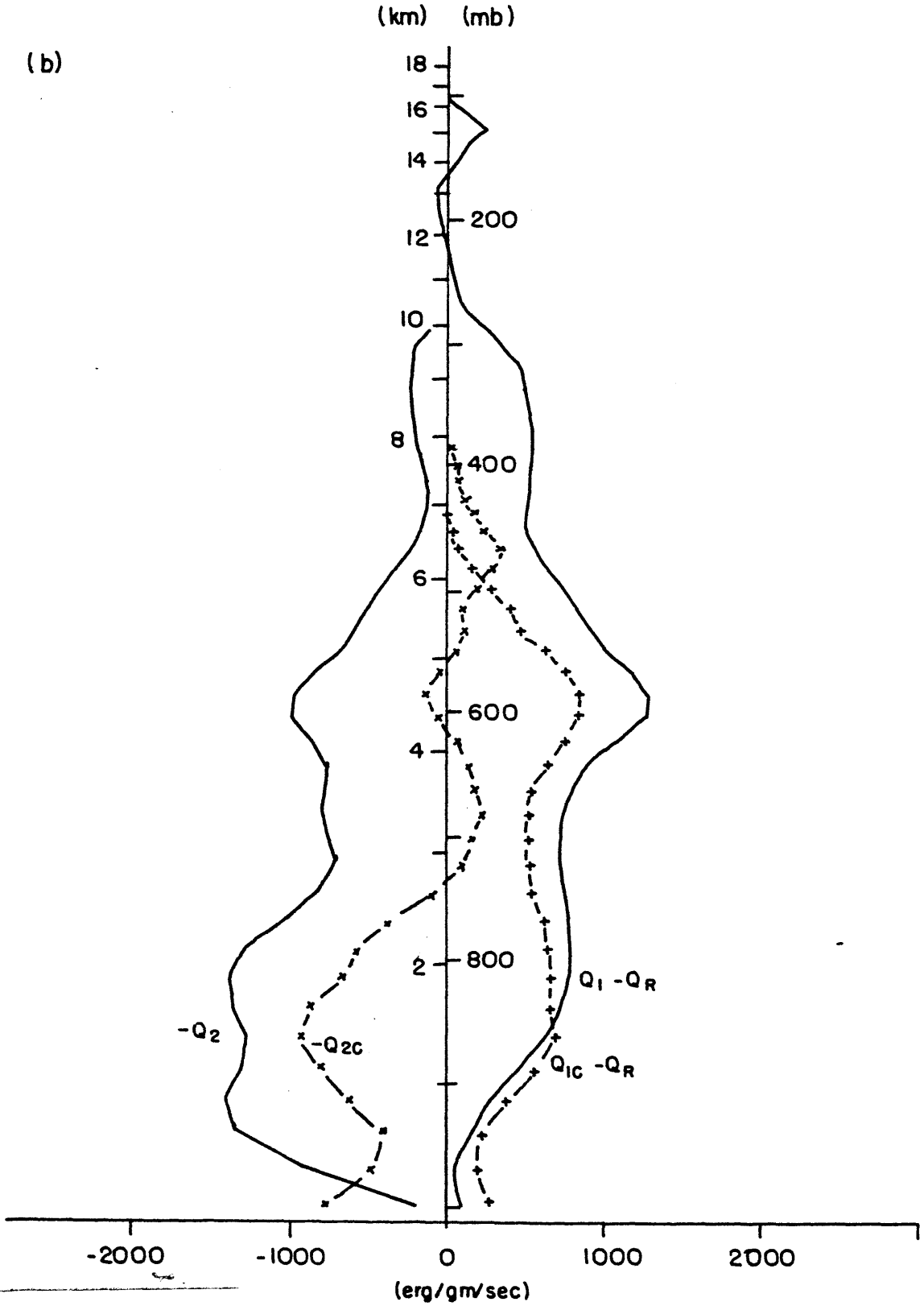


Fig. 6.8 continued.
solid and dashed lines, respectively.

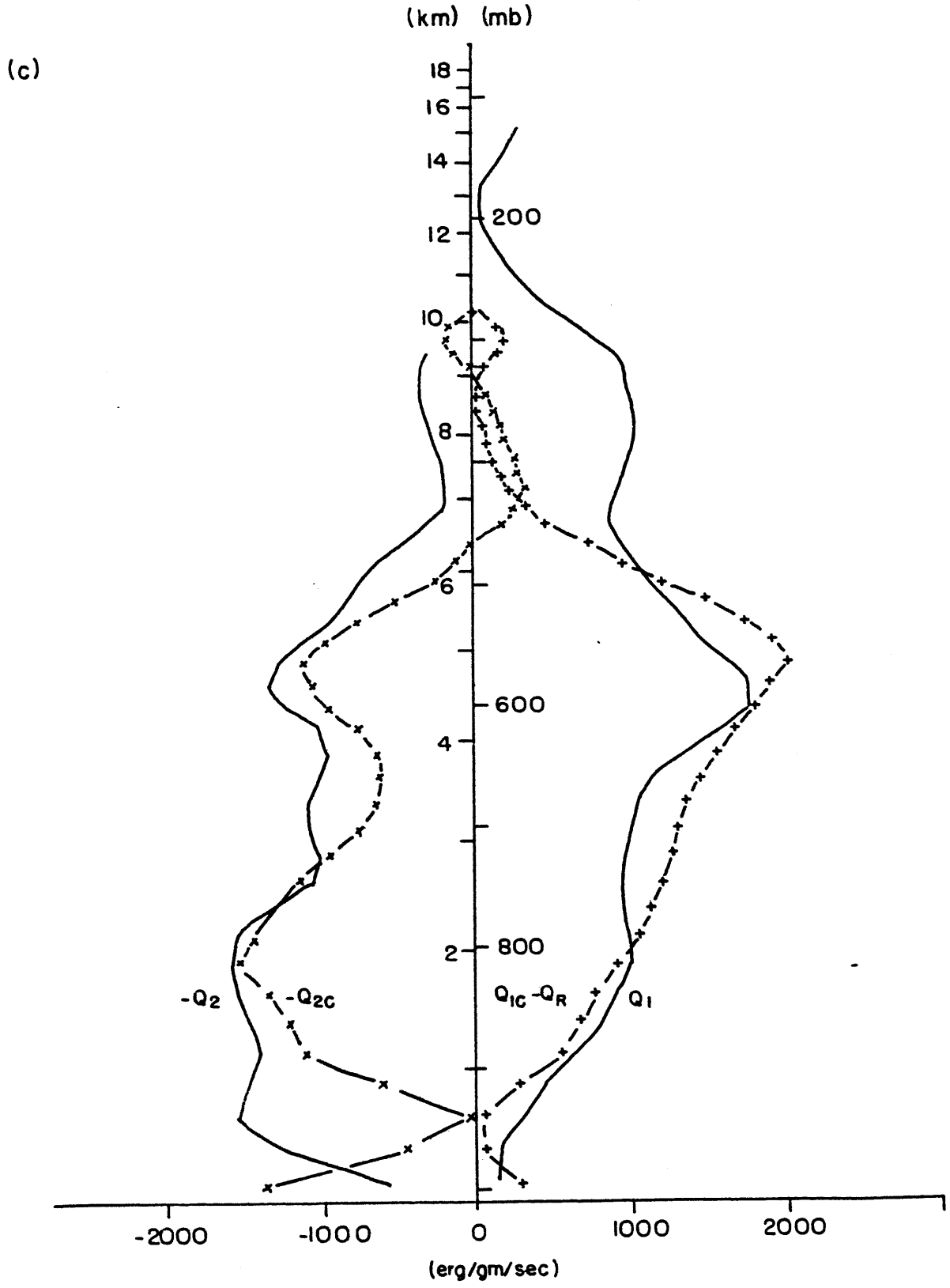


Fig. 6.8 continued.

not satisfying the budgets, the ensemble allows the environment to become more unstable; subsequent clouds are deeper. This process is quite evident if we plot the domain-averaged time changes of temperature and moisture (Fig. 6.9), and compare them to the cumulative temperature and moisture changes due to forcing (Fig. 6.4b). After 3 hr the changes in the model atmosphere above the nominal PBL are nearly those induced by forcing. The clouds which grow on this new, more unstable sounding are deeper and more vigorous (cf. Fig. 6.7b). After 6 hr the model profiles below 2 km are closer to the 3 hr profiles than to the values predicted from forcing alone. Above that level, there has been additional destabilization. Recalling the agreement in the budgets over the 6-9 hr period, it seems that these new profiles represent a sufficiently unstable sounding that clouds can grow over a fairly deep layer as the forcing demands. As a result of satisfying the budgets in the 6-9 hr period below 6 km, the 9 hr profiles (Fig. 6.8) are quite similar to the 6 hr profiles in the same region. This steadiness explains the similarity of successive cloud lifecycles which we saw in the 6-9 hr time behavior (Fig. 6.7c). Above the 6 km level the budgets are not satisfied, and so the profiles change with time. This last feature is discussed more fully below.

The successive intensification of the simulated cumulus ensemble is also visible in the rainfall produced in the 3 hr periods (Table 6.2). Over 0-3 hr the rainfall is deficient, compared to observations, while 6-9 hr produces 2.5 times the observed rain. This excess, of course, is consistent with approximately reproducing the budgets, since these yield rainfall estimates which peak at 9 hr (cf. Fig. 6.3). When we inspect the individual subensemble rainfall accumulations, we find that the

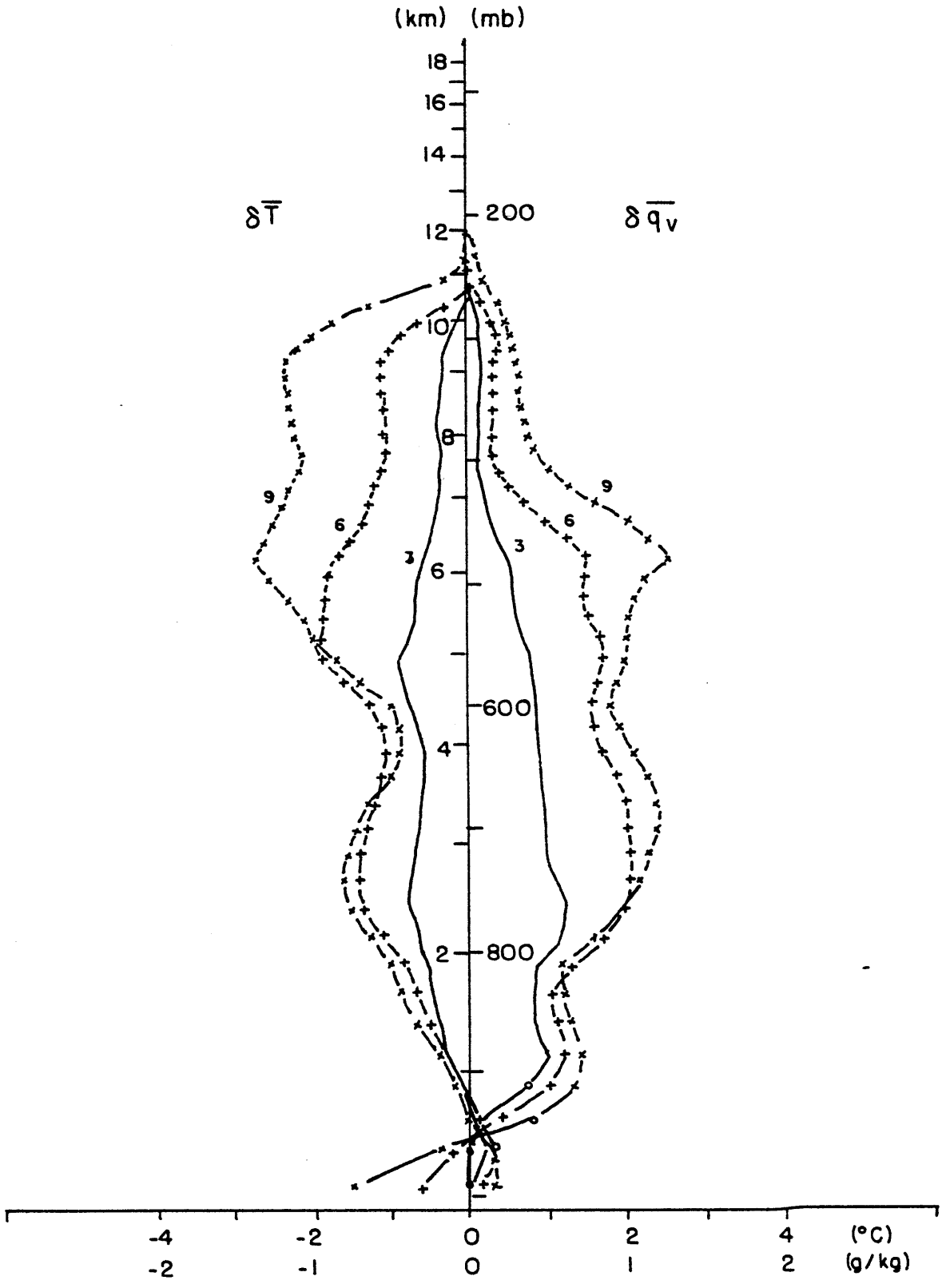


Fig. 6.9 Domain-averaged temperature and moisture changes from initial state at 3 hr intervals; Case LN1.NOM.

Table 6.2 Cloud populations (per 1° x1° lat.) and rainfall (3 hr accumulation) for the Cases in Chapter 6 (a) over 0-3, 3-6, and 6-9 hr, and (b) over (-3)-0 hr. Radar-derived rainfall is Hudlow and Patterson's (1979) estimate for the B Array.

(a)

Case, Radius (km)	0-3 hr Cloud Pop.	0-3 hr Rainfall (mm*10)	3-6 hr Cloud Pop.	3-6 hr Rainfall (mm*10)	6-9 hr Cloud Pop.	6-9 hr Rainfall (mm*10)
LN1.NOM 0.50	88.8	0.0	130.	0.0	169.	0.0
0.78	49.5	0.0	72.7	0.01	94.4	0.16
1.23	28.2	0.03	41.4	0.29	53.8	1.28
1.92	9.23	0.25	13.5	1.39	17.6	3.36
3.00	1.60	0.71 0.44	2.34	3.42 1.73	3.05	8.50 3.68
LN1.M20 0.50	96.8	0.0	175.	0.0	154.	0.0
0.78	54.0	0.0	97.7	0.0	86.0	0.15
1.23	30.8	0.02	55.7	0.36	49.0	1.20
1.92	10.1	0.24	18.2	1.56	16.0	2.96
3.00	1.74	0.82 0.56	3.15	4.07 2.15	2.77	7.41 3.09
LN1.M10 0.50	88.8	0.0	147.	0.0	161.	0.0
0.78	49.5	0.0	81.9	0.00	90.1	0.37
1.23	28.2	0.02	46.7	0.44	51.3	1.07
1.92	9.23	0.21	15.3	1.47	16.8	3.20
3.00	1.60	0.67 0.45	2.64	3.73 1.80	2.91	7.92 3.25
LN1.M30 0.50	110.	0.0	177.	0.0	177.	0.0
0.78	61.5	0.0	98.6	0.02	98.6	0.02
1.23	35.1	0.00	56.2	0.39	56.2	1.69
1.92	11.5	0.25	18.4	1.62	18.4	2.83
3.00	1.98	0.91 0.66	3.18	4.28 2.25	3.18	7.85 3.29
Radar	-	2.22 -	-	3.29 -	-	3.51 -

Table 6.2a continued.

Case, Radius (km)	0-3 hr Cloud Pop.	0-3 hr Rainfall (mm*10)	3-6 hr Cloud Pop.	3-6 hr Rainfall (mm*10)	6-9 hr Cloud Pop.	6-9 hr Rainfall (mm*10)
LN2.M20 0.50	42.3	0.0	57.6	0.0	73.1	0.0
0.78	48.8	0.0	66.4	0.03	84.3	0.08
1.23	35.5	0.01	48.3	0.53	61.4	0.86
1.92	12.3	0.28	16.8	1.43	21.3	3.94
3.00	1.90	0.90 0.60	2.59	3.90 1.90	3.29	8.07 3.17
AIC.M20 0.50	118.	0.0	199.	0.0	215.	0.0
0.78	48.4	0.0	81.1	0.0	87.6	0.0
1.23	19.8	0.00	33.1	0.18	35.8	0.52
1.92	8.06	0.16	13.5	1.07	14.6	1.94
3.00	3.29	1.05 0.89	5.51	4.72 3.46	5.95	7.73 5.26
LN3.M20 0.50	43.0	0.0	65.3	0.0	91.7	0.0
0.89	24.0	0.0	36.5	0.0	51.2	0.00
1.58	13.7	0.04	20.8	0.41	29.2	0.71
2.81	4.48	0.65	6.80	2.50	9.54	3.66
5.00	.775	1.67 0.98	1.18	5.34 2.42	1.65	8.36 3.98
LN1.M20 0.50	119.	0.0	119.	0.0	140.	0.02
from 0.78	66.4	0.0	66.4	0.01	78.4	0.45
-3 hr 1.23	37.8	0.02	37.8	0.72	44.7	1.18
1.92	12.4	0.68	12.4	1.51	14.6	3.08
3.00	2.14	1.51 0.81	2.14	4.38 2.13	2.53	8.12 3.38
Radar	-	2.22 -	-	3.29 -	-	3.51 -

(b)

Case, Radius (km)	-3-0 hr Cloud Pop.	-3-0 hr Rainfall (mm*10)
LN1.M20 0.50	73.7	0.0
from 0.78	41.1	0.0
-3 hr 1.23	23.4	0.00
1.92	7.66	0.09
3.00	1.33	0.34 0.25
Radar	-	0.47 -

largest clouds produce the bulk of the rainfall, even though these clouds make up a small fraction of the total cloud population. Lopez (1978) reports similar results (see Section 2.3).

Table 6.2 also displays the "final" populations of model clouds (based on satisfying the subcloud layer moisture budget). Summing the areas of these clouds, the total cloud coverage in the three periods for Case LN1.NOM is 3%, 4.4%, and 5.7%. As mentioned in Section 6.2, no census of clouds exists for Day 245 to provide a comparison. However, we do have Zipser and LeMone's (1980) tabulation of fractional flight path covered by "drafts" and "cores" for 6 days in GATE. Without carrying out a detailed computation (as we will do in the next Section for velocity distribution), we will assert that the total coverage in our model is in the same range as Zipser and LeMone's numbers. An analysis of satellite data by Cox and Griffith (1978) shows very high fractional cloud top coverage for all of the B Array on Day 245; only 3.3% was "clear". However, much of this coverage is in the form of layer clouds. The large scale saturation which our model shows in the 6-9 hr period is consistent with this observation.

One of the basic motivations for carrying out a modelling study such as this is the chance to examine features of the ensemble which are not readily accessible to observation. One example is the breakdown of $Q_{1c}-Q_R$ and Q_{2c} into the $P_{\psi i}$'s (subensemble contributions), displayed in Fig. 6.10. Recall that the mesoscale terms are identically zero for this Case. We see that the environment terms are small, except in the nominal PBL, where the bulk of the surface moisture is entering (due to the large area covered by the environment). In the net, of course, this is balanced by the PBL drying in the various subensembles. We see that

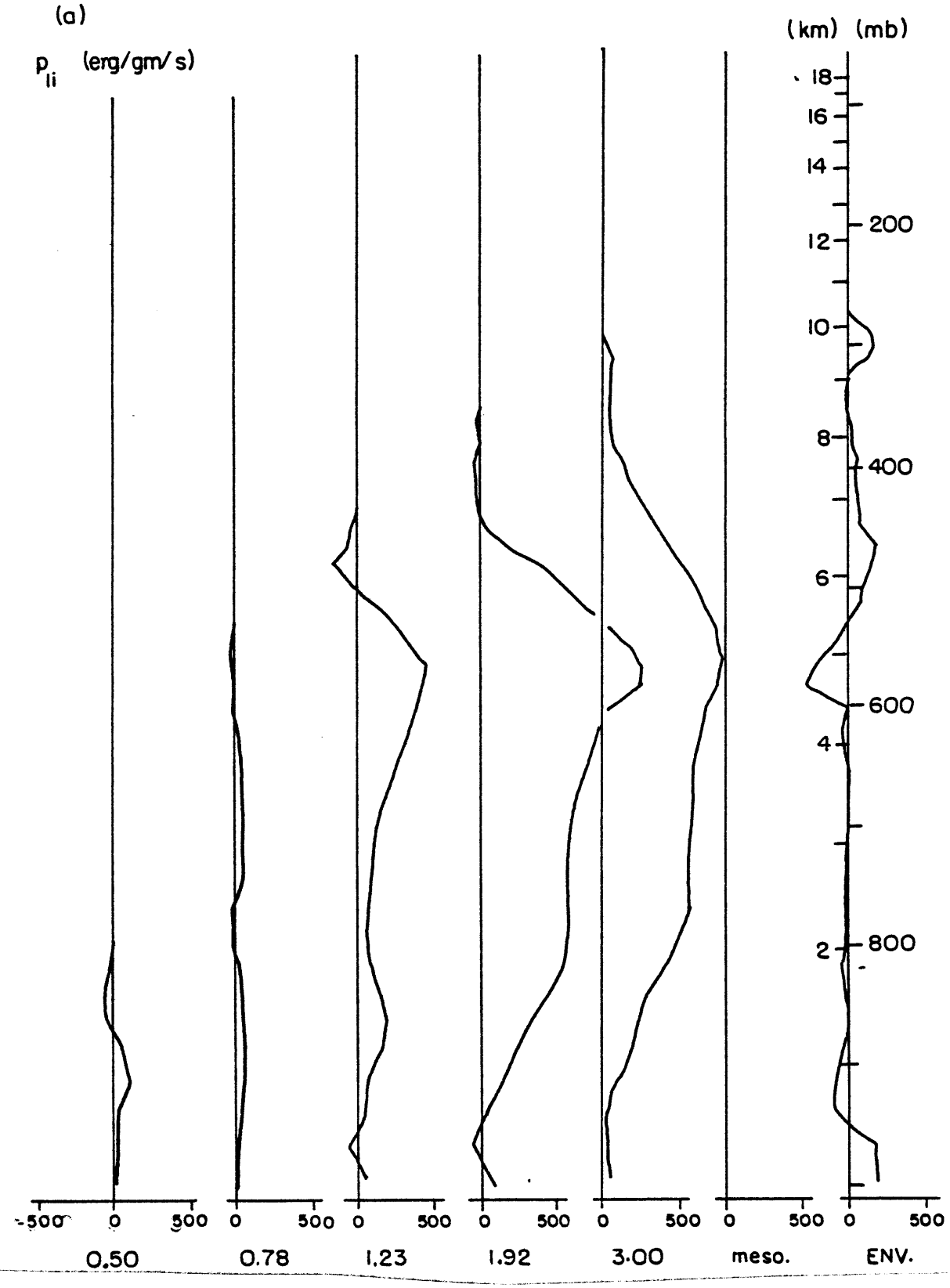


Fig. 6.10 Individual subensemble and region contributions to (a) heat, and (b) moisture budgets; Case LN1.NOM.

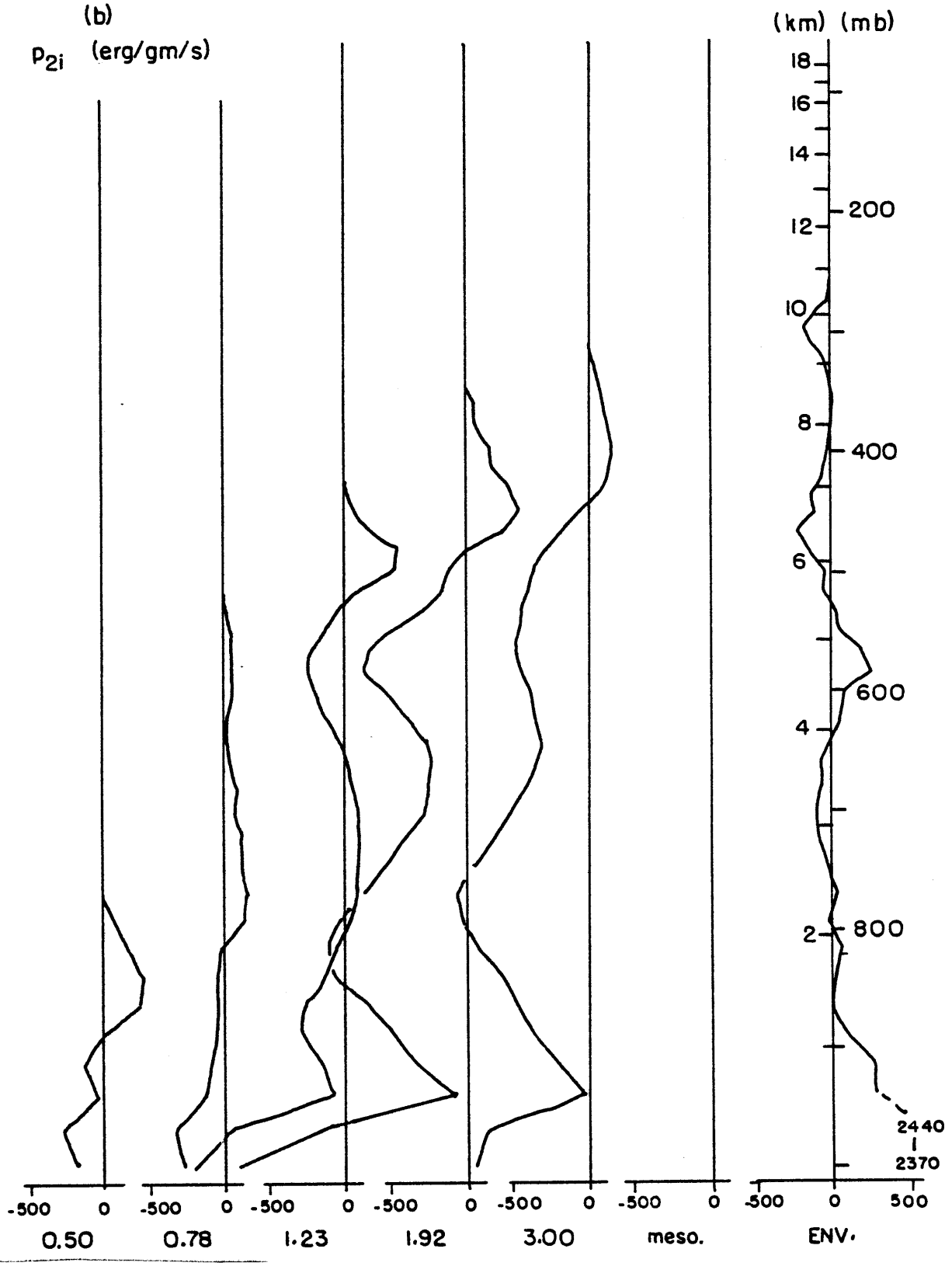


Fig. 6.10 continued.

the small clouds principally transport moisture upwards, while the larger clouds are responsible for most of the heating and drying, as expected.[1] The general shapes of the largest cloud's P_ψ profiles also conform to our expectations, based on the tests in Chapter 4 (Figs. 4.5a-b). It is gratifying to see the "tops" of the P_{ψ_i}'s occur at successively higher altitude for larger radii, justifying the use of cloud radius as a measure of cloud "size". Within this general result, however, the mid-level cloud one expects to see operating over, say, a half the depth of the deepest cloud is quite weak: The 0.78 km cloud has the smallest amplitude of the subensembles for both heat and moisture. This minimum is consistent with a result which many diagnostic budget studies display. Ogura and Cho (1973), Nitta (1975, 1977), Johnson (1976, 1977, 1980), and McBride (1981) all display a minimum in activity for clouds which top at mid-levels. As we will see, this interpretation is not entirely straightforward.

The other model-derived parameter which we will consider is vertical mass flux. Although the net large scale mass flux, $\overline{M}$, can be calculated from observations (examples of which are shown in Fig. 6.4a), the mass flux due to the cloud ensemble is very hard to derive. Fig. 6.11 presents the domain-averaged cloud updraft, cloud downdraft, net cloud, and environmental mass fluxes, M_u, M_d, M_c, and $\tilde{M}$ respectively. Recall that using tophat profile variables requires upward or downward motion for a given time, level, and region, unlike the time-averaged up- and downdrafts, both of which will be nonzero, in general. The progression

---

1 Parameterizations often assume that a single deep cloud type is carrying out all of the ensemble's heating and drying (see, e.g., Anthes, 1977).

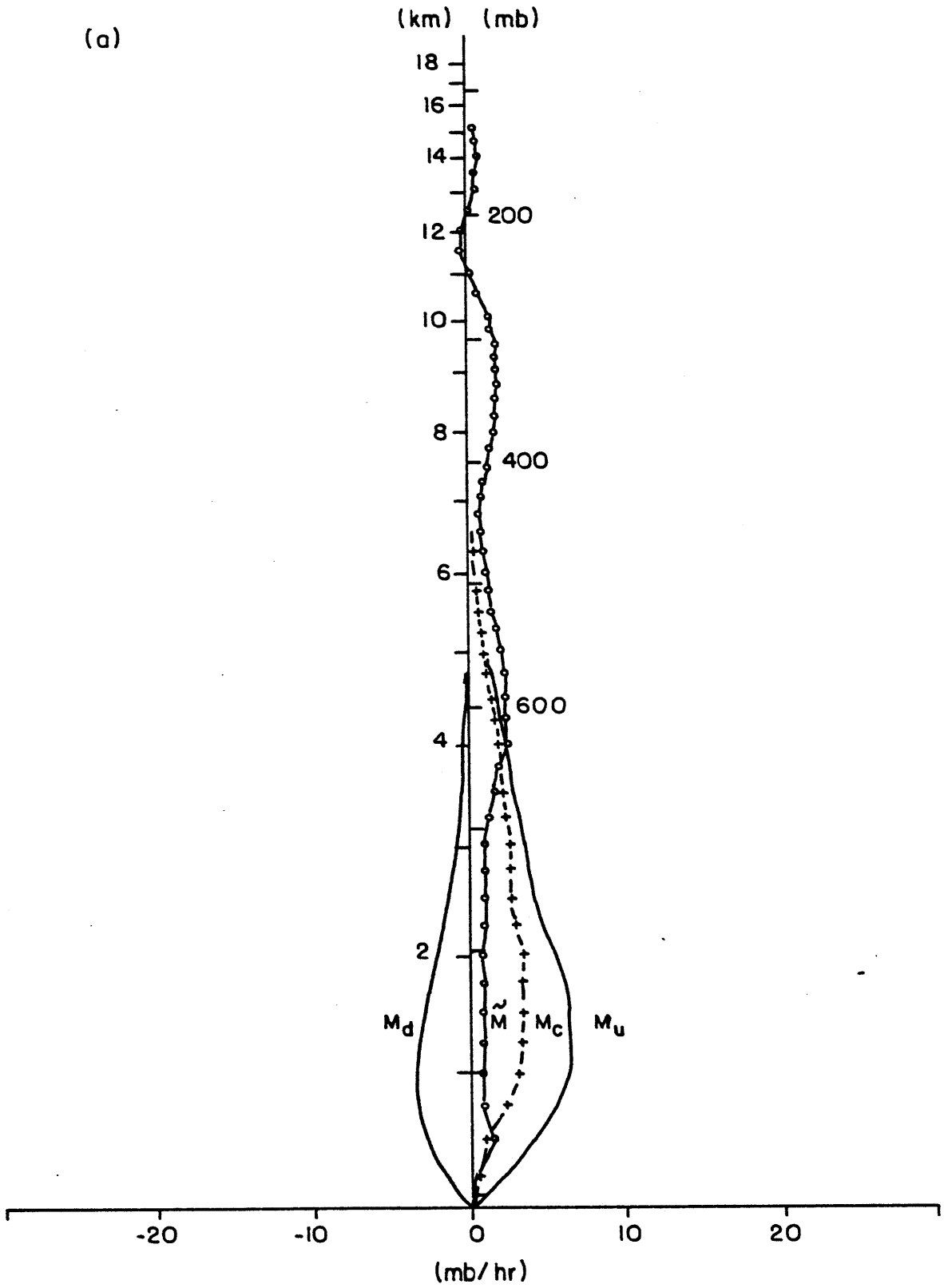


Fig. 6.11 Vertical mass fluxes in cloud updrafts (M_u), cloud downdrafts (M_d), clouds (M_c), and the environment ($\tilde{M}$) over (a) 0-3 hr, (b) 3-6 hr, (c) 6-9 hr; Case LN1.NOM.

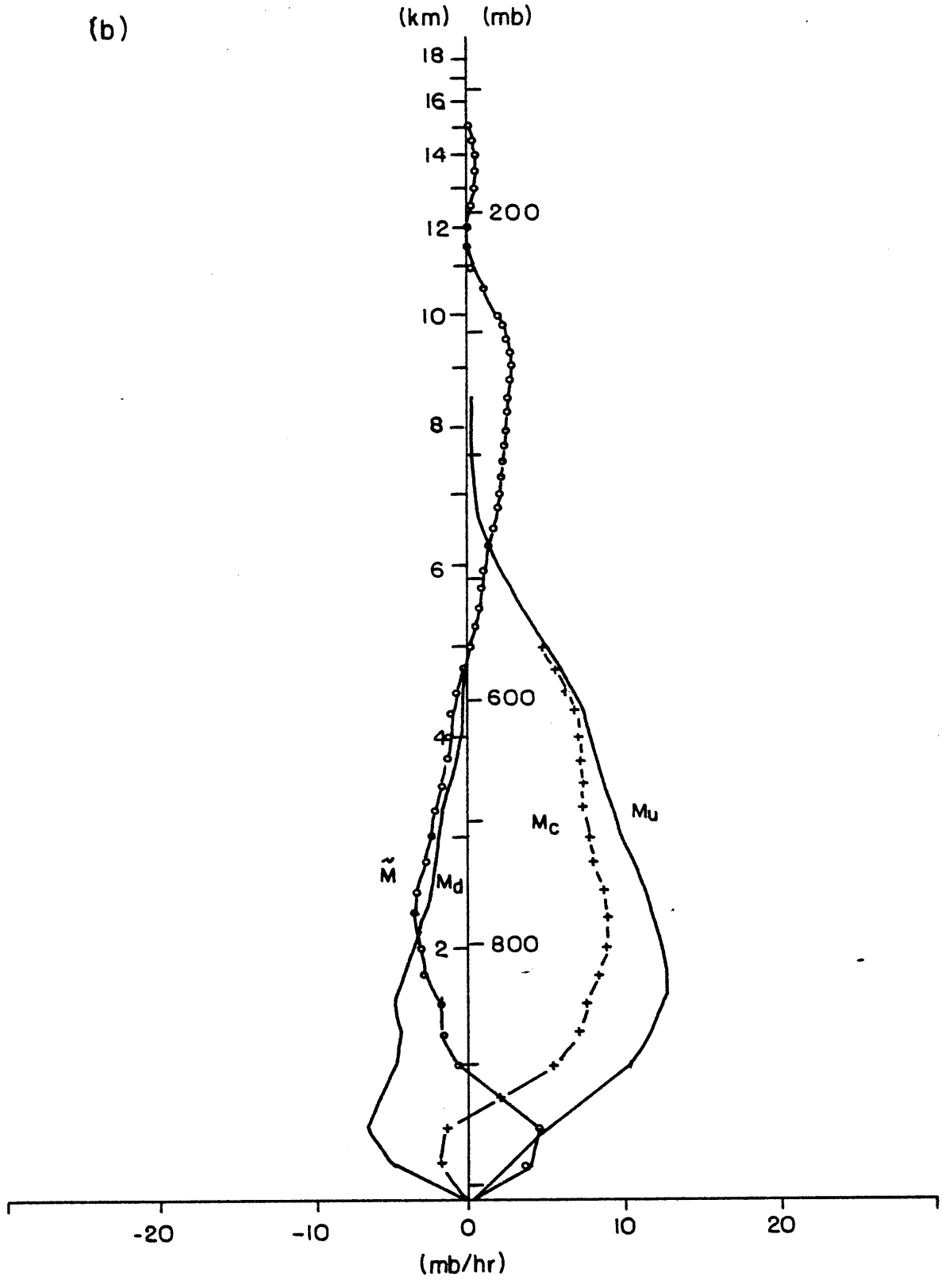


Fig. 6.11 continued.

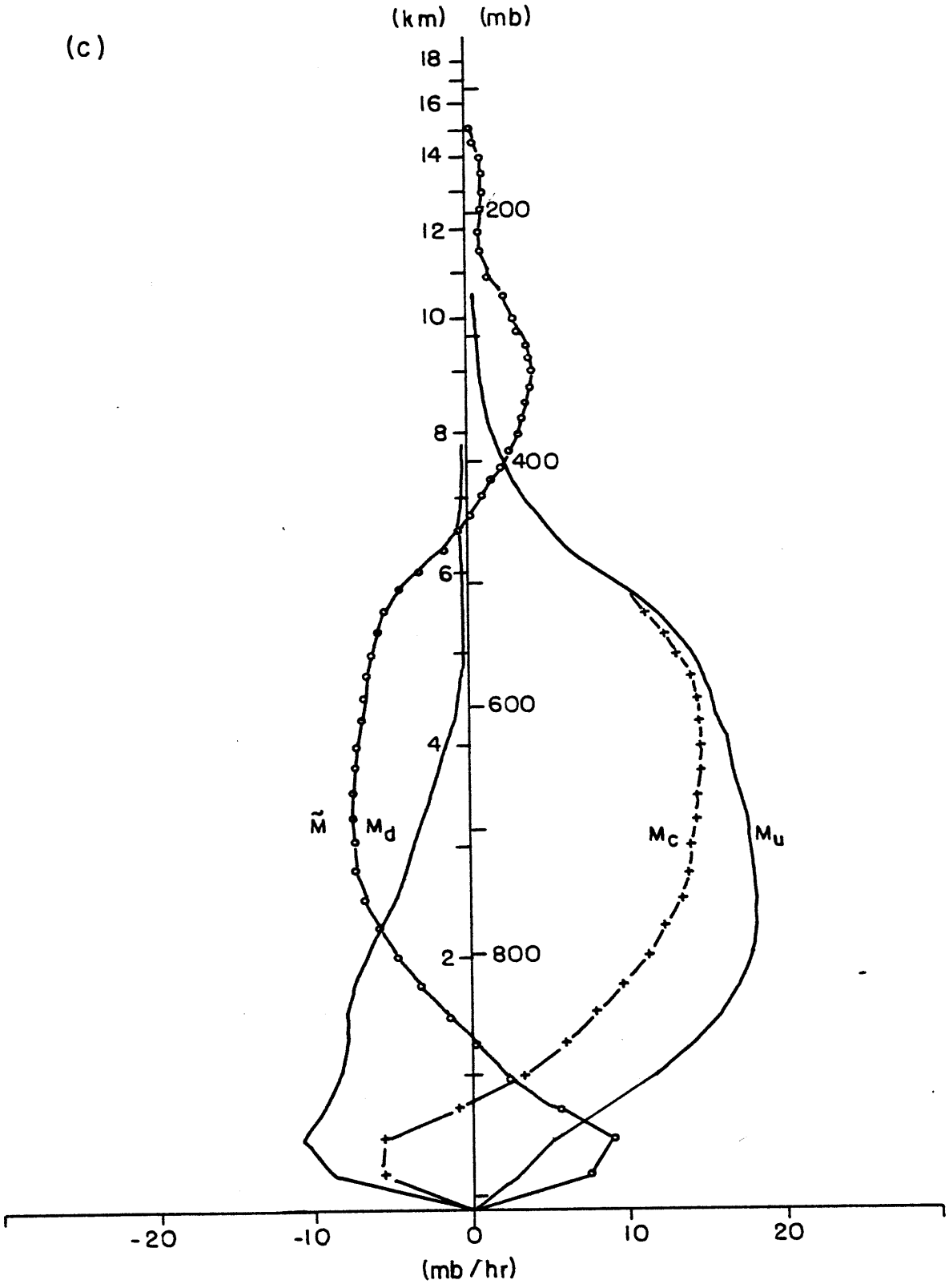


Fig. 6.11 continued.

of Figs. 6.11a-c shows a dramatic amplification of all mass fluxes with time, corresponding to the increasing vigor of individual clouds and to the increasing vigor of individual clouds and to the increasing number of clouds. After 0-3 hr we see downdraft mass flux predominating below cloud base (cf. Chapter 4). The result is to drive an upward mass flux in the environment. Above cloud base the updraft mass flux dominates, driving a substantial downward environmental mass flux. In all three periods the environmental mass flux nearly equals the large-scale average above the active convective layer.

Comparing our results to those of other studies, we see a high degree of similarity with the observations of LeMone and Zipser (1980), hereafter LZ, Zipser and LeMone (1980), and Zipser et al. (1981); M_c is small near cloud base and increases rapidly to a slowly varying mid-level value. Among currently available diagnostic budget studies, the overall profile of M_c is most similar to the M_c given by Johnson's (1980) "cumulus and mesoscale downdraft" model (Fig. 3.7). This result comes about even though Case LN1.NOM includes no explicit mesoscale structure. It is of particular interest that Johnson diagnoses upward environmental motion at upper levels, just as the current model does. The difference is that the destabilization implied thereby does not feed back in his model, whereas it does in ours. The M_c implied by Lord's (1982) cloud base mass flux distribution is also qualitatively similar to the current results, even though Lord neglects both cumulus downdrafts and mesoscale drafts. As with Johnson's model, the salient features are a small M_c near cloud base, increasing to a maximum at mid-levels, and decreasing thereafter. Recall from Chapter 3 that diagnostic budget studies without mesoscale structure show large amounts

of low-level vertical mass flux, as typified by the "no downdraft" curve on Fig. 3.7.

The behavior of the ensemble model without mesoscale structure (Case LN1.NOM) can be summarized as follows. Initially, the clouds are unable to grow very deep, and the observed budgets of heat and moisture are poorly simulated above the lowest few layers. Of course, satisfying the average moisture budget in the lowest 2 layers is guaranteed, since this constraint is needed to estimate the number of clouds. We will argue in Chapter 7 that this initial discrepancy is physically meaningful. As large scale lifting destabilizes the model atmosphere, deeper clouds appear. The budgets are more closely matched, meaning that the model environment is following the observed changes in the environment. Since these changes are small, the ensemble acts to oppose additional destabilization. This match of observed and simulated budgets occurs when the domain-averaged sounding differs from the original sounding. Subensemble contributions to the budgets tend to fall into two groups, shallow and deep clouds, with environmental contributions being small.

6.4 A case with mesoscale structure

We next examine a more general case, LN1.M20, in which mesoscale structure is included as described in Chapter 5. We retain the LN1 cloud distribution described in the previous Section, but now all of the clouds are growing within a region whose properties differ (in general) from those of the outer environment. The fractional cloud coverage over the mesoscale region is chosen to be 20%. This value is higher than the 10% coverage chosen in Case LN1.NOM on the grounds that subsidence (one part of the heat transport) probably occurs over a region larger than

the mesoscale region itself. The cloud-to-pressure domain ratio is also set at 20%. The method for deriving cloud number is as described above. The initial sounding is again taken as the 00Z Day 245 average (Fig. 6.5).

The time behavior of the subensembles is qualitatively similar to that in the previous Case, so examples of their behavior need not be shown. The mesoscale region is new, on the other hand, so we present a detailed time-height plot of vertical velocity in the mesoscale region for the 6-9 hr period (Fig. 6.12). Nonzero cloud water content occurs within the thin dashed lines.

The velocity field appears quite chaotic; there is no reason for it to appear otherwise. The cloud-induced accelerations in the mesoscale region must vary rapidly as each of the small number of subensembles undergoes rapid time variation within each lifecycle. We expect a gravity wave response to such non-steady forcing. The gravity waves are confined to a vertical channel; they cannot radiate in all directions, as a more detailed model would allow. There seem to be no secular trends in maximum velocity, so the main point we wish to make is that the time-averaged values we show for the mesoscale region do not always represent instantaneous conditions in that region. Presumably this rapid variation would be smoothed out if there were a large number of subensembles and if gravity wave energy was free to radiate away horizontally.

The other parameter displayed in Fig. 6.12, cloud water, exhibits two behaviors. In the 4-6 km layer there is an episodic appearance of cloud, associated with detrainment from individual subensembles. In the 9-10 km layer a persistent "anvil" forms from cloud detrainment and

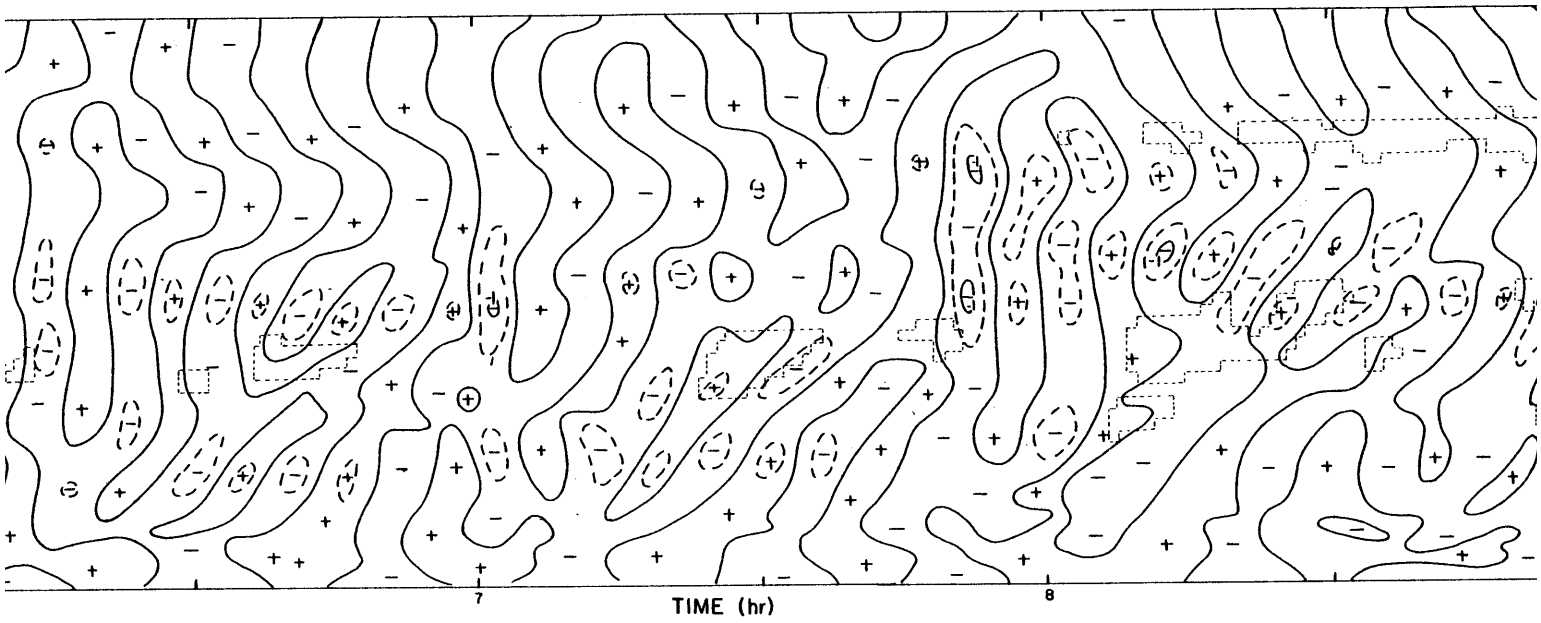


Fig. 6.12 Time-height plot of vertical velocity in the mesoscale region over 6-9 hr; Case LN1.M20.

advection from the outer environment. This comes about because the outer environment saturates sooner than the mesoscale region at the 10 km level, so that it subsequently serves as a source of cloud water for the mesoscale region. Further discussion of this point is given below.

The heat and moisture budgets generated by Case LN1.M20 are presented in Fig. 6.13. Many features are similar to the budgets generated by Case LN1.NOM. There is the same progression from relatively poor agreement over 0-3 hr to general agreement over 6-9 hr. Once again, the clouds are unable to grow vigorously until the environment is destabilized.

Within the general framework of this tendency, we also see systematic differences. Even over 0-3 hr Case LN1.M20 shows a qualitative agreement that LN1.NOM lacks. Note, for example, the extrema at 4.5 km. Over 3-6 hr there is better agreement with observation for LN1.M20 below 5.5 km, while LN1.NOM is less extreme above that level. Over 6-9 hr the two Cases are fairly similar below 6.5 km, except that LN1.M20 effects less drying over 1.5-4 km and more over 4-6 km. Above 6.5 km LN1.NOM displays less extreme changes with height.

The changes in domain-averaged temperature and water vapor associated with the budgets are shown in Fig. 6.14. Again, the general trends are the same as for Case LN1.NOM: At first, there is general cooling and moistening. Then the profiles settle into new states, starting from the bottom. The main differences come in the 3.5-5.5 km layer, which is dryer and warmer in Case LN1.M20, and the 5.5-8.5 km layer, in which case LN1.NOM is warmer and dryer (corresponding to the differences in the budgets).

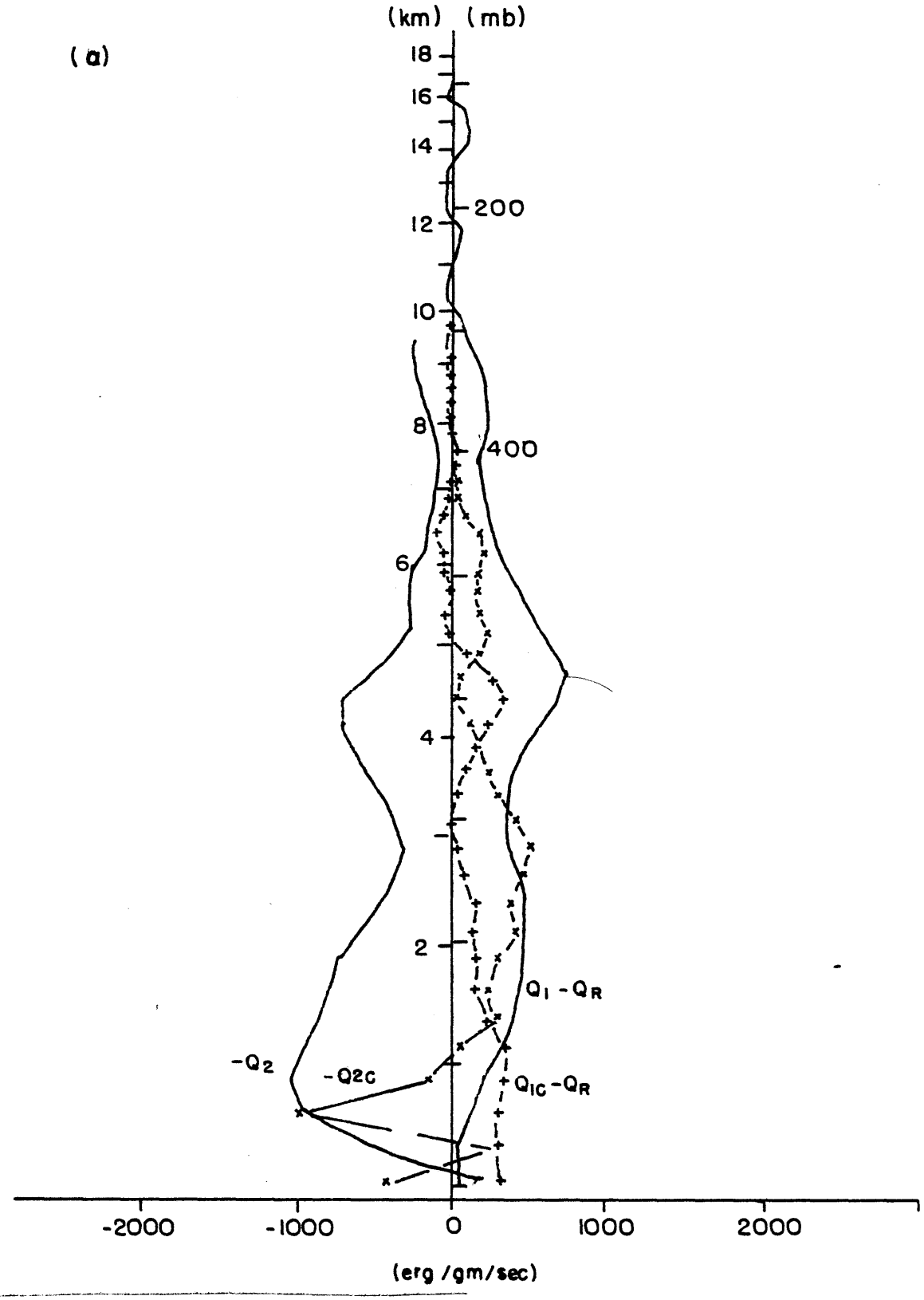


Fig. 6.13 As in 6.8 for Case LN1.M20.

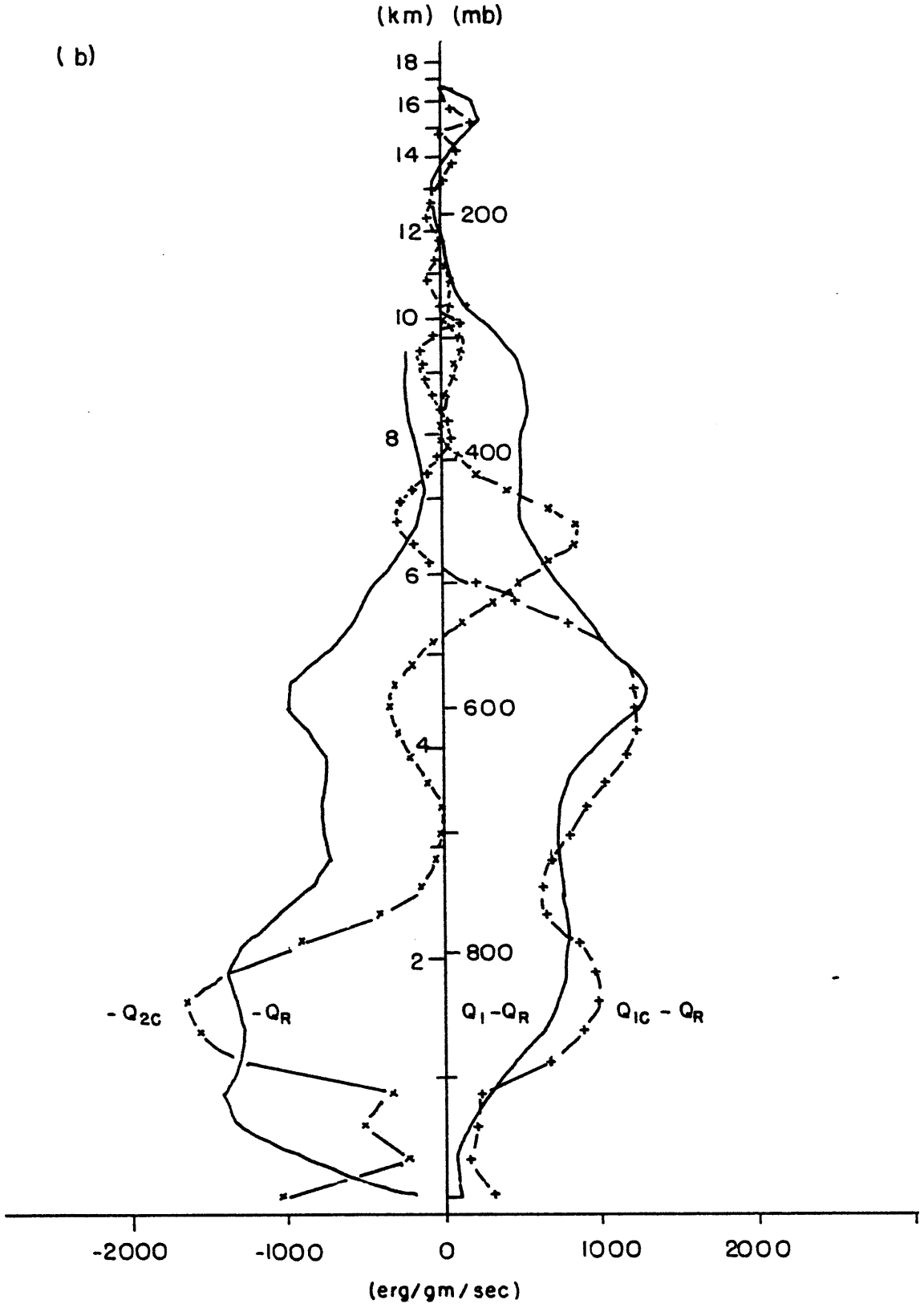


Fig. 6.13 continued.

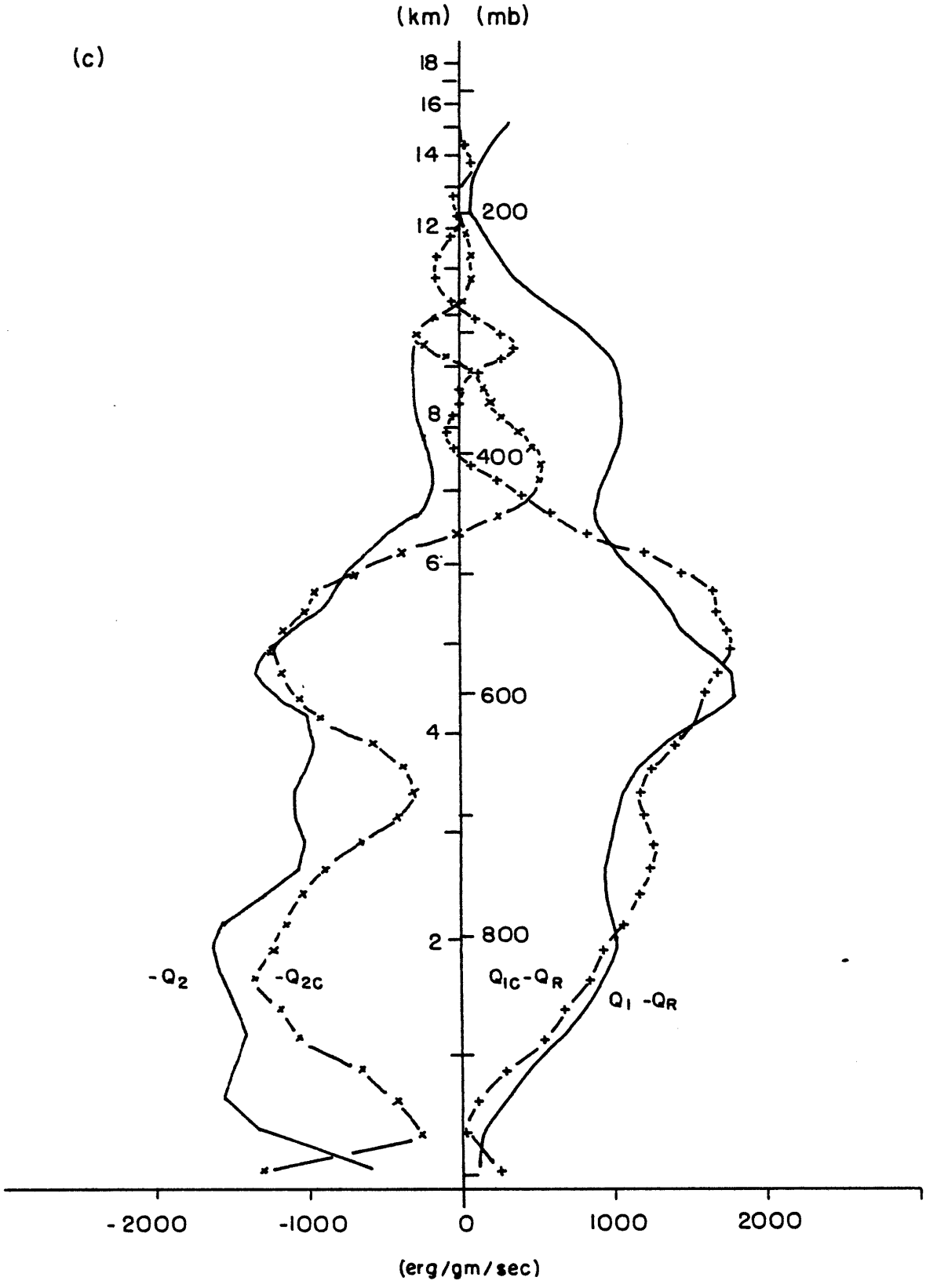


Fig. 6.13 continued.

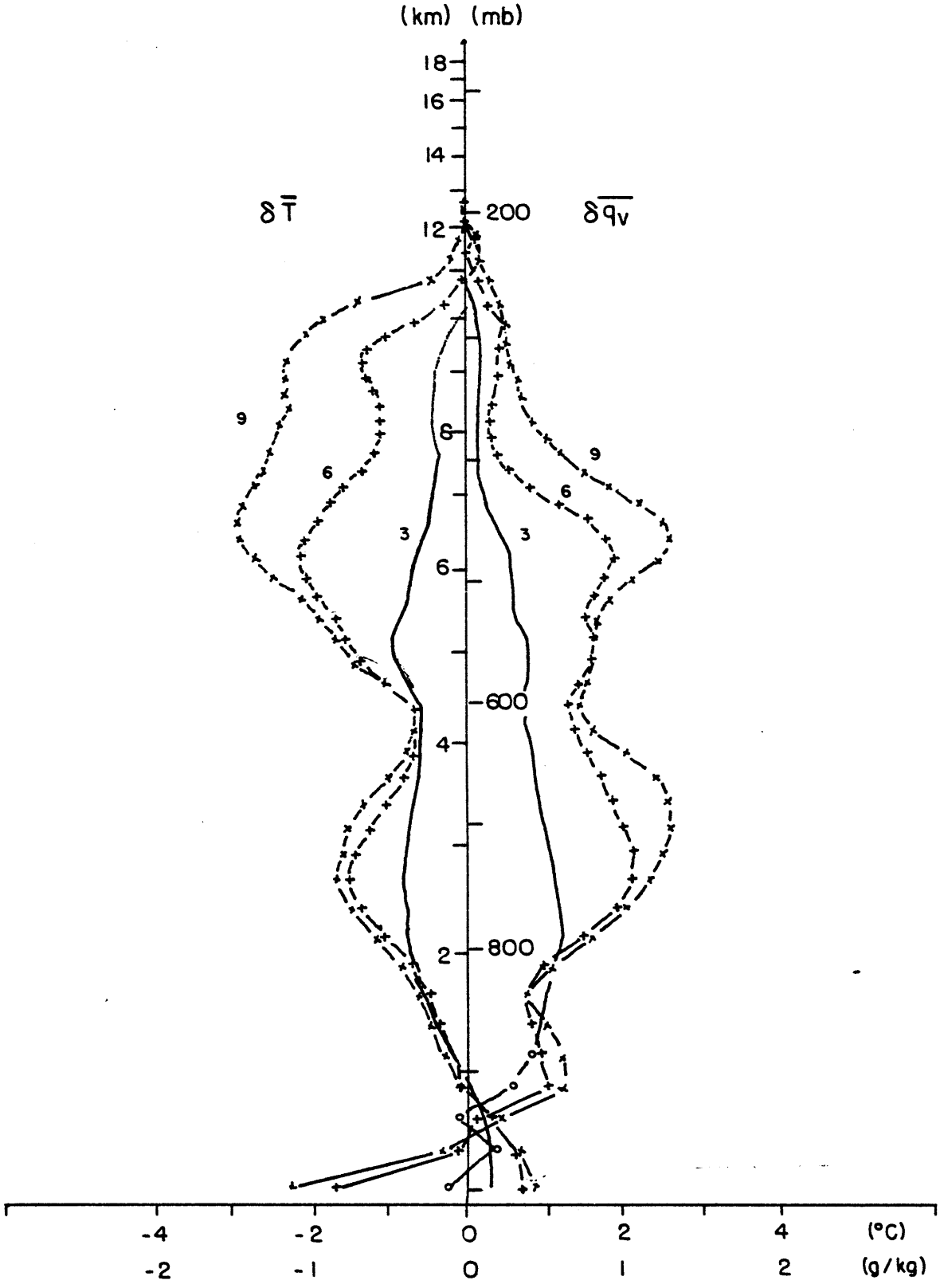


Fig. 6.14 As in 6.9 for Case LN1.M20.

The area-averaged rainfall (Table 6.2) shows similar tendencies, with more rain falling in the first 6 hr for LN1.M20 than LN1.NOM. The smaller rainfall over 6-9 hr reflects the smaller amount of drying which occurs in Case LN1.M20. Nonetheless, the radar-derived precipitation is still exceeded by a factor of 2.

What mechanism does the mesoscale region introduce that leads to these systematic differences? Recall from Chapter 5 the "mutual protection" hypothesis, that clouds modify their mesoscale environment such that successive generations of clouds can grow more vigorously than they could in the outer environment. By inspecting the temperature and water vapor changes in the outer environment and mesoscale region (Figs. 6.15a-b), we see that exactly such a process is occurring. The temperature profiles at a given time are very close in the two regions (and, therefore, close to the domain average), but the mesoscale region is always moister over the depth of the active convective layer (cf. Simpson and VanHelvoirt, 1980). When we compare these results to Case LN1.NOM (Fig. 6.8), we see that the LN1.M20 outer environment is dryer and slightly warmer over the 3-6 km layer, while the LN1.M20 mesoscale region is moister between 2 km and the top of the convective layer. At 3 hr the mesoscale is also moister between 2 km and cloud base. The drying exhibited below cloud base in the Case LN1.M20 mesoscale region is the consequence of removing moisture for the nascent clouds from the mesoscale region, while not providing any special way of transporting fresh subcloud air in from the outer environment.

The consequences of mutual protection are clearly visible when we examine the vertical mass fluxes generated by the model in Case LN1.M20 (Fig. 6.16). We still see the amplification and deepening of the mass

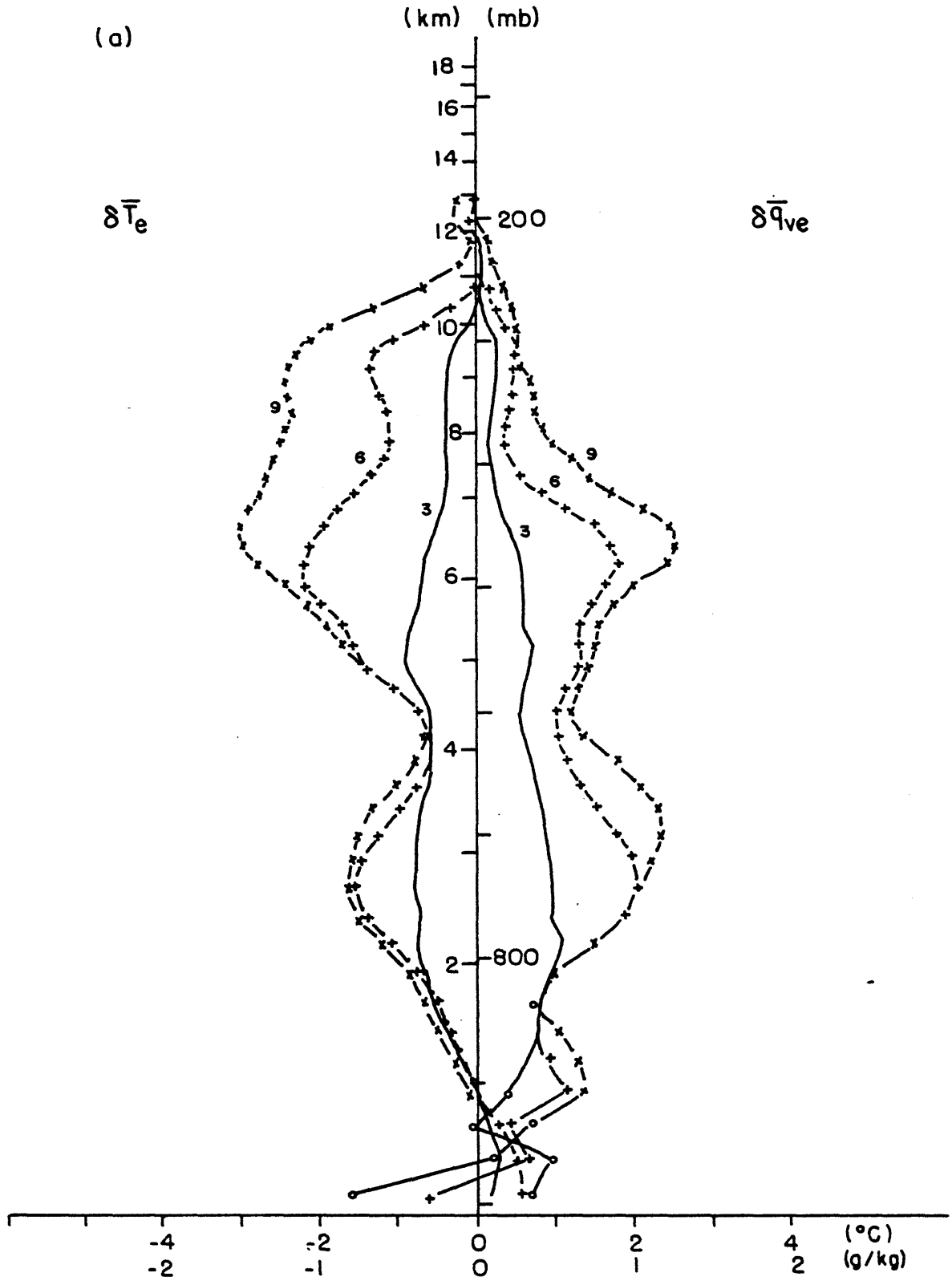


Fig. 6.15 As in 6.9 for Case LN1.M20, except for (a) outer environment-averaged, and (b) mesoscale region-averaged.

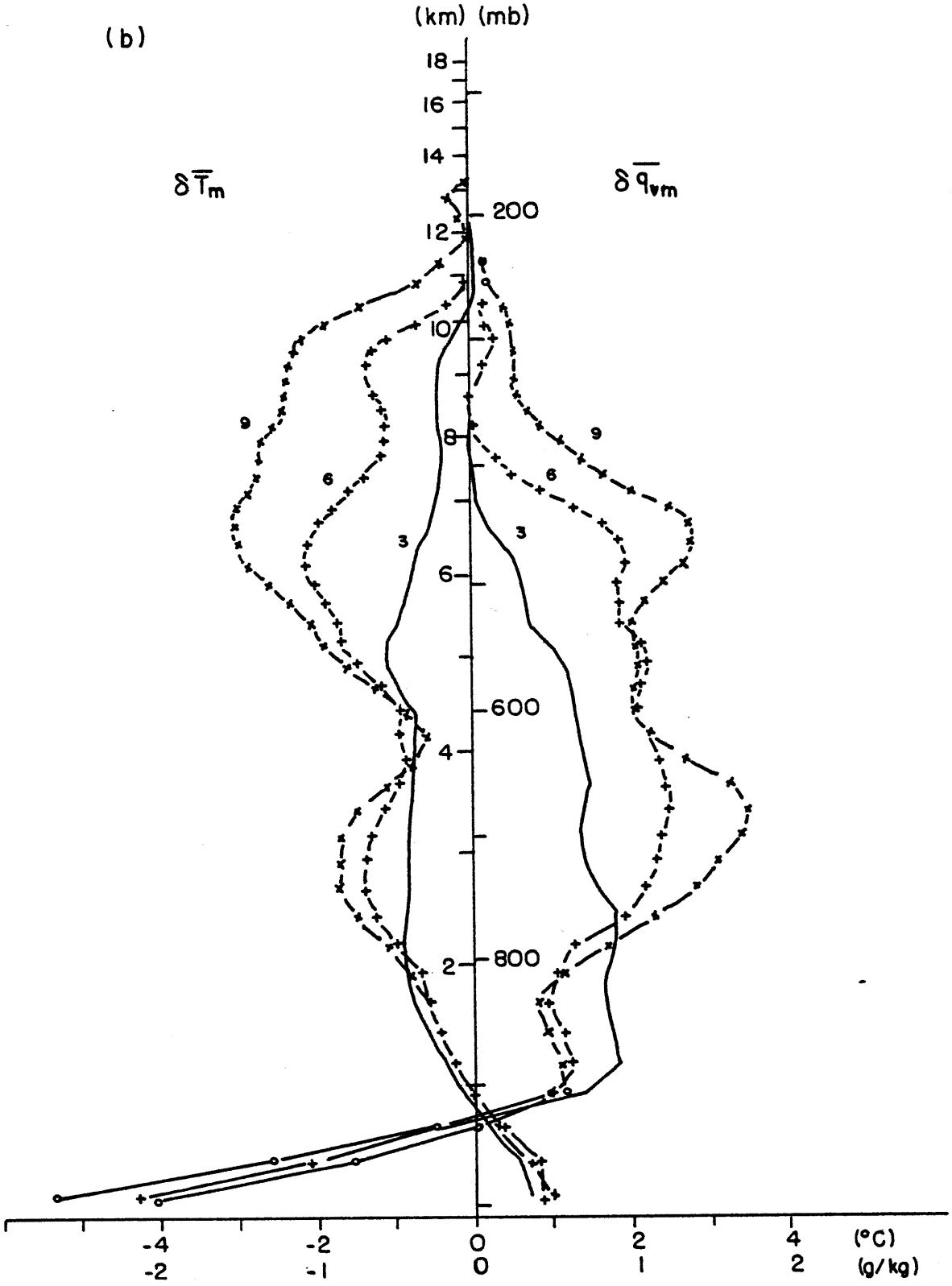


Fig. 6.15 continued.

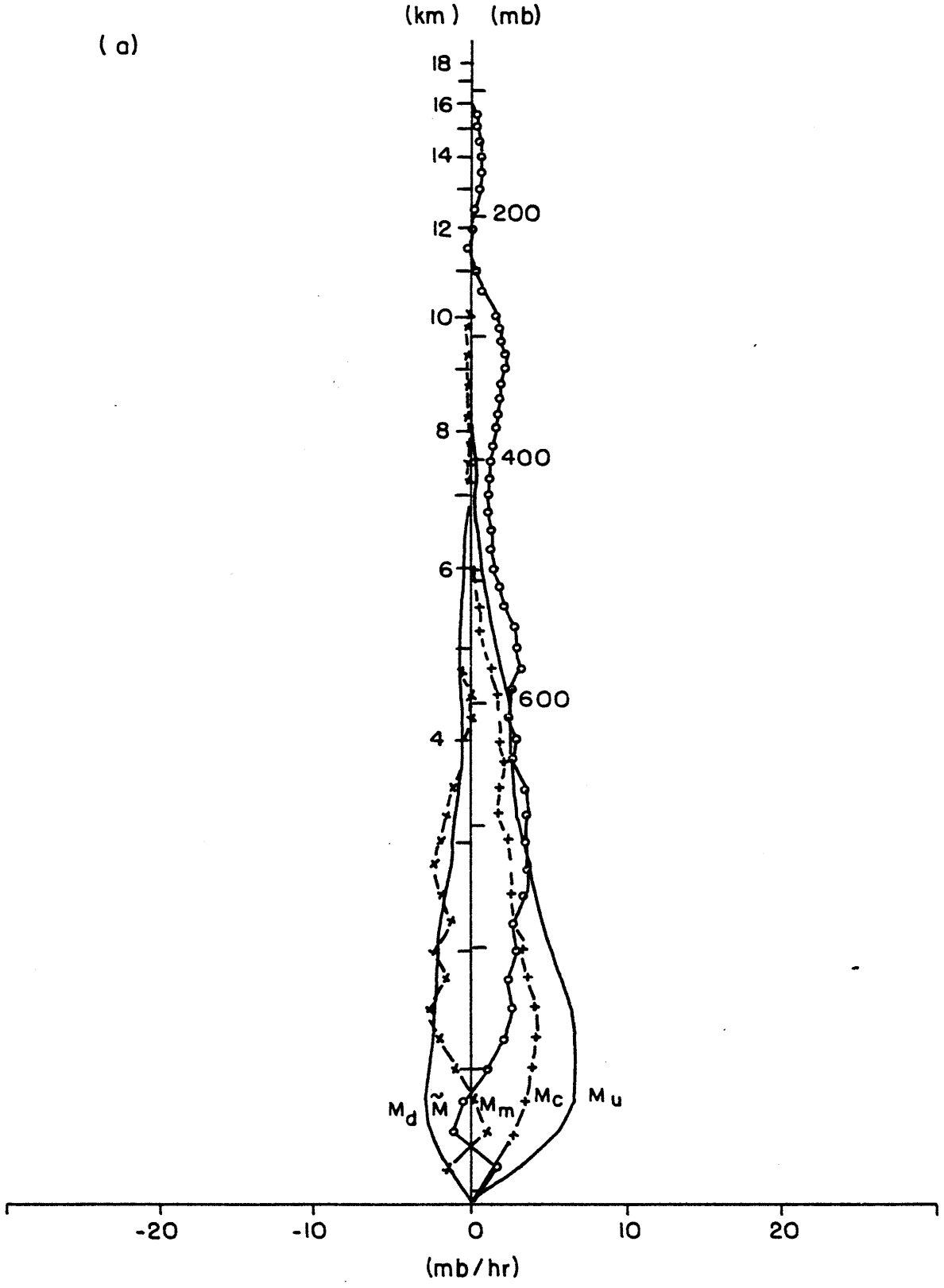


Fig. 6.16 As in 6.11 for Case LN1.M20, with vertical mass flux in the mesoscale region (M_m).

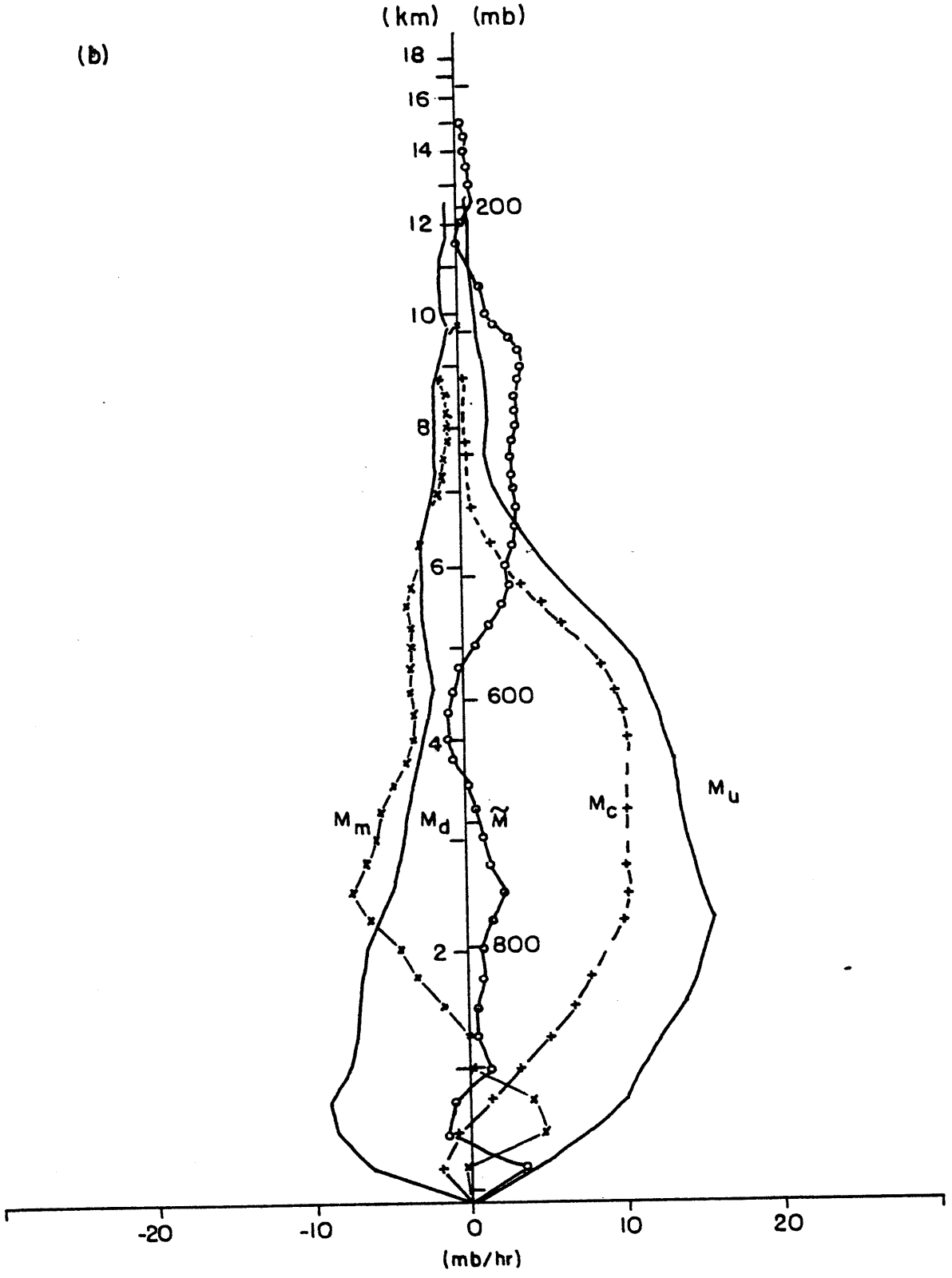


Fig. 6.16 continued.

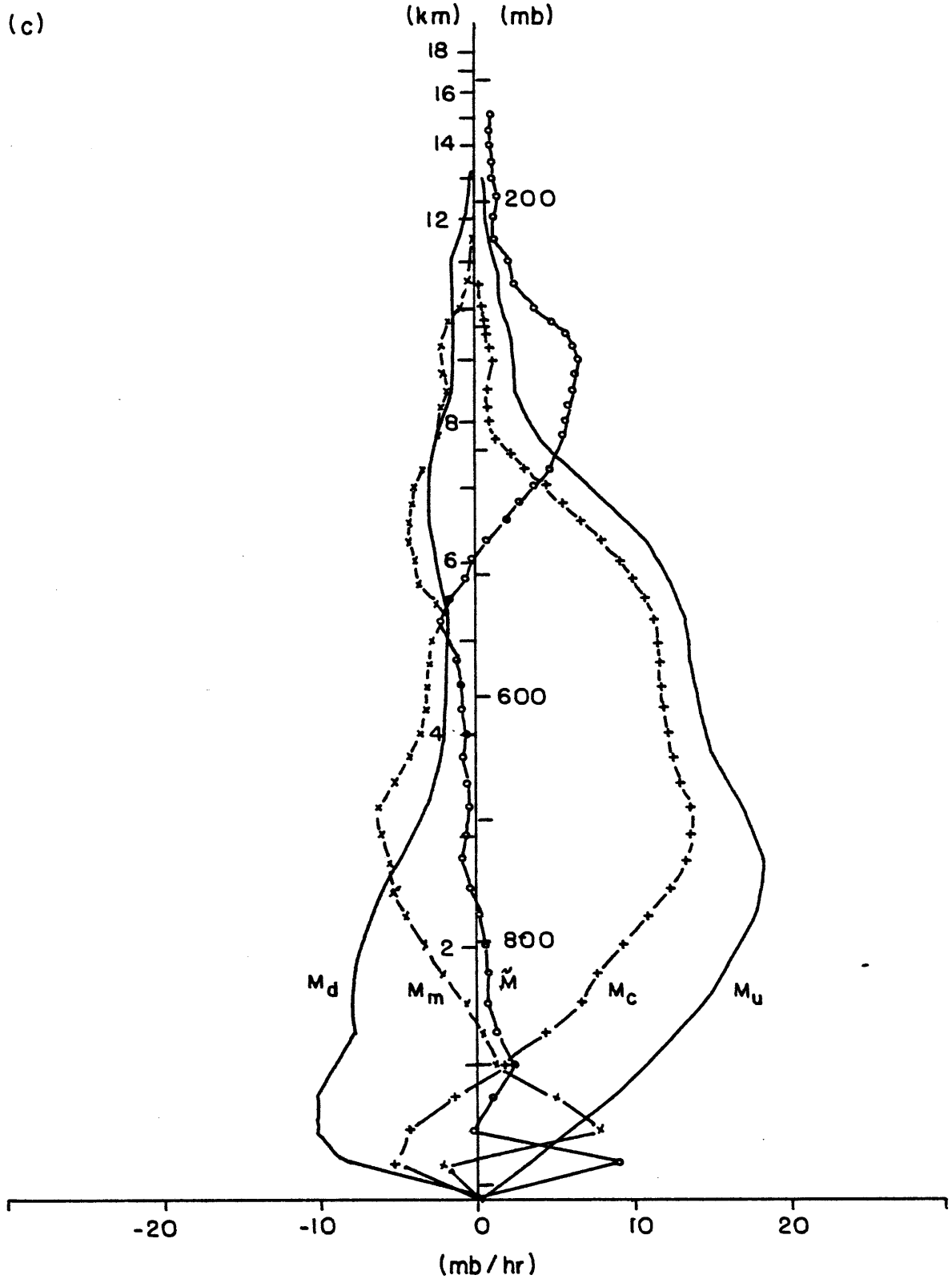


Fig. 6.16 continued.

fluxes associated with destabilization, as in Case LN1.NOM. Over 0-3 hr the net cloud mass flux, M_c, is relatively similar in the two Cases. Over 3-6 hr M_c is clearly larger (about 30% at 4.5 km) and the profile is shifted upwards for LN1.M20, which has mutual protection. Over 6-9 hr, when both Cases satisfy the budgets to the same degree, the respective M_c's become similar, although LN1.M20 has smaller values, except above 6 km and at 3 km. The general result of mutual protection, then, is to generate deeper clouds (an M_c profile which is shifted upwards, compared to the case without mesoscale structure), although the maximum value over the profile is not always larger than the corresponding no-mesoscale case.

When we try to compare the mass flux results of the present study to those of LZ in detail, we encounter some ambiguity due to their experimental technique:

1. LZ define a "core" as having $|w| > 1$ m/s, whereas our clouds are defined for any value of $|\overline{w}_a|$.
2. LZ present results measured along (essentially) 1-dimensional flight paths. In this method, the probability of sampling a wide cloud is higher than the probability of sampling a narrow cloud, since the wide cloud covers a larger area in the plane perpendicular to the flight path (see Fig. 6.17, Path A). In contrast, we know the cloud distribution.
3. LZ consider the length of cores along the flight path, with the requirement that cores have a minimum size of 0.5 km. However, they have made random samples through the clouds along chords which are in general shorter than the diameter (Fig. 6.17, Path B), so results at any specific size are due to all clouds with a diameter not less than

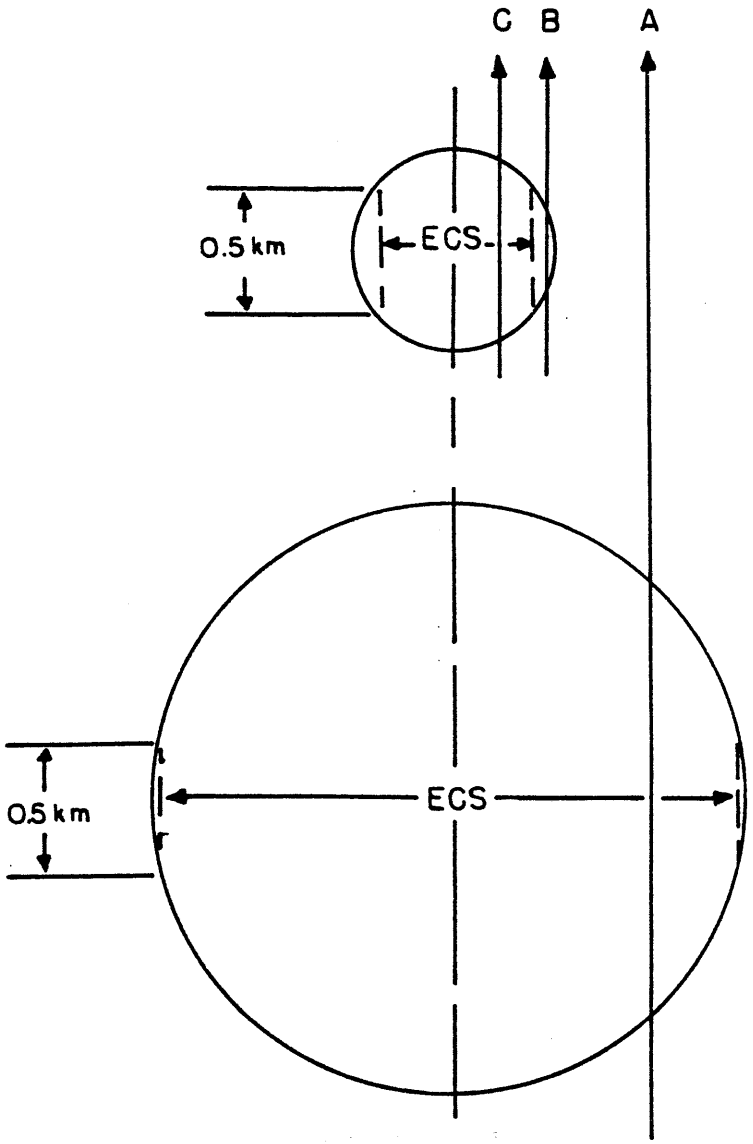


Fig. 6.17 Schematic diagram illustrating LeMone and Zipser (1980) flight paths. ECS is Effective Cross Section of a cloud (measured perpendicular to a flight path). Path A shows a flight sampling a large cloud, missing a smaller cloud. Path B shows a flight with an in-cloud path length > 0.5 km. Path C shows a flight with in-cloud path length < 0.5 km (even though cloud diameter > 0.5 km).

that size. In particular, our (round) clouds are all of diameters which qualify them as cores, but chords very close to the edges will be too short to contribute to core results (Fig. 6.17, Path C).

As a limited test, we have gathered up- and downdraft statistics over 6-9 hr for Case LN1.M20 in a procedure consistent with LZ:

1. The effective cross section, ECS, of a cloud is defined as the cloud's perpendicular width which provides an in-cloud flight path length of not less than 0.5 km (see Fig. 6.17). The total ECS of a subensemble is simply the subensemble population times the ECS of one cloud, since all members of a subensemble are identical.
2. The range of vertical velocities is quantized into 0.25 m/s intervals.
3. At each timestep and level, each subensemble is assigned to the bin whose vertical velocity interval contains the subensemble's vertical velocity.
4. The total ECS of the subensemble is accumulated in the assigned bin, regardless of subensemble radius.
5. At the end of the 3 hr, the 50 percentile and 10 percentile vertical velocities are determined at each level for $\overline{w}_a > 1$ m/s and $\overline{w}_a < -1$ m/s separately.
6. The accumulated sums are averaged over 4 vertical layers with boundaries at 0.00, 0.62, 2.50, 4.37, 8.12 km, which approximately correspond to LZ's boundaries, and Step 4 is repeated.

At this point the virtues of our model are apparent; unlike other simple models we have the cloud radii, cloud numbers, and time histories of vertical velocity, which the procedure requires.

Fig. 6.18 shows the 50 and 10 percentile level-by-level results,

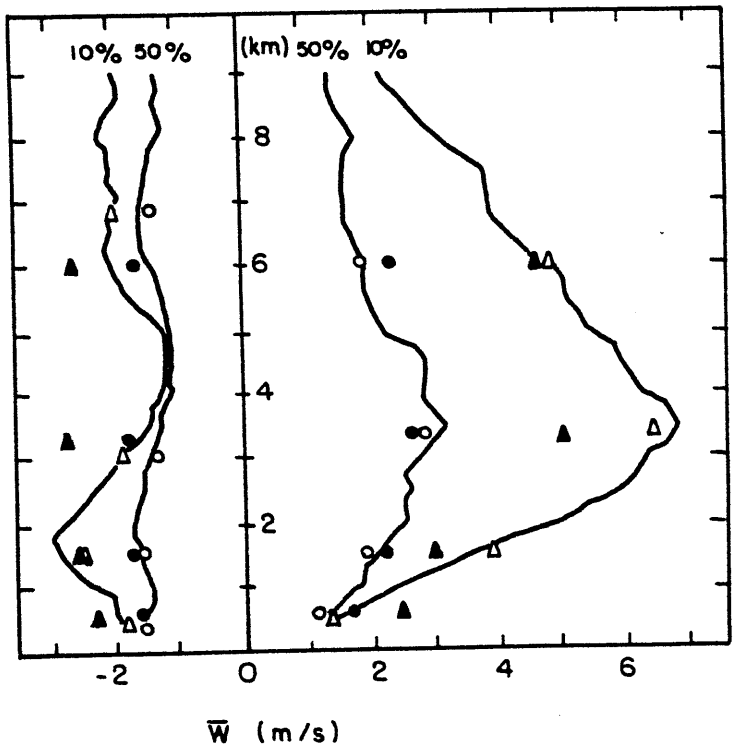


Fig. 6.18 Up- and downdraft average vertical velocity 50 percentile (o) and 10 percentile (Δ) speeds as a function of height. Solid symbols are LeMone and Zipser's (1980) GATE aircraft samples of "cores". All other data are for Case LN1.M20 over 6-9 hr, processed as in Section 6.4. Lines are level-by-level values, isolated symbols are layer averages, plotted at event-weighted heights.

plotted as solid lines, the 50 and 10 percentile layer results, plotted as o and Δ at ECS-weighted heights, and LZ's 50 and 10 percentile layer results, plotted at number-weighted heights. Inspecting the layer results, we see excellent agreement between LZ and the current study for the 50 percentile updrafts above cloud base. The 10 percentile updrafts also show substantial agreement. Our model's larger 10 percentile values at 1.5 and 3.5 km probably reflect 1. the destabilization which has taken place over the first 6 hr, and 2. uncertainty in LZ's estimates due to a small sample size (5-6 events above the 10% level). The largest discrepancy comes in the subcloud layer, where our model is apparently generating updrafts which are much weaker than LZ observed. In contrast, downdrafts show excellent agreement in the lowest two layers. We interpret these results as indicating that the net downward mass flux which our model generates at cloud base is larger than it should be, due to a deficiency in creating strong, low-level updrafts. Finally, the model downdrafts in the upper two layers are weaker than LZ's. This result is traced back to the distinct minimum in the level-by-level downdraft statistics over 4-5 km. Detailed time-height plots of vertical velocity for the various subensembles (not shown) disclose that this level is above the significant precipitation-driven downdrafts and below the level of cloud top downdrafts. In any event, these model cloud downdrafts are to be considered incomplete, since the simple model geometry precludes simultaneous up- and downdrafts (as simulated, e.g., by Simpson, et al., 1982). Within the limitations discussed, our simulated vertical velocities correspond rather well to LZ's observed vertical velocity distributions.

Returning to the mass flux profiles in Fig. 6.16, we also see a sec-

ond effect of including mesoscale structure: Over most of the convective layer M_m is downward. One interesting result after 0-3 hr is that $\tilde{M}$ is much closer to zero in Case LN1.M20 than in LN1.NOM. That is, the "extra" mass flux generated by the clouds is compensated by sinking in the mesoscale region, rather than in the outer environment, given the extra degree of freedom. Johnson (1980) displays a similar result (Fig. 3.7); the parallel becomes obvious if we sum M_c and M_m in Fig. 6.16. Houze and Cheng (1981) show a reduction in M_c+M_m when M_m is allowed, so by implication their M also decreases (in the region where $\tilde{M}$ is downward). We can see from Fig. 6.19 that the mesoscale region is as important as any subensemble for the total mass flux profile (for the particular subensembles chosen).

The exceptions to the statements above come at the surface and in the upper part of the convective layer, where M_m helps drive larger $\tilde{M}$ than we see in Case LN1.NOM. Such sinking in the mesoscale region and rising in the outer environment results in saturation in the outer environment and drying in the mesoscale region, the opposite of our conventional picture of anvil formation. We examine this problem by averaging the various terms in the vertical velocity equation for the mesoscale region in Case LN1.M20 over 6-9 hr (corresponding to Fig. 6.16c), displayed as Fig. 6.20a. The total acceleration (——) is small, but nonzero, since the velocity profile at 9 hr is not identical to that at 6 hr. The vertical advection of momentum (-o-) and residual diffusion (- - -) are small, except the latter near the lower boundary. The important terms include buoyancy due to virtual temperature (-·-), vertical perturbation pressure gradient (-+-), horizontal advection of vertical momentum (-•-), and liquid water drag (-x-).

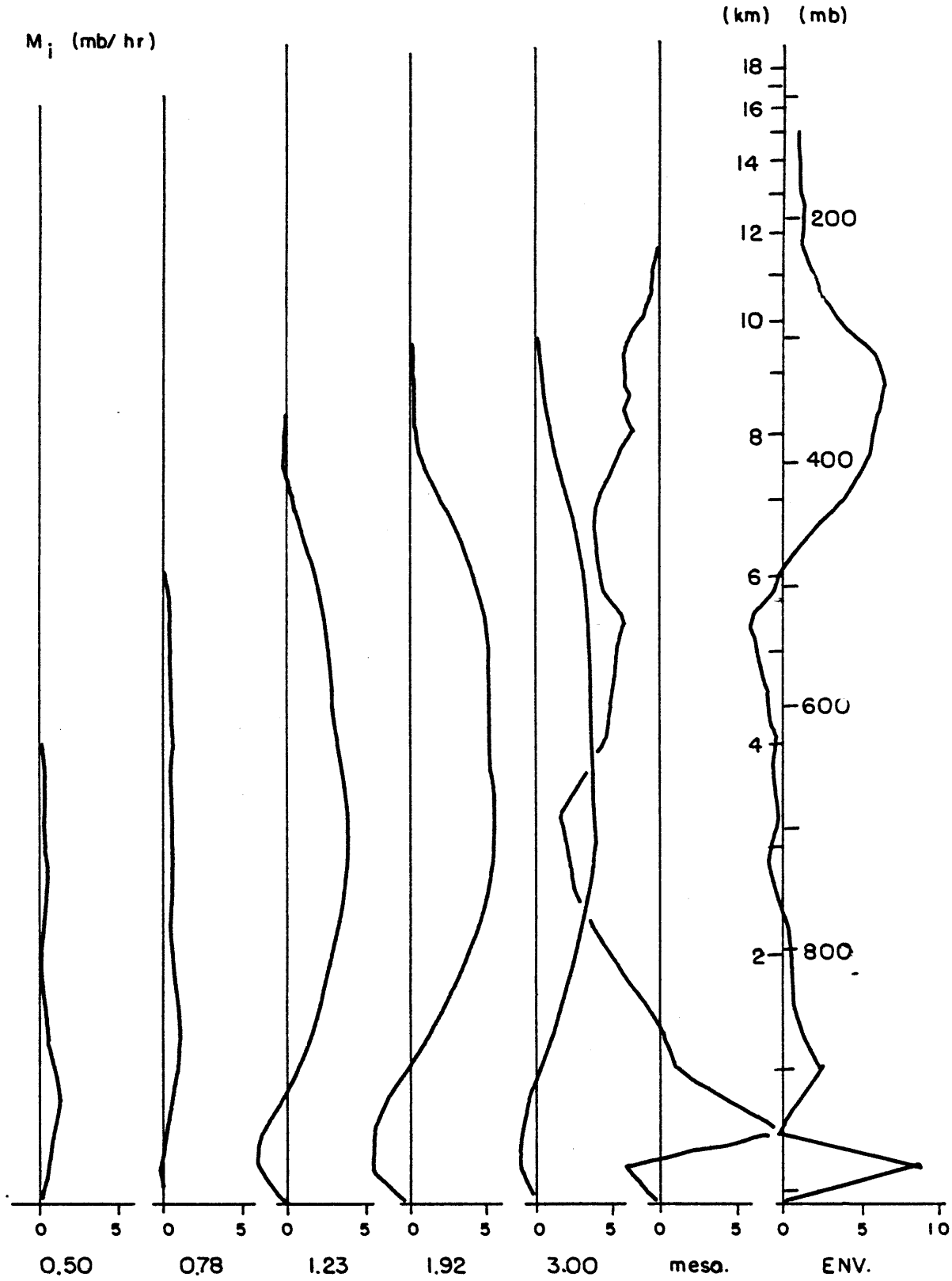


Fig. 6.19 Subensemble and region contributions to vertical mass flux; Case LN1.M20.

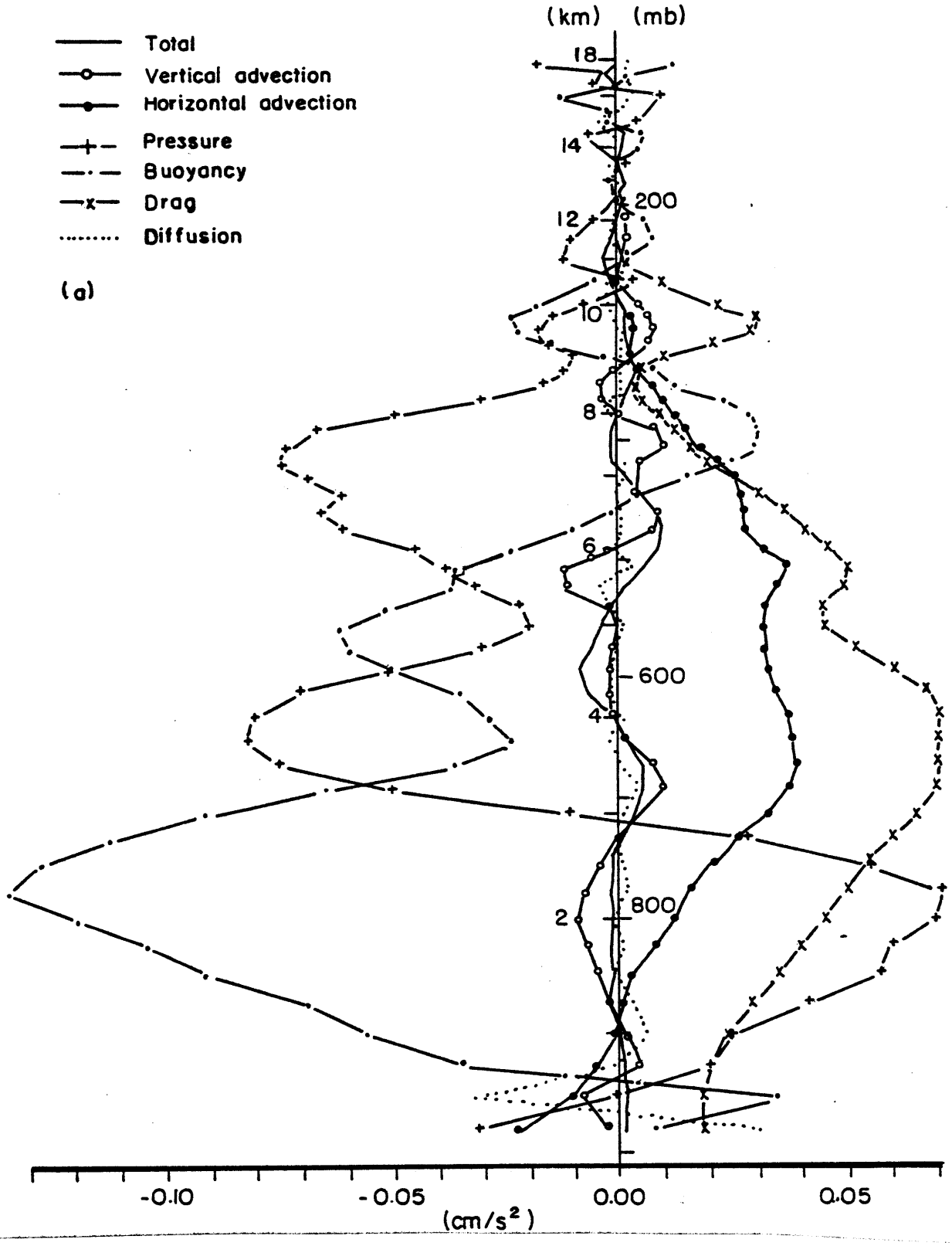


Fig. 6.20 Accelerations in the mesoscale region vertical velocity equation, averaged over 6-9 hr for Case LN1.M20, (a) with and (b) without vertical perturbation pressure gradient in the mesoscale region.

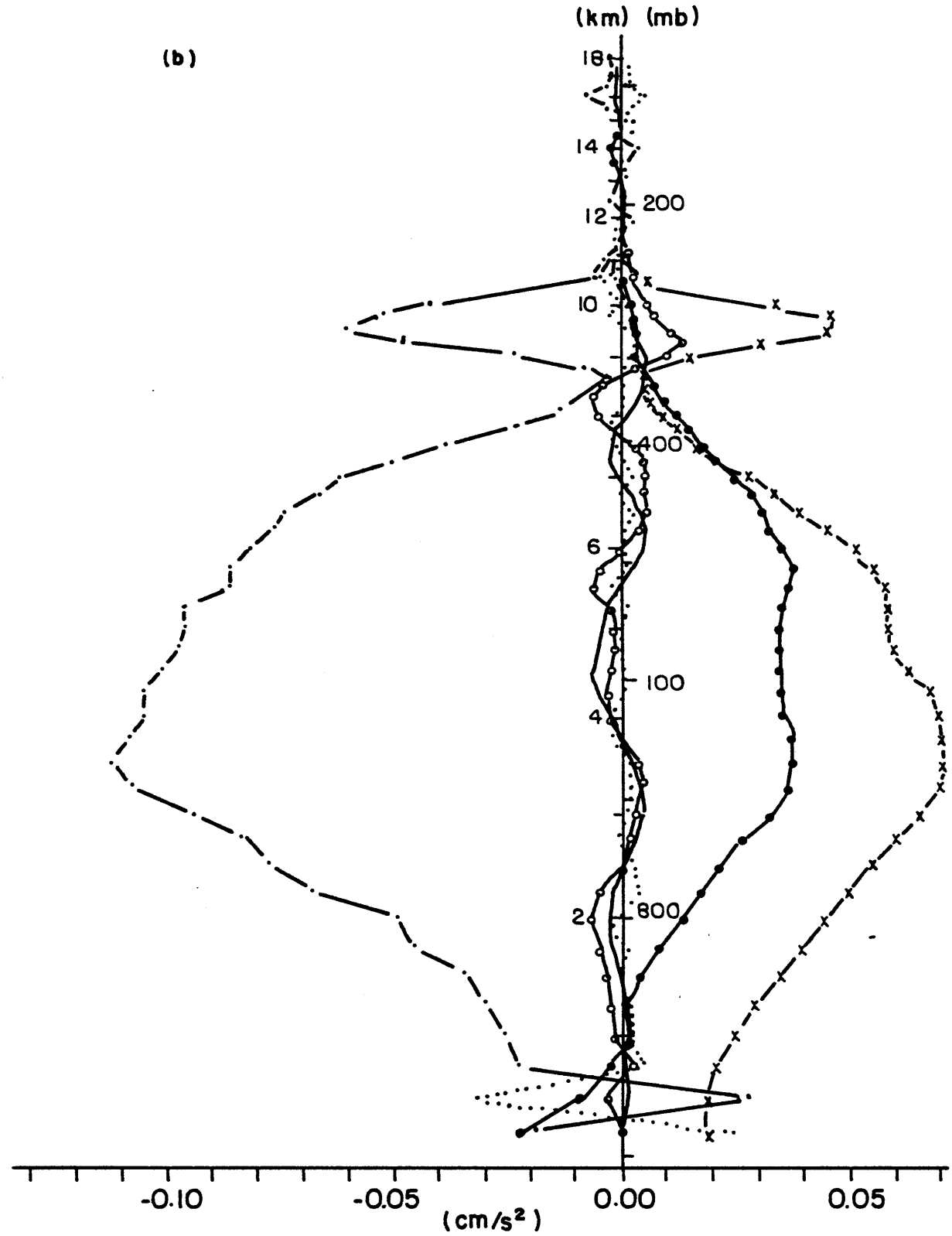


Fig. 6.20 continued.

In the current form of the model, the last three terms are dominated by ensemble forcing. That is, "drag" is positive because the clouds have liquid water, but the mesoscale region doesn't. Horizontal advection of vertical momentum predominently results from the detrainment of cloud air with upward momentum, except below cloud base, where detrainment carries downward momentum into the mesoscale region. Perturbation pressure is simply the reaction of the cloud pressure fields on the mesoscale region.[2] The only dominant term which is left for the mesoscale region to adjust is buoyancy. That is, the dominant contributions to buoyancy, condensation/evaporation and the vertical advection of virtual potential temperature, must jointly balance the other accelerations, on the average. Now clouds detrain liquid water over a deep layer (cf. Fig. 4.5) and the mesoscale region is unsaturated (initially), so evaporative cooling is guaranteed to be taking place over a deep layer. The sinking we observe advects in higher virtual potential temperature to achieve approximate balance. In particular, it is obvious that sinking must occur to generate the positive net buoyancy in the 6.5-9 km layer in the face of detrainment from the deep clouds.

The correctness of this assessment can be tested numerically by "turning off" the pressure forcing on the mesoscale region by the clouds and rerunning the 6-9 hr period of Case LN1.M20. No re-estimate was made for the number of clouds, since the computed moisture budget in the nominal PBL was within 10% of the observed. Fig. 6.20b shows that horizontal advection of momentum and drag are substantially the same, while

---

2 Qualitatively, extrema in pressure forcing coincide with the fastest changes in the corresponding M_c; see Fig. 6.16c.

total acceleration, vertical advection of momentum, and diffusion (except near the surface) are still small. The virtual potential temperature profile has been adjusted such that the buoyancy forcing nearly equals the sum of the buoyancy and pressure gradient forcings in the previous calculation. Although the net buoyancy forcing is very different, M_m is much the same with or without pressure forcing (Fig. 6.21). This demonstrates that evaporation and subsidence are large and opposing terms, with net buoyancy forcing left as a small difference. Fig. 6.21 also displays a consistent response to the change in net buoyancy forcing: The three levels at which the perturbation pressure is the least negative, 2, 5.5, and 9 km, are the three levels around which the most additional downward mass flux occurs when pressure forcing is turned off in the mesoscale region.

Brown's (1979) slab-symmetric model displays similar results when initialized with a pre-existing tropical easterly wave. His cumulus clouds are modelled as plume-clouds with a constant entrainment rate of 0.2/km, and the model is extrinsically closed by assuming that cloud base mass flux is a fixed proportion of the large scale mass flux at 900 mb. His model shows mesoscale subsidence in the region of active convection in response to evaporative cooling. In fact, Brown's model initially displays net environmental cooling and subsidence at the cloud top level. The difference between Brown's study and our study is that his plume-clouds immediately grow to high levels, whereas destabilization must occur in our model before deep clouds appear. The result is that Brown finds mesoscale regions of saturation 50-90 min after initialization, rather than the unrealistically long 8 hr in our model. This difference in initial cloud height is probably due to two factors.

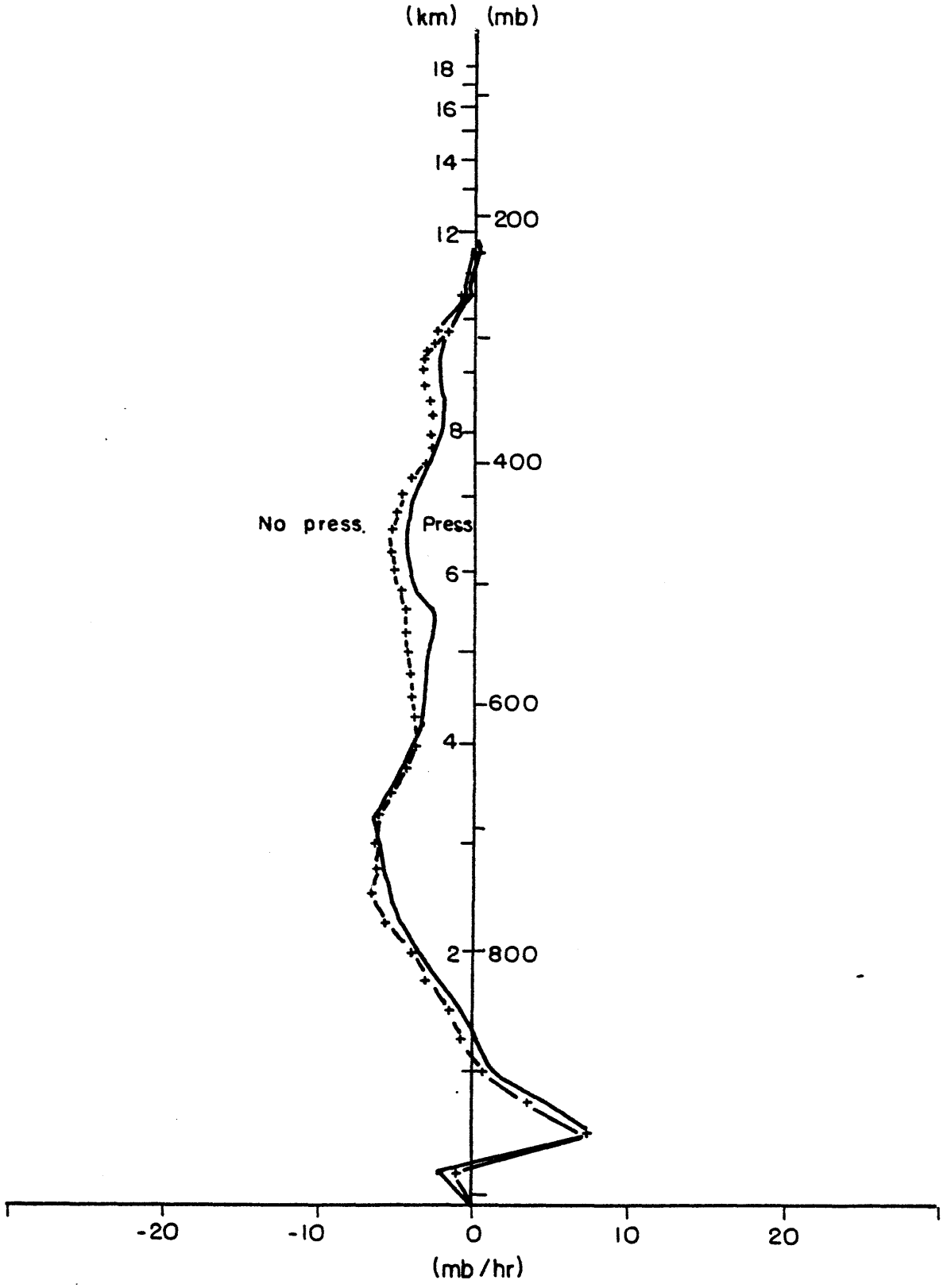


Fig. 6.21 Vertical mass flux in the mesoscale region, averaged over 6-9 hr for Case LN1.M20, with and without vertical perturbation pressure gradient in the mesoscale region.

The less important is that the particular soundings used to initialize the models differ. the more important is that Brown can specify a small fractional entrainment rate, while our entrainment is predicted. As summarized in Chapter 4, Randall and Huffman (1982) show that our model's entrainment has a relatively weak dependence on radius.

We now move on to examine the heating and drying associated with individual subensembles and regions to see how including mesoscale structure modifies these processes. As a function of subensemble radius, the $P_{\psi i}$'s in Fig. 6.22 display the same character as did those for Case LN1.NOM: Two "shallow" subensembles primarily transport moisture upwards, and three "deep" subensembles primarily heat and dry. Although the 0.78 km subensemble displays some minor effects through mid-levels in both budgets and the mass fluxes (Fig. 6.17), it is still true that there is a minimum in activity for clouds topping at mid-levels. In both Cases the deep clouds show a shift in the profiles upwards as radius increases, but the large variations in the values at the 3.5 and 5 km levels shown by LN1.NOM are reduced in LN1.M20. Also, the cooling and moistening at the tops of the deep LN1.NOM clouds are reduced in LN1.M20. In both cases the contributions by the (outer) environment are small, but mesoscale contributions are substantial, when allowed; as with the mass fluxes, they are as much as a third of the observed apparent source terms.

It is useful to further decompose the $P_{\psi i}$'s into their constituent processes to assess the importance of each (displayed in Fig. 6.23). In turn, they are net condensation (Fig. 6.23a), vertical eddy flux convergence of heat (Fig. 6.23b) and moisture (Fig. 6.23c), and vertical turbulent flux convergence of heat (Fig. 6.23d) and moisture

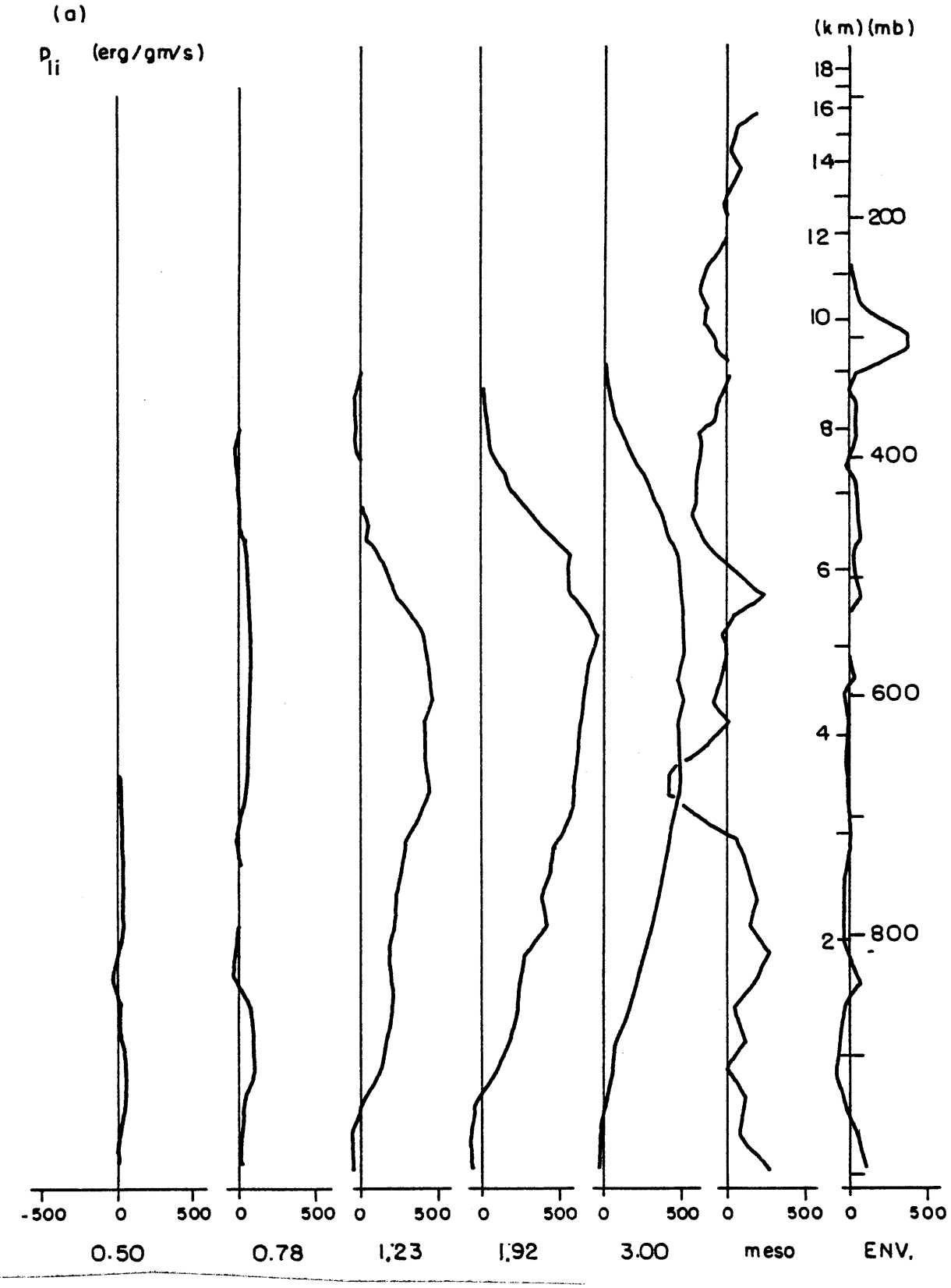


Fig. 6.22 As in Fig. 6.10 for Case LN1.M20.

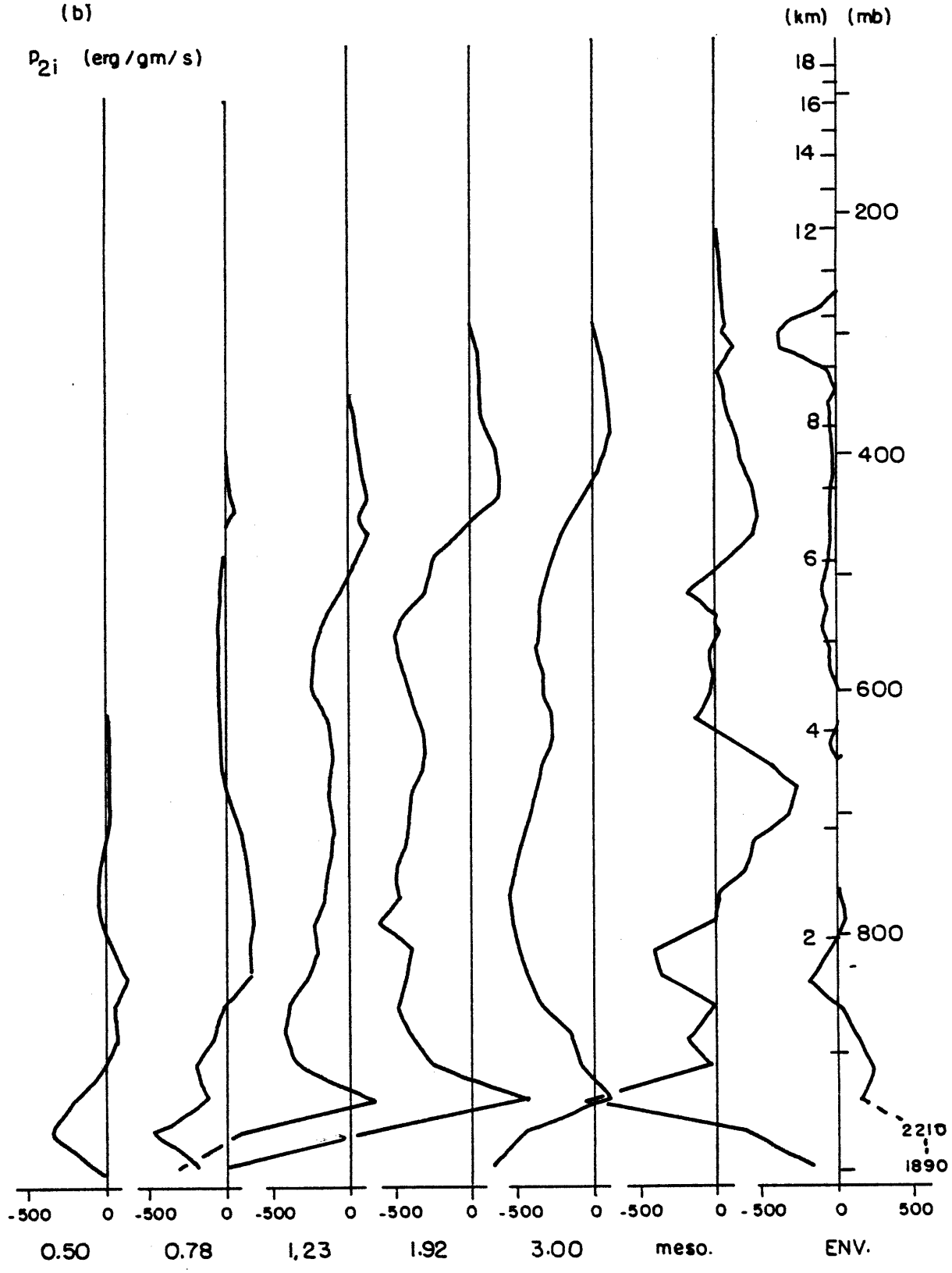


Fig. 6.22 continued.

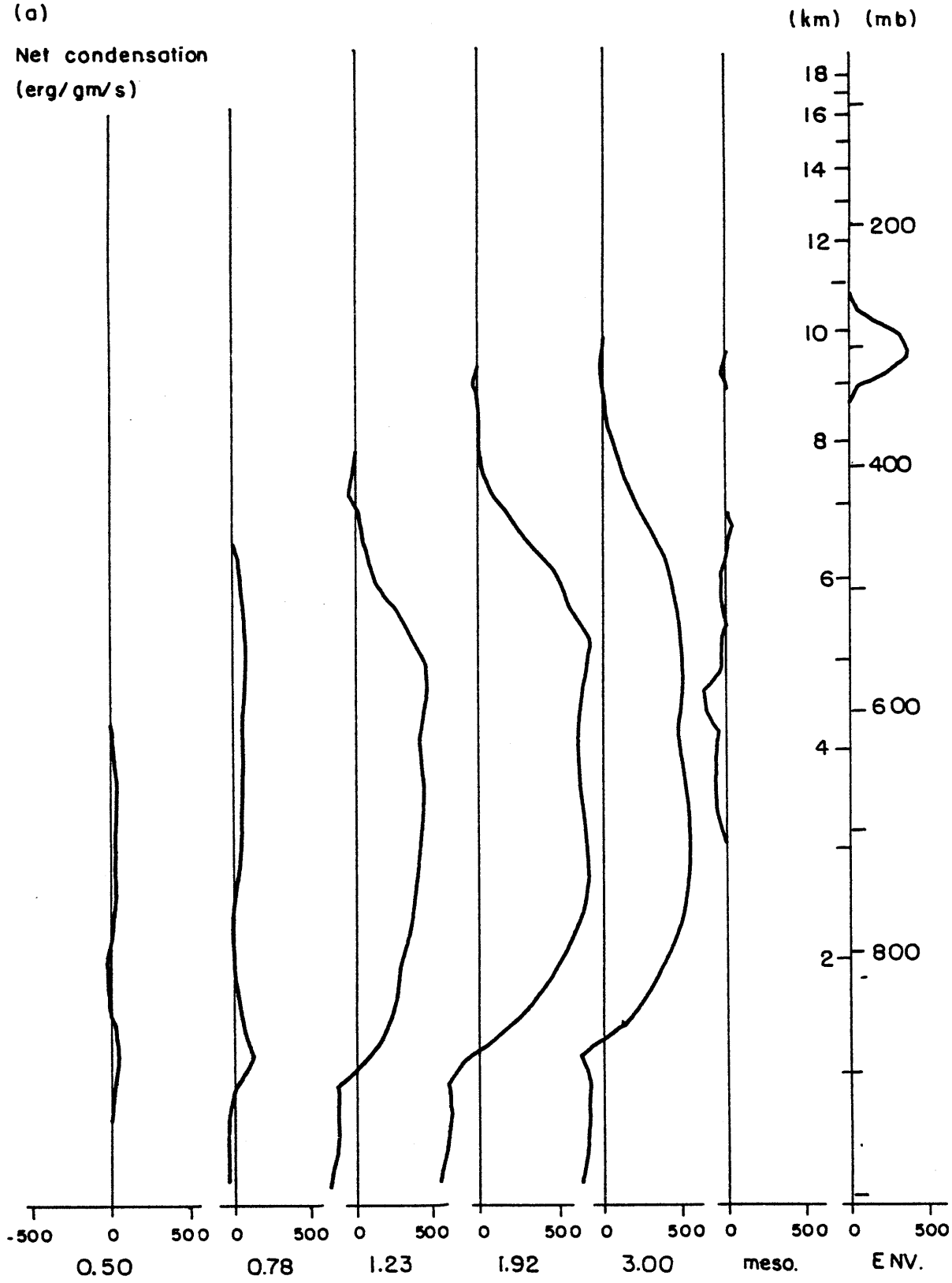


Fig. 6.23 Subensemble and region contributions to the heat and moisture budgets over 6-9 hr for Case LN1.M20 for various processes; (a) net condensation, (b) vertical eddy heat flux convergence,

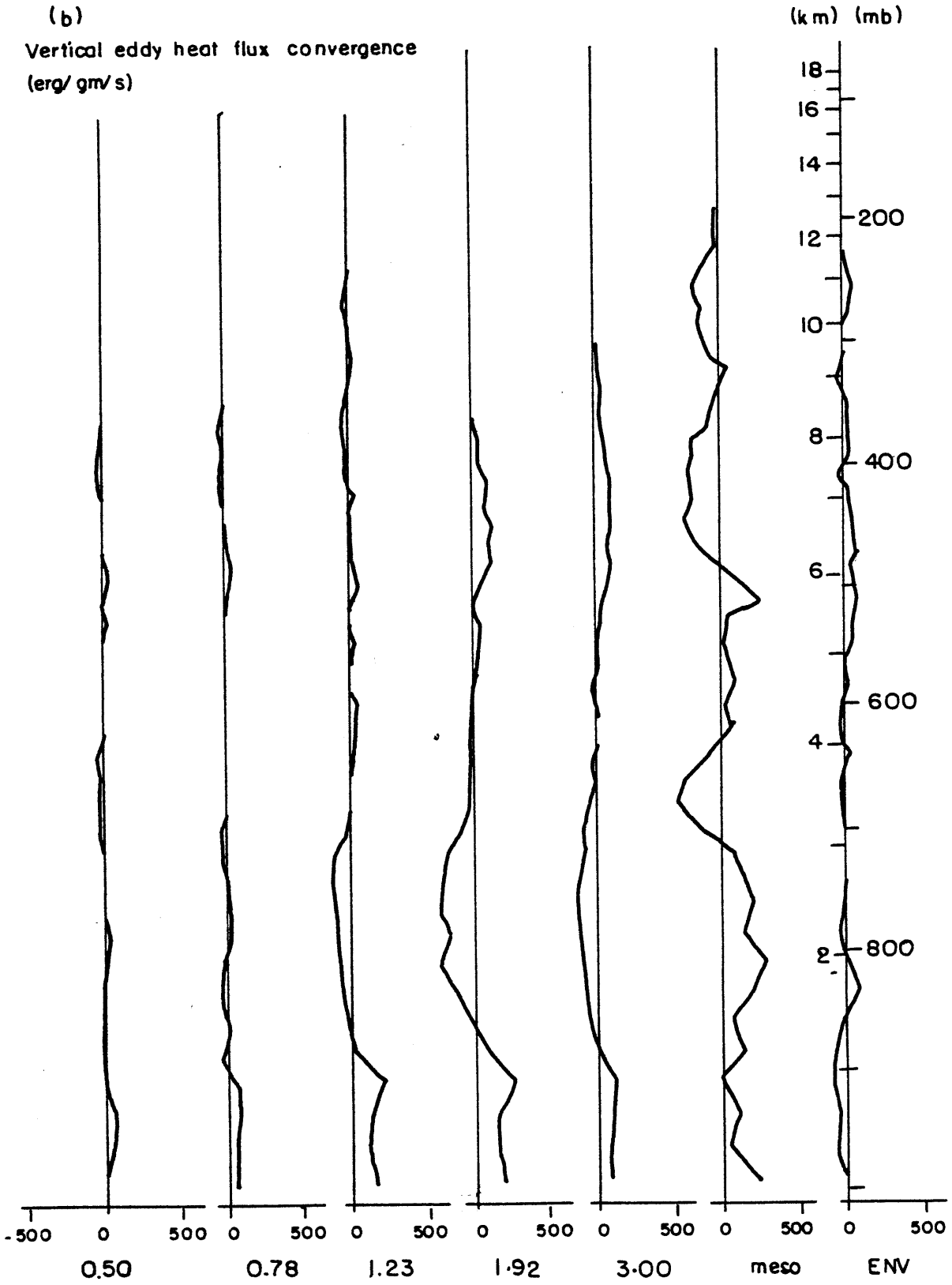


Fig. 6.23 continued.
(c) vertical eddy vapor flux convergence, (d) vertical turbulent heat flux convergence, (e) vertical turbulent vapor flux convergence (see Appendix E for formulae).

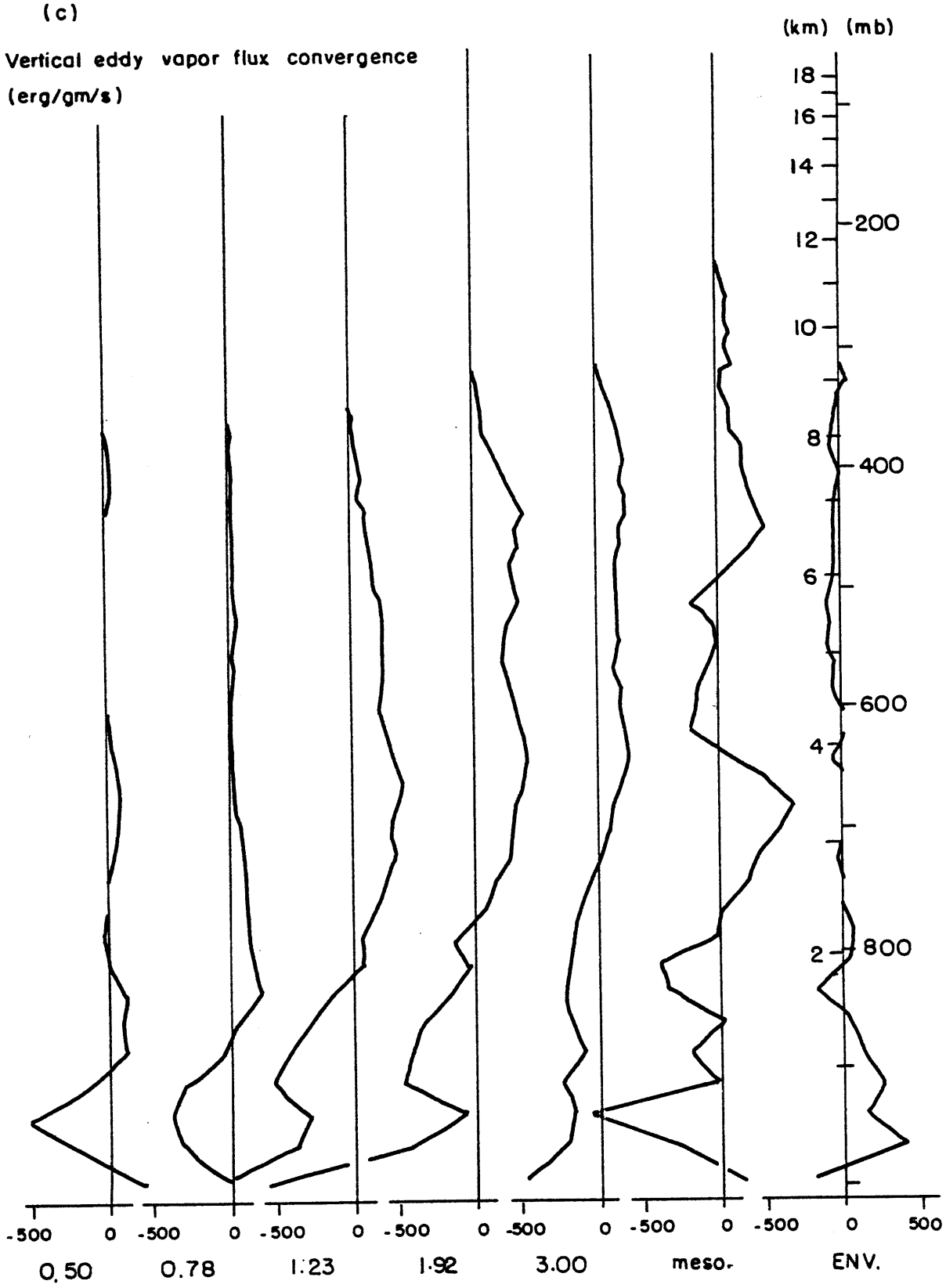


Fig. 6.23 continued.

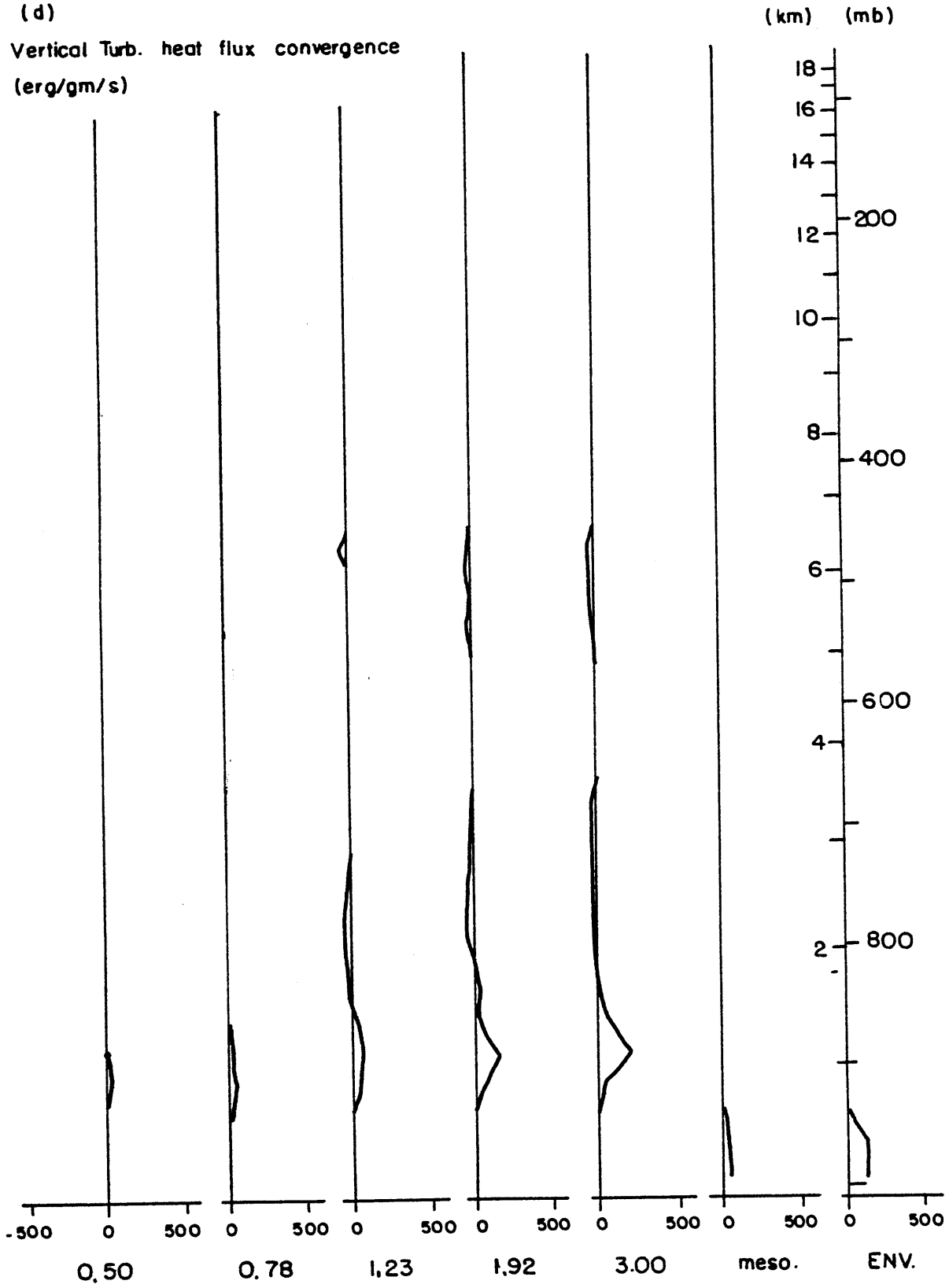


Fig. 6.23 continued.

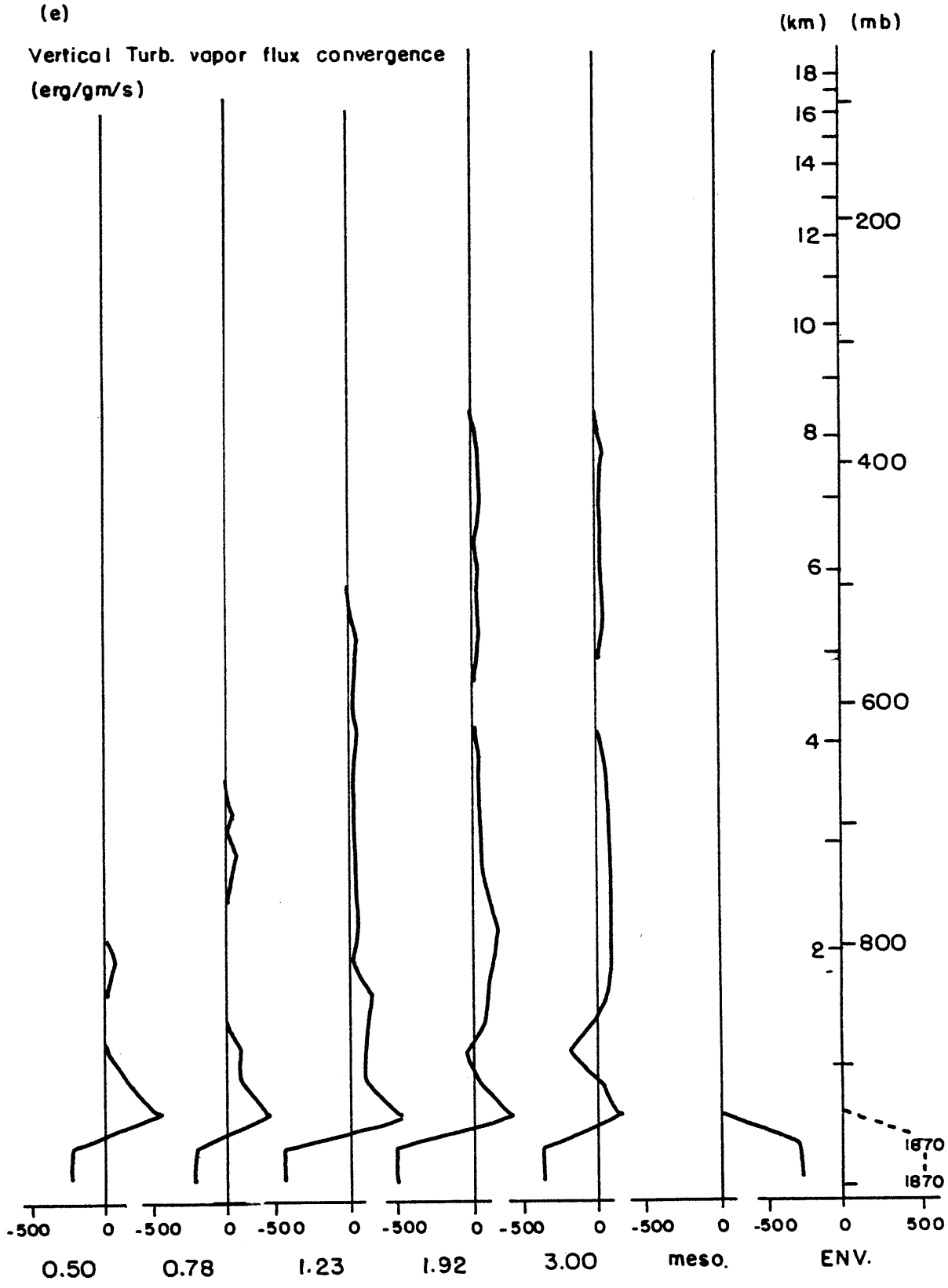


Fig. 6.23 continued.

(Fig. 6.23e).

Net condensation[3] shows a relatively smooth variation with height, with rain evaporation dominating in the nominal PBL, a mixture of cloud and rain evaporation dominating around 1 km, and net condensation dominating above that. The sharp variation in net condensation at cloud top which we see in the one-cloud model (Fig. 4.5b) is replaced by a much more gradual decline with height. Evaporation in the mesoscale region (3-6 km) is due to the liquid detrained while the region was saturated at that level (recall Fig. 6.12). Condensation in the outer environment over 9-10 km is the result of upward mass fluxes in that region.

The vertical eddy flux convergence of heat is smaller than the condensation, as various researchers have pointed out (e.g., Anthes, 1977), but it is not negligible. The general pattern is to cool the lower cloud and warm the upper cloud and the subcloud - cloud base layer. The vertical eddy flux convergence of moisture is not nearly as innocuous. In all cases the subcloud - cloud base layer is dried and the bulk of the cloud is moistened, eventually overwhelming condensation at the cloud top. Our analysis shows that vertical eddy flux convergences of heat and moisture contribute the great bulk of the mesoscale budget terms, and they tend to be anticorrelated. One likely means for achieving this result is recurrent vertical variation in vertical velocity while the mesoscale is moister/cooler or drier/warmer than the outer environment.

---

3 Recall that net condensation = (condensation) - (evaporation) - (latent heat of liquid detrained into subsaturated air) + (latent heat of liquid entrained if the region is subsaturated) ; see Appendix E.

The vertical turbulent flux convergences are small, except for moisture below 1 km. In the lowest two layers we see the removal of moisture to form the nascent clouds in the subensembles and the surface flux moistening in the outer two regions. The moistening just above that layer is due to the formation of the nascent cloud by saturating the perturbation region. Above 1 km heat and moisture turbulent flux convergences are anticorrelated; a thin layer of warming and drying occurs just above 1 km, while cooling and moistening are seen through the remainder of the cloud (when present).

We summarize this Section by noting that the qualitative behavior of the model with mesoscale structure follows that of the model without mesoscale structure as described in the last Section; initially anemic cloud growth becomes stronger with time due to large scale destabilization. Eventually, some new environment is created in which deep clouds grow. On the other hand, the configuration with mesoscale structure displays several additional processes. First, "mutual protection" occurs. The moisture detrained by one generation of clouds provides a local environment (the mesoscale region) which is moister than the large scale environment. Such moistening "protects" the next generation from entraining dry air. The result is deeper convection with less moistening in the domain. A second result of mesoscale structure is modification by mesoscale transports. The mesoscale contributions to the heat, moisture, and mass budgets at some levels are significant fractions of the contributions by all cumulus clouds. The bulk of the mesoscale region's heat and moisture terms seem to occur when the region is warmer/dryer or cooler/moister than the outer environment. Over the convective layer the mesoscale mass flux nearly compensates the "extra"

mass flux in the cloud ensemble, resulting in a small outer environment mass flux. On the other hand, there is also downward mass flux at the top of the convective layer, suppressing anvil formation in the mesoscale region and promoting it in the outer environment. A balance of forces analysis shows that such sinking is required, on the average, to compensate negative buoyancy due to evaporative cooling and the various accelerations imposed by the cloud ensemble. Although Brown (1979) found a similar effect in the early stages of his model simulation, the persistent downward motion in our model seems excessive.

The results discussed above rely on a particular value for cloud coverage in the mesoscale region, a particular cloud distribution, and a particular starting time. In the next four Sections we test the importance of these choices. Except in the last, we initialize the model from 00Z Day 245.

6.5 Test of varying mesoscale region cloud coverage

We first examine the effects of varying the fractional cloud coverage in the mesoscale region. Two Cases were simulated, 10% coverage (LN1.M10) and 30% coverage (LN1.M30). As the Case labels indicate, the LN1 cloud distribution was used. The respective heat and moisture budgets are displayed in Figs. 6.24 and 6.25. Again, we see a great deal of similarity. In the bulk of the convective layer the main difference is better agreement in both budgets around the 3 km level over 3-6 hr for M30 than for M10. In fact, there is a small, but systematic improvement at that level and time as one moves to a larger fractional cloud coverage (that is, Cases NOM, M10, M20, M30; Figs. 6.8b, 6.24b, 6.20b, 6.25b). A similar progression results over 3-6 and 6-9 hr

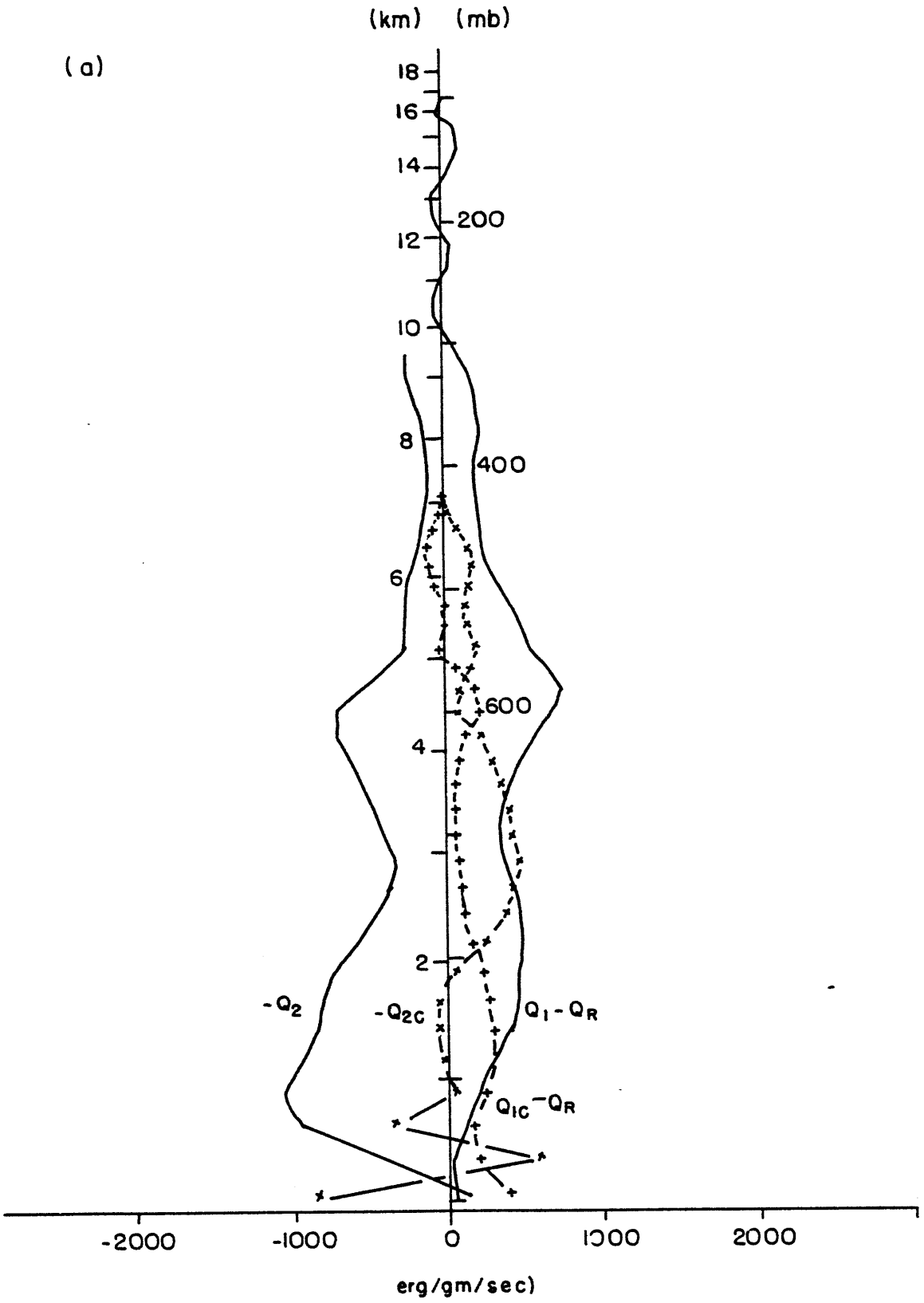


Fig. 6.24 As in Fig. 6.8 for Case LN1.M10.

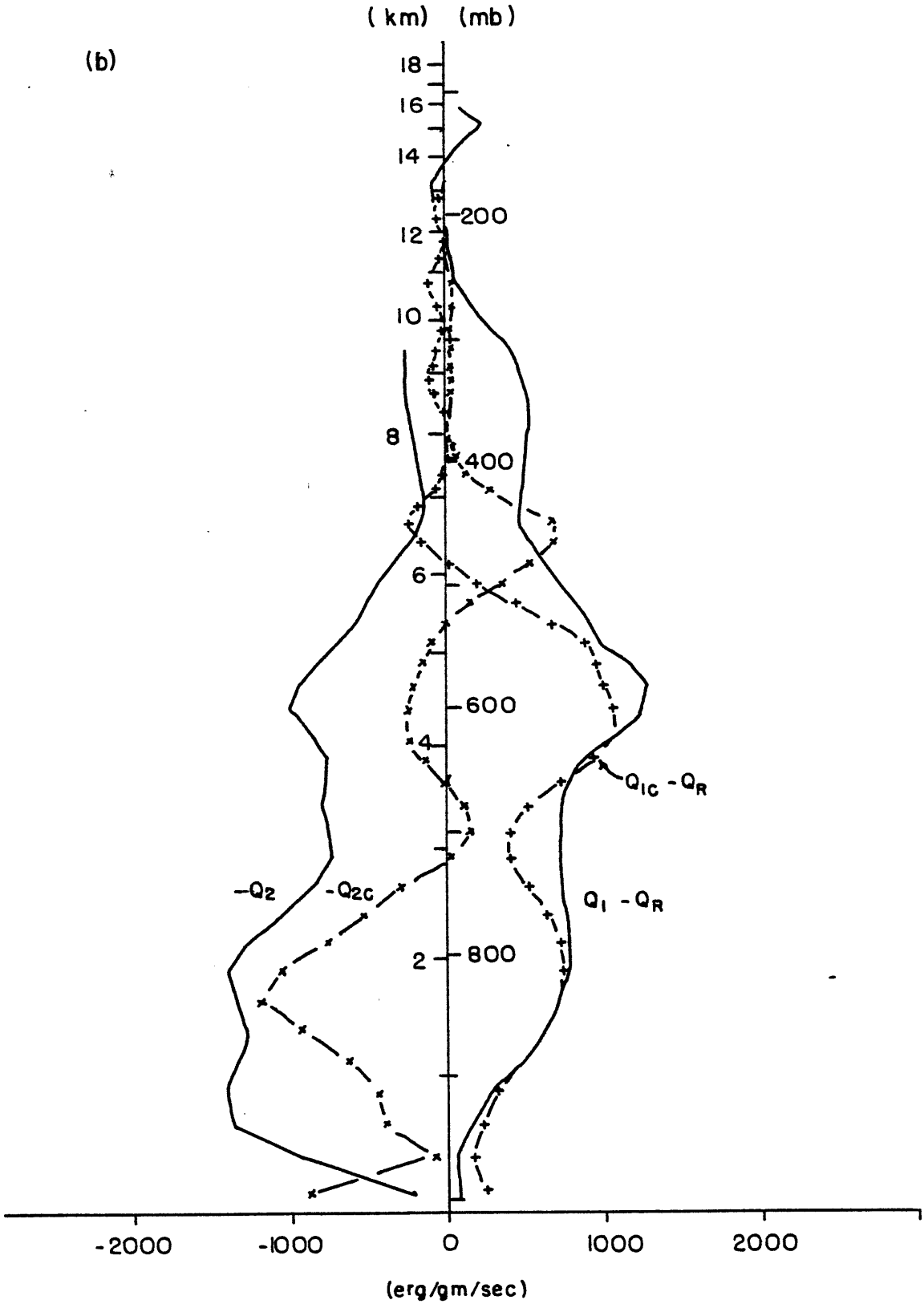


Fig. 6.24 continued.

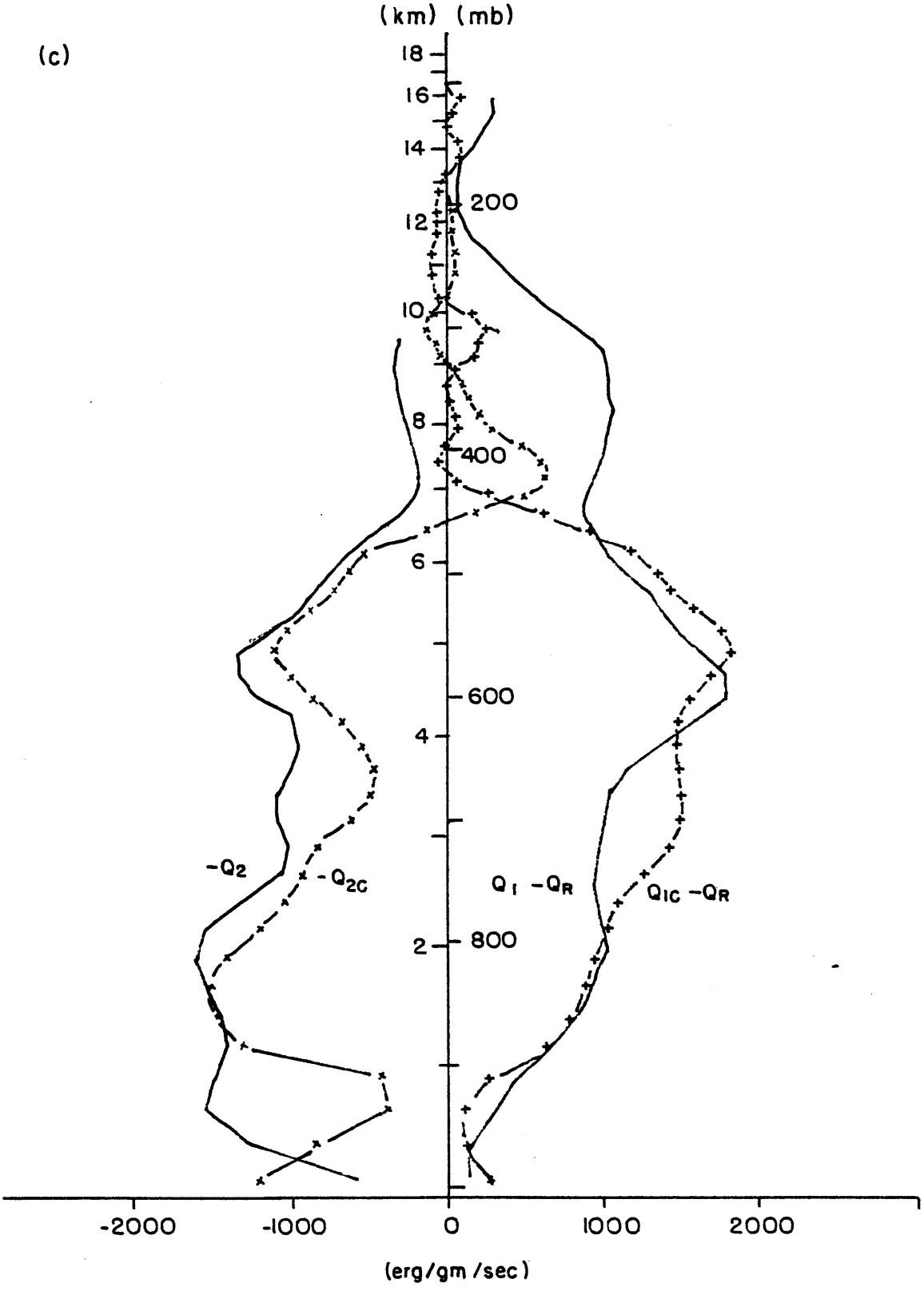


Fig. 6.24 continued.

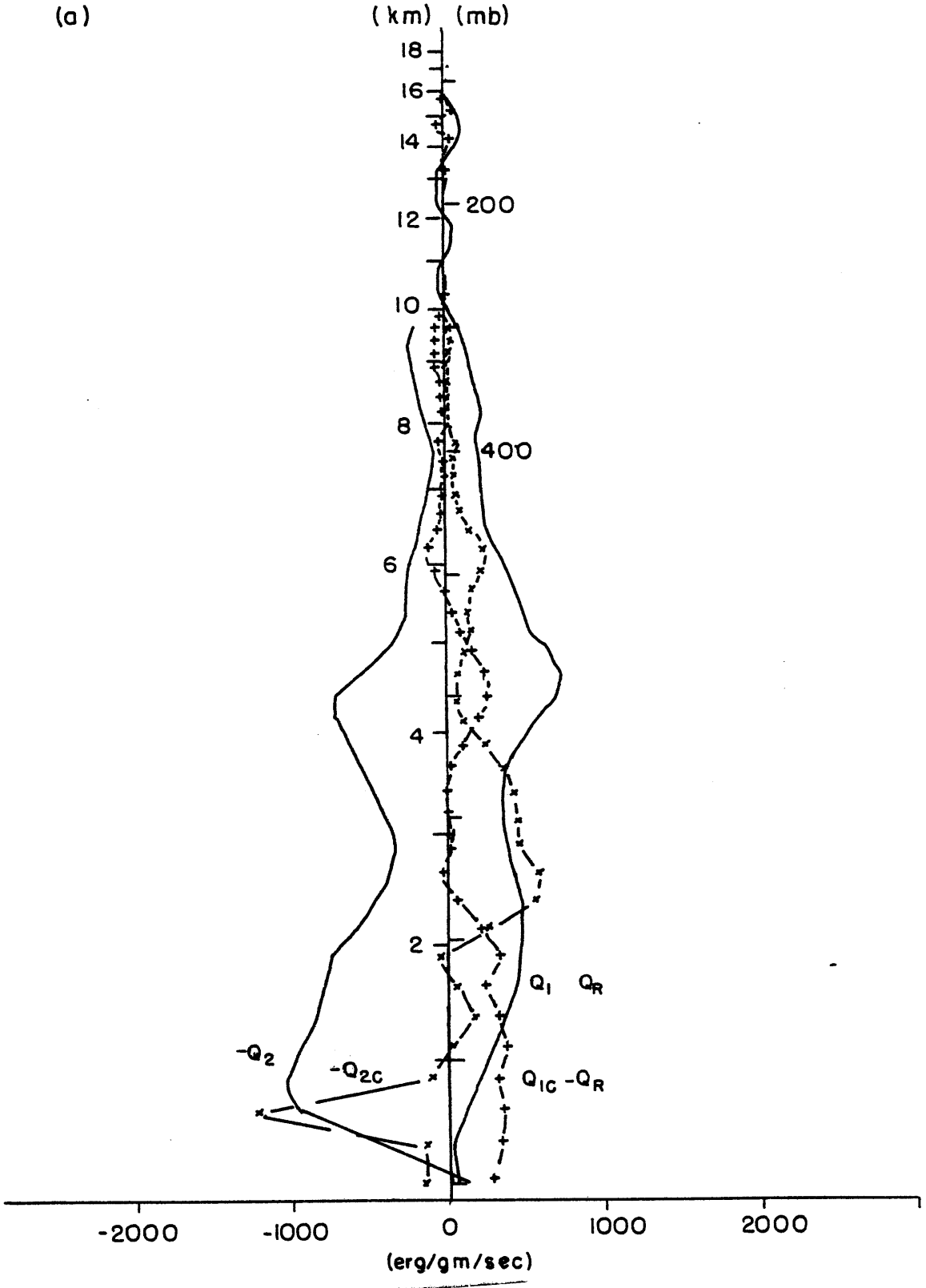


Fig. 6.25 As in Fig. 6.8 for Case LN1.M30.

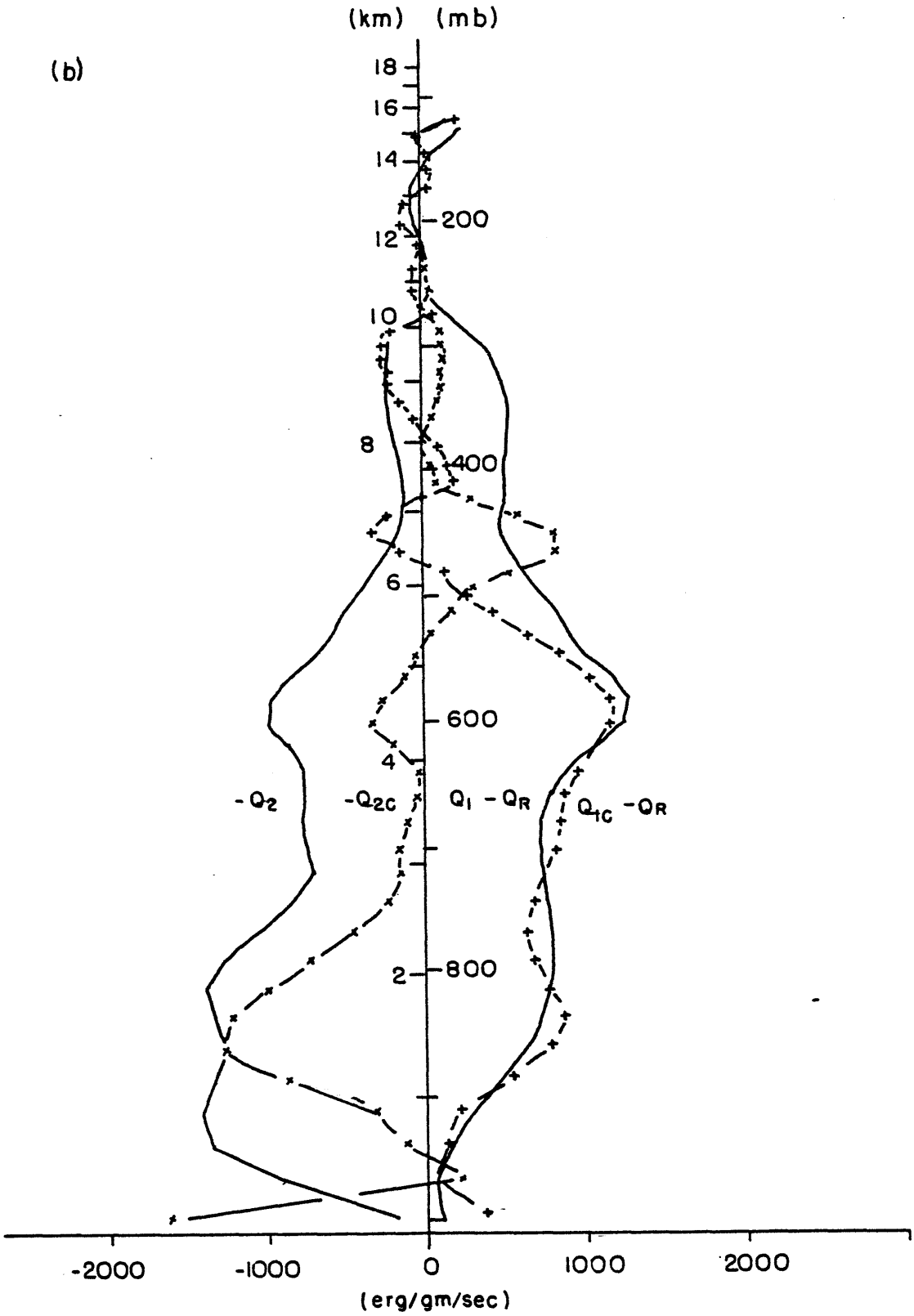


Fig. 6.25 continued.

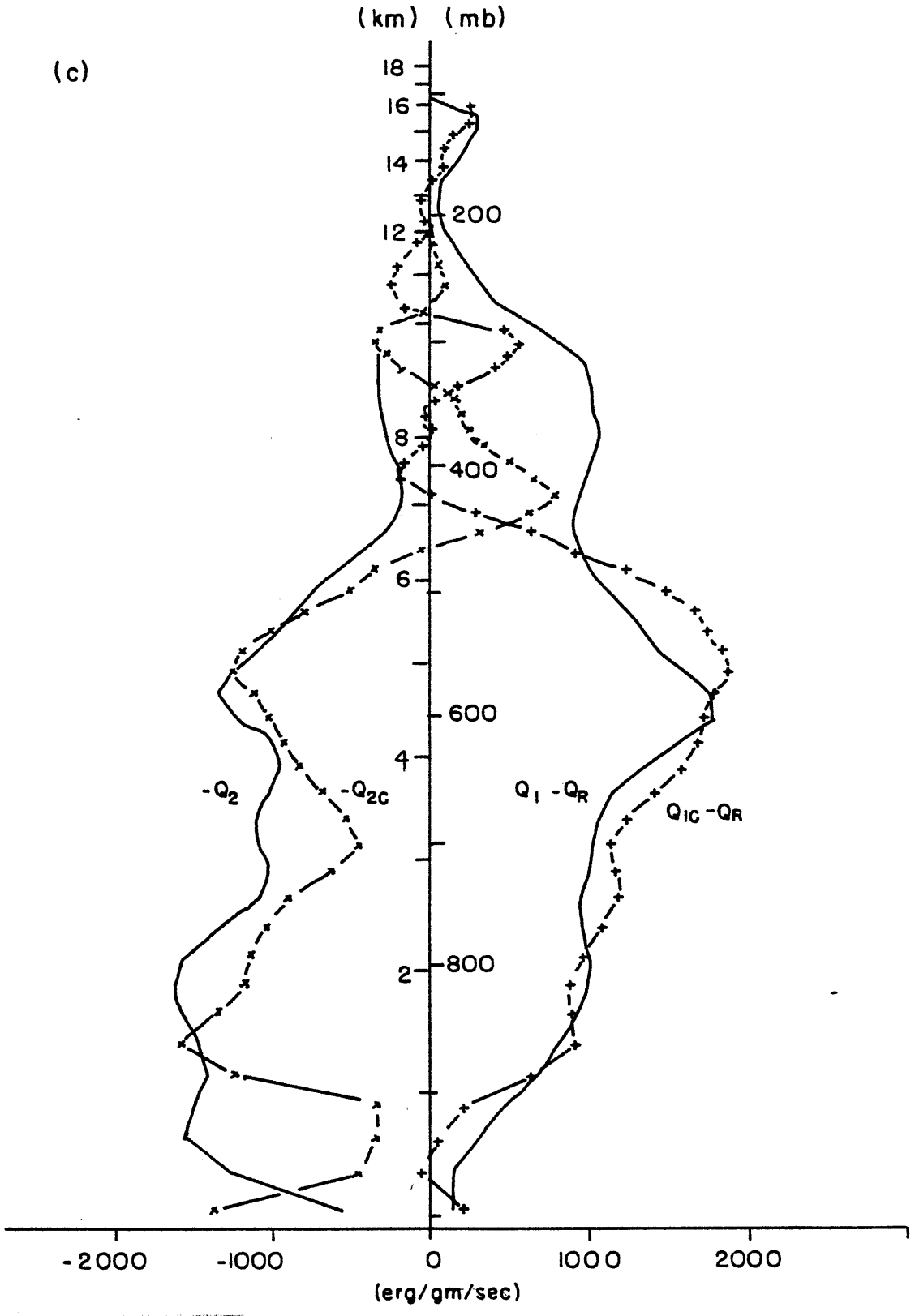


Fig. 6.25 continued.

(Figs. 6.8c, 6.24c, 6.20c, 6.25c) above 9 km, where we saw that net sinking in the mesoscale region forces additional condensation in the outer environment compared to Case NOM. That is, as fractional coverage in the mesoscale increases, M_m becomes more negative. On the other hand, over the 5.5-7.5 km layer during these periods the three Cases with mesoscale structure are much closer to one another than to Case LN1.NOM.

Improved agreement with the budgets is reflected in an increase in rainfall (Table 6.2), as a rule, so LN1.M30 has more rainfall over 0-3 and 3-6 hr than LN1.M10.

This test indicates that changing fractional cloud coverage in the mesoscale region can cause weak, systematic differences, with large coverage leading to better agreement with the observed budgets. However, either configuration produces relatively good agreement in the last 3 hr.

6.6 Test of varying cloud distribution

We next vary the cloud distribution, while keeping the mesoscale region fractional cloud coverage at 20%. The first distribution is a new lognormal distribution, LN2. As before, there are 5 subensembles whose radii form a geometric progression between 0.50 and 3.00 km; the 99.9 percentile cloud radius is 3.00 km. The difference is that 30% of the clouds are given radius 0.50 km (versus 50% in LN1), giving more clouds to all of the other subensembles (Fig. 6.6). The resulting heat and moisture budgets (Fig. 6.26) are quite similar to the original Case LN1.M20. The largest differences are a general decrease in Q_{1c} and a large decrease in the Q_{2c} peak at 1.5 km over 3-6 hr for LN2.M20. The

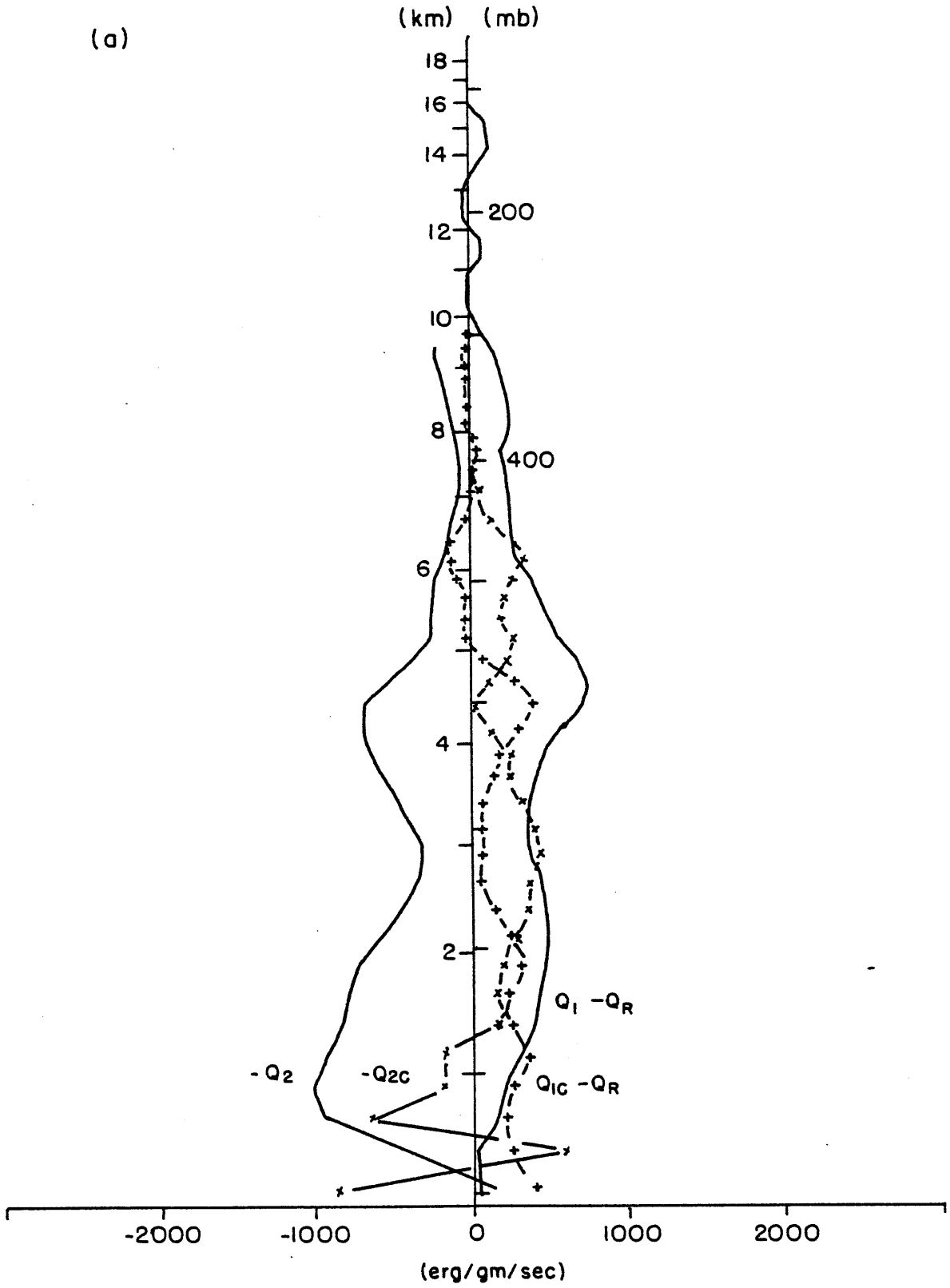


Fig. 6.26 As in Fig. 6.8 for Case LN2.M20.

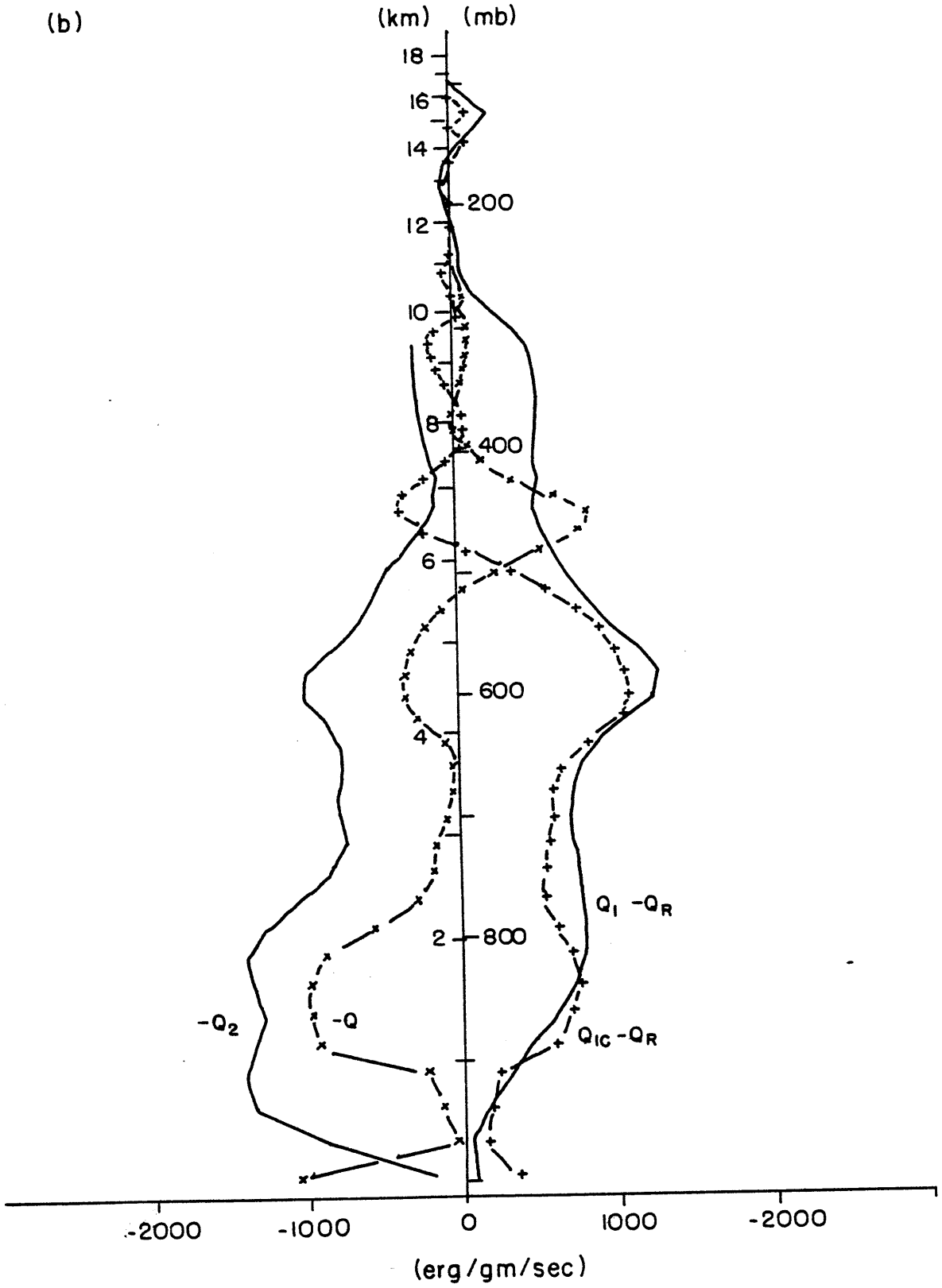


Fig. 6.26 continued.

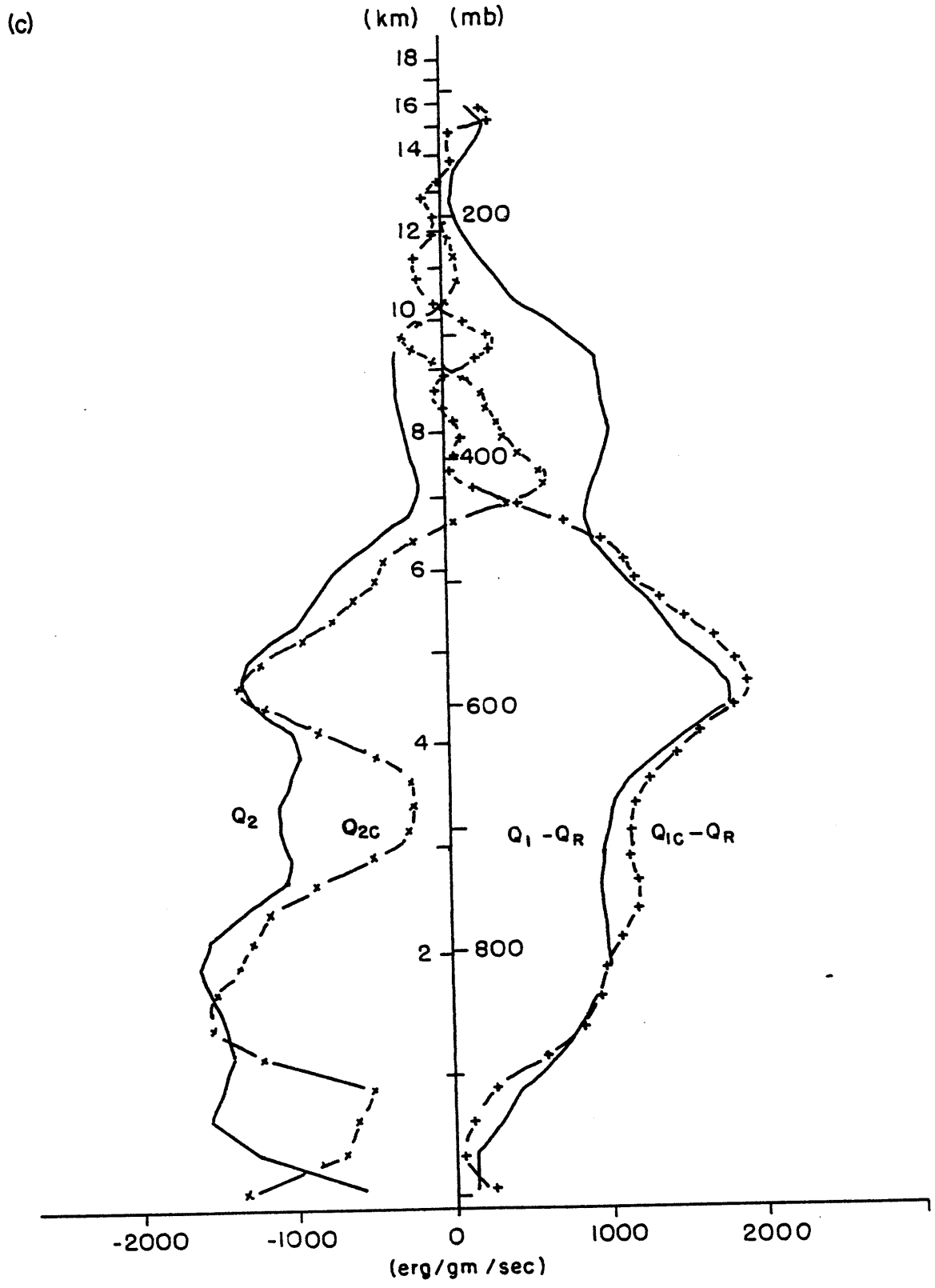


Fig. 6.26 continued.

result, of course, is that quite similar model budgets are generated by the two Cases over 6-9 hr on different soundings.

The second distribution to be tested is a "constant area" distribution, AIC. Specifications are as above, but each subensemble covers the same total area (Fig. 6.6). This yields relatively more small and large clouds than LN1. As in the previous Case, the model heat and moisture budgets (Fig. 6.27) are similar to those for LN1.M20. The only truly systematic difference is a small increase in drying and heating in the 1-3 km layer over 0-3 hr for AIC.M20. It is of interest to see what contributions each subensemble makes to the budgets (Fig. 6.28), given the large differences between the AIC and LN1 distributions, but the similarity of the results. Although there is some qualitative similarity between corresponding profiles in Figs. 6.28 and 6.22, the $P_{\psi i}$'s for the two Cases are not just scaled versions of each other. The 1.22 km subensemble is not only reduced in amplitude, but both P_1 and P_2 change sign around the 2 km level, quite unlike Case LN1.M20. The 1.96 km subensemble P_ψ's are smaller than their LN1.M20 counterparts, except below 2 km, where they nearly match. P_2 for the 3.00 km subensemble is larger, except at 4 km. In general, the AIC.M20 mesoscale region P_ψ's have larger values, with corresponding peaks occurring at different altitudes.

The rainfall (Table 6.2) for AIC.M20 is larger in the first 6 hr, consistent with closer agreement with the observed budgets. The increase apparently comes about because there are relatively more large clouds, which produce more rain.

Once again, we see that a substantial change in the model configuration yields similar budgets once the environment is suitably modified.

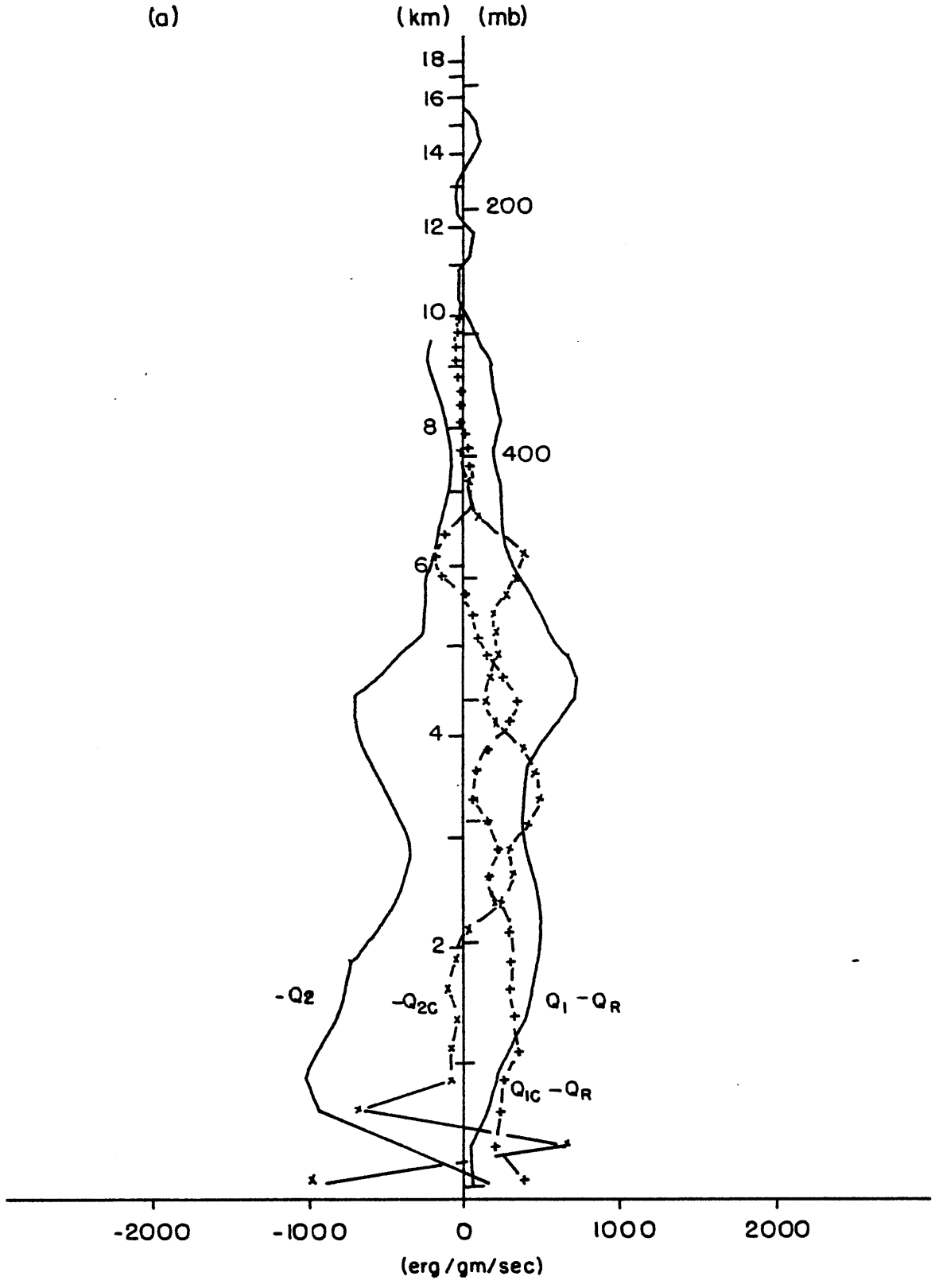


Fig. 6.27 As in Fig. 6.8 for Case AIC.M20.

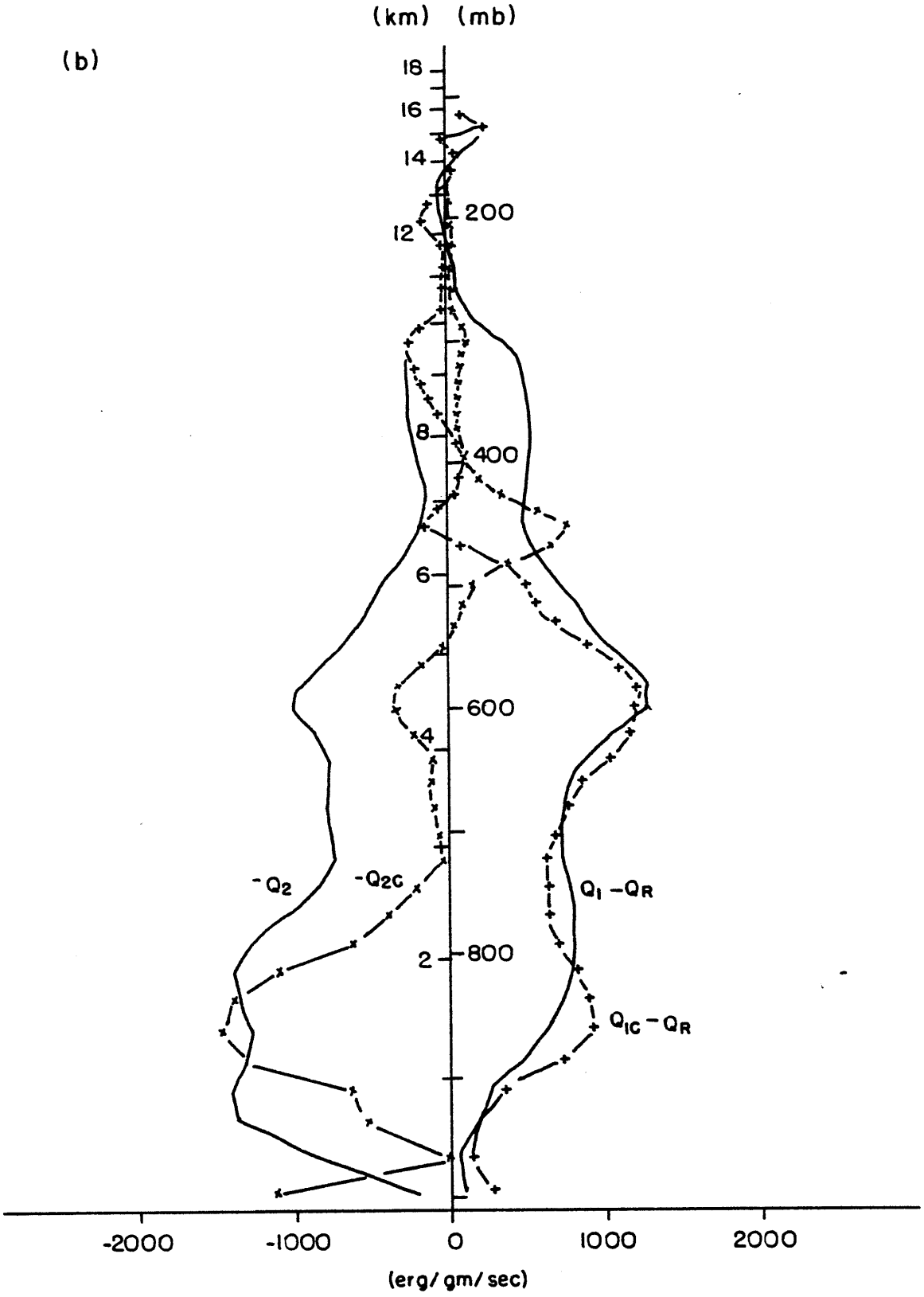


Fig. 6.27 continued.

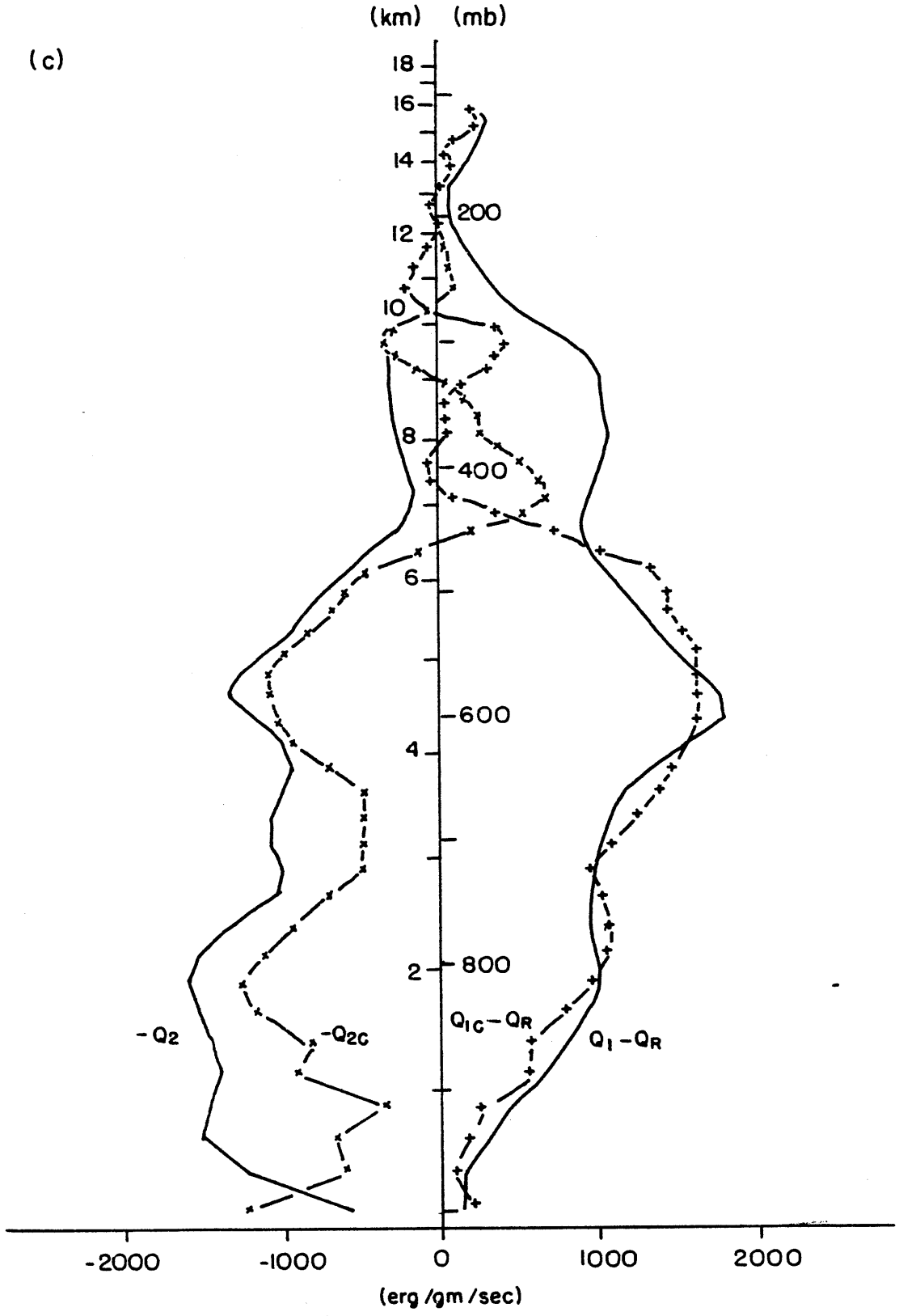


Fig. 6.27 continued.

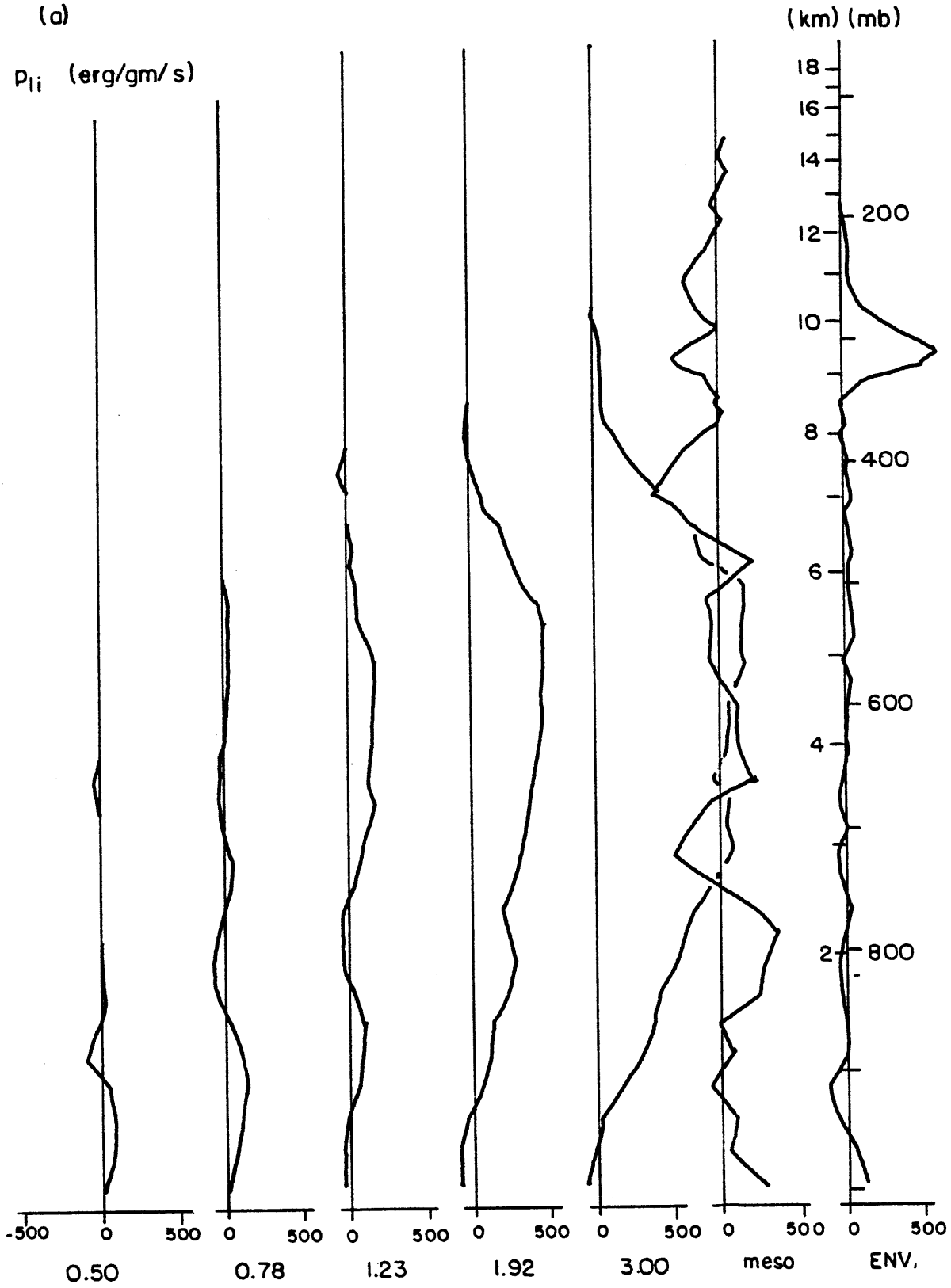


Fig. 6.28 As in Fig. 6.10 for Case AIC.M20.

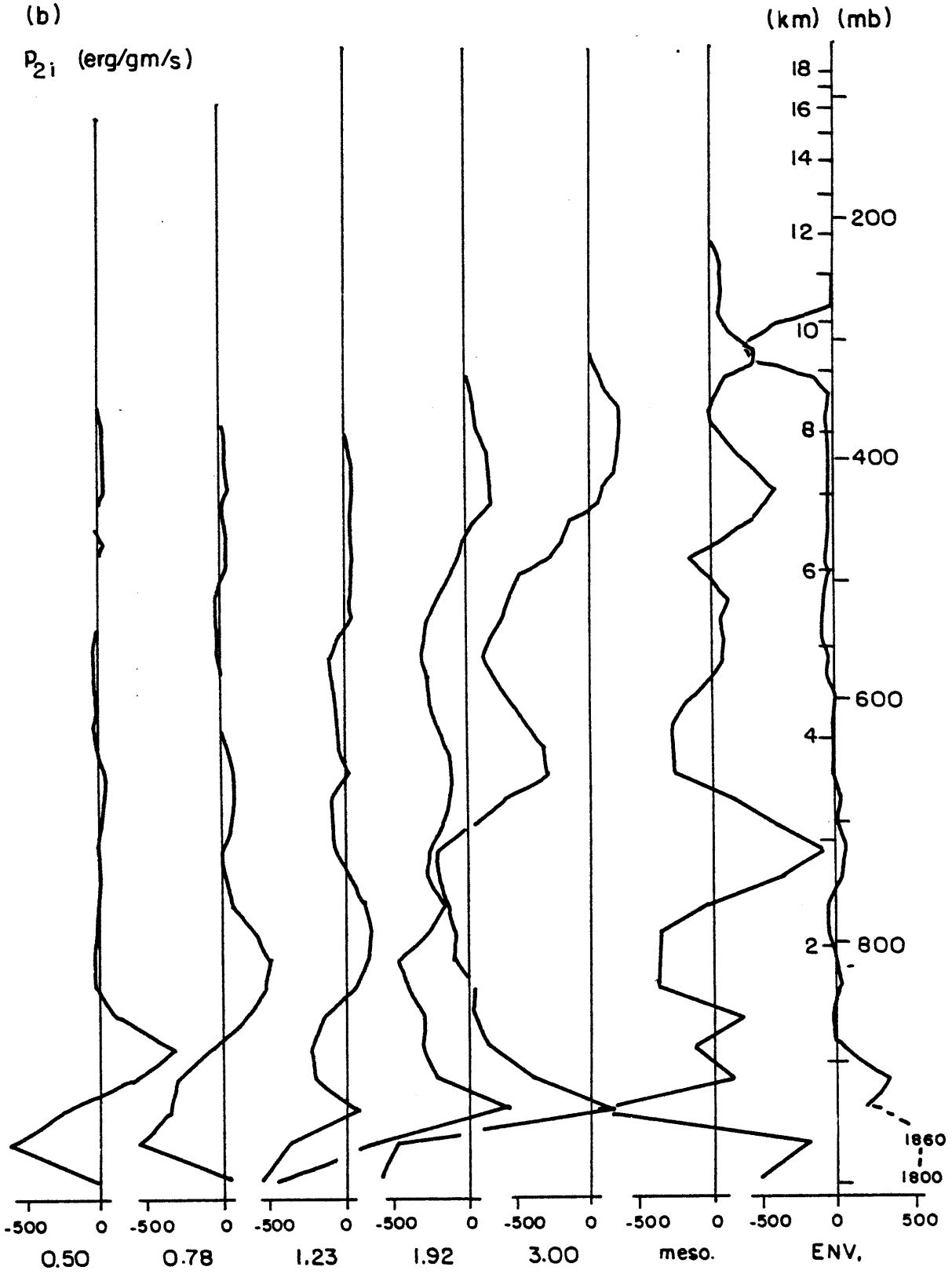


Fig. 6.28 continued.

Considering the LN2.M20 results, it seems that the cloud distribution can change the environmental profiles which are considered "suitable".

6.7 Test of increasing the allowed range of cloud radii

One of the basic assumptions on the cloud distribution is that we can choose a maximum cloud size. Since we have not been able to satisfy the budgets at upper levels, it seems logical to test the effects of choosing a larger maximum cloud size. Most parameters in Case LN3.M20 are as in Case LN1.M20 (20% fractional cloud coverage over the mesoscale region, 50% of the clouds assigned to the 0.50 km subensemble, a geometric progression of radii), except that the 99.9 percentile cloud radius is 5.00 km, rather than 3.00 km (see Fig. 6.6).

When this configuration is run for 9 hr, starting at 00Z Day 245, the simulated heat and moisture budgets (Fig. 6.29) show qualitative agreement with previous Cases. However, we also see that LN3.M20 is closer to the observed budgets than the other Cases. In particular, both budgets are better in LN3 in most of the convective layer over 0-3 hr, in the 5.5-7 km layer over 3-6 hr, and in the 6.5-8 km layer over 6-9 hr, as well as Q_{2c} being better around 1 and 3 km over 3-6 and 6-9 hr. Such improved agreement has two effects: First, of course, the domain-averaged temperature and moisture profiles are closer to the observed profiles. After 9 hr the Case LN3.M20 profiles (Fig. 6.30) are systematically warmer and drier than the corresponding case LN1.M20 profiles (Fig. 6.15a) over the depth of the convective layer. In addition, the mesoscale region is more uniformly moistened above 2 km, comparing Figs. 6.30 and 6.15b.

The second effect of improved budgets is that the model clouds see a

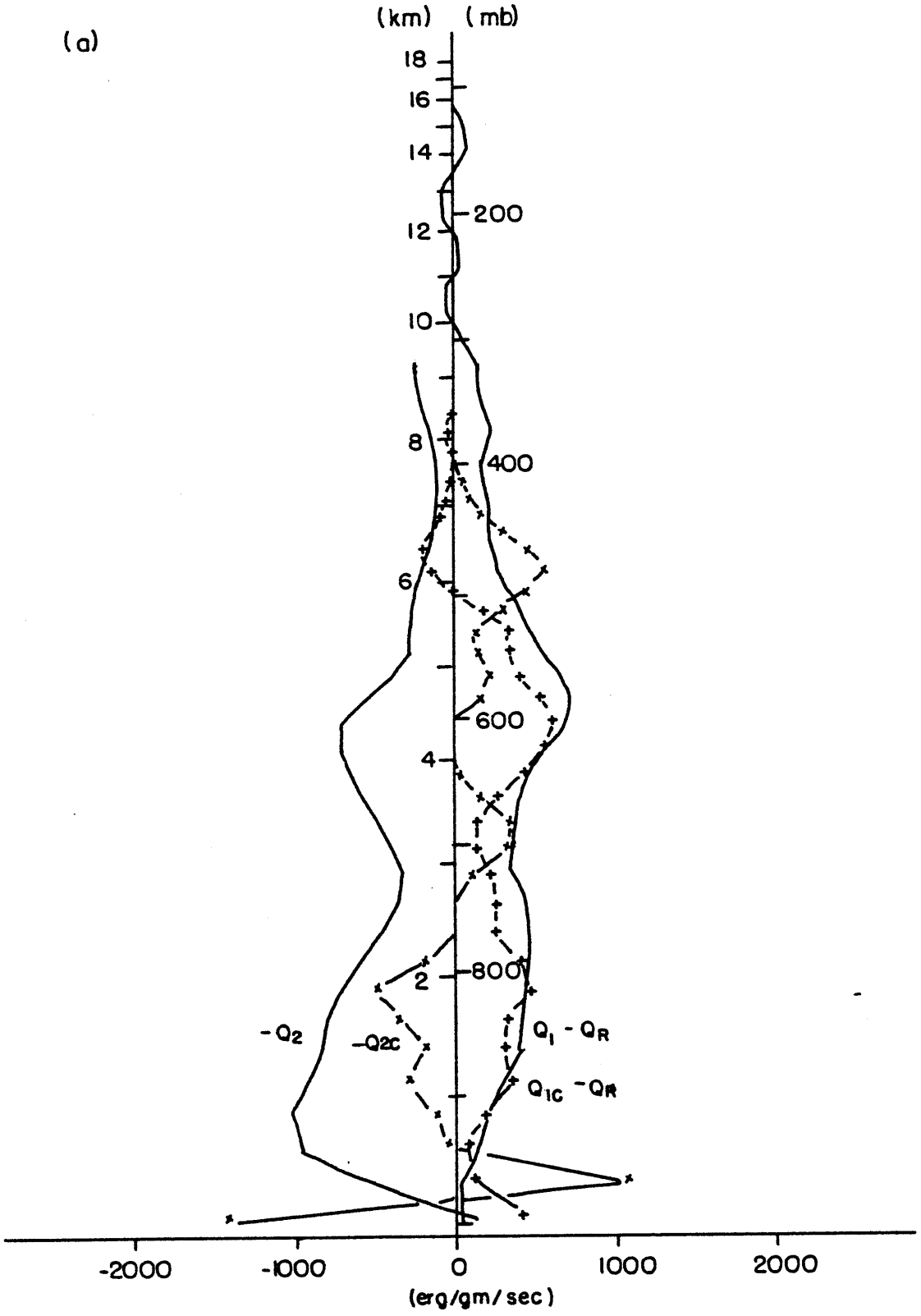


Fig. 6.29 As in Fig. 6.8 for Case LN3.M20.

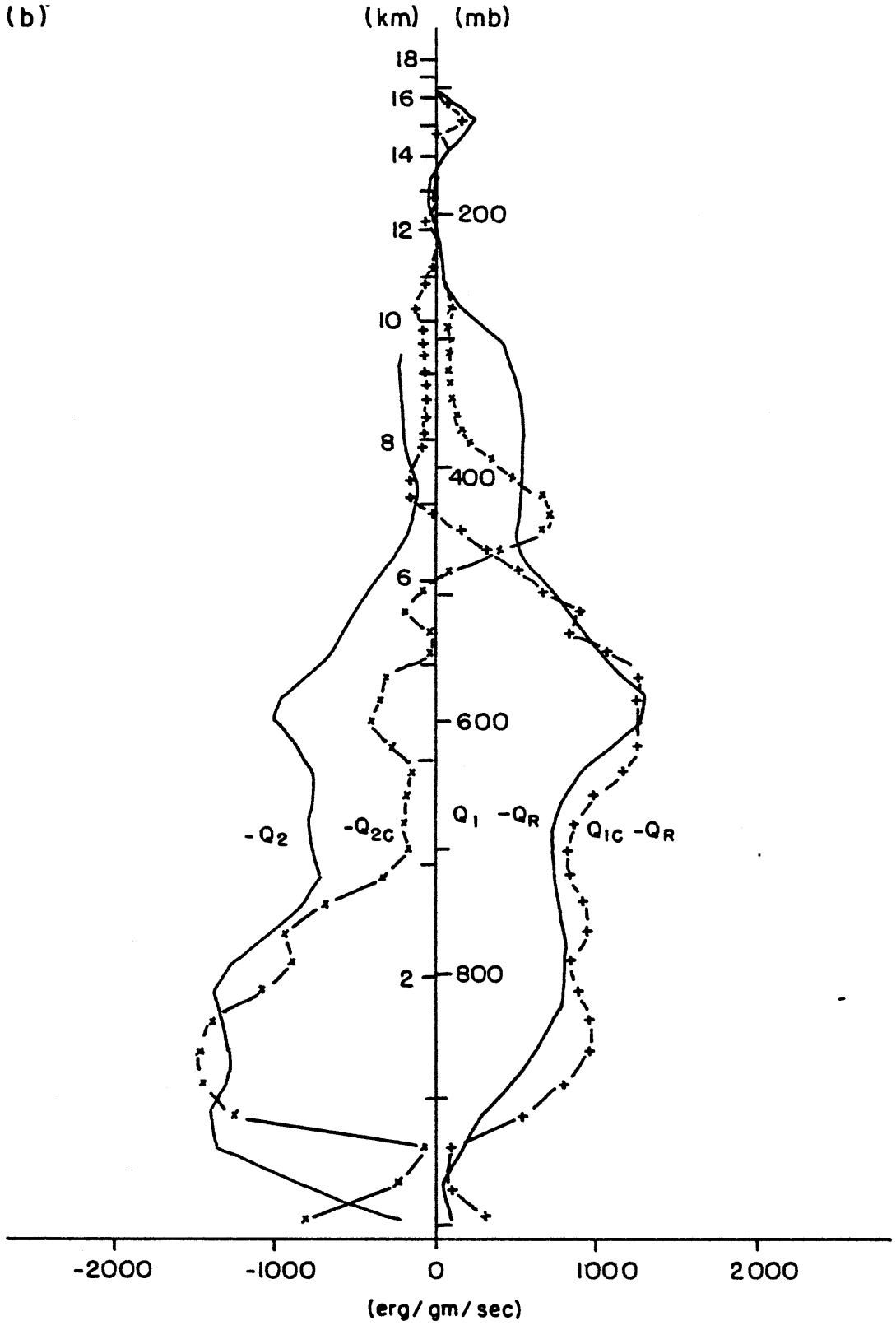


Fig. 6.29 continued.

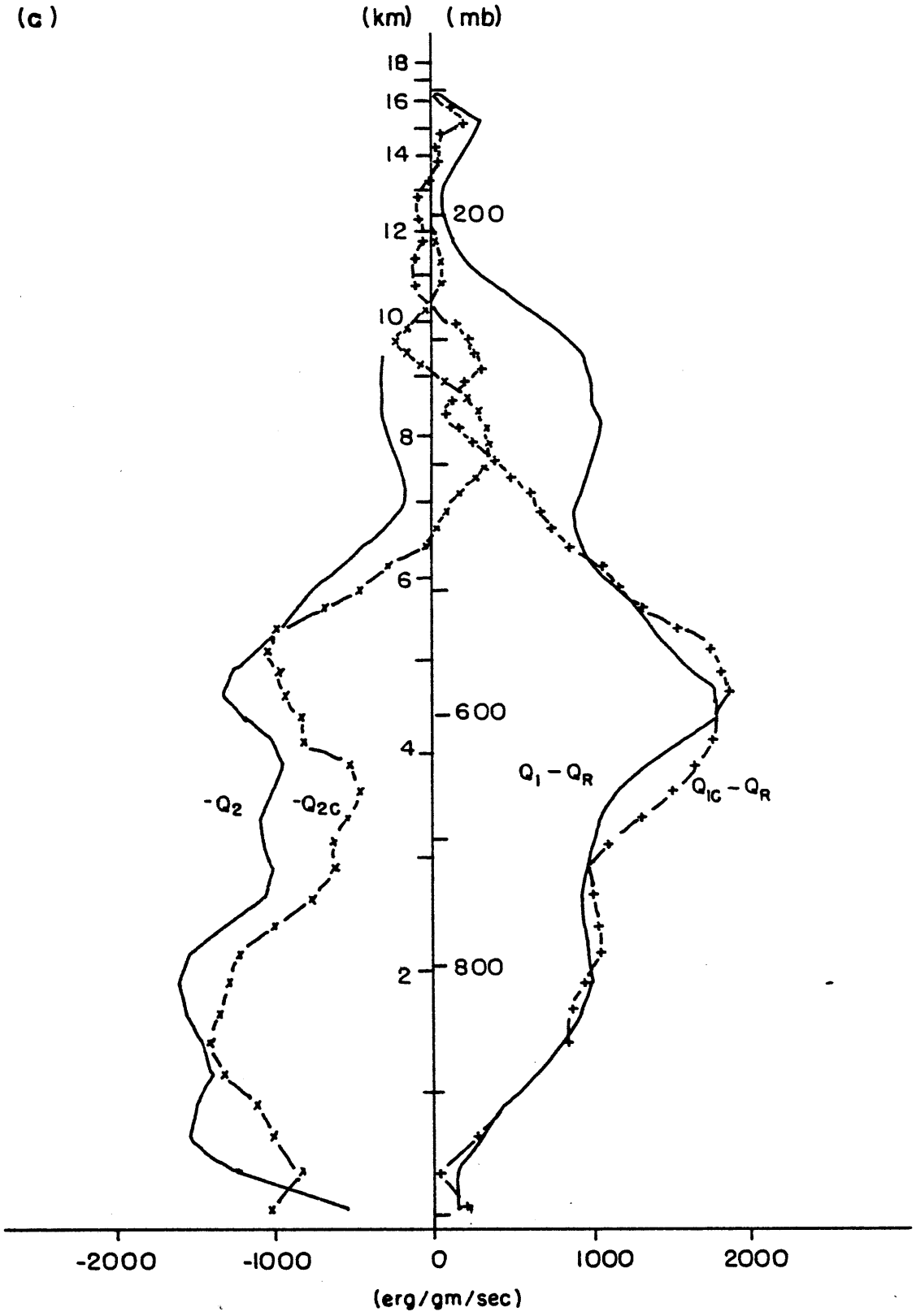


Fig. 6.29 continued.

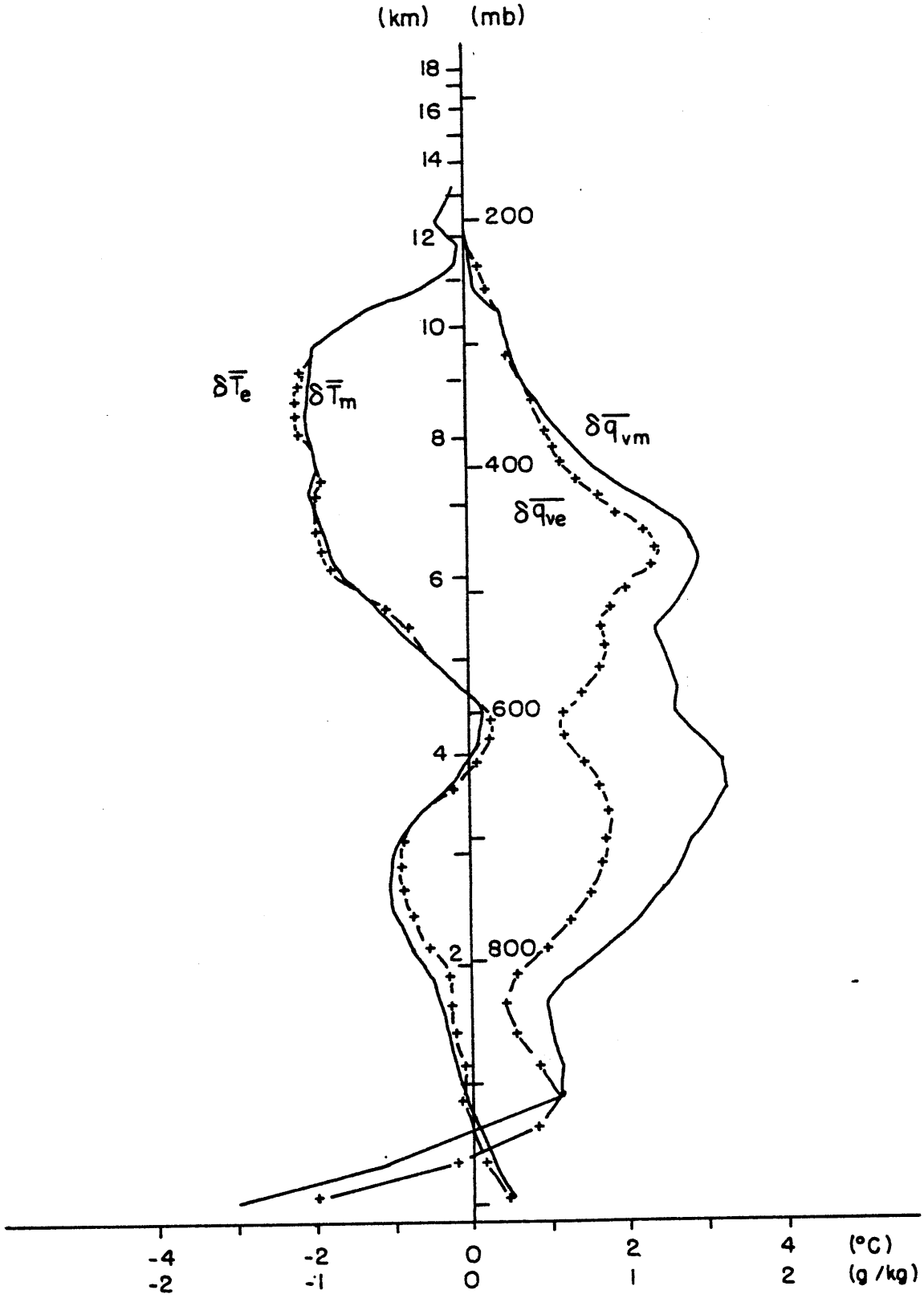


Fig. 6.30 As in Fig. 6.9 for Case LN3.M20, after 9 hr for outer environment-averaged (-+-) and mesoscale region-averaged (——).

more stable environment, so they are less vigorous. This result is best displayed by comparing the $P_{\psi i}$'s for Case LN3.M20 (Fig. 6.31) to the $P_{\psi i}$'s for Case LN1.M20 (Fig. 6.22) over 6-9 hr. The outstanding example of this effect is the 1.58 km subensemble in LN3.M20. In radius, it falls about halfway between the 1.22 and 1.92 km radius subensembles in LN1.M20, yet its transports have quite different vertical profiles than either of the LN1.M20 subensembles. Another example is that the LN1.M20 3.00 km subensemble profiles are much closer to the LN3.M20 5.00 km subensemble profiles than to the LN3.M20 2.92 km subensemble profiles.

The conclusion of this test is that increasing the upper limit of cloud radius improves the agreement between simulated and observed budgets. However, contrary to our expectations, most of the improvement is the result of more realistic convection in the previously active convective layer, rather than a more realistic depth of the convective layer. Rainfall (Table 6.2) is consistent with better simulation of the budgets.

6.8 Test of starting 3 hr earlier

The last sensitivity test we perform is to start the LN1.M20 model configuration at 21Z Day 244 (referred to hereafter as time -3 hr). This test is carried out to see whether the modifications which take place in the first 3 hr change the model behavior at subsequent times, compared to runs started at 00Z Day 245. The 3 hr budgets are displayed in Fig. 6.32. Inspecting the (-3)-0 hr budgets (Fig. 6.32a), we see no particular pattern of agreement between simulation and observation. This result is not too serious, since all budgets are small com-

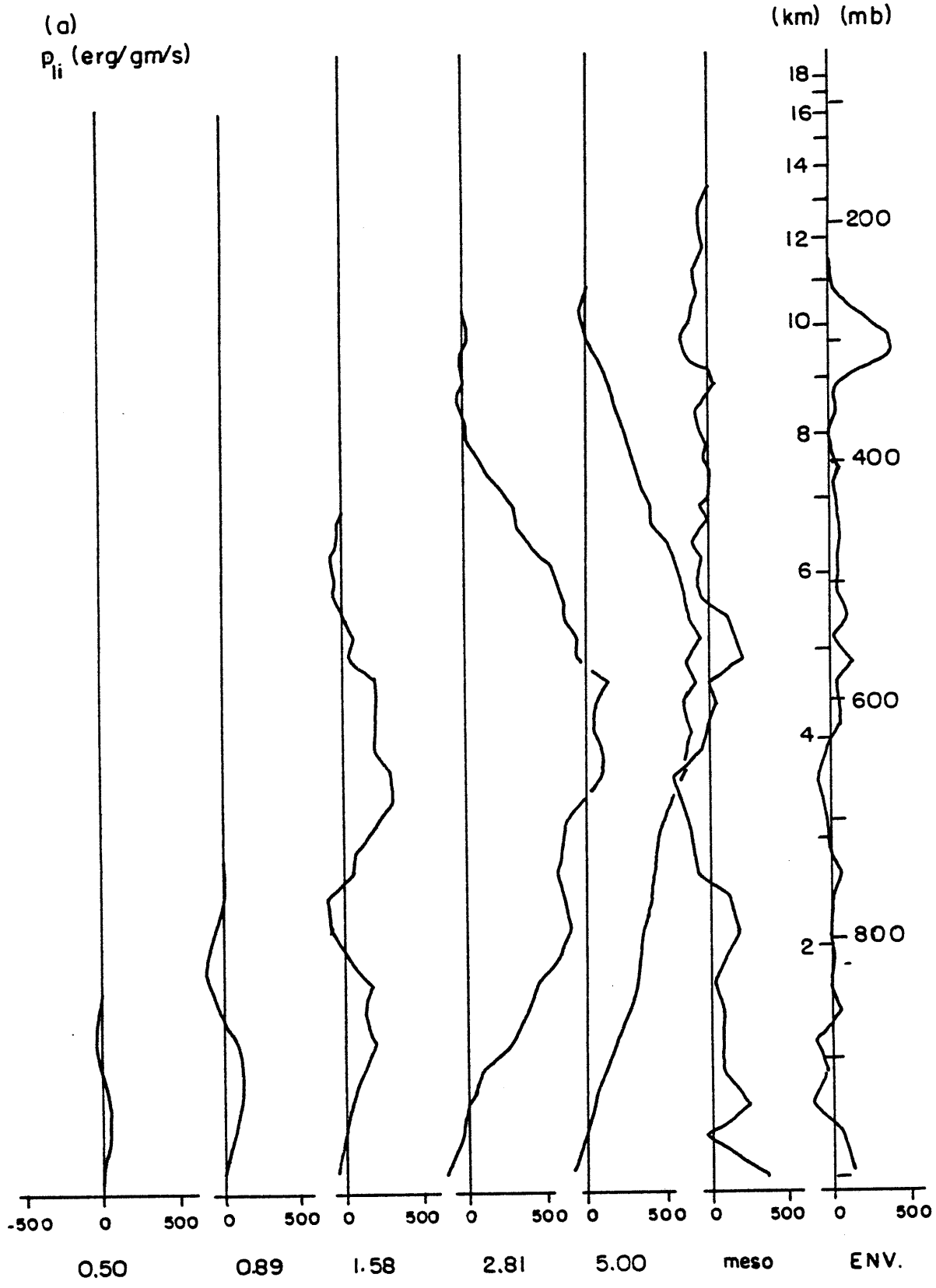


Fig. 6.31 As in Fig. 6.10 for Case LN3.M20.

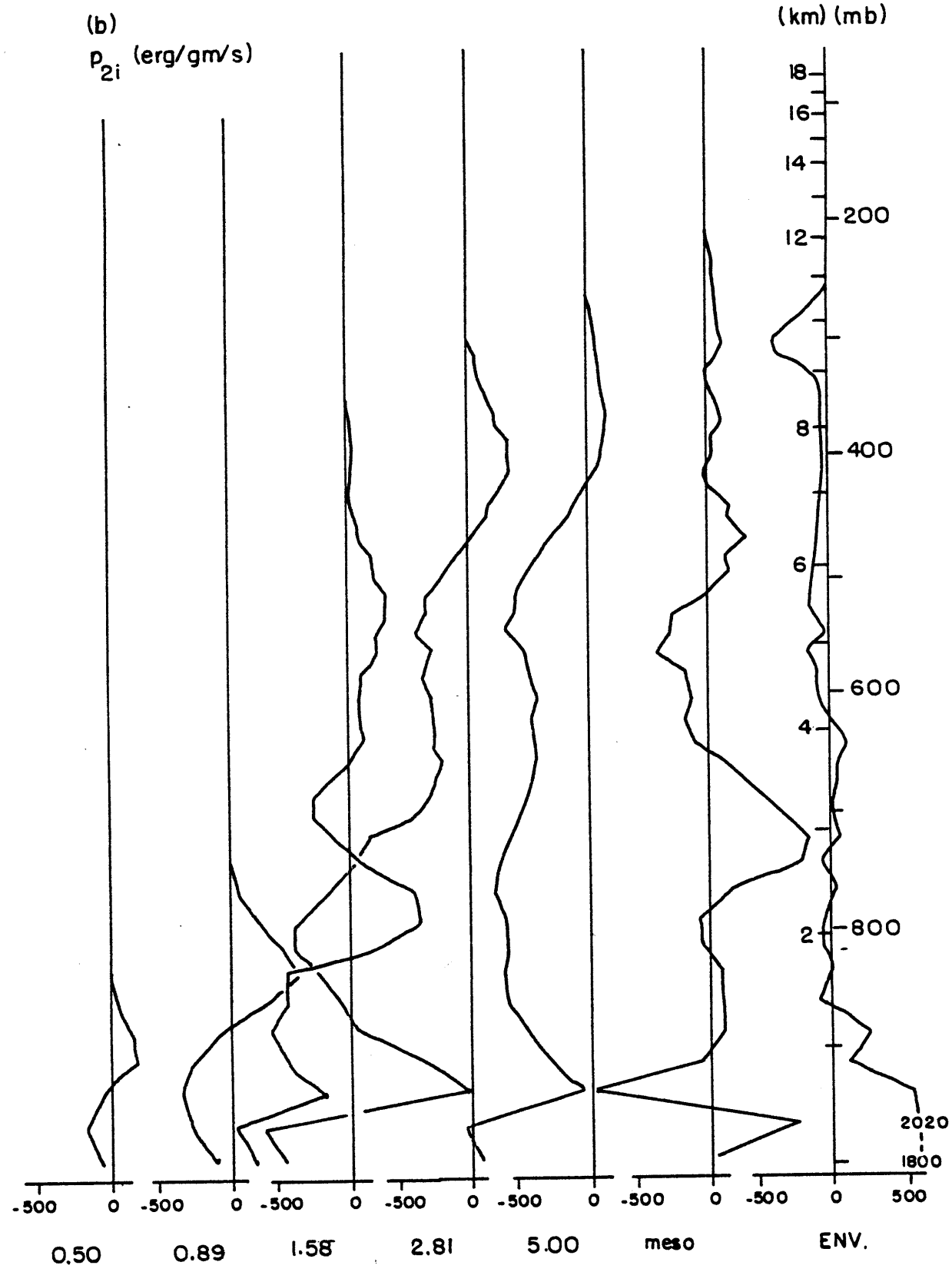


Fig. 6.31 continued.

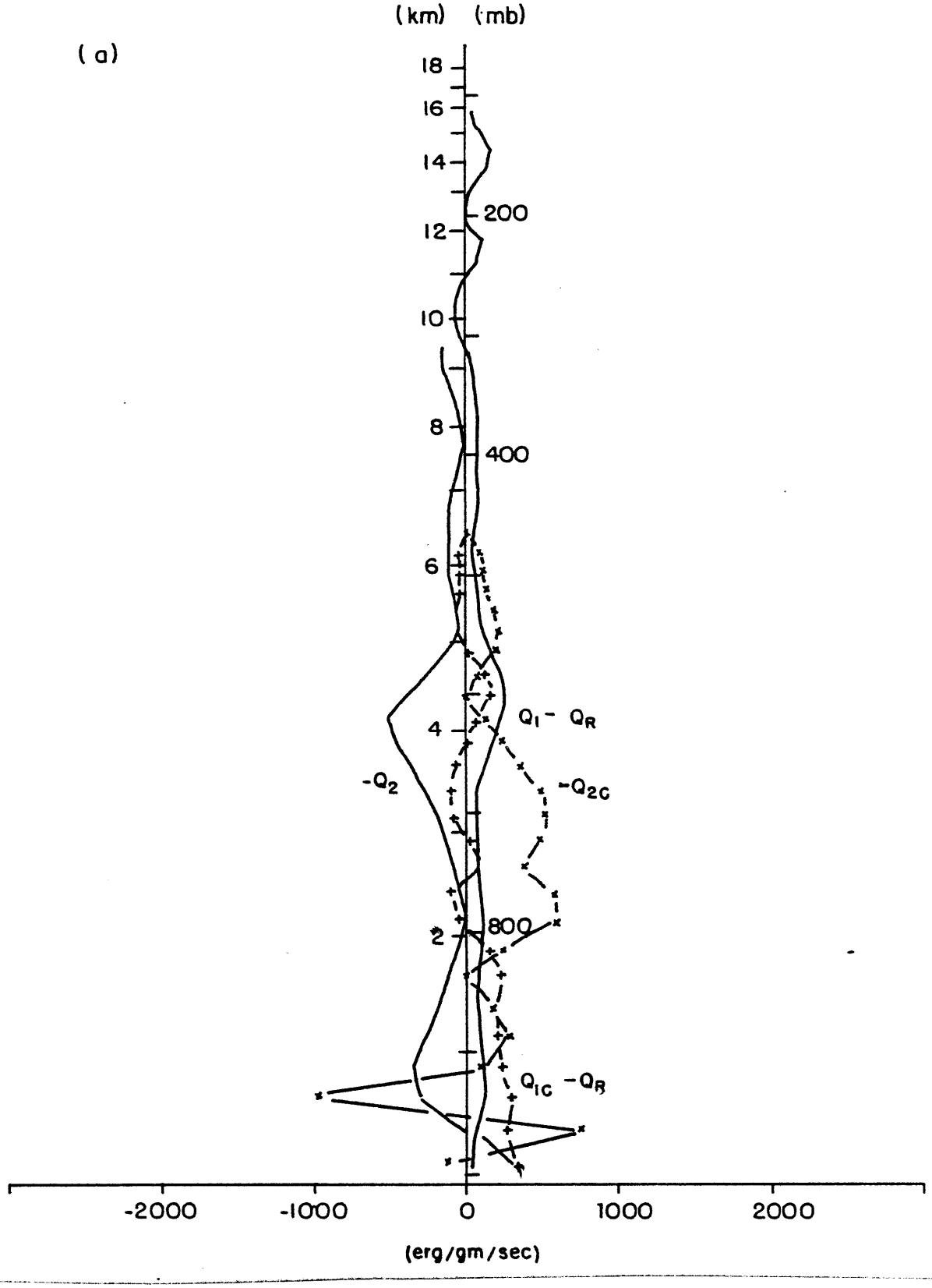


Fig. 6.32 As in Fig. 6.8 for Case LN1.M20 starting at 21Z Day 244, except (a) (-3)-0 hr, (b) 0-3 hr, (c) 3-6 hr, (d) 6-9 hr.

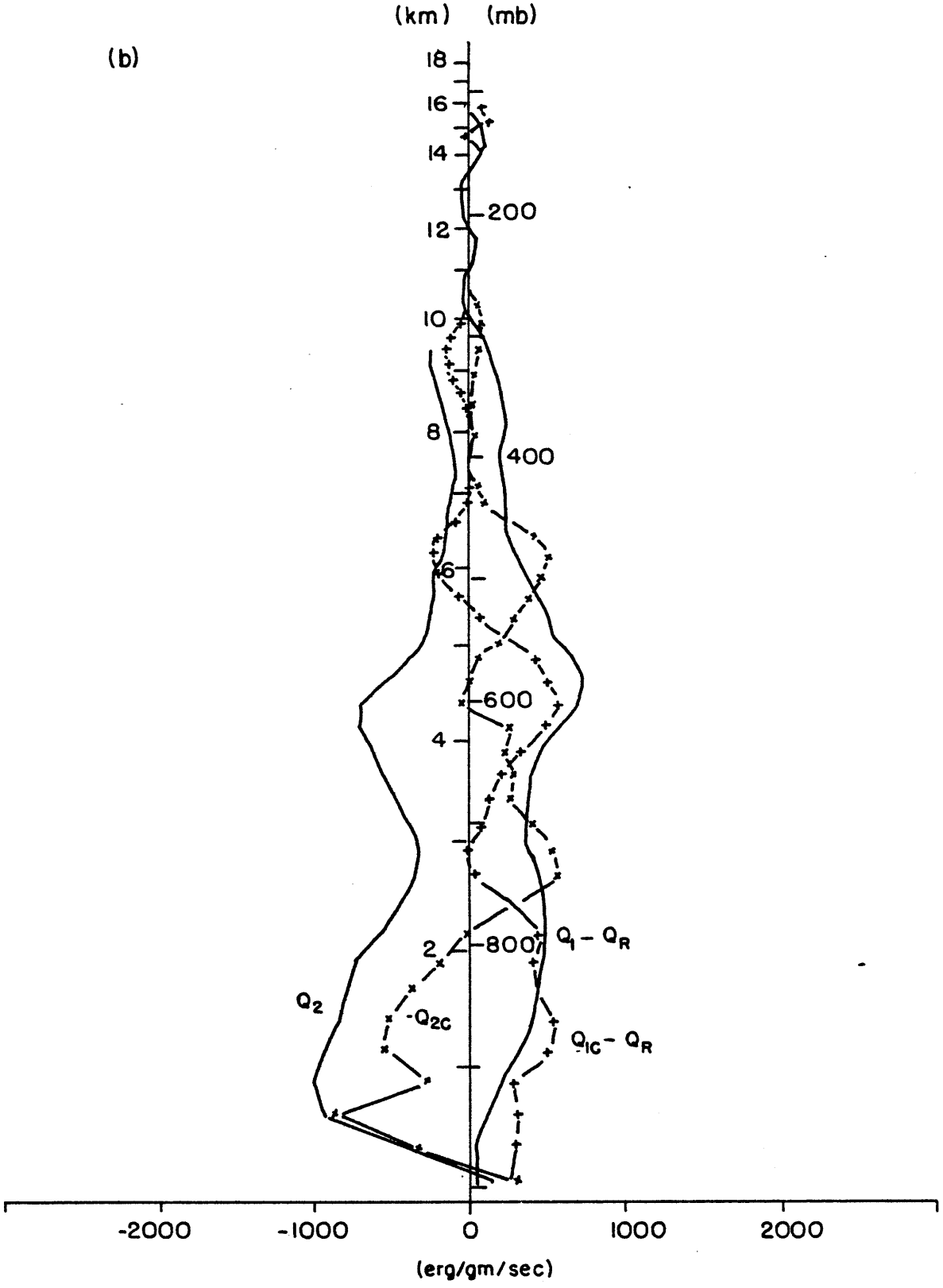


Fig. 6.32 continued.

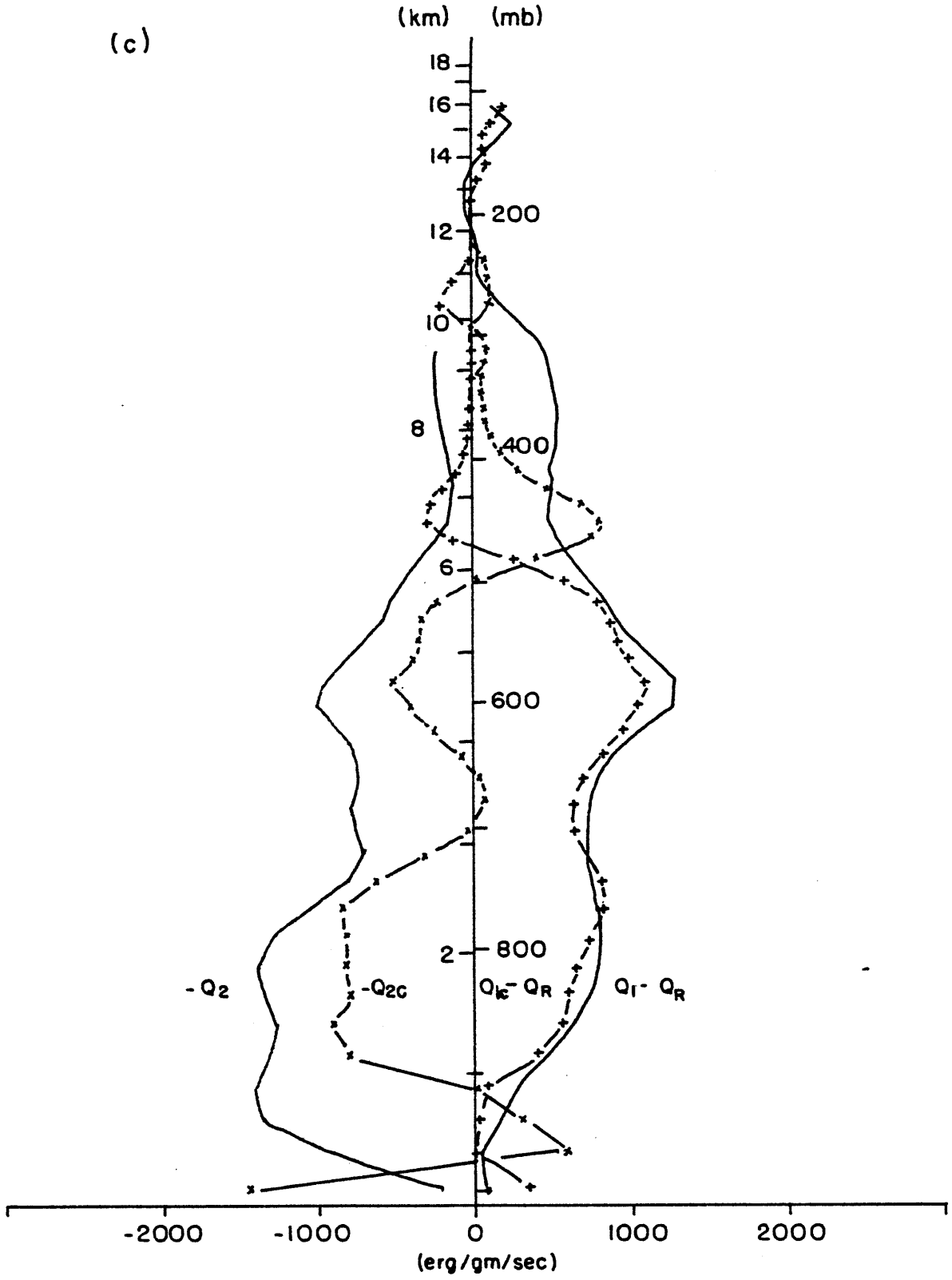


Fig. 6.32 continued.

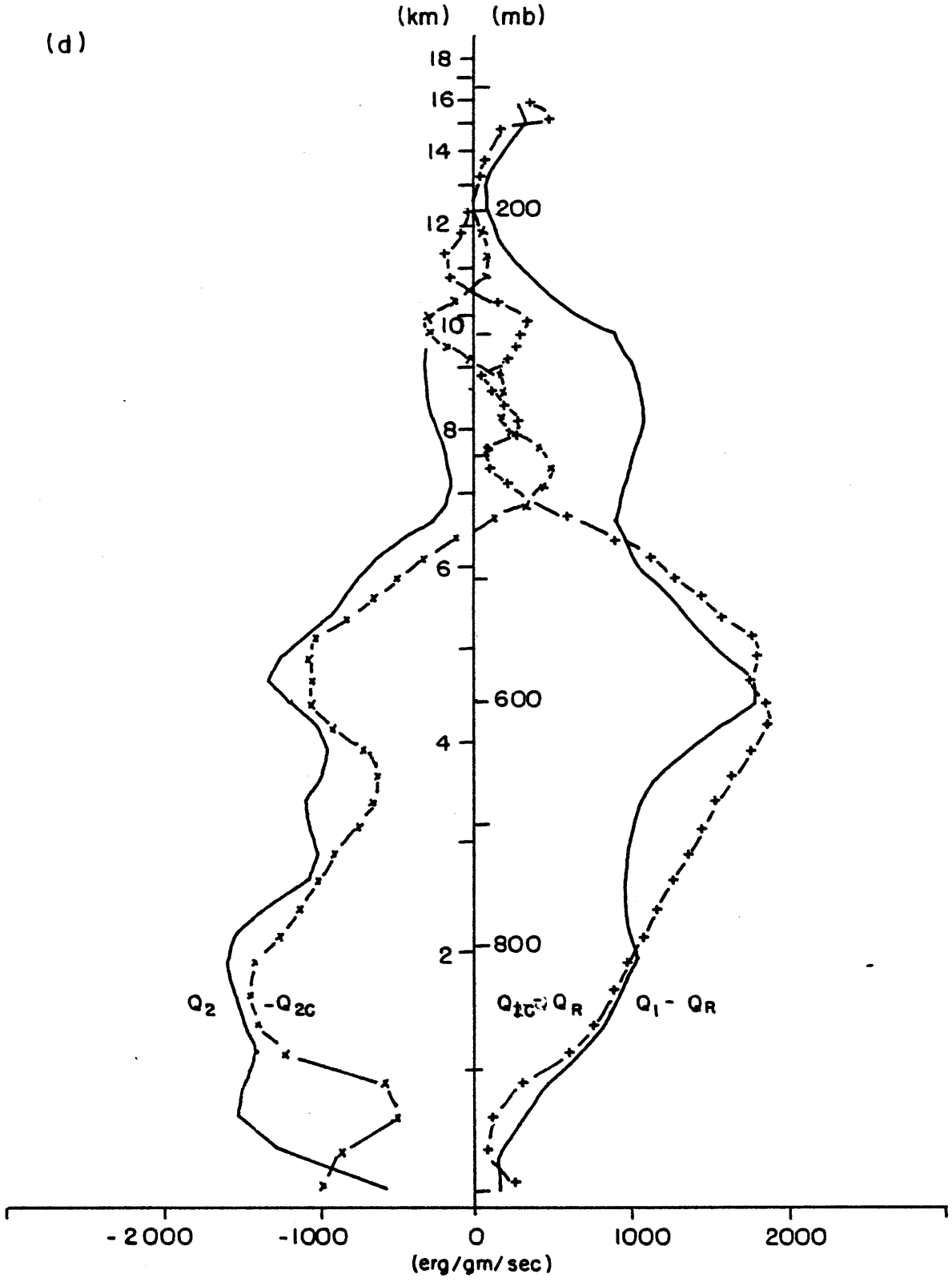


Fig. 6.32 continued.

pared to the later budgets. In the following 3 periods, we tend to see improvement over the budgets for the LN1.M20 configuration started at 00Z Day 245 (Fig. 6.13): Over 0-3 hr both budgets improve in the 1-2.5 km layer. Over 3-6 hr both budget profiles are shifted upwards, improving Q_{1c}, although Q_{2c} is about the same, on balance. Over 6-9 hr Q_{2c} improves slightly below 6.5 km.

As we would expect from this discussion of budgets, the rainfall is larger over 0-3 hr and 6-9 hr, but nearly the same over 3-6 hr.

Despite these differences, the general similarities between Cases lead us to conclude that the changes induced in the first 3 hr do not significantly change the subsequent model behavior. Thus, it was legitimate to start the integration for the various tests above at the later time (00Z Day 245), reducing the amount of computation needed to move the model into a period of intense convective activity.

6.9 Summary

We have presented a detailed analysis of the behavior of a new cumulus ensemble model in several configurations on Day 245 of GATE. In all Cases, we see that the model is unable to grow deep clouds at first, then deeper clouds appear as the large scale lifting destabilizes the environment. Starting near cloud base, the increasingly powerful convection balances the large scale tendencies over deeper layers with time, setting up new "average" profiles. Over those layers the observed heat and moisture budgets are nearly reproduced by the model. On the other hand, the model is unable to grow clouds which generate significant budget effects at high levels. This result is discussed in Chapter 7.

Throughout these simulations the smallest clouds remain shallow, acting mainly to transport moisture up from the subcloud layer. There is relatively little activity in clouds which top out at mid-levels.

The simple mesoscale structure considered in this model introduces two primary effects. First, it allows mutual protection: One generation of clouds moistens its immediate vicinity, so that the succeeding generation is protected from entraining dry outer environment air. This results in more vigorous cloud growth. The second effect is that at some levels mesoscale contributions to the budgets are significant fractions of the contributions generated by all cumulus clouds. Most of the mesoscale region's heat and moisture budgets appear to come from dry/warm or cool/moist events. In the mass flux we see that including the mesoscale region nearly reduces the outer environment's mass flux to zero over much of the convective layer.

Tests show that the model is not too sensitive to the changes in cloud distribution or mesoscale region size explored in this Chapter. Apparently, small changes in the domain-averaged profiles of temperature and moisture are sufficient to allow different configurations of the model to yield similar budget results. Changing the maximum radius to a larger size improves the model's agreement with observation in a particular way. The largest clouds do not grow deeper. Rather, they allow the environment to destabilize less before the ensemble satisfies the budgets over about the same depth as in previous model configurations.

7. Summary and Concluding Remarks

In this study we have examined the heating, drying, and mass transport characteristics of cumulus ensembles. We have also examined the role of mesoscale organization in the cumulus ensemble.

To carry out these goals, a numerical model has been designed. We relaxed many of the assumptions of previous simple models and retained easily observed quantities in specifying the model design;

1. the model follows the spectral diagnostic approach, in which the model is closed by requiring that the simulated and observed apparent sources of heat and moisture agree (in the present study this condition was reduced to agreement in the subcloud layer moisture budget);
2. each cloud is modelled as a distinct entity;
3. the numbers of clouds are free parameters, allowing comparison with observed population statistics;
4. the model is economical enough to be used extensively;
5. the model is time-dependent, allowing the relaxation of many questionable assumptions which other simple models contain;
6. the model includes mesoscale structure, as required by our second goal and motivated by observation.

We first adapted a time-dependent, axisymmetric, anelastic model of an isolated cumulus cloud with cloud pressure perturbations and a detailed warm rain microphysical parameterization (after Asai and Kasahara, 1967, and Yau, 1980). An analysis of entrainment showed that it does not introduce horizontal scale dependence into the cloud. Tests showed that scale dependence is due primarily to pressure perturbations. The Kessler (1969) microphysical parameterization was shown to yield

large errors at cloud top and below cloud base, compared to the Yau and Austin (1979) parameterization.

We then generalized the cumulus cloud model into a cumulus ensemble model, in which the environment contains many clouds. As in the one-cloud model, each variable is represented by tophat profiles. The mesoscale is introduced as a distinct region with values different from those in the outer environment. For simplicity, all clouds were assumed to reside in the mesoscale region. For GATE, the vertical velocity in the initial cloud perturbation has been shown to be unimportant; however the depth of the moisture perturbation has been shown to be very important. This result is consistent with the Scorer and Ludlam (1953) bubble model of clouds, in which large clouds start from large bubbles, which are amalgams of many small bubbles.

We examined the heating, drying, and mass transport characteristics of a cumulus ensemble (the first goal of the thesis) by applying the cumulus ensemble model to an easterly wave case observed during GATE. Several different model configurations have been studied. The cloud distribution and mesoscale-to-pressure domain ratio were specified, and the total number of clouds was chosen to satisfy the subcloud layer moisture budget.

For all model configurations, the initial cloud growth was weak, leading to poor early agreement between observed and simulated cloud budgets. This imbalance resulted in the progressive destabilization of the environment by large scale processes which moistened and cooled aloft. Deeper clouds then appeared, more realistically simulating the observed budgets, and preventing further destabilization. This process is similar to that which Soong and Tao (1980) showed. This suggests

that the destabilization is a necessary precondition for deep convection in GATE soundings. Differences between observed and simulated ensemble budgets are not necessarily due to model errors. Rather, the differences can be the result of initializing the model with a large scale average environmental sounding. This result is reminiscent of Randall and Huffman's (1980) finding that cumulus clumps require some time to become organized. The result is quite similar to Warner's (1979) observation that cells in a convective line tended to be quite small at the ends of the line, and large only at the center of the line.

Once the destabilization of the initial sounding has taken place, most of the model configurations give similar results for the net cumulus-mesoscale heating and drying. Adjustments to the cloud population distribution are apparently balanced by small changes in the environmental profiles of temperature and humidity. A test in which the maximum cloud radius was increased produced the best agreement between the observed and simulated budgets, but the depth of the convective layer continued to be less than observed. By satisfying the budgets more quickly than in the other tests, this configuration allowed less destabilization. Cloud growth was correspondingly less vigorous, so that maximum cloud height continued to fall short of the tallest clouds observed.

In the adjusted state, the ensemble model showed a range of cloud heights directly, but not linearly, related to the assigned radii. In general, the model included shallow, weak clouds, whose principle function was to transport moisture upwards, and deep, vigorous clouds, which carried out the bulk of the ensemble's heating, drying, and mass transport. Clouds with intermediate top heights were not very active.

We examined the role of mesoscale organization in the cumulus ensemble (the second goal of the thesis) by comparing results from the mesoscale and no-mesoscale versions of the model for the same GATE case. The mesoscale version exhibited more vigorous convection. Analysis of the moisture fields showed the mesoscale region to be moister than the outer environment. This is consistent with Randall and Huffman's (1980) "mutual protection" hypothesis, that each generation of clouds tends to create locally favorable conditions for succeeding generations of clouds.

The mesoscale region itself was shown to contribute significantly to the various budgets. Most of the heating and drying due to the mesoscale seemed to occur when the mesoscale region was warm/dry or cool/moist. The mesoscale mass flux was downward at most levels, driven by evaporative cooling (as Brown, 1979, also showed in his model). Introducing the mesoscale region reduces the outer environment's mass flux nearly to zero over the depth of the convective layer. Downward mesoscale mass flux at the top of the active convective layer drove upward motion in the outer environment, leading it to saturate before the mesoscale region. We believe that this unrealistic sequence of events is the result of the model's lack of very deep clouds.

The principle failing of the current cumulus ensemble model is its inability to simulate the very deep cumulus clouds that are observed, even after a fair amount of destabilization at mid-levels. Plume-cloud models (as in Arakawa and Schubert, 1974) achieve deep clouds by specifying a very small entrainment rate, but we are not free to make that specification; Randall and Huffman (1982) show that the cumulus cloud model on which the cumulus ensemble model is based exhibits only a weak

relationship between cloud radius and lateral entrainment rate.

This impression is bolstered by considering the heat and moisture budgets. In general, the simulated and observed sensible heat budgets agree more closely than the corresponding latent heat budgets. The entrainment/detrainment of sensible heat is a relatively small term (Arakawa and Schubert, 1974); it can therefore be inaccurately modelled without significant negative impact on the simulated sensible heat budget. The remaining terms, namely the vertical transport of heat inside the model cloud and the simulated condensational heating should be reasonable. The corresponding terms in the latent heat budget should also be reasonable, because we have intentionally employed a detailed microphysical parameterization in order to make the moisture budget as accurate as possible. Thus, we believe that errors in the latent heat budget must be associated with incorrect entrainment/detrainment. Recall that the constant radius assumption is the entrainment closure assumption in our model (see Chapter 4). The constant cloud radius assumption, although physically plausible, is unduly restrictive. Ryan and Lalousis (1979) have provided one example of a cloud with tophat profiles and a radius which varies as a function of time and height. We hope to follow a similar course in the future.

A second plan for the future is to consider cloud top entrainment. Paluch (1979), among others, has presented observations indicating that some clouds may contain air from cloud top and cloud base, with relatively little lateral entrainment. The current one-cloud model exhibits cloud top entrainment due to numerical diffusion (Randall and Huffman, 1982); an explicit parameterization is clearly needed.

A third plan for the future is the addition of the ice phase of

water. Yau (1980), among others, shows that this change results in deeper simulated clouds, and various researchers show that melting in mesoscale downdrafts can be important for driving mesoscale downdrafts (see Zipser, 1977).

The proximate results of each suggestion above would be an improved numerical model of an isolated cumulus cloud. The indirect result would be to improve the cumulus ensemble model, since the ensemble depends on the cloud. It is our opinion that simple, time-dependent models such as the one used in this study represent an important middle stage between fully prognostic models and the diagnostic models now in use.

Finally, there is a need for more observations of cumulus ensembles. Such research is expensive, in general, but there is a critical need for data with which models such as ours can be compared. The automated cell-tracking procedure reported by Crane (1979) holds promise as a relatively straightforward way of deriving echo populations. The aircraft data presented by LeMone and Zipser (1980) points to a useful way of compiling that data. Doppler radar studies have the potential for shedding light on groups of clouds, at least in a composite sense.

Appendix A. Symbols

a cloud radius, cloud region

A area

b pressure domain radius

B virtual temperture buoyancy

c condensation

$C_{ij,i'j'}$ stabilization profile (B.2)

C_p specific heat of air at constant pressure

Def deformation (4.26)

e evaporation

E lateral mass entrainment (4.3)

F anelastic pressure forcing (C.7)

F_L F due to large scale lifting

$\hat{F}_\psi$ turbulent flux of ψ, with components $(F_\psi)_r$, $(F_\psi)_\varphi$, $(F_\psi)_z$

$(F_\psi)_n$ component of F normal to cloud boundary (4.4)

g gravitational acceleration

H_o initial cloud perturbation depth

I_{ij} cloud intensity (B.3)

J_{ij} instability field (see B.1)

J_o, J_1 Bessel functions of the first kind of order 0 and 1

K mixing coefficient

K_h, K_m heat and momentum mixing coefficients

k_z scaling constant in (4.26)

L latent heat of vaporization of water

M vertical mass flux; subscripts c, d, i, m, md, u refer to cloud, cloud downdraft, single cloud, mesoscale, mesoscale downdraft, cloud updraft; $\bar{(\ )}$, $\tilde{(\ )}$ refer to large scale, outer environment averages

$M_b(p)$ cloud base mass flux for clouds detraining at pressure p

N_x number of clouds in region x

p pressure

p_o surface pressure

P subensemble budget contribution (6.1)

q mixing ratio; subscripts c, r, v refer to cloud, rain, vapor

Q liquid water drag

Q_R radiative heating

Q_x budget contribution by a region in (E.8)

Q_ψ general variable for observed budgets

Q_1, Q_2 observed apparent source of heat and apparent sink of moisture

Q_{1c}, Q_{2c} model-generated Q_1, Q_2

r radius

R cloud radius

R rainfall rate

R.H. relative humidity

Ri Richardson number (4.26)

r random number field (B.3)

s dry static energy ($C_p T + gz$)

S_ψ source function for ψ

t time

T, T_d temperature and dew point

u radial (horizontal) velocity

$\vec{V}$ velocity vector

w vertical velocity

W(R) raindrop terminal velocity

W_{max} maximum vertical velocity in a cloud column

W_o initial cloud perturbation maximum vertical velocity

x,y,z Cartesian coordinates

δz vertical grid spacing

α_{ij} stabilization rate (see B.1)

γ constant in (B.3)

Δ_z length scale in (4.26)

ϵ a small distance

θ, θ^* potential and saturation equivalent potential temperatures

μ_k zeroes of J_1

π 3.14159

π_k coefficients in Fourier-Bessel expansion of π'

π' cloud perturbation pressure

π'_L part of π' due to large scale lifting

ρ_o anelastic density of air

σ a/b

τ seeding rate (see B.3)

ϕ dummy variable

φ azimuthal coordinate

$\bar{\Phi}$ microphysical source functions; subscripts c, r, v refer to cloud, rain, vapor dummy variable

$\Delta\psi$ $\overline{\psi}_b - \overline{\psi}_a$

ψ_i where i=0,1,2,3; coefficients of plane-fit to GATE data

(D.1)

ω vertical pressure velocity

$( )_f$ changes by large scale processes

$( )_{peak}$ maximum value over cloud lifecycle

$\hat{( )}_x$ value on boundary of x

$\overline{( )}_x$ average over region x

$( )'$ deviation from large scale average

$\overline{( )}^x$ pie-slice average to x (4.5)

$\dot{( )}$ time derivative

$\delta( )$ change from initial profiles

Appendix B. A Stochastic Model of Cumulus Clumping

B.1 Introduction

This Appendix contains an extended summary of Randall and Huffman (1980), describing a simple gridcell-cloud numerical model of a cumulus cloud ensemble. The results of this "clumping" study provide a useful supplement to the approach adopted in the main body of the thesis: The basic dynamic of the mesoscale version of the time-dependent ensemble model described in Chapter 5 is area-average destabilization (by lifting), causing clouds to stabilize their immediate surroundings (the mesoscale region), which then has properties different from the environment. Although the model provides detailed cloud behavior, the simplified geometry precludes statements about the shape of the mesoscale feature or the mechanisms of its initiation. In contrast, the clumping model sacrifices cloud details in order to provide insights on the spatial and temporal behavior associated with this general stabilization - local destabilization dynamic.

Recall from Chapter 2 that a "clump" is a group of cumulus clouds whose members are much more closely spaced than the average spacing over the population, and which maintains its identity over many cloud lifetimes.[1] As we saw in Chapter 2, many observations of cumulus ensembles implicitly describe clumps. Although chance groupings will occur even in a completely random cloud field, both the observed persistence of clumps over many individual cloud lifetimes and the observed tendency

---

1 We prefer "clump" to "cluster" because the term "cloud cluster" has been widely used to refer to the satellite-observed cloud features, of small synoptic scale, which are associated with tropical waves.

for the most vigorous clouds to occur preferentially in clumps strongly suggest that there exists a dynamical mechanism which favors the formation of clumps and tends to maintain them through time. Since clumping seems to occur in a wide variety of synoptic contexts (as long as cumulus clouds are present), the mechanism must be rather fundamental, in the sense that no special circumstances are required to trigger it.

As with the time-dependent ensemble model (see Chapter 5) the clumping model is simplified by neglecting surface forcing, synoptically-controlled mesoscale forcing, downdraft forcing, and vortex ring advection. Also, net heating on the mesoscale is ignored. We simply focus on the mutual protection hypothesis, that cumulus clouds tend to create, in their near environments, relatively favorable conditions for the development of succeeding clouds.

Although modern studies (e.g., Arakawa and Schubert, 1974) have emphasized that cumulus clouds are self-stabilizing, in the sense that they tend to relieve the conditional instability of their environment, the distribution of the rate of stabilization over the volume around an isolated cloud has not been discussed in the literature.

B.2 Model formulation

In this section we present a model designed to test the hypothesis that clumps spontaneously develop and persist through time because the rate of stabilization has a local minimum on the cloud. The same model will also be used to show that persistent clumps do not occur if the rate of stabilization decreases monotonically away from the cloud. A discussion of the physical processes which tend to produce a local minimum of the rate of stabilization on the cloud is postponed until Section

B.4.

Consider a square grid of points. In practice, we use a grid 50 points on a side. Each point represents a vertical column which may or may not contain a cloud. We define over the grid a prognostic variable, J, which represents the degree of conditional instability, i.e., the positive area on a tephigram; clouds are permitted if J is positive. The prognostic equation for J is

$$\dot{J}_{ij} = \alpha_{ij} - \sum_{i'j'} C_{ij,i'j'} I_{i'j'} , \qquad (B.1)$$

where the subscripts i and j denote a particular column, α_{ij} is the forcing due to all non-cloud processes (given a spatially uniform, time-independent positive value in this study), and the summation term represents the tendency of nearby clouds to reduce J_{ij}, i.e., to "stabilize". The rate at which column ij is stabilized by cloud activity in column i'j' is determined by the stabilization profile $C_{ij,i'j'}$, which satisfies

$$\sum_{ij} C_{ij,i'j'} = 1 , \quad \text{for all } i'j' \qquad (B.2)$$

and by $I_{i'j'}$, which is a measure of the intensity of convection in column i'j'. In order to evaluate the summation in (B.1) for columns near the grid boundary, we use cyclic boundary conditions in the i and j directions. The value of I_{ij} is determined from

$$I_{ij} = \begin{cases} 0 , & \text{if } J_{ij} < 0 \text{ or } r_{ij} > \tau \\ \gamma J_{ij} , & \text{otherwise.} \end{cases} \qquad (B.3)$$

Here r_{ij} is a random number between zero and one, τ a prescribed "seed-

ing rate", and γ a prescribed constant. The seeding rate represents the area-averaged rate of occurrence of "seeds", which we define as sub-cloud-layer perturbations suitable for the formation of a cloud.

In writing (B.1), we have assumed that the net stabilization of a given column, by clouds in two or more neighboring columns, can be obtained simply by adding the effects that the clouds would produce if they acted in isolation. We have also assumed, in writing (B.3), that the local intensity of convection is independent of the activity of neighboring clouds (except as that activity is reflected, through time, in the J field).

If we ignore the stochastic forcing of the model, i.e., if $\tau = 1$, then (B.1) and (B.3) have the steady, horizontally homogeneous solution

$$J = \alpha/\gamma \quad , \quad I = \alpha \quad . \tag{B.4}$$

This shows that increasing the forcing increases both the degree of conditional instability and the level of cloud activity. For $\tau < 1$, we expect the area-averaged values of J and I, denoted by $\overline{J}$ and $\overline{I}$, respectively, to approximately satisfy

$$\overline{J} = \alpha/(\gamma\tau) \quad , \quad \overline{I} = \alpha \quad . \tag{B.5}$$

B.3 Results

We have performed experiments using the axially symmetric stabilization profiles shown in Fig. 3.6. The "peak" stabilization profile decreases monotonically with radius, while the "dip" profile has a local minimum at zero radius. All results presented here are for $\alpha = 5.0$, $\gamma = 1.6$, and $\tau = 0.10$. The values of α and γ have been chosen simply to obtain convenient values of J and I (see Eq. B.4). The value of τ has

been chosen with a view to observations of the fractional area covered by active cumulus cells.

Figs. B.1a and B.1b show the predicted I field, averaged over time steps 110-124, for the peak and dip profiles, respectively. The apparent disorder for the peak is in clear contrast with the distinct, regular clumped pattern for the dip. For the latter profile, the largest values of I occur within the regularly spaced maxima. We shall now confirm these subjective impressions by objective methods, and we shall also show that the temporal structure for the dip is much more orderly than for the peak.

Figs. B.2a-B.2b show the predicted J field at timestep 125 for the peak and dip profiles. The spatial structures of the peak and dip results are markedly different. First, for the dip there is more power at small scales. This simply reflects the introduction of the scale defined by the radius of maximum stabilization. A second, more spectacular, difference is that the range of values of J for the dip greatly exceeds that for the peak. The dip maxima exceed the peak maxima by about a factor of 2 and, whereas the peak minima are always positive, some of the dip minima are negative.

Figs. B.3a and B.3b show the lagged spatial correlation of J for the peak and dip. The spatial distribution of J is quite regular for the dip; we see (imperfect) concentric rings of alternating positive and negative correlation. Negative features tend to be separated from neighboring positive features by about five columns - the assumed radius of maximum stabilization. In contrast, the peak results show no evidence of spatial regularity.

The temporal structures of the two stabilization profiles also differ

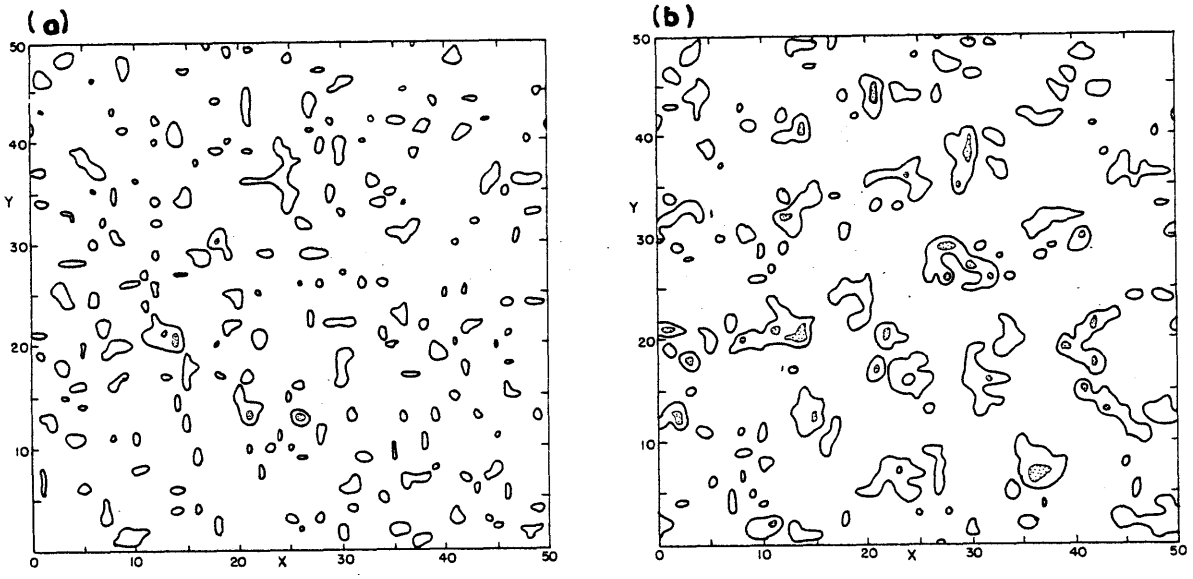


Fig. B.1 The predicted I field over steps 110-124: (a) peak, (b) dip. The contour interval is 8, with the zero line omitted; particularly intense regions are stippled. (RH, Fig. 2)

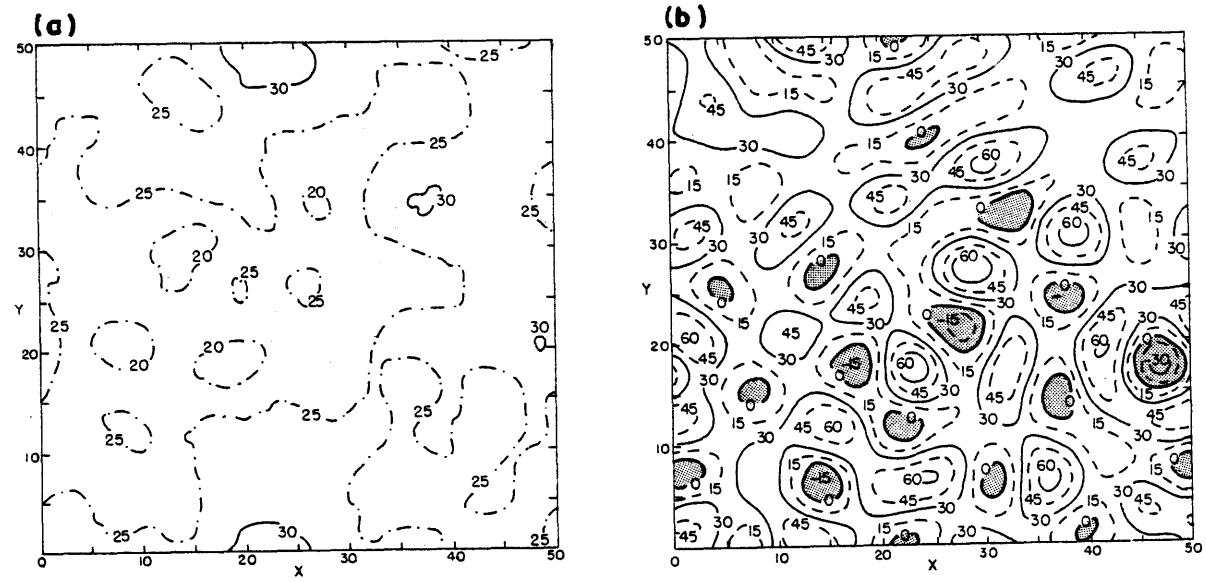


Fig. B.2 The predicted J field: (a) peak, step 125; (b) dip, step 125. The contour interval is 15, with negative values shaded. (RH, Figs. 3b, 3f)

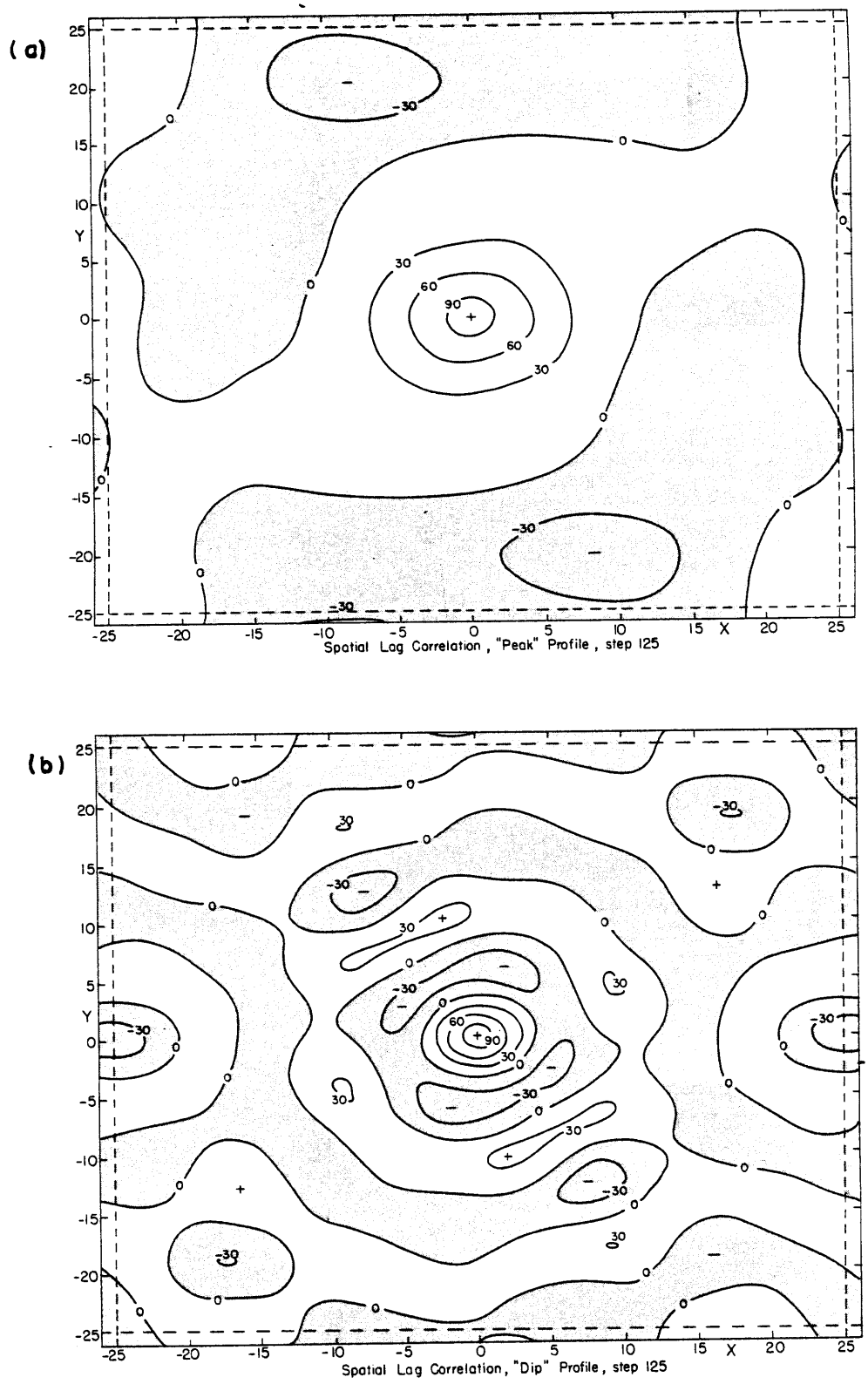


Fig. B.3 Lagged spatial autocorrelations of J, percent: (a) peak, step 125; (b) dip, step 125. Negative areas are shaded. (RH, Figs. 4b, 4d)

greatly. Fig. B.4 shows the lagged time autocorrelation of J for both stabilization profiles. The past history of the J field is quickly forgotten for the peak, but is long remembered for the dip.

Whereas the features of the dip results tend to become more intense with time, the maxima and minima of the peak results quickly reach a statistical equilibrium. This is shown in Fig. B.5, which depicts the time evolution of the maximum, minimum, and area-averaged values of J for both the peak and the dip. In addition to the very evident time dependence of J_{max} and J_{min}, for the dip, we also see that J_{min} becomes negative. This is significant, because wherever $J < 0$ clouds cannot occur (see Eq. B.3). The persistent regions of negative J in Fig. B.2b are holes in the cloud field. Some of the holes are ringed by active clouds (cf. Fig. B.1b); the pattern is somewhat similar to open cellular convection (Agee and Dowell, 1974).

Other experiments (not shown) reveal that, regardless of the choice of stabilization profile, the time- and domain-averaged values of J and I agree well with the values given by (B.5). Also, it is of some interest that as the seeding rate is decreased (by decreasing τ; see Eq. B.3) the average of I over those columns where $I = 0$ increases, i.e., the clouds become more vigorous. But because the number of active columns is smaller, the area-averaged value of I is not changed. This suggests that the rate at which subcloud-layer perturbations trigger new clouds influences the intensity of individual clouds more than it influences the overall level of convective activity.

In summary, our results show no evidence of clumping for the peak profile, but for the dip profile we find that the largest values of I occur in persistent, regularly spaced patches on the scale of the radius

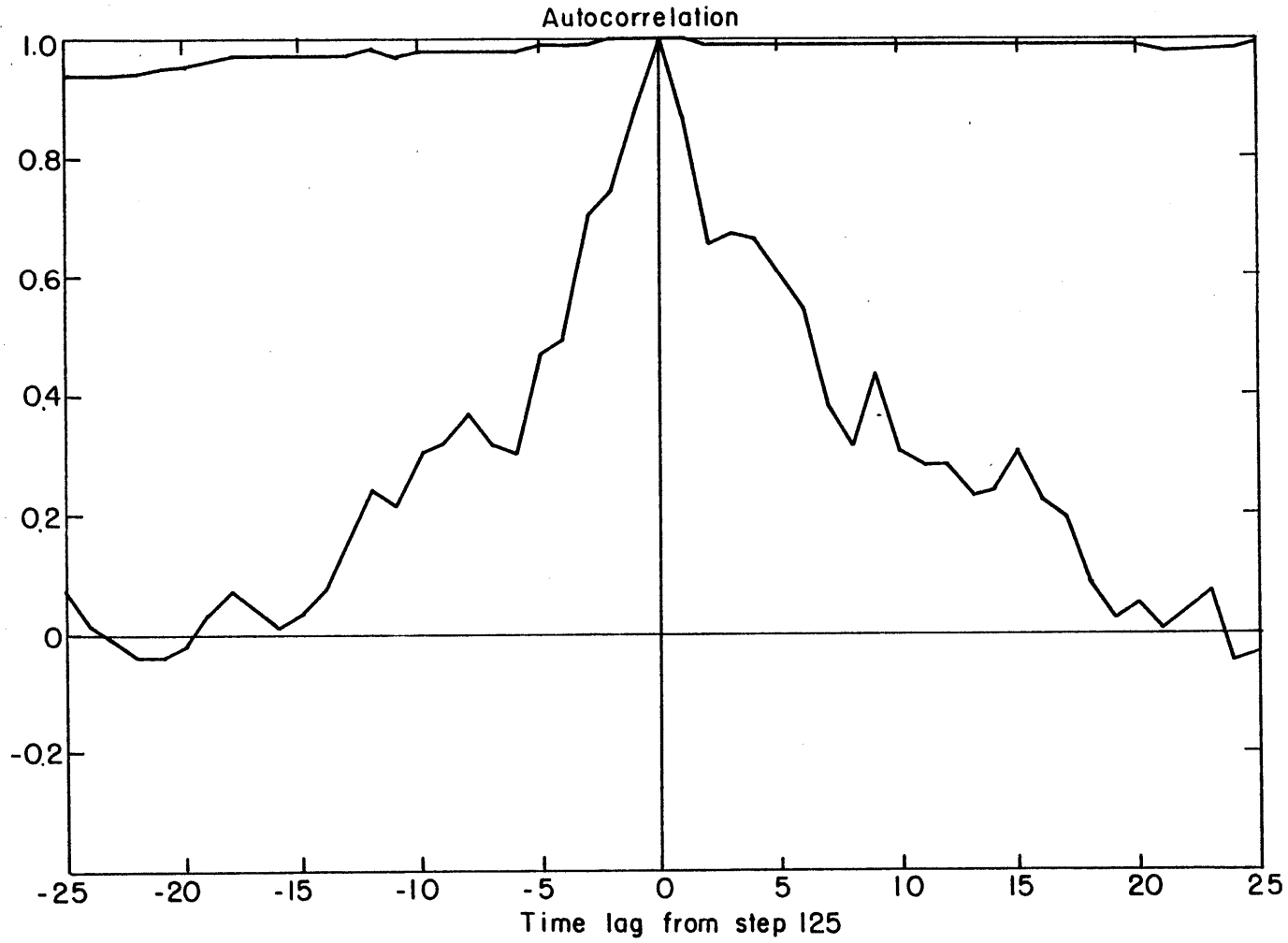


Fig. B.4 Time autocorrelation of J, lagged from step 125: lower curve is peak, upper curve is dip. (RH, Fig. 5)

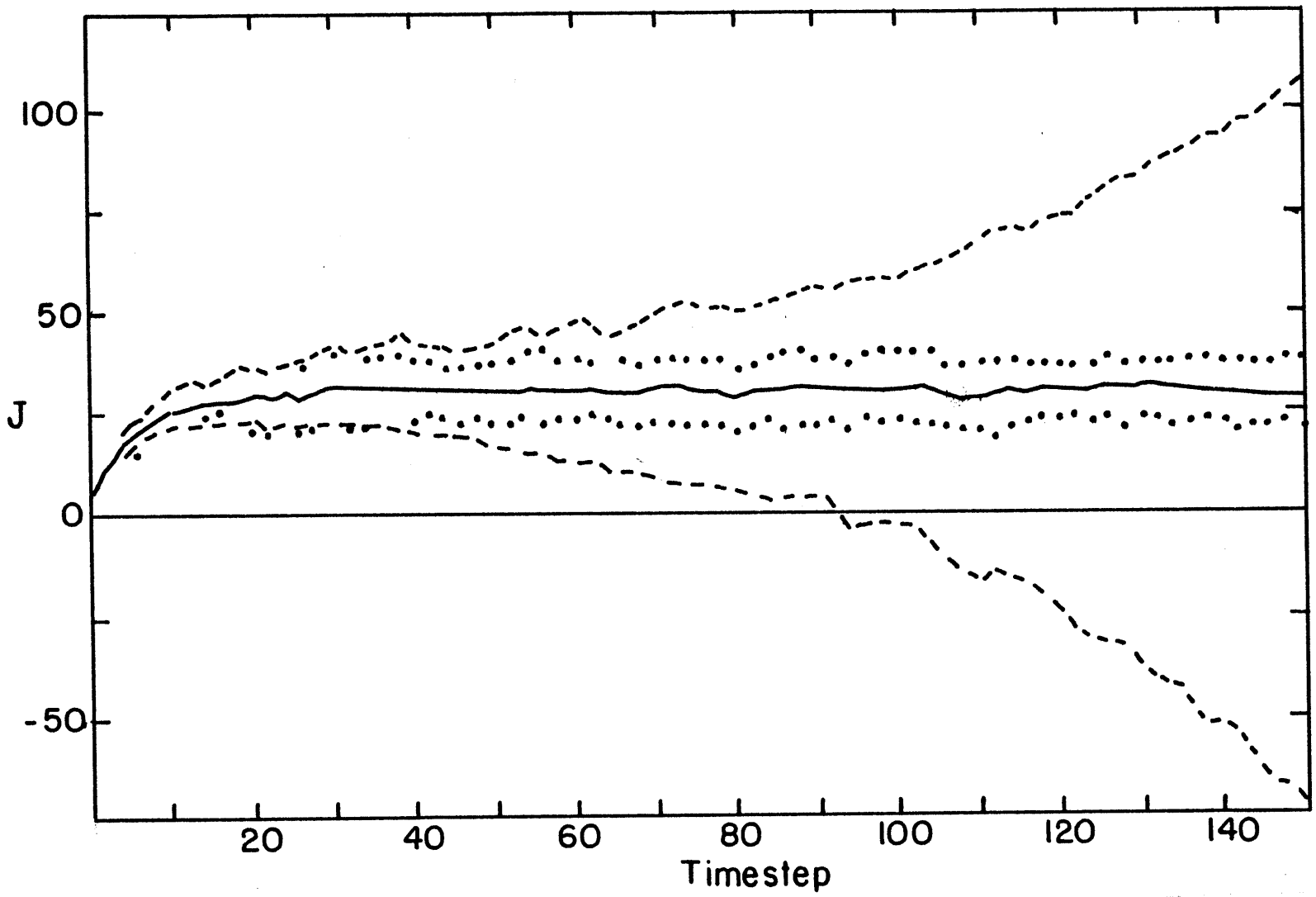


Fig. B.5 Time evolution of J: solid line is the spatial average for both peak and dip, dotted lines are maximum and minimum values for peak, dashed lines are maximum and minimum values for dip. (RH, Fig. 6)

of maximum stabilization, and that cloud-free holes form and persist in the vicinity of these patches of intense convection.

B.4 The stabilization profile

Since our simple model predicts that the assumed shape of the stabilization profile strongly influences the clumpiness of the model cloud field, we now discuss the physical process of stabilization, and argue that the dip profile is more realistic than the peak profile.

As is well-known, clouds tend to modify their environments by the three very different mechanisms of induced subsidence, detrainment and radiative cooling (Fig. B.6). Subsidence tends strongly to stabilize a broad area by warming and drying, but detrainment actually tends to destabilize a local region by moistening, and both detrainment and radiation tend to destabilize in a small area by cooling near the cloud top.

However, recent observational and theoretical studies show that the small-scale temperature anomaly associated with a cloud or small group of clouds has only a short lifetime. In an analysis of the GATE data, Grube (1979) found that cumulus-induced subsidence does indeed produce mesoscale warming events, which are characteristically displaced from the associated rain events by distances on the order of 30 km. She also reported that these warm anomalies are quickly smeared out from the mesoscale to synoptic scale. This observation may be explained by the argument of Schubert et al. (1980), who point out that whenever cumulus convection tends to create a temperature anomaly whose scale is less than the Rossby radius of deformation, the well-known geostrophic adjustment process (see the review by Blumen, 1972) acts to remove the temperature anomaly through the dispersive propagation of inertia grav-

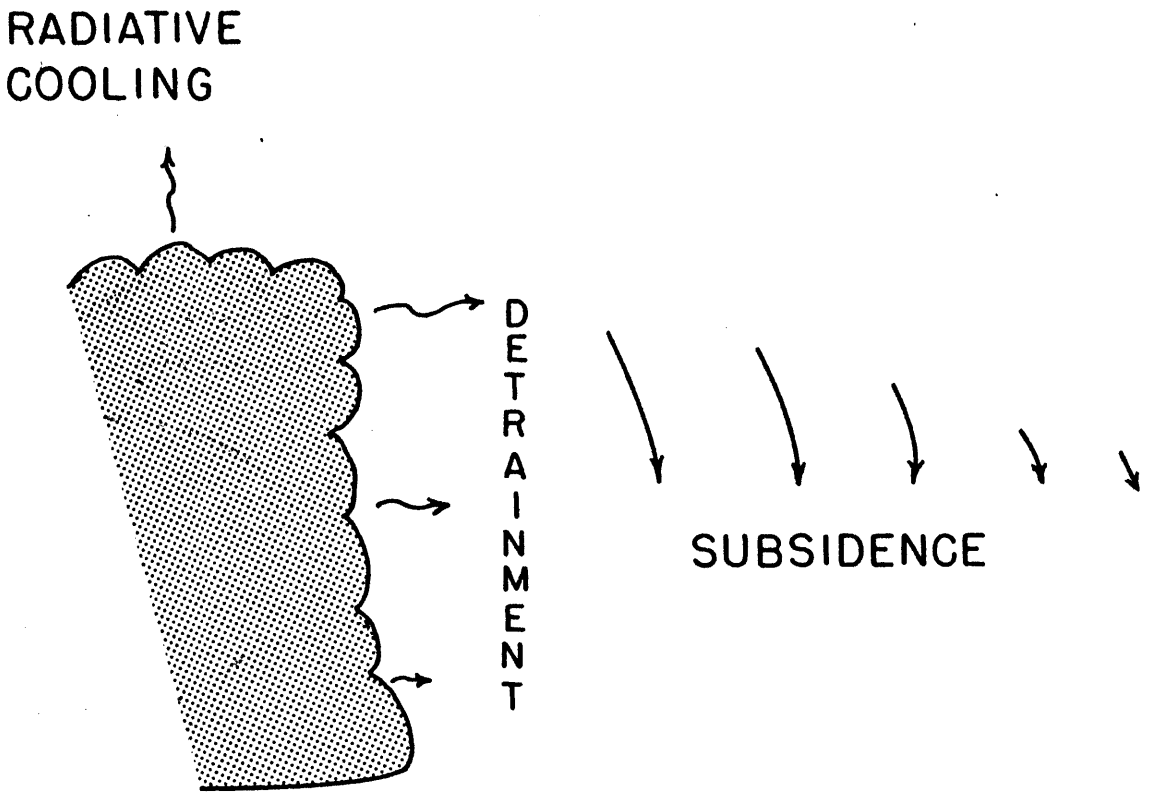


Fig. B.6 Schematic diagram illustrating a cloud's modification of its environment through induced subsidence, detrainment, and radiative cooling. (RH, Fig. 7)

ity waves.

These considerations suggest that during and immediately after the period of active cloud growth cloud-induced temperature and moisture anomalies both occur within the mesoscale environment, while the longer term impact of a cloud on its mesoscale environment is felt mainly in the moisture field, which is relatively undisturbed by the geostrophic adjustment process. On either time scale, the stabilization profile will have a local minimum on the cloud.

As discussed by Cho (1978), numerical studies of cumulus convection show that simulated clouds are insensitive to lateral boundaries placed more than about five cloud radii away from the cloud. This suggests that the radius of maximum stabilization must lie within five cloud radii, i.e., within the mesoscale.

B.5 Discussion and conclusions

We have demonstrated that the spatial and temporal structure of cumulus activity is strongly influenced by the distribution of the rate of stabilization over the volume around each individual cloud. In our model, clumping occurs if the stabilization profile has a maximum at an intermediate distance from the cloud, but not otherwise. Although the model studied here is obviously too schematic to provide conclusive proof, it is reasonable to say that the mutual protection mechanism is consistent with the appearance of vigorous convection inside mesoscale regions. Therefore, in the context of the mesoscale version of the time-dependent ensemble model, the clumping model assures us that we are justified in specifying a mesoscale region containing clouds and then employing the mutual protection mechanism. On a more speculative note,

the clumping study suggests that the mesoscale region modelled in the time-dependent ensemble model is actually divided into separate mesoscale features which have diameters on the order of 10 large cloud radii. Although this result is based on the subjective choice of the radius of maximum stabilization, it corresponds to the size ranges of clumps given by Lopez (1978) and Plank (1969).

Appendix C. A Two-Cylinder Cloud Model

C.1 Introduction

As a supplement to Chapter 4 this appendix summarizes arguments and equations which are used to formulate the two-cylinder cloud model on which the ensemble model is based. First, the model equations are summarized. Second, the microphysical parameterizations are reviewed. Third, the treatment of the pressure perturbation is discussed. Finally, the numerical method and boundary conditions are mentioned.

C.2 Model equations

Equations similar to the inner cylinder conservation equations (4.20-4.22) may be derived for the outer region and for the whole domain by averaging over r=a to r=b and r=0 to r=b, respectively. The explicit horizontally averaged equations are as follows:

Vertical motions

$$\frac{\partial \overline{w}_a}{\partial t} + \frac{2}{a}\hat{u}_a\hat{w}_a + \frac{1}{\rho_0}\frac{\partial}{\partial z}\left[\rho_0 \overline{w}_a^2 + \overline{(F_w)}_{z,a}\right] = -C_p\theta_0\frac{\partial \overline{\pi_a'}}{\partial z} + g\overline{B}_a - g\overline{Q}_a \quad (C.1)$$

where $B = \frac{\delta\theta}{\theta_0} + 0.61\,\delta q_v$

$$Q = q_c + q_r$$

$$\sigma^2\overline{w}_a + (1-\sigma^2)\overline{w}_b = \overline{w} \quad (C.2)$$

Continuity of air

$$\frac{2}{a}\hat{u}_a + \frac{1}{\rho_0}\frac{\partial}{\partial z}(\rho_0\overline{w}_a) = 0 \quad (C.3)$$

$$\frac{2}{b}\hat{u}_b + \frac{1}{\rho_0}\frac{\partial}{\partial z}(\rho_0\overline{w}) = 0 \quad (C.4)$$

Continuity of water substances and thermodynamic equation

$$\frac{\partial}{\partial t}\begin{bmatrix}\overline{\delta q_v}\\ \overline{q_c}\\ \overline{q_r}(R)\\ \overline{\delta\theta}\end{bmatrix}_{a,b} + \text{HOR.ADV.}_{a,b} + \frac{1}{\rho_o}\frac{\partial}{\partial z}\begin{bmatrix}\rho_o\,\overline{q_v}\,\overline{w} & (\overline{F_v})_z\\ \rho_o\,\overline{q_c}\,\overline{w} & (\overline{F_c})_z\\ \rho_o\,\overline{q_r}(R)\,(\overline{w}+\overline{W}(R)) & 0\\ \rho_o\,\overline{\theta}\,\overline{w} & (\overline{F_\theta})_z\end{bmatrix}_{a,b} = \begin{bmatrix}\overline{\Phi_v}\\ \overline{\Phi_c}\\ \overline{\Phi_r}(R)\\ \overline{S}\end{bmatrix}_{a,b} \quad (C.5)$$

with $\text{HOR.ADV.}_a = \frac{2}{a}\hat{u}_a\begin{bmatrix}\hat{q}_v\\ \hat{q}_c\\ 0\\ \hat{\theta}\end{bmatrix}_a$, $\text{HOR.ADV.}_b = -\frac{2a}{b^2-a^2}\hat{u}_a\begin{bmatrix}\hat{q}_v\\ \hat{q}_c\\ 0\\ \hat{\theta}\end{bmatrix}_a + \frac{2b}{b^2-a^2}\hat{u}_b\begin{bmatrix}\hat{q}_v\\ \hat{q}_c\\ 0\\ \hat{\theta}\end{bmatrix}_b$.

The argument R in the rainwater equations refers to the discrete raindrop size classes in the P microphysics and reminds us of the assumed exponential raindrop size distribution in the K microphysics (see next section). Note that horizontal advection of rainwater has been neglected, as discussed in Section 4.5. Additionally, non-zero vertical turbulent fluxes have been included for cloudy regions with low Richardson number (see Section 4.5). Note in Eq. 4.26 that the cloud radius is introduced by the dependence on cross-sectional area, A. A large-scale vertical velocity, $\overline{w}$, may be prescribed, leading to radial motion across the outer edge of the domain, $\hat{u}_b$. In contrast to the situation at the cloud boundary (r=a), we are free to choose the value of the variables which are carried across the outer boundary (r=b). The best choice for case studies is to pick the values such that the total flux of heat and moisture across r=b matches the values given by data.

The diabatic heating (S) includes condensation/evaporation and a prescribed radiative heating (applied equally in both regions). The vapor and heating terms of each region also include prescribed moistening and heating rates due to surface fluxes of those quantities.

C.3 Microphysical parameterizations

One of the principle difficulties in modelling cumulus clouds is handling water in its various phases. Not only do we see three phases, but two (ice and liquid) exhibit size distributions, and a given size class within a phase may interact with any size class within any phase (including itself). Simplification is clearly necessary.

A general simplification for this model is to neglect the ice phase. It is clear that the resulting model clouds will be less vigorous above the freezing level, but tests by Yau (1980) indicate that the differences are relatively small. In fact, the additional growth at cloud top seems to be at the expense of rainfall and total condensation.

The simple approach to handling water is the Kessler (1969) parameterization, hereafter referred to as the K microphysics. This method carries two liquid water variables, cloud and rain. Cloud water forms (CC) whenever supersaturation occurs and evaporates (EC) instantly upon subsaturation. It is advected and mixed as a property of the air parcel in which it resides. Whenever the cloud water content surpasses a set threshhold, it is assumed to "autoconvert" into rainwater (AU) at a set rate (these being 1 g/m^3 and 0.001/s, respectively). The rainwater is assumed to exist as drops which exhibit a Marshall-Palmer (1948) distribution, so average values may be computed for rain fall velocity, which also depends on height, accretion of cloud by falling raindrops (AC), which also depends on cloud water content, and evaporation (ER), which also depends on subsaturation.

The more sophisticated approach to handling water is the Yau and Austin (1979) parameterization, hereafter referred to as the P microphysics. This method carries 11 liquid water variables, cloud and 10 rain-

drop size classes (see Table C.1). The treatment of cloud and autoconversion is as for K, except the autoconverted water is assigned to rain category 1 rather than being spread over the whole size spectrum. Thereafter, the rain is modelled explicitly category by category, including evaporation (ER), accretion (AC), collection (CO), and breakup, both spontaneous (BS) and impact (BI). In addition, mass is directly shifted from one category to another as the raindrops grow or shrink (SH). Fig. C.1 helps illustrate the interactions.

The microphysical source terms in (C.5) may be written

$$\begin{bmatrix} \overline{\Phi}_v \\ \overline{\Phi}_c \\ \overline{\Phi}_r(R) \end{bmatrix}_{a,b} = \begin{bmatrix} -cc + EC + \sum_R ER \\ cc - EC - Au - \sum_R AC \\ -\sum_R ER + Au + AC + CO + BS + BI - SH \end{bmatrix}_{a,b} \qquad (C.6)$$

where AU=0 unless R=1 in P, CO=BS=BI=SH=0 in K (since the distribution is assumed), and the sums range over 1 to 10 for P, but only over 1 in K.

C.4 Perturbation pressure treatment

Most of the simple cloud models developed over the last 30 years assume that the pressure inside a cloud instantly adjusts to the pressure in the environment. This assumption eliminates pressure forcing from the vertical acceleration equation, and so eliminates a computationally difficult term. At first, this simplification seemed to be supported observationally (e.g., Byers and Braham, 1949), but recent observations call it into question. Marwitz (1973), Davies-Jones (1974), and others have reported cases in which the updraft at cloud base is negatively buoyant. The most plausible explanation is that pressure forcing is driving the cloud-base motion, in which case non-

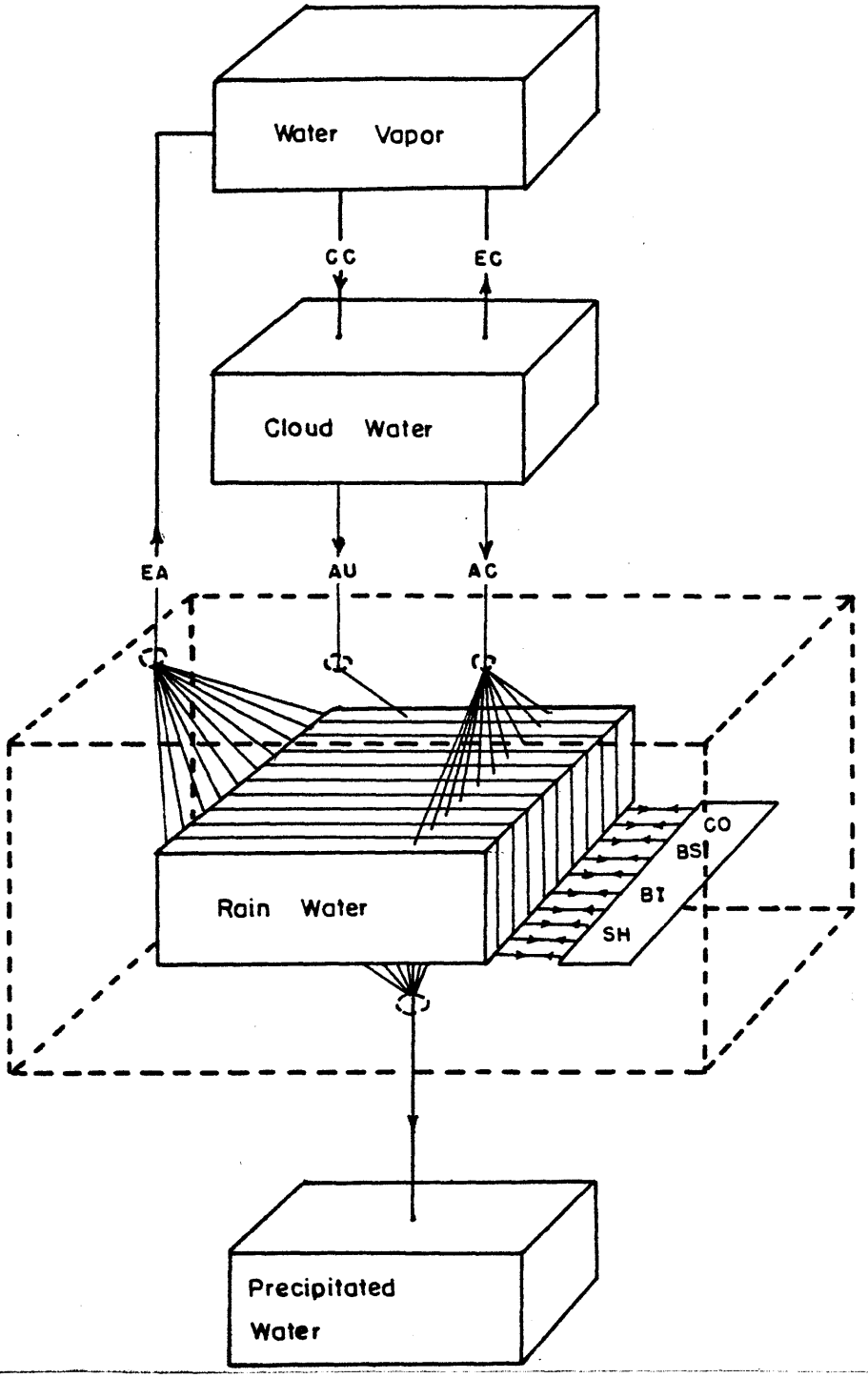


Fig. C.1 Schematic representation of Model P microphysical interactions: cloud water condensation (CC), cloud water evaporation (EC), rain water evaporation (ER), autoconversion of cloud droplets into rain drops (AU), accretion of cloud droplets by rain drops (AC), rain drop collection by larger rain drops (CO), spontaneous (BS) and induced (BI) rain drop breakup, and "spectral" shifting of mass from one rain drop class to another (SH). Model K parameterizes all interactions within the dashed box.

Table C.1 Size categories for liquid water.

Category	Range (cm)	Median Radius (cm)	Fall Velocity (m/s)
Cloud	0-.002	0.001	0.01
Rain 1	.002-.008	0.005	0.23
2	.008-0.04	0.025	1.95
3	0.04-0.07	0.055	4.10
4	0.07-0.10	0.085	5.74
5	0.10-0.13	0.115	6.91
6	0.13-0.16	0.145	7.73
7	0.16-0.19	0.175	8.29
8	0.19-0.22	0.205	8.66
9	0.22-0.25	0.235	8.90
10	0.25-0.28	0.265	9.06

hydrostatic forcing is need for accurate modelling. Additionally, together with vertical turbulent fluxes, the non-hydrostatic pressure forcing introduces the cloud radius into the equations. As shown in Chapter 4, this allows clouds of different radii to grow to different maximum heights.

The explicit modelling of pressure perturbations in simple cloud models has a short history. Lee (1971) assumed Gaussian profiles for all variables, but constrained the cloud to have a constant vertical mass flux. Holton (1973) expanded the horizontal pressure field in Bessel functions and retained the first mode to derive the horizontally-averaged pressure equation for a one-dimensional model. This study closely follows Yau (1980).

The anelastic pressure equation is

$$c_p \nabla \cdot (\theta_o \nabla \pi') = -\nabla \cdot (\vec{V} \cdot \nabla \vec{V}) + g \frac{\partial}{\partial z} B - g \frac{\partial}{\partial z} Q = F \qquad (C.7)$$

where the right-hand side is referred to as the forcing function, F. If we apply the equation to a horizontally-uniform field of lifting, the resulting forcing function, F_L, will generally be non-zero, causing some pressure response π'_L. However, in this model we assume that the large-scale lifting is in hydrostatic balance, inplying that the large-scale processes are just counteracting π'_L in the equation of vertical motion. If the various components of the pressure perturbation are small enough to be additive, we can simulate this balance by subtracting the large-scale terms from both sides of the pressure equation,

$$c_p \nabla \cdot (\theta_o \nabla \pi') = F - F_L \qquad (C.8)$$

where we have retained π' as the cloud-scale perturbation. In cylindrical coordinates, (C.8) becomes

$$c_p\left[\rho_o\theta_o + \frac{1}{r}\frac{\partial}{\partial r}\left(r\frac{\partial \pi'}{\partial r}\right) + \frac{\partial}{\partial z}\left(\rho_o\theta_o\frac{\partial \pi'}{\partial z}\right)\right] = \frac{\partial}{\partial z}\rho_o g(B-a)$$

$$+\frac{1}{r}\left[\frac{\partial^2}{\partial r^2}\left(r\rho_o\overline{u}^2\right) + 2\frac{\partial^2}{\partial r\partial z}\left(r\rho_o\overline{u}\,\overline{w}\right) + \frac{\partial^2}{\partial z^2}\left(r\rho_o\overline{w}^2\right)\right] \qquad (C.9)$$

$$-\frac{1}{r}\left[\frac{\partial^2}{\partial r^2}\left(r\rho_o u^2\right) + 2\frac{\partial^2}{\partial r\partial z}\left(r\rho_o u w\right) + \frac{\partial^2}{\partial z^2}\left(r\rho_o w^2\right)\right]$$

and in the two-cylinder framework the variables have the values in Table C.2.

We have argued in Section 4.5 that the horizontal gradient of perturbation pressure should be zero at the domain edge, and with rigid, free-slip surfaces and B=0 at the top and bottom boundaries, the boundary conditions for (C.9) are

$$\frac{\partial \pi'}{\partial r} = 0 \quad \text{at } r=0,\ r=b$$

$$\frac{\partial \pi'}{\partial z} = 0 \quad \text{at } z=H \qquad (C.10)$$

$$c_p\theta_o\frac{\partial \pi'}{\partial z} = -gQ \quad \text{at } z=0$$

Given the homogeneous lateral boundary condition, we expand the perturbation pressure in a Fourier-Bessel series

$$\pi' = \sum_{k=0}^{N} \pi_k J_o(\mu_k r) \qquad (C.11)$$

where μ_k is the solution of

$$J_1(\mu_k b) = 0$$

and J_o and J_1 are the Bessel functions of the first kind of order zero and one, respectively. The algebra is sufficiently simple that the Bessel functions are calculated only once and carried in constants. At each timestep the pressure mode coefficients (the π_k's) are calculated

Table C.2 Variable values for evaluating anelastic pressure.

	Inner cylinder	Outer cylinder	Large-scale
B	$\overline{B}_a \left(= \frac{\overline{\delta\theta_a}}{\theta_o} + 0.61\,\overline{\delta q_{va}}\right)$	$\overline{B}_b \left(= \frac{\overline{\delta\theta_b}}{\theta_o} + 0.61\,\overline{\delta q_{vb}}\right)$	*
Q	$\overline{Q}_a \left(= \overline{q_{ca}} + \sum_R \overline{q_{ra}}\right)$	$\overline{Q}_b \left(= \overline{q_{cb}} + \sum_R \overline{q_{rb}}\right)$	*
w	$\overline{w}_a$	$\overline{w}_b$	$\overline{w}$
u	$\frac{r}{a}\hat{u}_a$	$\frac{r^2-a^2}{rb}\frac{\hat{u}_b}{1-\sigma^2} + \frac{b^2-r^2}{r^2}\frac{\sigma^2}{1-\sigma^2}\hat{u}_a$	$\frac{r}{b}\hat{u}_b$

* Term not needed in calculation.

and used to construct horizontal averages inside the cloud and outside the cloud. Due to the simplicity of the model's radial structure there is no need to explicitly compute the deviation pressure field. The total number of pressure modes used in the current model is 20, more than Yau (1977) thought to be necessary. Yau (1977) presents details on computing π_k.

C.5 Computational considerations

The calculations are carried out on a staggered grid; velocities are carried on respective grid box edges (vertical on the tops, horizontal on the sides) and all other variables are defined at grid box centers. The computational scheme is forward in time and upstream in space, with vertical advection solved by the modified upstream method (Soong and Ogura, 1973) which conserves the advected quantities linearly. Additionally, to control spurious internal gravity waves, the velocities are computed at step n+.5, then used to advance the rest of the computations from step n to step n+1. The linear stability analysis in Yau (1977) shows this scheme to be conditionally stable for timesteps less than 100 s.

The upper and lower boundary conditions, as hinted above, are free-slip and rigid,

$$\frac{\partial(\rho_o u)}{\partial z} = w = 0 \quad \text{at } z=0,\ z=H\ . \tag{C.12}$$

The staggered grid precludes the need for explicit conditions on $\delta\theta$, δq_v, q_c, although B and Q are needed for the perturbation pressure calculation',

$B = 0 \quad z=0,\ z=H$

$$Q = 0 \quad z=H \tag{C.13}$$

$$Q = Q_{sfc} \quad z=0 \ .$$

The non-zero liquid content (surface rainfall) is given at z=0 by linear extrapolation from the first two grid centers above z=0, except when it yields negative rainfall rates.

Appendix D. GATE Data Analysis

D.1 Introduction

GATE was a large international meteorological and oceanographic observing project carried out in the tropical eastern Atlantic in the summer of 1974. Several researchers have produced analyses of various parameters for Phase III, covering the period 30 August through 18 September. In all cases the region which the parameters represent is the "B array" of ships, covering roughly 2 degrees of latitude by 2 degrees of longitude (Fig. 6.1). This appendix briefly describes important points of the analyses used in this study, including upper air soundings, heat and moisture budgets, radiative transfer, and precipitation.

D.2 Soundings and budgets

Thompson et al. (1979) carried out the heat and moisture budget analysis for the B array, with average upper air soundings as a byproduct. They started by applying the method of least squares to fit all fields to linear equations in space and time for horizontal surfaces at 25 mb intervals:

$$\psi = \psi_0 + \psi_1 x + \psi_2 y + \psi_3 t \, . \qquad \text{(D.1)}$$

"Final", error-checked data from all B array ships for each level within ±6 h of the nominal observation time were used for the fit. All subsequent calculations treat these fits as exact in the horizontal and in time, with finite differences performed in the vertical. This limits the results to average values over the B array.

Vertical pressure velocity was calculated by applying mass continuity to the divergence of the fitted winds,

$$\omega(p) = \int_{p}^{p_s} \left(\frac{\partial u}{\partial x} + \frac{\partial v}{\partial y} \right) dp \qquad (D.2)$$

$$\simeq \int_{p}^{p_s} (u_1 + v_2)\, dp \qquad (D.3)$$

The vertical pressure velocity was forced to be zero at the surface and 100 mb by adjusting divergences according to the O'Brien (1970) method with weights inversely proportional to the number of observations.

It is then possible to solve the large-scale forms of Equations 2.1 and 2.2 to derive the apparent heat source and moisture sink.

For use in the current work it was necessary to interpolate the analysis of T, q_v, Q_1, Q_2, ω on a 3 h, 25 mb grid to an analysis of T, R.H., Q_1, Q_2, w on a 3 h, 250 m grid. Water vapor was converted to relative humidity first, since that varies more linearly with height than mixing ratio. Vertical air motion was linearly interpolated as vertical pressure velocity, then converted to vertical velocity. The remaining variables were interpolated using trapezoidal integration, since the model used in this study considers all other variables to be layer averages. Note that trapezoidal integration and linear interpolation give the same answer if the height grid layer is contained within the pressure grid layer.

D.3 Radiative transfer

Cox and Griffith (1978) undertook the massive task of systematically computing radiative divergence budgets for various time and space intervals during Phase III. The basic spacing for the computation was 100 mb in the vertical, 0.5 deg. lat. by 0.5 deg. long. in the horizontal, and 1 h in time. For each basic grid element the satellite-estimated

fractional cloudiness as a function of height and various synoptic data are used to estimate longwave, shortwave, and total radiation. The model was tuned for typical values of the parameters during GATE.

This study makes use of the Cox and Griffith tabulation of daily-average longwave and shortwave radiation over the B array. It is physically reasonable that area-averaged radiative divergence should have a relatively smooth vertical profile, but our model grid spacing is less than 100 mb, particularly at upper levels. As a result, we interpolate the radiative data to the model grid in a four-step process. An area-preserving interpolator-smoother[1] is applied three times to divide the 100 mb layers into 12.5 mb layers, then these are interpolated by trapezoidal integration to obtain radiative divergences over layers 250 or 500 m thick. An example of interpolation to 500 m layers is shown in Fig. D.1 for the 2 September B array 24 h average longwave component.

---

1 At each level we compute the centered finite-difference vertical derivative, then halve the pressure grid interval. The values for the two half-layers are adjusted such that their average equals the value of the old full layer (preserving area) and the finite-difference vertical derivative that they form equals the derivative already computed (smoothing the profile):

$$\frac{\psi(k+.25) + \psi(k-.25)}{2} = \psi(k)$$

$$\frac{\psi(k+.25) - \psi(k-.25)}{.5} = \frac{\psi(k+1) - \psi(k-1)}{2}$$

This formulation exactly preserves linear progressions in layer values as a function of pressure.

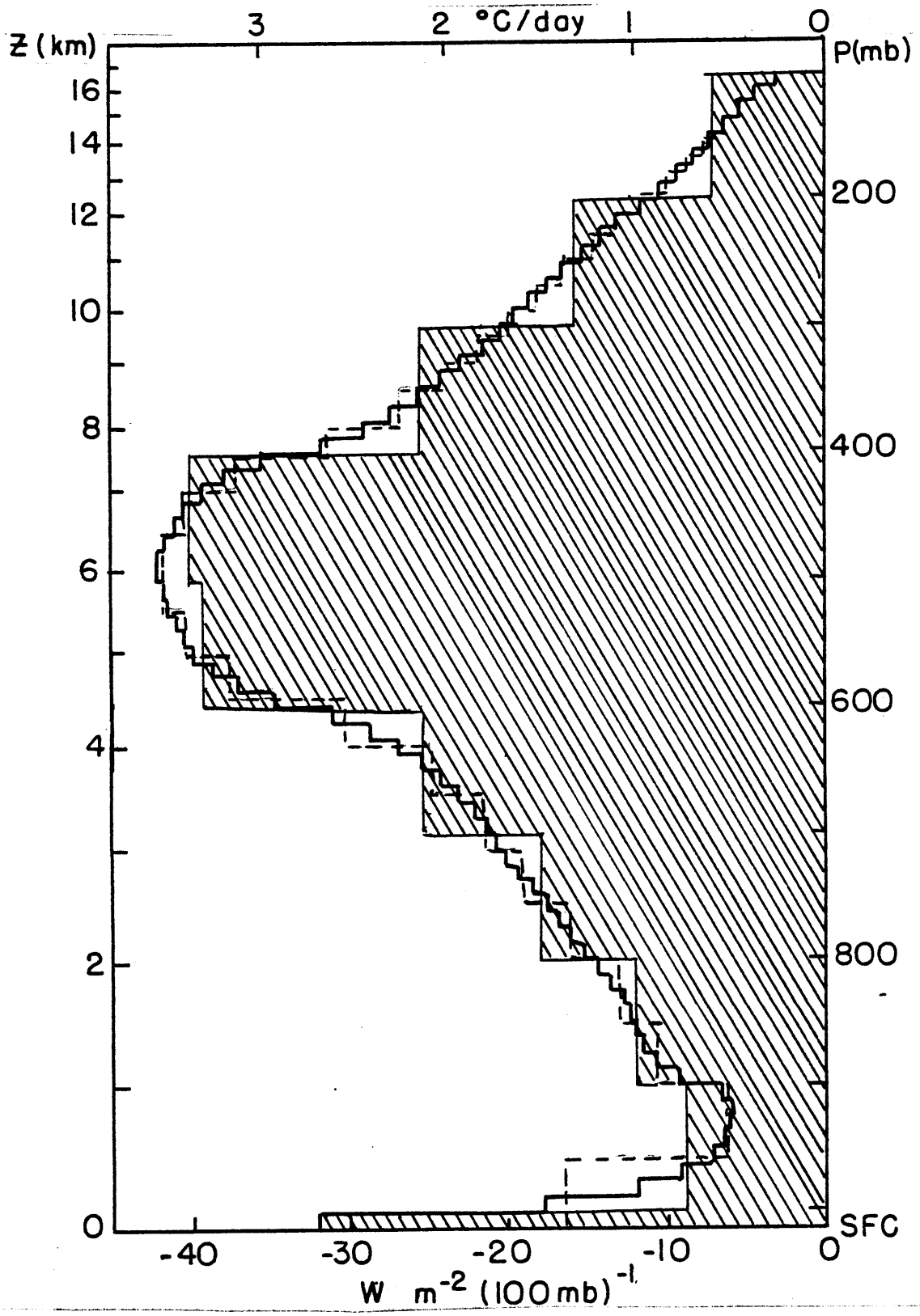


Fig. D.1 Example of interpolating Cox and Griffith (1978) radiation data (shaded) to 500 m layers (dashed). Results of the last interpolation in p-space are shown as a heavy solid line. The particular case is 2 September 1974, long-wave, B Array.

D.4 Precipitation

The precipitation patterns over the GATE array have been quantitatively analyzed by Hudlow and Patterson (1979). For Phase III they merged rainfall estimates from 4 quantitative C-band radar (as available) to derive hourly rainfall estimates on a 4 km by 4 km grid. They then constructed various spatial and temporal averages, including 3 h averages over the B array.

Although radar estimation introduces errors, Hudlow and Patterson argue that the alternatives of satellite estimation or averaging over (widely-scattered) surface raingages probably introduces more errors. Thompson et al. (1979) show good agreement between these radar estimates and the precipitation implied by the large-scale moisture budgets.

Appendix E. Budget Derivation

One useful way of examining the actions of the cloud ensemble is to compute budgets. That is, one keeps a record of the contributions that various processes make to the heat and moisture content of each level in the atmosphere. the formulae for this book-keeping are based on the anelastic conservation equation for intensive scalar ψ with turbulent flux $\vec{F}_\psi$ and source function S'_ψ,

$$\frac{\partial}{\partial t} + \nabla\cdot(\vec{V}\psi) = -\nabla\cdot\vec{F}_\psi + S'_\psi . \qquad (E.1)$$

As before, we ignore turbulent flux divergences, except the vertical component inside clouds and the nominal PBL, and assume that all variables are homogeneous within a region ("tophat" profile), then horizontally average (E.1) for the large scale environment, a mesoscale region, and a cloud:

Environment:

$$A_e\frac{\partial\psi_e}{\partial t}+\oint_e \hat{V}_e\hat{\psi}_e\,ds-\oint_m \hat{V}_m\hat{\psi}_m\,ds-\sum_i A_i N_{ei}\hat{V}_{ei}\hat{\psi}_{ei}+\frac{A_e}{\rho_o}\frac{\partial}{\partial z}\left(\rho_o w_e\psi_e\right)=A_e\left(S'_{\psi e}-\frac{\partial F_{\psi ze}}{\partial z}\right) \qquad (E.2)$$

Mesoscale:

$$A_m\frac{\partial\psi_m}{\partial t}+\oint_m \hat{V}_m\hat{\psi}_m\,ds \qquad -\sum_i A_i N_{mi}\hat{V}_{mi}\hat{\psi}_{mi}+\frac{A_m}{\rho_o}\frac{\partial}{\partial z}\left(\rho_o w_m\psi_m\right)=A_m\left(S'_{\psi m}-\frac{\partial F_{\psi zm}}{\partial z}\right) \qquad (E.3)$$

Cloud:

$$A_i\frac{\partial\psi_i}{\partial t}+A_i\hat{V}_i\hat{\psi}_i \qquad +\frac{A_i}{\rho_o}\frac{\partial}{\partial z}\left(\rho_o w_i\psi_i\right)=A_i\left(S'_{\psi i}-\frac{\partial F_{\psi zi}}{\partial z}\right) \qquad (E.4)$$

where the variables represent

$\hat{\psi}_x$ value of ψ on the outer boundary of region x,

$\hat{V}_x$ value of the normal velocity on the outer boundary of region x,

$\oint_x ds$ line integral around the outer boundary of region x,

x index for the various regions, e for the environment, m for the mesoscale region, and i for a cloud of the i^{th} subensemble.

It is useful to define the large scale horizontal average and deviation from the average as

$$\bar{\phi} = \frac{1}{A}\left[A_e \phi_e + A_m \phi_m + \sum_i N_{ei} A_i \phi_{ei} + \sum_i N_{mi} A_i \phi_{mi}\right] \qquad \text{(E.5a)}$$

$$\phi' = \phi - \bar{\phi} \qquad \text{(E.5b)}$$

with ϕ representing ψ or w and $(\,)_{xi}$ representing variables of the i^{th} subensemble embedded in region x (= e or m). It is also useful to write the heat source as a sum of condensational heating, S, and radiational heating, Q_R. Finally, we define the condensational heating as the net condensation at a level in a region minus the latent heat of liquid carried away laterally into a subsaturated region, plus the latent heat of liquid carried in laterally when the region itself is unsaturated. This definition is useful because it assigns evaporative cooling to the source region of the liquid. Specifically, cloud water detrained from each cumulus reduces the condensational heating in that cloud, rather than appearing as a large, undifferentiated cooling in the environment. In budget analyses the current approach is to be favored. Substituting (E.3) and (E.4) into (E.2) and applying (E.5a)

$$A\frac{\partial\bar{\psi}}{\partial t}+\oint_e \hat{V}_e\hat{\psi}_e\,ds+\frac{A}{\rho_o}\frac{\partial}{\partial z}(\rho_o\bar{w}\bar{\psi})=A_e S_{\psi e}+A_m S_{\psi m}+\sum_i N_{ei}A_i S_{\psi ei}+\sum_i N_{mi}A_i S_{\psi mi}$$

$$-A_e\frac{\partial F_{\psi ze}}{\partial z}-A_m\frac{\partial F_{\psi zm}}{\partial z}-\sum_i N_{ei}A_i\frac{\partial F_{\psi zei}}{\partial z}-\sum_i N_{mi}A_i\frac{\partial F_{\psi zmi}}{\partial z}+\frac{A}{\rho_o}\frac{\partial}{\partial z}(\rho_o\bar{w}\bar{\psi}) \qquad \text{(E.6)}$$

$$-\frac{A_e}{\rho_o}\frac{\partial}{\partial z}(\rho_o w_e\psi_e)-\frac{A_m}{\rho_o}\frac{\partial}{\partial z}(\rho_o w_m\psi_m)-\sum_i N_{ei}\frac{A_i}{\rho_o}\frac{\partial}{\partial z}(\rho_o w_{ei}\psi_{ei})-\sum_i N_{mi}\frac{A_i}{\rho_o}\frac{\partial}{\partial z}(\rho_o w_{mi}\psi_{mi}) \ .$$

Under the tophat profile assumption, (E.6) is nearly (2.1) or (2.2) in height coordinates multiplied through by A; the source terms include condensation/evaporation, the turbulent flux terms represent sub-grid scale contributions to $\frac{A}{\rho_o}\frac{\partial}{\partial z}(\rho_o\overline{w'\psi'})$, and the last line of (E.6) is the explicit part of $\frac{A}{\rho_o}\frac{\partial}{\partial z}(\rho_o\overline{w'\psi'})$. The left side of (E.6) equals the total area times the large scale apparent source, $A\cdot Q_\psi$, where

$$Q_\psi=\begin{cases} Q_1-Q_R\,, & \psi = s \quad \text{(sensible heat)} \\ -Q_2\ , & \psi = Lq_v \ \text{(latent heat)}\ . \end{cases}$$

A particularly compact form results if we eliminate the terms involving A_e by applying (E.5a) to (E.6). Collecting terms on the basis of region, we have

$$A\left\{Q_\psi-S_{\psi e}+\frac{1}{\rho_o}\frac{\partial}{\partial z}\left[\rho_o\bar{w}(\psi_e-\bar{\psi})\right]+\frac{\partial F_{\psi ze}}{\partial z}\right\}$$

$$=A_m\left\{S_{\psi m}-S_{\psi e}+\frac{1}{\rho_o}\frac{\partial}{\partial z}\left[\rho_o w_m(\psi_e-\psi_m)\right]+\frac{\partial}{\partial z}(F_{\psi ze}-F_{\psi zm})\right\} \qquad \text{(E.7)}$$

$$+\sum_i N_{ei}A_i\left\{S_{\psi ei}-S_{\psi e}+\frac{1}{\rho_o}\frac{\partial}{\partial z}\left[\rho_o w_{ei}(\psi_e-\psi_{ei})\right]+\frac{\partial}{\partial z}(F_{\psi ze}-F_{\psi zei})\right\}$$

$$+\sum_i N_{mi}A_i\left\{S_{\psi mi}-S_{\psi e}+\frac{1}{\rho_o}\frac{\partial}{\partial z}\left[\rho_o w_{mi}(\psi_e-\psi_{mi})\right]+\frac{\partial}{\partial z}(F_{\psi ze}-F_{\psi zmi})\right\} \ .$$

Note the parallels among the coefficients. We define

$$\overline{S_\psi} := Q_\psi = \begin{cases} Q_1 - Q_R, \\ -Q_2 \end{cases} \qquad \psi = \begin{cases} \text{sensible heat} \\ \text{latent heat} \end{cases}$$

$$\overline{F_{\psi z}} \equiv 0$$

$$\mathcal{Q}_x = \left\{ S_{\psi x} - S_{\psi e} + \frac{1}{\rho_0} \frac{\partial}{\partial z} \left[\rho_0 w_x (\psi_e - \psi_x) \right] + \frac{\partial}{\partial z} (F_{\psi z e} - F_{\psi z x}) \right\},$$

so that (E.7) reduces to

$$A\overline{\mathcal{Q}} = A_m \mathcal{Q}_m + \sum_i N_{ei} A_i \mathcal{Q}_{ei} + \sum_i N_{mi} A_i \mathcal{Q}_{mi} . \tag{E.8}$$

In this study we adopt a less compact notation which isolates Q_ψ on the left side and separates the environment's source and PBL turbulent flux divergence terms:

$$\begin{aligned} A Q_\psi = {} & A_e S_{\psi e} + \frac{A}{\rho_0} \frac{\partial}{\partial z} \left[\rho_0 \overline{w} (\overline{\psi} - \psi_e) \right] - A_e \frac{\partial}{\partial z} F_{\psi z e} \\ & + A_m \left\{ S_{\psi m} + \frac{1}{\rho_0} \frac{\partial}{\partial z} \left[\rho_0 w_m (\psi_e - \psi_m) \right] - \frac{\partial}{\partial z} F_{\psi z m} \right\} \\ & + \sum_i N_{ei} A_i \left\{ S_{\psi ei} + \frac{1}{\rho_0} \frac{\partial}{\partial z} \left[\rho_0 w_{ei} (\psi_e - \psi_{ei}) \right] - \frac{\partial}{\partial z} F_{\psi z ei} \right\} \\ & + \sum_i N_{mi} A_i \left\{ S_{\psi mi} + \frac{1}{\rho_0} \frac{\partial}{\partial z} \left[\rho_0 w_{mi} (\psi_e - \psi_{mi}) \right] - \frac{\partial}{\partial z} F_{\psi z mi} \right\}, \end{aligned} \tag{E.9}$$

We retain the differences inside the eddy flux terms because the individual terms are much larger than the differences. The eddy flux terms are not the traditional contributions to $\overline{w'\psi'}$, although they have nearly the same values for the cloud terms. For brevity, we define

$$\begin{aligned} P_{\psi e} &\equiv A_e S_{\psi e} + A \frac{1}{\rho_0} \frac{\partial}{\partial z} \left[\rho_0 \overline{w} (\overline{\psi} - \psi_e) \right] - A_e \frac{\partial}{\partial z} F_{\psi z e} \\ P_{\psi m} &\equiv A_m \left\{ S_{\psi m} + \frac{1}{\rho_0} \frac{\partial}{\partial z} \left[\rho_0 w_m (\psi_e - \psi_m) \right] - \frac{\partial}{\partial z} F_{\psi z m} \right\} \\ P_{\psi i} &\equiv N_{mi} A_i \left\{ S_{\psi mi} + \frac{1}{\rho_0} \frac{\partial}{\partial z} \left[\rho_0 w_{mi} (\psi_e - \psi_{mi}) \right] - \frac{\partial}{\partial z} F_{\psi z mi} \right\} \end{aligned} \tag{E.10}$$

and $N_{ei} = 0$ in this study (see Chapter 5), so that (E.9) is

$$A Q_{\psi} = P_{\psi e} + P_{\psi m} + \sum_i P_{\psi i} \qquad \text{(E.11)}$$

References

Agee, E.M., and K.E. Dowell, 1974: Observational studies of mesoscale cellular convection. J. Appl. Meteor., 13, 46-53.

Aitchison, J., and J.A.C. Brown, 1963: The Lognormal Distribution. Cambridge University Press, 176pp.

Anthes, R.A., 1977: A cumulus parameterization scheme utilizing a one-dimen- sional cloud model. Mon. Wea. Rev., 105, 270-286.

Arakawa, A., 1974: Modeling clouds and cloud processes for use in climate models. Report of the International Study Conference on the Physical Basis of Climate Modeling, Stockholm, 29 July - 10 August 1974. GARP Publication Series No. 16.

-----, and W.H. Schubert, 1974: Interactions of a cumulus cloud ensemble with the large-scale environment, part I. J. Atmos. Sci., 31, 674-701.

Arkell, R., and M. Hudlow, 1977: GATE International Meteorological Radar Atlas. CEDDA, Washington, D.C., 222 pp. (Stock No. 003-019-00038-1)

Asai, T., and A. Kasahara, 1967: A theoretical study of the compensating downward motions associated with cumulus clouds. J. Atmos. Sci., 24, 487-496.

Austin, P.M., and R.A. Houze, Jr., 1972: Analysis of the structure of precipitation patterns in New England. J. Appl. Meteor., 11, 926-935.

-----, and -----, 1973: A technique for computing vertical transports by precipitating cumuli. J. Atmos. Sci., 31, 674-701.

Ball, F.K., 1960: Control of inversion height by surface heating. Quart. J. Roy. Meteor. Soc., 86, 483-494.

Battan, L.J., and J.B. Theis, 1970: Measurement of vertical velocities in convective clouds by means of pulsed-doppler radar. J. Atmos. Sci., 27, 293-298.

Betts, A.K., 1974: Thermodynamic classification of tropical convective soundings. Mon. Wea. Rev., 102, 760-764.

Blumen, W., 1972: Geostrophic adjustment. Rev. Geophys. Space Phys., 10, 485-528.

Brown, J.M., 1979: Mesoscale unsaturated downdrafts driven by rainfall evaporation: A numerical study. J. Atmos. Sci., 36, 313-338.

Browning, K.A., and T.W. Harrold, 1969: Air motion and precipitation

growth in a wave depression. Quart. J. Roy. Meteor. Soc., 95, 288-309.

Byers, H.R., and R.R. Braham, 1949: The Thunderstorm Project. U.S. Weather Bureau, U.S. Dept. of Commerce, Washington, DC, 287 pp. (NTIS PB234515)

Cheng, C.-P., and R.A. Houze, Jr., 1979: The distribution of convective and mesoscale precipitation in GATE radar echo patterns. Mon Wea. Rev., 107, 1370-1381.

-----, and -----, 1980: Sensitivity of diagnosed convective fluxes to model assumptions. J. Atmos. Sci., 37, 774-783.

Cho, H.-R., 1977: Contributions of cumulus cloud life-cycle effects to the large-scale heat and moisture budget equations. J. Atmos. Sci., 34, 87-97.

-----, 1978: Some statistical properties of a homogeneous and stationary shallow cumulus cloud field. J. Atmos. Sci., 35, 125-138.

Cotton, W.R., 1975: On parameterization of turbulent transport in cumulus clouds. J. Atmos. Sci., 32, 548-564.

Cox, S.K., and K.T. Griffith, 1978: Tropospheric radiative divergence during Phase III of the GARP Atlantic Tropical Experiment (GATE). Atmos. Sci. Pap. No. 291, Colorado State University, 166 pp.

Charney, J.G., and A. Eliassen, 1964: On the growth of the hurricane depression. J. Atmos. Sci., 21, 68-74.

Crane, R.K., 1979: Automatic cell detection and tracking. IEEE Trans. Geosci. Electr., GE-17, 250-262.

Davies-Jones, R., 1974: Discussion of measurements inside high-speed thunderstorm updrafts. J. Appl. Meteor., 13, 710-717.

Emanuel, K.A., 1979: Inertial instability and mesoscale convective systems. Part I: Linear theory of inertial instability in rotating viscous fluids. J. Atmos. Sci., 36, 2425-2449.

Fraedrich, K., 1976: A mass budget of an ensemble of transient cumulus clouds determined from direct cloud observations. J. Atmos. Sci., 33, 262-268.

Frank, W.M., 1979: Individual time period analyses over the GATE ship array. Mon. Wea. Rev., 107, 1600-1616.

Fritsch, J.M., and C.F. Chappell, 1980: Numerical prediction of convectively driven mesoscale pressure systems. Part I: convective parameterization. J. Atmos. Sci., 37, 1722-1733.

-----, -----, and L.K. Hoxit, 1976: The use of large scale budgets for

convective parameterization. Mon. Wea. Rev., 104, 1408-1418.

Fujita, T.T., 1981: Tornadoes and downbursts in the context of generalized planetary scales. J. Atmos. Sci., 38, 1511-1534.

Gordon, N.D., 1978: Numerical simulation of a long-lasting mesoscale convective line. Sc.D. Thesis, M.I.T., 219 pp.

Gray, W.M., 1965: Calculation of cumulus vertical draft velocities in hurricanes from aircraft observations. J. Appl. Meteor., 4, 463-474.

Grube, P.G., 1979: Convection induced temperature change in GATE. Atmos. Sci. Pap. No. 305, Colorado State University, 128 pp. (NTIS PB-298 130/6GA)

Heymsfield, G.M., 1978: Kinematic and dynamic aspects of the Harrah tornadic storm analyzed from dual-doppler radar data. Mon. Wea. Rev., 106, 233-254.

Hill, F.F., and K.A. Browning, 1979: Persistence and orographic modulation of mesoscale precipitation areas in a potentially unstable warm sector. Quart. J. Roy. Meteor. Soc., 105, 57-70.

Hill, G.E., 1974: Factors controlling the size and spacing of cumulus clouds as revealed by numerical experiments. J. Atmos. Sci., 31, 646-673.

-----, 1977: Initiation mechanism and development of cumulus convection. J. Atmos. Sci., 34, 1934-1941.

Holton, J.R., 1973: A one-dimensional cumulus model including pressure perturbations. Mon. Wea. Rev., 101, 201-205.

Houghton, H.G., and H.E. Cramer, 1951: A theory of entrainment in convective currents. J. Meteor., 8, 95-102.

Houze, R.A., Jr., 1973: A climatological study of vertical transports by cumulus convection. J. Atmos. Sci., 30, 1112-1123.

-----, 1977: Structure and dynamics of a tropical squall-line system. Mon. Wea. Rev., 105, 1540-1567.

-----, and C.A. Leary, 1976: Comparison of convective mass and heat transports in tropical easterly waves computed by two methods. J. Atmos. Sci., 33, 424-429.

-----, and C.-P. Cheng, 1977: Radar characteristics of tropical convection observed during GATE: Mean properties and trends over the summer season. Mon. Wea. Rev., 105, 964-980.

-----, and -----, 1981: Inclusion of mesoscale updrafts and downdrafts in computations of vertical fluxes by ensembles of tropical clouds.

J. Atmos. Sci., 38, 1751-1770.

-----, -----, C.A. Leary, and J.F. Gamache, 1980: Diagnosis of cloud mass and heat fluxes from radar and synoptic data. J. Atmos. Sci., 37, 753-773.

Hudlow, M.D., and V.L. Patterson, 1979. GATE Radar Rainfall Atlas. CEDDA, NOAA, Washington, D.C., U.S. Gov't. Printing Off., 155 pp. (Stock No. 003-019-00046-2)

Johnson, R.H., 1976: The role of convective-scale precipitation downdrafts in cumulus and synoptic-scale interactions. J. Atmos. Sci., 33, 1890-1910.

-----, 1977: Diagnosis of convective and mesoscale motions during Phase III of GATE. J. Atmos. Sci., 37, 733-753.

-----, 1980: Diagnosis of convective and mesoscale motions during Phase III of GATE. J. Atmos. Sci., 37, 733-753.

Jones, R.W., 1980: A three dimensional tropical model with release of latent heat by the resolvable scales. J. Atmos. Sci., 37, 930-938.

Kessler, E., 1969: On the distribution and continuity of water substance in atmospheric circulation. Meteor. Monogr., 10, No. 32, 84 pp.

Klemp, J.B., P.S. Ray, and R.B. Wilhelmson, 1980: Analysis of merging storms on 20 May 1977. Preprints, 19th Conf. on Radar Meteor., April 15-18, 1980, Miami Beach, 317-324.

Kreitzburg, C.W., and H.A. Brown, 1970: Mesoscale weather systems within an occlusion. J. Appl. Meteor., 9, 417-432.

Kuo, H.L., 1965: On the formation and intensification of tropical cyclones through latent heat release by cumulus convection. J. Atmos. Sci., 22, 40-63.

Leary, C.A., and R.A. Houze, 1980: The contribution of mesoscale motions to the mass and heat fluxes of an intense tropical convective system. J. Atmos. Sci., 37, 784-796.

Lee, J.L., 1971. A Numerical Study of Shallow Convection. Report no. 19 to Nat. Sci. Found. under Grant GA-13818. Dept. of Meteor., Penn. State Univ.

LeMone, M.A., and E.J. Zipser, 1980: Cumulonimbus vertical velocity events in GATE, Part I: Diameter, intensity and mass flux distributions. J. Atmos. Sci., 37, 2444-2457.

Lilly, D.K., 1962: On the numerical simulation of buoyant convection. Tellus, 14, 148-172.

López, R.E., 1973: Cumulus convection and larger scale circulations: II. Cumulus and mesoscale interactions. Mon. Wea. Rev., 101, 856-870.

-----, 1977: The log-normal distribution and cumulus cloud populations. Mon. Wea. Rev., 105, 865-872.

-----, 1978: Internal structure and development processes of C-scale aggregates of cumulus clouds. Mon. Wea. Rev., 106, 1488-1494.

Lord, S.J., 1982: Interaction of a cumulus cloud ensemble with the large-scale environment. Part III: Semi-prognostic test of the Arakawa-Schubert cumulus parameterization. To appear in J. Atmos. Sci., 39.

Ludlam, F.H., 1980. Clouds and Storms. Penn. State U. Press, University Park, PA, 467 pp. (ISBN 0-271-00515-7)

Malkus, J.S., 1957: Trade cumulus groups: Some observations suggesting a mechanism of their origin. Tellus, 9, 33-44.

Marshall, J.S., and W.M.K. Palmer, 1948: The distribution of raindrops with size. J. Meteor., 5, 165-166.

Marwitz, J.D., 1973: Trajectories within the weak echo regions of hailstorms. J. Appl. Meteor., 12, 1174-1182.

McBride, J.L., 1981: An analysis of diagnostic cloud mass flux models. J. Atmos. Sci., 38, 1977-1990.

Murray, F.W., 1971: Humidity augmentation as the initial impulse in a numerical cloud model. Mon. Wea. Rev., 99, 37-48.

-----, and L.R. Koenig, 1972: Numerical experiments on the relation between microphysics and dynamics in cumulus convection. Mon. Wea. Rev., 100, 717-732.

-----, and -----, 1975: Cumulus cloud energetics as revealed in a numerical model of cloud dynamics: Part II. Computational results. Pure and Appl. Geophys., 113, 926-947.

Nicholls, S., and M.A. LeMone, 1980: The fair weather boundary layer in GATE: The relationship of subcloud fluxes and structure to the distribution and enhancement of cumulus clouds. J. Atmos. Sci., 37, 2051-2067.

Nitta, T., 1975: Observational determination of cloud mass flux distribution. J. Atmos. Sci., 32, 73-91.

-----, 1977: Response of cumulus updraft and downdraft to GATE A/B-scale motion systems. J. Atmos. Sci., 34, 1163-1186.

O'Brien, J.J., 1970: Alternative solutions to the classical vertical

velocity problem. J. Appl. Meteor., 9, 197-203.

Ogura, Y., and H.-R. Cho, 1973: Diagnostic determination of cumlus cloud populations from observed large-scale variables. J. Atmos. Sci., 30, 1276-1286.

Ooyama, K., 1971: A theory of parameterization of cumulus convection. J. Meteorol. Soc. Jap., 49, 744-756.

Paluch, I.R., 1979: The entrainment mechanism in Colorado cumuli. J. Atmos. Sci., 37, 125-130.

Plank, V.G., 1965: The cumulus and meteorological events of the Florida peninsula during a particular summertime period. Environmental Res. Pap. No. 151, Air Force Cambridge Res. Labs, 146 pp. (NTIS AD-629 933)

-----, 1969: The size distribution of cumulus populations. J. Appl. Meteor., 8, 46-67.

Randall, D.A., and G.J. Huffman, 1980: A stochastic model of cumulus clumping. J. Atmos. Sci., 37, 2068-2078.

-----, and -----, 1982: Entrainment in a simple cumulus cloud model. Submitted to J. Atmos. Sci.

Reed, R.J., D.C. Norquist, and E.E. Recker, 1977: The structure and properties of African wave disturbances as observed during Phase III of GATE. Mon Wea. Rev., 105, 317-333.

Ryan, B.F., and P. Lalousis, 1979: A one-dimensional time-dependent model for small cumulus. Quart. J. Roy. Meteor. Soc., 105, 615-628.

Schubert, W.H., 1974: Cumulus parameterization theory in terms of feedback and control. Atmos. Sci. Pap. No. 226, Colorado State University, 19 pp.

-----, J.J. Hack, P.L. SilvaDias, and S.R. Fulton, 1980: Geostrophic adjustment in an axisymmetric vortex. J. Atmos. Sci., 37, 1464-1484.

Scorer, R.S., and F.H. Ludlam, 1953: Bubble theory of penetrative convection. Quart. J. Roy. Meteor. Soc., 79, 94-103.

Simpson, J., and G. Van Helvoirt, 1980: GATE cloud-subcloud interactions examined using a three-dimensional cumulus model. Cont. to Atmos. Phys., 53, 106-134.

-----, -----, and M. McCumber, 1982: Three dimensional simulations of cumulus congestus clouds on GATE day 261. To appear in J. Atmos. Sci., 39.

Smagorinsky, J., 1956: On the inclusion of moist adiabatic processes in numerical prediction models. Ber. Dtsch. Wetterdienstes, 5, 82-90.

Sommeria, G., 1976: Three-dimensional simulation of turbulent processes in an undisturbed trade wind boundary layer. J. Atmos. Sci., 33, 216-241.

-----, and M.A. LeMone, 1978: Direct testing of a three-dimensional model of the planetary boundary layer against experimental data. J. Atmos. Sci., 35, 25-39.

Soong, S.-T., and Y. Ogura, 1973: A comparison between axi-symmetric and slab-symmetric cumulus cloud models. J. Atmos. Sci., 30, 879-893.

-----, and -----, 1976: A determination of the tradewind cumuli population using BOMEX data and an axi-symmetric cloud model. J. Atmos. Sci., 33, 992-1007.

-----, and -----, 1980: Response of tradewind cumuli to large-scale processes. J. Atmos. Sci., 37, 2035-2050.

-----, and W.-K. Tao, 1980: Response of deep tropical cumulus clouds to mesoscale processes. J. Atmos. Sci., 37, 2016-2034.

Stailey, J.E., 1978: Comparison of precipitating cumulus cells: Model-generated versus radar-observed. MS Thesis, MIT, 134 pp.

Stommel, H., 1947: Entrainment of air into a cumulus cloud. J. Meteor., 4, 91-94.

Thompson, R.M., Jr., S.W. Payne, E.E. Recker, and R.J. Reed, 1979: Structure and properties of synoptic-scale wave disturbances in the Intertropical Convergence Zone of the eastern Atlantic. J. Atmos. Sci., 36, 53-72.

Warner, J., 1970: The microstructure of cumulus cloud. Part III: The nature of the updraft. J. Atmos. Sci., 27, 682-688.

-----, 1977: Time variation of updraft and water content in small cumulus clouds. J. Atmos. Sci., 34, 1306-1312.

Warner, C., 1979. Cloud Measurements on Day 245 of GATE. Technical Report No. 5, Dept. of Envir. Sci., U. of Virginia, Charlottesville, 50 pp.

Yamasaki, M., 1977: A preliminary experiment of the tropical cyclone without parameterizing the effects of cumulus convection. J. Meteor. Soc. Jap., 55, 11-31.

Yanai, M., S. Esbensen, and J. Chu, 1973: Determination of average bulk properties of tropical cloud clusters from large-scale heat and moisture budgets. J. Atmos. Sci., 30, 611-627.

Yau, M.-K., 1977: Microphysical-dynamical processes and interactions in a precipitating cumulus cell model. Sc.D. Thesis, MIT, 256 pp.

-----, 1979: Pressure perturbation and cumulus convection. J. Atmos. Sci., 36, 690-694.

-----, 1980: A two-cylinder model of cumulus cells and its application in computing cumulus transports. J. Atmos. Sci., 37, 2470-2485.

-----, and P.M. Austin, 1979: A model for hydrometeor growth and evolution of raindrop size spectra in cumulus cells. J. Atmos. Sci., 36, 655-668.

Zipser, E.J., 1969: The role of organized unsaturated convective downdrafts in the structure and rapid decay of an equatorial disturbance. J. Appl. Meteor., 8, 799-814.

-----, 1977: Mesoscale and convective scale downdrafts as distinct components of squall-line structure. Mon. Wea. Rev., 105, 1568-1589.

-----, and M.A. LeMone, 1980: Cumulonimbus vertical velocity events in GATE. Part II: Synthesis and model core structure. J. Atmos. Sci., 37, 2458-2469.

-----, R.J. Meitin, and M.A. LeMone, 1981: Mesoscale motion fields associated with a slowly moving GATE convective band. J. Atmos. Sci., 38, 1725-1750.